Investigation of Electrical and Optical Characterisation of HBTs for Optical Detection

A thesis submitted to The University of Manchester for the degree of
Doctor of Philosophy
in the Faculty of Engineering and Physical Sciences

2016

Yongjian Zhang

SCHOOL OF ELECTRICAL AND ELECTRONIC ENGINEERING

MICROWAVE & COMMUNICATION SYSTEMS RESEARCH GROUP

List of Contents

List of Figures

List of Tables

Abstract

The University of Manchester

Yongjian Zhang

Doctor of Philosophy

Investigation of electrical and optical characterisation of HBTs for optical detection

2016

In this thesis, a detailed study of the electrical and optical characterisations of Heterojuction Bipolar Transistors (HBTs) for optical detection is presented. By comparing both DC and optical characterisations between $In_{0.49}Ga_{0.51}P$/GaAs Single Heterojuction Bipolar Transistors (SHBTs) and Double Heterojuction Bipolar Transistors (DHBTs), the advantages of using the DHBT as a short wavelength detector are shown. Phenomena related to the base region energy band bending in the DHBT caused by a self-induced effective electric field is discussed and its effects on the performance of the device are elaborated.

The use of an eye diagram has been employed to provide requisite information for performance qualification of SHBT/DHBT devices. These give a more detailed understanding compared to conventional S-parameters method. A detailed comparison of $In_{0.49}Ga_{0.51}P$/GaAs SHBT and DHBT performance using an eye diagram as a functional tool by adopting a modified T-shaped small signal equivalent circuit are given. By adopting this modified T-shaped small signal equivalent circuit, the use of $In_{0.49}Ga_{0.51}P$/GaAs Double Heterojuction Phototransistors (DHPT) as a short wavelength photodetector is analysed. It is therefore shown that an eye diagram can act as a powerful tool in HBTs/HPTs design optimisations, for the first time in this work.

In order to predict the spectral response (SR) and optical characterisations of GaAs-based HPTs, a detailed theoretical absorption model is also presented. The layer dependence of an optical flux absorption profile, along with doping dependent absorption coefficients are taken into account for the optical characterisation prediction. With the aim of eliminating the limitation of current gain as a prerequisite, analytical modelling of SR has been developed by resolving the continuity equation and applying realistic boundary conditions. Then, related physical parameters and a layer structure profile are used to implement simulations. A good agreement with the measured results of the $Al_{0.3}Ga_{0.7}As$/GaAs HPT is shown validating the proposed theoretical model.

Declaration

That no portion of the work referred to in the thesis has been submitted in support of an application for another degree or qualification of this or any other university or other institute of learning.

Copyright Statement

Acknowledgements

I take this opportunity to express my profound gratitude and deep regards to my supervisor Professor A. A. Rezazadeh for his exemplary guidance, monitoring and constant encouragement throughout the course of this project. I would like to thank him for giving me the opportunity to do my research. During my time as a PhD student I have consequently felt a great support and freedom to develop in my own direction for which I am very grateful. I not only enjoyed doing this project, but also learned a lot of new things.

I would like to thank my postgraduate colleagues Dr. Hassan A. Khan, Dr. Emerson P. Sinulingga, Peter B. Kyabaggu, Mohammad A. Alim, Mayahsa M. Ali and Norshakila Haris for their helpful assistance and friendly advice.

I would like to express my gratitude to my parents-in-law Yongbin Fan & Jianjun Wang, and my parents Maoye Zhang & Quanmin Zhang for their unconditional and unfailing emotional support throughout my PhD studies.

Finally I would like to thank my wife Shushen and son Xuanrui for their understanding, encouragement, support and unwavering love.

List of Publications

Journals

[1] Khan, H. A., Rezazadeh, A. A., Zhang, Y. “Photoresponse Modelling and Analysis of InGaP/GaAs Double-HPTs”, IEEE Journal of Quantum Electronics, Vol. 50, issue 12, pp. 1044-1051, 2014.

Conferences

[2] Zhang, Y., Rezazadeh, A. A., Khan, H. A., Sinulingga, E. P., Kyabaggu, P. B., Alim, M. A. “Simulation and analysis of InGaP/GaAs DHPTs using eye diagrams for short wavelength optical detection”, Proceedings of European Microwave Week Conference, Rome, Italy, pp. 524-527, Oct. 2014.

[3] Alim, M. A., Rezazadeh, A. A., Ali, M. M., 1, Sinulingga, E. P., Kyabaggu, P. B.,, Zhang, Y., Gaquière, C. “Thermal Characterisation of AlGaN/GaN HEMT on Silicon Carbide Substrate for High Frequency Application”, Proceedings of European Microwave Week Conference, Rome, Italy, pp. 210-213, Oct. 2014.

[4] Alim, M. A., Rezazadeh, A. A., Gaquiere, C., Mayahsa, M. A., Zhang, Y., Haris, N., Kyabaggu, P. B. “Nonlinearity Measurement and Analysis of 0.25μm GaN HEMT Over Frequency and Temperature Using Two-Tone Intermodulation Distortion”, Accepted for oral presentation in the 45th European Microwave Conference, Paris, France, September, 2015.

[5] Alim, M. A., Rezazadeh, A. A., Gaquiere, C., Mayahsa, M. A., Haris, N., Kyabaggu, P. B., Zhang, Y. “0.25μm AlGaN/GaN HEMT Nonlinearity Modelling and Characterization Over a Wide Temperature Range”, Accepted for oral presentation in the 10th European Microwave Integrated Circuits Conference, Paris, France, Sept. 2015.

[6] Haris, N., Kyabaggu, P. B., Alim, M. A., Zhang, Y., Rezazadeh, A. A. “Device Considerations and Characterisation of Double-Channel GaAs pHEMT Schottky Diodes for Limiter Applications”, Accepted as a poster in the 10th European Microwave Integrated Circuits Conference, Paris, France, Sept. 2015.

[7] Kyabaggu, P. B., Haris, N., Rezazadeh, A. A., Alim, M. A., Sinulingga, E. P., Zhang, Y. “Design and Realisation of a pHEMT Diode MMIC Power Limiter using 3D GaAs Multilayer CPW Technology”, Accepted for oral presentation in the 10th European Microwave Integrated Circuits Conference, Paris, France, Sept. 2015.

Chapter 1. Introduction

1.1 Introduction

Heterojunction Bipolar Transistors (HBTs) were proposed and patented by W. Shockley in 1948 and 1951, respectively [1]. A detailed theory and analysis was developed by H. Kromer [2]. HBTs are formed by two back to back connected p-n junctions, which consist of the emitter, base and collector layers. By appropriately selecting two semiconductors with different band gaps to form a heterojunction, electrons and holes can be controlled separately and independently [3] and therefore some of the issues with conventional bipolar Si transistors can be addressed. These advantages over standard Si-based homostructure bipolar transistors allow III-V HBTs to be used in broad variety of applications over the last decade [4]. Specifically, GaAs-based HBTs demonstrate the capability of handling high-power output densities at microwave frequencies.

The role of heterojunction transistors in optoelectronics industry has also been increasing in realising various broad-band communication systems, such as fibre-radio wireless communication systems and high-bit-rate fibre-optic communications systems [5]. The internal transistor reduces post-amplification requirements resulting in optimum receiver configuration [6]. In particular efficient conversion between optical signals and electrical signals becomes challenging. Thus, an efficient interface between optical and microwave is key for achieving higher performance and improved integration in optoelectronic systems [6]. Accurate spectral models for GaAs and InP based material systems have been studied for both short and long wavelength communication [7-10]. Previously pin photodiodes have been extensively employed for photodetection. However, subsequent amplification and a trade-off between the intrinsic layer width and the transit time is still an issue, in spite of their simple biasing and operation [11-12]. Avalanche photodiodes (APDs) on the other hand, due to multiplication process, an additional noise component, known as "excess noise" is produced and added to the signal. This increases the noise-equivalent power accordingly. Similarly, Schottky photodetectors cannot provide any internal amplification for the signal and have a very high leakage current for higher temperatures.

Phototransistors are therefore beneficial as they provide high internal gain without the avalanche noise [13-15]. In addition, their inherent compatibility with HBTs allows Monolithic-Microwave Integrated-Circuit (MMIC) integration [16-17]. This allows standard manufacture of monolithically integrated photoreceivers (HBTs/HPTs) for microwave- and millimetre- wave photoreceivers in optical communication systems [18]. Further, compared with field-effect devices, for instance, Metal–Semiconductor Field-Effect transistors (MESFETs) or High Electron Mobility Transistors (HEMTs), Heterojuction Phototransistors (HPTs) are also capable of handling high power density with higher linearity, superior power-added-efficiency, and smaller frequency noise advantages [19].

HBTs can be of two types: single-HBT and double-HBT. DHBTs contain wide-bandgap emitter and collector to form two heterojunctions, and offer several advantages such as smaller turn-on voltage, lower Base-Collector leakage current, larger breakdown voltage and temperature-insensitive current gain compared to SHBTs. From the application's point of view, these characteristics make DHBTs attractive enough to fit the requirements and technical challenges of power applications, such as high voltage operation and high breakdown voltage [20]. Therefore for newer optical communication systems, DHBTs are employed to build compact, high-performance equipment [21-22]. The role of DHBTs is critical in these MMIC photoreceivers. And analysis of both DC and optical characterisations is the key focus for this work.

The devices used in this work include various geometry SHBTs and DHBTs fabricated at the Microwave Engineering Research group, The University of Manchester. The prior work of this group includes analysis and modelling of SHBTs and this current work focusses on DHBTs with analysis and measurements on various DC and optical parameters.

S-parameters are known as a common tool to characterise the RF performance of semiconductor components. However, information about digital data can not be obtained through this method. Therefore, eye diagrams, which are produced by overlapping various segments of output signal, are capable of characterising circuits or devices for digital application as a complementarity [23]. It is reported [24] that eye diagrams can be used to visually depict the output response of any circuit to an input signal and to validate circuits. Eye parameters extracted from eye diagrams can offer a great deal of information about deterioration of the transmitted signal. By carefully analysing them, this information can be directly attributed to the physics of the devices. Hence in this thesis, for the first time, eye diagrams are adopted as a tool to characterise microwave and optical devices (SHBTs/DHBTs) using a modified small signal circuit and help device optimisation [25].

Spectral response (SR) is also a key parameter of HPTs. Therefore, extensions to SHBTs [26-28], various workable models for DHBTS are discussed. This provides a detailed insight into the behaviours of HPTs used for phototransistors through SR theoretical modelling. This study will clearly show the relationship between the modelled parameters on the one side, and the physical parameters on the other. Only such an understanding will allow for the optimisation of devices, while with the possibility of investigating various physical processes inside a device, may lead to the intuitive understanding of device function.

1.2 Outline of the thesis

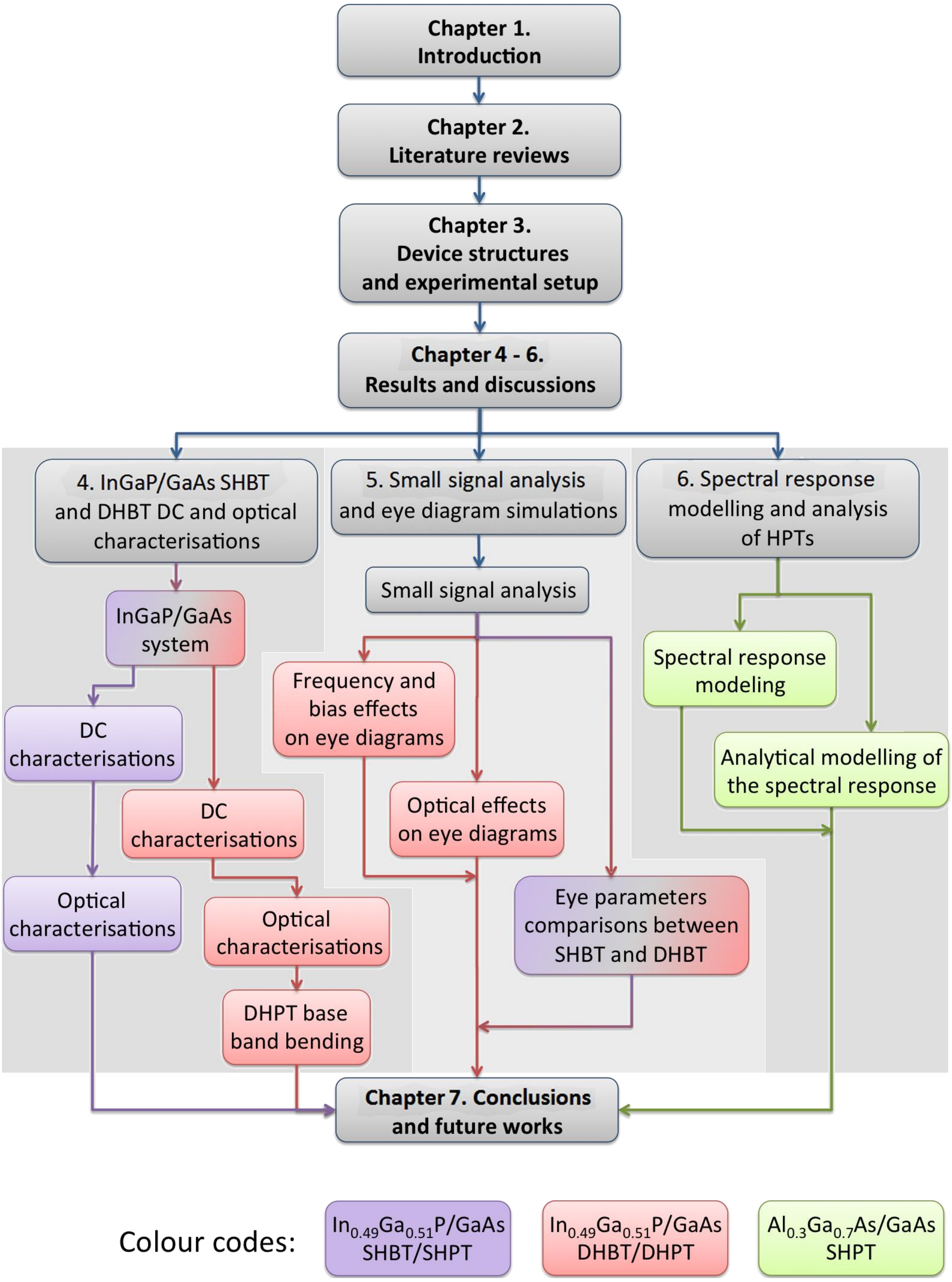

Figure 1.2.1: Flow chart of the thesis

Chapter 1: ***Introduction***

A general discussion of the aims and objectives for this project is presented. And the structure of the thesis and the content are outlined.

Chapter 2: ***Literature review***

Firstly, physical based electrons and holes operation theory for BJT and HBT are described using current equations. Then emitter-base abrupt and material systems for HBTs are discussed. Secondly, optical detection principles, including comparisons between different types of photodetectors are given. HBTs operations under 2-terminal and 3-terminal configurations are shown. Lastly, eye diagram definition and different eye diagram parameters are explained in detail.

Chapter 3: ***Device structures and experimental setup***

The doping profiles, layer structures and micrographs of the devices under test include $In_{0.49}Ga_{0.51}P$/GaAs SHBT (on MR873), DHBT (on MR1095) with emitter contact diameter = 100µm and $Al_{0.3}Ga_{0.7}As$/GaAs SHBT (on K15) with emitter contact diameter = 130µm, are presented. After that, the simulation setup for the generation eye diagram is discussed. In the next section, block diagrams of the setup to characterise laser diodes and measured output characteristics of LD-635-5I laser diode are given. Lastly, an experimental setup to obtain the DC electrical characteristics and the SR of HPTs is shown using a block diagram.

Chapter 4: ***$In_{0.49}Ga_{0.51}P$/GaAs SHBT and DHBT DC and optical characterisations***

In this chapter, firstly, the $In_{0.49}Ga_{0.51}P$/GaAs SHBT DC and 2-terminal optical characterisations are shown. These are followed by the optical characterisations of the device under base current bias, and the voltage bias condition. Accordingly, the same measurement procedures are carried out, using $In_{0.49}Ga_{0.51}P$/GaAs DHBT. The comparison between the two devices is presented. When the DHBT is used as a short wavelength photodetector, the B-C junction works as a uni-travelling-carrier; meanwhile, the base self-induced field caused base band bending is discussed and the measurement elaborated.

Chapter 5: ***Small signal analysis and eye diagram simulations***

The eye diagram shown in this chapter can be used, not only as a mere visual measurement tool, but also as a tool to characterise devices. The T-shaped small signal equivalent circuit and parameters are presented. By adopting the small signal model, the eye diagram simulation results of the $In_{0.49}Ga_{0.51}P$/GaAs DHBT are shown. Eye parameters and their dependencies on bitrate, bias and optical input power are discussed. Later, a comparison between $In_{0.49}Ga_{0.51}P$/GaAs SHBT and DHBT using an eye diagram is shown.

Chapter 6: ***Spectral response and analysis of HPTs***

$Al_{0.3}Ga_{0.7}As$/GaAs SHBT is the focus of attention in this chapter and the device's spectral response is successfully achieved by detailed modelling. A detailed layer absorption model is shown, and the physical parameters as well as the layer structures are taken account of, in order to carry out the simulation. A good agreement between simulated and measured results is achieved.

Chapter 7: ***Conclusion and future work***

The success of each sub-chapter of chapter 4 in achieving the initial objectives is concluded and some aspects for further analysis are identified.

References

[1] Shockley, W. “Circuit Element Utilizing Semiconductive Material”, United States Patent 2,569,347, 1951.

[2] Abernathy, C. R., Pearton, S. J., Ren, F., Hobson, W. S., Fullowan, T. R., Katz, A., Jordan, A. S. and Kovalchick, J. “Carbon doping of III-V compounds grown by MOMBE”, Proceedings of the Second International Conference on Chemical Beam Epitaxy and Related Growth Techniques - (ICCBE-2), December 11, 1989 - December 13, 1989.

[3] Ahmad, T., Rezazadeh, A.A., Gill, S.S. “Improved Parameter Extraction Method for Microwave HBTs”, Modelling, Design and Application of MMIC's, IEE Colloquium on, pp. 5/1-5/8, 17 Jun 1994.

[4] Y. Zhang, A. A. Rezazadeh, H. A. Khan, E. P. Sinulingga, P. B. Kyabaggu, and M. A. Alim, "Simulation and Analysis of InGaP/GaAs DHPTs Using Eye Diagrams for Short Wavelength Optical Detection," presented at the IEEE European Microwave Week Rome, Italy, 2014.

[5] Ito, H., Nagatsuma, T., Ishibashi, T. “Recent development on uni-traveling-carrier photodiodes and their applications”, Proc. LEOS, San Diego, CA , vol.1, pp. 386-387, 2001.

[6] Khan, H. “Spectral response modelling and analysis of heterojuction bipolar phototransistors”, Ph.D thesis, Microwave and Communication Systems Research Group, School of Electrical and Electronics Engineering, University of Manchester, 2010.

[7] H. A. Khan, A. A. Rezazadeh, S. Sohaib, and T. Tauqeer, "Detailed Analysis on the Spectral Response of InP/InGaAs HPTs for Optoelectronic Applications," Quantum Electronics, IEEE Journal of, vol. 48, pp. 576-580, 2012.

[8] H. A. Khan, A. A. Rezazadeh, and S. Sohaib, "Modeling and analysis of the spectral response for AlGaAs/GaAs HPTs for short wavelength optical communication," Journal of Applied Physics, vol. 109, pp. -, 2011.

[9] H. A. Khan and A. A. Rezazadeh, "Impact of surface recombination on the responsivity of GaAs- and InP-based heterojunction photo-transistors," in Microwave Integrated Circuits Conference (EuMIC), 2011 European, 2011, pp. 49-52.

[10] H. A. Khan, A. A. Rezazadeh, and R. Saleem, "Impact of Collection Efficiency on the Optical Responsivity of Lattice Matched InP/InGaAs Heterojunction Phototransistors," Japanese Journal of Applied Physics, vol. 51, p. 072202, 2012.

[11] Ishii, K., Nosaka, H., Ida, M., Kurishima, K., Enoki, T., Shibata, T., Sano, E.

"High-input-sensitivity, low-power 43 Gbit/s decision circuit using InP/InGaAs DHBTs", Electronics Letters, vol. 38, pp. 557-558, 2002.

[12] Frimel, S. M. and Roenker, K. P. "Thermionic-field-diffusion model for Npn bipolar heterojunction phototransistors", Journal of Applied Physics, vol. 82, pp. 1427, 1997.

[13] Hafez, W., Lai, J. W. and Feng, M. "Low-power high-speed operation of submicron InP-InGaAs SHBTs at 1 mA", IEEE Electron Device Letters, vol. 24, pp. 427-429, 2003.

[14] Jiang, N. and Ma, Z. "Current gain of SiGe HBTs under high base doping concentrations", Semiconductor Science and Technology, vol. 22, pp. 168-72, 2007.

[15] Sano, E., Kurishima, K., Nakajima, H. and Yamahata, S. "High-speed, low power lightwave communication ICs using InP/InGaAs double heterojunction bipolar transistors", IEICE Transactions on Electronics, vol. E83-C, pp. 2000-2006, 2000.

[16] Shimura, T., Komaru, M., Izumi, S., Kuragaki, T., Sakai, M., Nakano, H., Terazono, S., Nagahama, K., Nishitani, K., Otsubo, M. "High power density and high efficiency AlGaAs/GaAs heterojunction bipolar transistors for high power MMICs", presented at 23rd International Conference on Solid State Devices and Materials - SSDM '91, August 27, 1991 - August 29, 1991, Yokohama, Japan, 1991.

[17] Di Forte-Poisson, M. A., Delage, S. L. and Cassette, S. "GaAs-based materials for heterojunction bipolar transistors: Reliability results and MMIC applications", papers presented at the ICMAT 2001 Symposium N: Materials for Optoelectronics and High frequency Electronics applications, vol. 4, issue 6, pp. 503-511, 2001.

[18] Leven. A., Hill, M., Houtsma, V., Kopf. R., Baeyens. Y, "InP-based double-heterostructure phototransistors with 135 GHz optical-gain cut off frequency", Electronics Letters, vol. 40, issue 13, p. 833-834, 2004.

[19] Rezazadeh, A.A. and Sotoodeh, M. "Design and technology of InGaP/GaAs DHBTs", Advanced Semiconductor Devices and Microsystems, The Third International Euro Conference pp. 119-125, 16-18 Oct. 2000

[20] Kamitsuna, H., Matsuoka, Y., Yamahata, S., Shigekawa, N. "Ultrahigh-Speed InP/InGaAs DHPTs for OEMMICs", IEEE Transactions on Microwave Theory and Techniques, vol. 49, no. 10, pp. 1921-1925, October 2001.

[21] Kamitsuna, H., Yokosuka, Matsuoka, Y., Yamahata, S., Kurishima, K. "A monolithically integrated photoreceiver realized by InP/InGaAs double-heterostructure bipolar transistor technologies for optical/microwave interaction systems", Gallium Arsenide Integrated Circuit (GaAs IC)

Symposium, 1995. Technical Digest 1995. 17th Annual IEEE, pp. 185-188, Oct. 29 1995-Nov. 1 1995.

[22] “Eye diagram Measurement in Advanced Design System”, pp. 4-5, Agilent Technologies.

[23] Selli, G, et al. “Validation of equivalent circuits extracted from S-parameter data for eye-pattern evaluation”, Electromagnetic Compatibility, EMC 2004, USA, 9-13, vol. 2, pp. 666 – 671, Aug. 2004.

[24] Zhang, Y., Rezazadeh, A. A., Khan, H. A., Sinulingga, E. P., Kyabaggu, P. B., Alim, M. A. “Simulation and analysis of InGaP/GaAs DHPTs using eye diagrams for short wavelength optical detection”, Proceedings of European Microwave Week Conference, Rome, Italy, pp. 524-527, Oct. 2014.

[25] H. A. Khan and A. A. Rezazadeh, "Analytical modeling of the spectral response of heterojunction phototransistors," IEEE Electron Device Letters, vol. 30, pp. 1158-1160, 2009.

[26] H. A. Khan, Rezazadeh, Ali A., Subramaniam, Suba C., "Spectral response modelling of heterojunction phototransistors for short wavelength transmission," in European Microwave Integrated Circuit Conference, EuMIC 2008, October 27, 2008 - October 31, 2008, Amsterdam, Netherlands, 2008, pp. 346-349.

[27] S. A. Bashar, "Study of indium tin oxide (ITO) for novel optoelectronic devices," UMIST, Manchester, pp. 106-109, 1998.

[28] S. Bashar and A. Rezazadeh, "Fabrication and spectral response analysis of AlGaAs/GaAs and InP/InGaAs HPTs with transparent ITO emitter contacts," IEE Proceedings-Optoelectronics, vol. 143, pp. 89-93, 1996.

Chapter 2. Literature Review

2.1 Operation theory of Bipolar Junction Transistor

The bipolar junction transistor, one of the most important semiconductor devices, was invented by a research team at Bell Laboratories [1]. It has been used extensively in high-speed circuits, analog circuits and power applications [1].

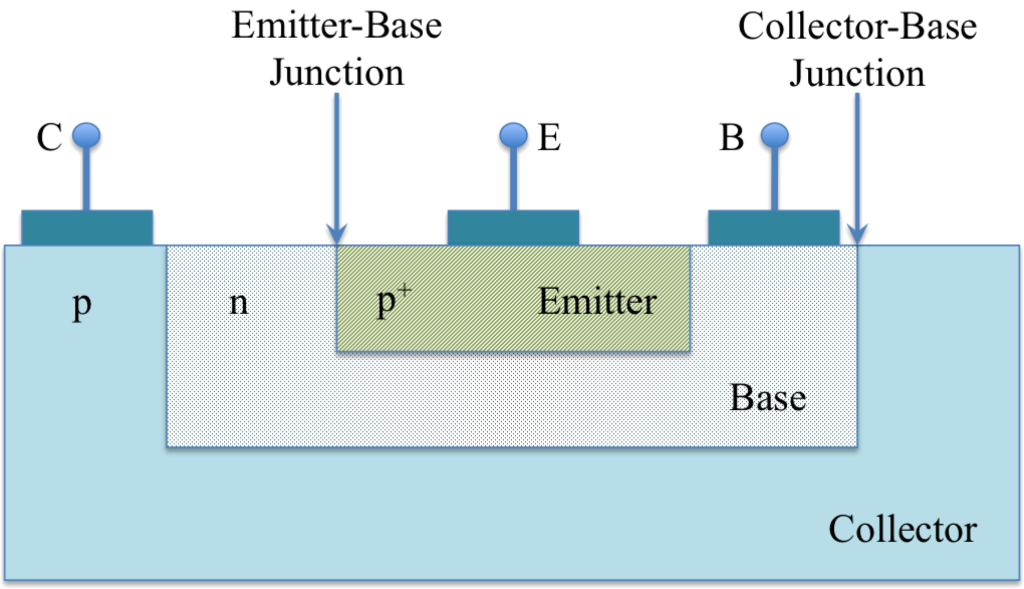

Figure 2.1.1: Perspective view of a silicon n-p-n bipolar transistor

Figure 2.1.1 shows a typical silicon p-n-p bipolar transistor. It is formed as two p-n junctions combined together. All three parts of the bipolar transistor are made from the same material. According to figure 2.1.1, the transistor has a heavily doped p^+ region called the “emitter”. The narrow central n region between the two p regions is the “base”. The last lightly doped p region is described as the “collector”. There is also another kind of structure available, which is the n-p-n transistor, which has a complemental configuration to the p-n-p transistor. Generally in a high frequency area the n-p-n structure of a silicon transistor is chosen. This is because the electron diffusion constant in silicon is larger than that of the hole. This means the transit time of electrons across the base area is shorter than that of the hole. The frequency response could be improved.

Normally, bipolar transistors work in the active mode, which means the emitter-base junction is forward biased and the collector-base junction is reverse biased. The biased condition is shown in figure 2.1.2:

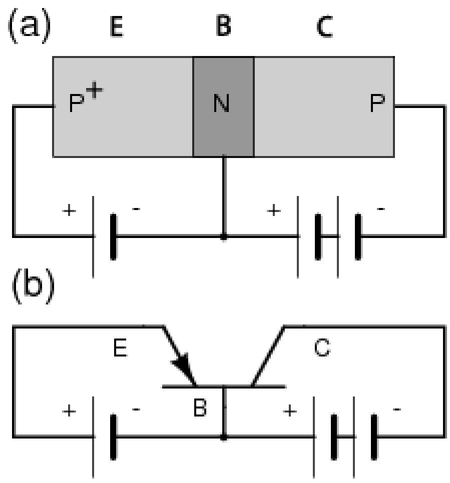

Figure 2.1.2: (a) One dimensional view of p-n-p bipolar transistor biased in active mode (b) p-n-p bipolar transistor schematic symbols biased configuration

The bipolar transistor does not work simply as two diodes connected back to back. The corresponding situation when the transistor works in the active mode is shown in figure 2.1.3.

Figure 2.1.3(a) illustrates the schematic connection of a p-n-p bipolar transistor working with a common base configuration. The charge densities and the electric fields are shown in figure 2.1.3(b) and (c). Due to different biasing conditions, the depletion region width of the emitter-base junction and collector-base junction is different. The energy band diagram of the device operating under the active mode is shown in figure 2.1.3(d):

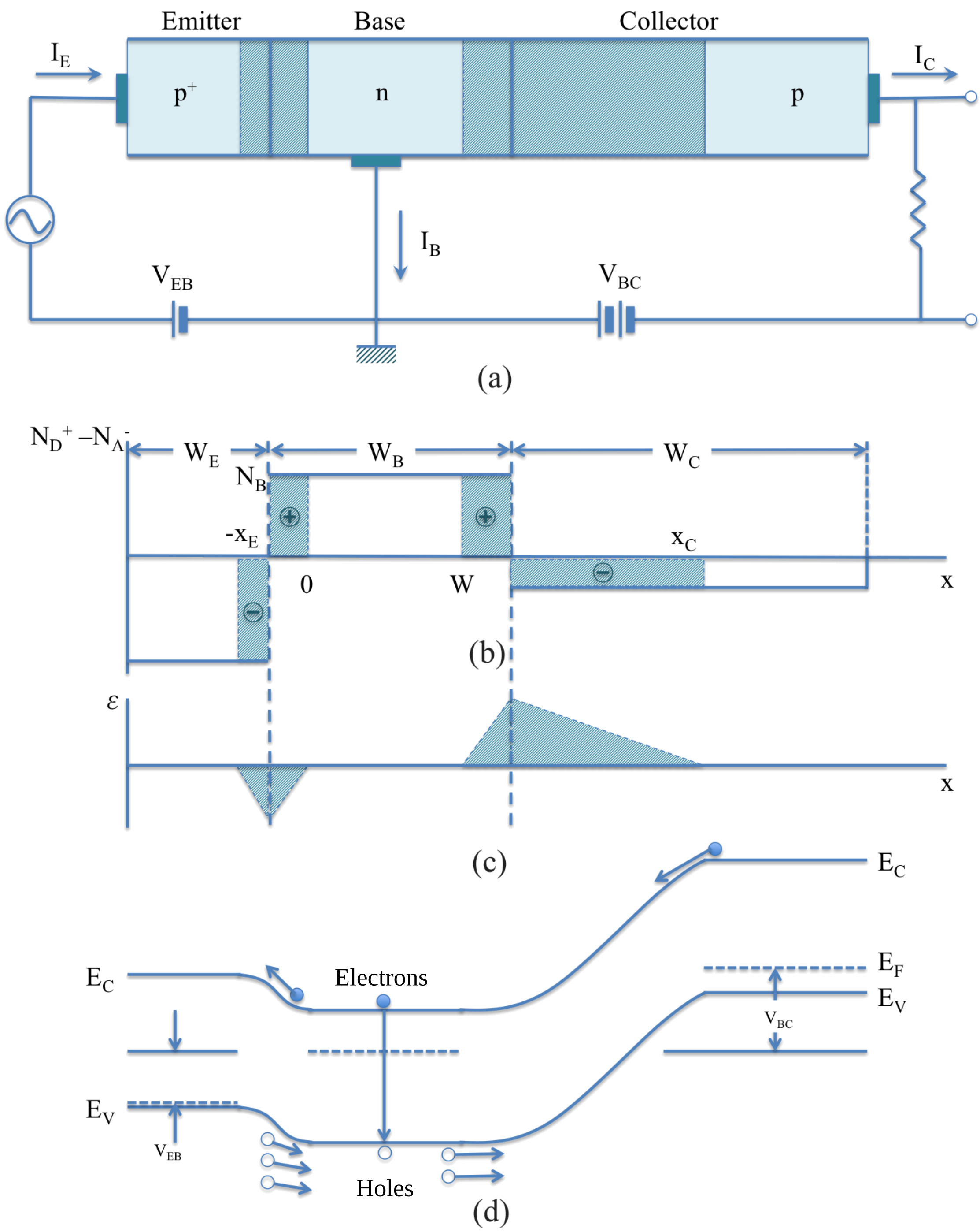

Figure 2.1.3: (a) One dimensional view of p-n-p bipolar transistor biased in active mode. (b) Doping profiles and depletion regions under biasing condition. (c) Electric field profile. (d) Energy band diagram. [1]

In figure 2.1.3 we notice that due to the biasing circuit, we are hopeful that the holes injected from the emitter to the base can finally reach the collector. This requires the base of the bipolar transistor to be thin. Assuming there is no generation recombination in the depletion region, the base width should be narrow so that holes can diffuse through it without recombination. If most of the injected holes in the base can arrive at the collector successfully, the collector hole current will nearly equal that of the emitter hole current.

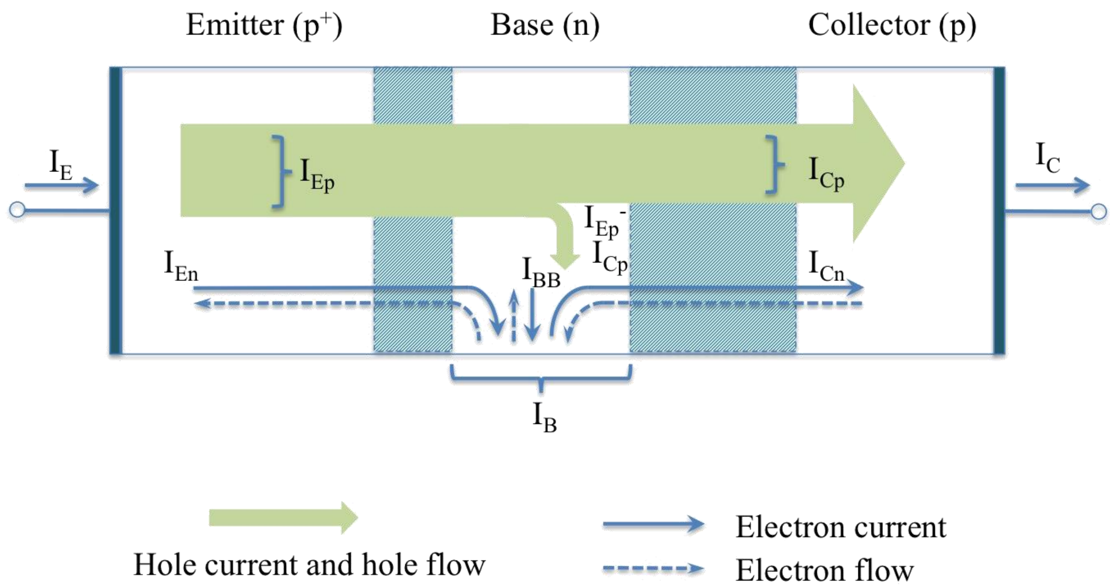

Figure 2.1.4: Various current components in a p-n-p transistor in active mode of operation [1]

The various current components in a p-n-p bipolar transistor biased in active mode are shown in figure 2.1.4. Here I_{Ep} is known as the holes that are injected from emitter to base. It is the main current in the transistor. In the base there are many current components. I_{En} is the current created by the electrons that are injected from base to emitter. By heavy doping in emitter or heterojunction, I_{En} can be reduced. I_{BB} is equal to I_{Ep} - I_{Cp}, which is the electron current from the exoteric circuit, which aims to replace the recombined electrons. I_{Cn} is the current generated by electrons drifting from collector to base.

Using Kirochoff's current law, the following equations can be expressed [1]:

$$I_E = I_{Ep} + I_{En} \tag{2.1.1}$$

$$I_C = I_{Cp} + I_{Cn} \tag{2.1.2}$$

$$I_B = I_E - I_C = I_{En} + (I_{Ep} - I_{Cp}) - I_{Cn} \tag{2.1.3}$$

The common base current gain α_0 is defined as:

$$\alpha_0 \equiv \frac{I_{Cp}}{I_E} \tag{2.1.4}$$

Then we get:

$$\alpha_0 = \frac{I_{Cp}}{I_{Ep} + I_{En}} = (\frac{I_{Ep}}{I_{Ep} + I_{En}})(\frac{I_{Cp}}{I_{Ep}}) \tag{2.1.5}$$

One part of equation 2.1.5 is defined as the emitter efficiency γ:

$$\gamma \equiv \frac{I_{Ep}}{I_E} \tag{2.1.6}$$

The other part is called base transport factor α_T:

$$\alpha_T \equiv \frac{I_{Cp}}{I_{Ep}} \tag{2.1.7}$$

So $\alpha_0 = \gamma\ \alpha_T$, and the equation 2.1.2 can be rewritten as:

$$I_C = \alpha_0 I_E + I_{Cn} \tag{2.1.8}$$

I_{Cn} is the base and collector current while emitter is the open circuit. It can also be defined as I_{CBO} which is the C-B leakage current. Then the equation 2.1.8 becomes:

$$I_C = \alpha_0 I_E + I_{CBO} \tag{2.1.9}$$

Because the current in all three terminals of a transistor is related to the minority carriers' distribution in the base region [1], we use the field-free steady-state continuity equation and boundary conditions for active mode. Equations 2.1.6 and 2.1.7 can be developed as:

$$\gamma = \frac{1}{1 + \frac{D_E}{D_p} \cdot \frac{N_B}{N_E} \cdot \frac{W}{L_E}} \tag{2.1.10}$$

$$\alpha_T \approx 1 - \frac{W^2}{2{L_p}^2} \tag{2.1.11}$$

where: D_p diffusion is constant, D_E diffusion is constant in emitter, N_B is impurity doping in base, N_E is impurity doping in emitter, W is Base region thickness, L_E is Emitter diffusion lengths and L_p is diffusion length of holes.

From equation 2.1.10 we know that in order to improve emitter efficiency γ, the ratio of N_B / N_E should be decreased. That is the reason why the emitter needs to be heavily doped and the base lower doped also; that is, since the diffusion length of holes is almost constant. Equation 2.1.11 shows that the only way to improve base transport factor α_T is to reduce base width. That is the reason why the bipolar transistor has a narrow base. However, high emitter doping and low base doping also bring many drawbacks. High doping emitter causes high E-B capacitance and low base doping causes high base resistance. Both of these drawbacks may reduce transistor high frequency performance. Heterojunction can solve this problem, and this will be discussed later.

Next, the common emitter current gain β_0 is defined as [1]:

$$\beta_0 = \frac{\alpha_0}{1-\alpha_0} \tag{2.1.12}$$

The collector-emitter leakage current I_{CEO} for $I_B = 0$ is defined as [1]:

$$I_{CEO} \equiv \frac{I_{CBO}}{1-\alpha_0} \tag{2.1.13}$$

Finally equation 2.1.8 becomes:

$$I_C = \frac{\alpha_0}{1-\alpha_0} I_B + \frac{I_{CBO}}{1-\alpha_0} = \beta_0 I_B + I_{CEO} \tag{2.1.14}$$

2.2 Operation theory of Heterojunction Bipolar Transistor

2.2.1 Heterojunction bipolar transistor

The concept of Heterojunction Bipolar Transistors (HBTs) was proposed by W. Shockley in 1948 and granted a patent in 1951 [2]. Later, H. Kromer developed the detailed theory and analysis of HBTs [3]. If the appropriate band gap and electric fields are selected carefully, electrons and holes can be controlled separately and independently [4]. That is the advantage which homostructures cannot achieve.

The idea of HBTs is that two semiconductors with different band gaps are used to form a heterojunction. A wide band gap material (e.g. InGaP, AlGaAs) is used to fabricate the emitter, while a narrow band gap material (e.g. InGaAs, GaAs) is used for the base. This can thus form an emitter-base junction called a "Heterojunction". The energy diagram for a heterojunction is shown in figure 2.2.1:

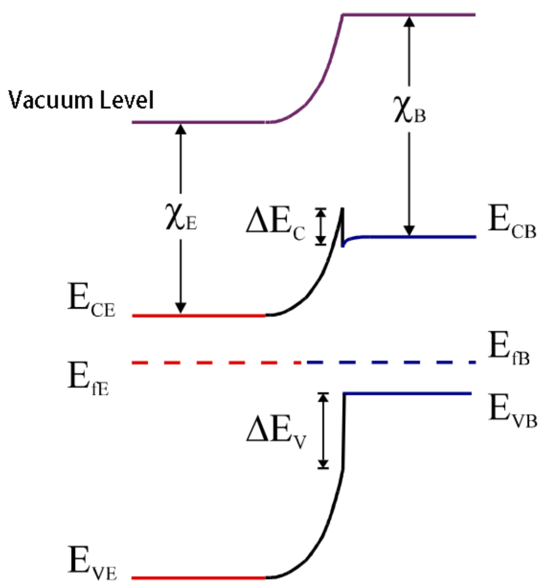

Figure 2.2.1: Energy band diagram of a wide band gap N-type emitter and a narrow band gap P-type base Heterojunction [4]

As figure 2.21 shows Fermi level is aligned between two sides of the heterojunction. The electron affinities of both emitter and base are different, while the band gap energies are different also. Therefore, discontinuities appear both in the conduction band and the valence band. The conduction band discontinuity is:

$$\Delta E_C = \chi_B - \chi_E \tag{2.2.1}$$

The valence band discontinuity is ΔE_v, making the total band gap discontinuity:

$$\Delta E_g = \Delta E_c + \Delta E_v \tag{2.2.2}$$

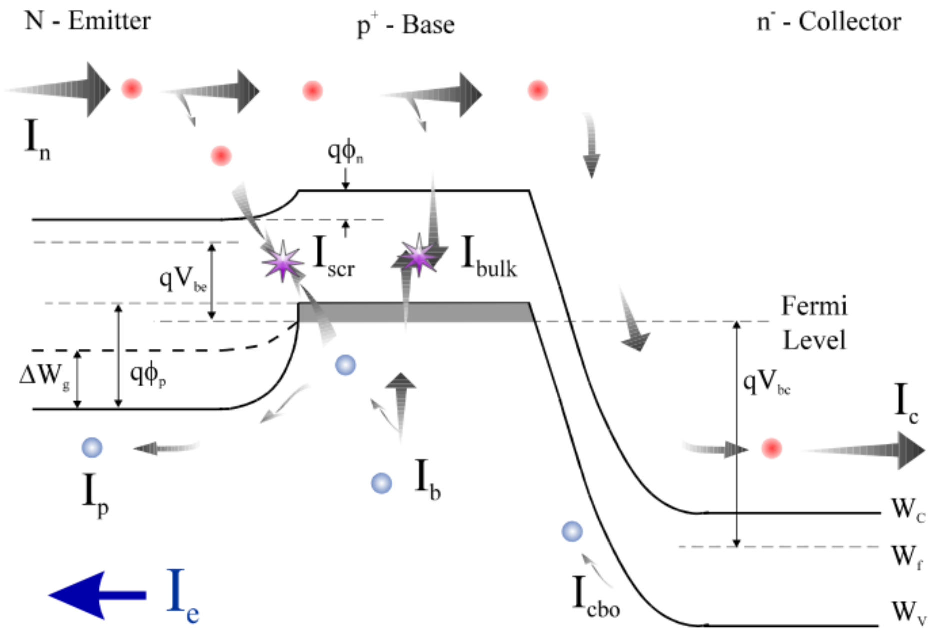

Figure 2.2.2: Band diagram of a n-p-n HBT biased in emitter ground configuration [4]

The operating principle of a HBT is similar to a BJT. The band diagram of a n-p-n HBT biased in an emitter ground configuration is shown in figure 2.2.2. Here it is assumed that there is no band edge discontinuity for the conduction band due to the emitter junction grading.

The following current components can be summarised as:

Emitter current:

$$I_e = I_n + I_p + I_{scr} \tag{2.2.3}$$

Base current:

$$I_b = I_p + I_{bulk} + I_{scr} - I_{cbo} \tag{2.2.4}$$

Collector current:

$$I_c = I_n - I_{bulk} + I_{cbo} \tag{2.2.5}$$

where I_n is the current of electrons injected from emitter to base, I_p is the current of holes injected from the base into the emitter, I_{scr} is the current from recombination in the emitter-base space charge layer, I_{bulk} is the bulk recombination in the base layer and I_{cbo} is the current from holes flowing from collector to base due to the B-C junction's reversed biasing.

So the DC current gain can be expressed as:

$$\beta = \frac{I_c}{I_b} = \frac{I_n - I_{bulk} + I_{cbo}}{I_p + I_{bulk} + I_{scr} - I_{cbo}} \tag{2.2.6}$$

The operation of the device mainly depends on current contribution I_n. Other components are insignificant components [4]. This is since the base width is much smaller than the diffusion length in base. So I_{bulk} is small. Compared with I_n and I_p, the thermal regeneration current I_{cbo} and space charge recombination current I_{scr} are, respectively, quite small. So the DC current gain can be expressed as:

$$\beta = \frac{I_n}{I_p} \tag{2.2.7}$$

In terms of electron and hole injection current densities, the equations can be given as [5]:

$$J_{EN} = \frac{N_D q D_{nb}}{W_b} \exp\left(\frac{-qV_n}{kT}\right) \tag{2.2.8}$$

$$J_{EP} = \frac{N_A q D_{pe}}{L_{pe}} \exp\left(\frac{-qV_p}{kT}\right) \tag{2.2.9}$$

where: V_n is the conduction valence band potential barrier for holes, V_p is the valence band potential barrier for electrons, D_{nb} is the diffusion constant of holes in the base, D_{pe} is the diffusion constant of holes in the emitter, N_D is the donor concentration in the emitter, N_A is the acceptor concentration in the base, W_b is the base thickness, L_{pe} is the diffusion length of holes in the emitter.

Thus, the equation of DC current gain can be rewritten as [5]:

$$\beta = \frac{N_D D_{nb} L_{pe}}{N_A D_{pe} W_b} \exp[\frac{q}{kT}(V_p - V_n)] \tag{2.2.10}$$

Since there is no discontinuity in the conduction band, the band gap discontinuity is given as:

$$\Delta E_g = q(\mathrm{V}_p - V_n) \tag{2.2.11}$$

The above equation can be expressed as [5]:

$$\beta = \frac{N_D D_{nb} L_{pe}}{N_A D_{pe} W_b} \exp(\frac{\Delta E_g}{kT}) \tag{2.2.12}$$

It can be noticed from this equation that energy gap discontinuity is exponential, so evidently it can affect the DC gain. However, the doping ratio effect becomes even, regardless. The drawback mentioned in BJT can be solved by using a heterojunction. Increasing the base doping and reducing the emitter doping will reduce both the base resistance and emitter-base capacitance. And current gain here can still keep to a very high level, while the hole injection current becomes negligible. Thus the base current becomes $I_b \cong I_{scr} + I_{bulk}$. And since $I_n >> I_{bulk}$, I_c is approximated as I_n, the current becomes:

$$\beta = \frac{I_n}{I_{scr} + I_{bulk}} \tag{2.2.13}$$

2.2.2 Abrupt emitter-base HBTs

In abrupt heterojunction transistors there is an abruption in the E-B junction as shown in figure 2.2.1. In this kind of structure a discontinuity of conduction band ΔE_c acts as an extra barrier which will collect the injected electrons and increase the recombination losses at the junction, thereby reducing the current gain [6]. It increases the emitter-base forward bias voltage requirement and is undesirable in terms of HBT structure. In this case, the band gap discontinuity becomes:

$$\Delta E_g = \Delta E_c + \Delta E_v \tag{2.2.14}$$

$$\Delta E_v = \Delta E_g - \Delta E_c = q(V_p - V_n) \tag{2.2.15}$$

where ΔE_v shows valance band discontinuity, the current gain is given as:

$$\beta = \frac{N_D D_{nb} L_{pe}}{N_A D_{pe} W_b} \exp\left(\frac{\Delta E_v}{kT}\right) \tag{2.2.16}$$

The undesirable ΔE_c can be reduced or even removed by grading the junction or choosing the proper materials. So in the next part, the material systems used for HBTs will be discussed.

2.2.3 Material systems for HBTs

As discussed before, a large ΔE_c is undesirable. This is because it adds an extra barrier for electrons injecting from emitter to base. This will increase the emitter-base forward bias voltage, thus reducing the current gain. On the other hand, ΔE_v can limit reverse injection holes from base to emitter, which bring a lot of benefit to a HBT. So the $\Delta E_v / \Delta E_c$ value becomes a significant value in both design and analysis. Table 2.2.1 shows band discontinuities for various HBT material heterostructures.

Table 2.2.1: Band discontinuities for various HBT material heterostructures [5, 7]

HBT Material structure	$\Delta E_c\left(eV\right)$	$\Delta E_v\left(eV\right)$	$\Delta E_g\left(eV\right)$	$\Delta E_v / \Delta E_c$
$Al_{0.3}Ga_{0.7}As / GaAs$	0.28	0.15	0.43	0.54
$In_{0.5}Ga_{0.5}P / GaAs$	0.12	0.38	0.5	3.17
$InP / In_{0.53}Ga_{0.47}As$	0.25	0.34	0.59	1.36
$In_{0.52}Al_{0.48}As / In_{0.53}Ga_{0.47}As$	0.32	0.12	0.44	0.38
$In_{0.5}Al_{0.5}P / GaAs$	0.31	0.62	0.93	2
$Si / Si_{0.75}Ge_{0.25}$	0.02	0.13	0.15	6.5

From the values in table, $Si/Si_{0.75}Ge_{0.25}$ seems to be excellent material for HBTs, offering a very high $\Delta E_v / \Delta E_c$ rate. That correspondingly means that very high gain can be achieved. However, the mobility of Si and silicon based devices is lower than for other materials [8]. This characteristic limits the frequency response of the device, so although high gain can be achieved, it is only suitable for low frequency applications.

AlGaAs/GaAs HBT has been widely studied. It has an excellent circuit performance including good high frequency performance, high current gain high f_t and high f_{max}. But the conduction discontinuity ΔE_c is large. Although using grading can remove the ΔE_c, some drawbacks still cannot be avoided. Grading can increase the number of scattering centres, thus resulting in a larger recombination current and the reduction of current gain [9]. InGaP/GaAs HBT has a relatively small ΔE_c and large valence band offset. This is desirable according to the previous analysis, which increases electrons from the emitter to the base and reduces holes from the base to the emitter. Another factor is that InGaP/GaAs HBT is easier to manufacture using wet etching than AlGaAs/GaAs HBT [9]. Compared with AlGaAs, InGaP exhibits a low surface recombination velocity and better thermal conductivity. At the same time, breakdown voltage is larger in the AlGaAs/GaAs heterojunction.

AlGaAs and InGaP have a band gap of 1.92 *eV* and 1.86 *eV* respectively. According to the wavelength sensitive to these materials, if an emitter is made from them, optical communication energy of 900nm (1.38e*V*), 1300nm (0.95*eV*), and 1550nm (0.8*eV*) can go through them without absorption. So the emitter acts as if its transparent when these materials are used, if the base is made from GaAs, which has a band gap of 1.42*eV*, is sensitive to wavelength around 800nm and suitable for short wavelength communication. For long haul optical communication, 1550nm is chosen due to its high capacity and low attenuation. So InGaAs with band gap 0.75*eV* is good for the base material. It is also sensitive to 1300nm, which has been reported by Dr. Bashar and Prof. Rezazadeh [4]. The InP/InGaAs heterojunction has a larger ΔE_v than ΔE_c. In addition, InGaAs shows lower surface recombination velocity than GaAs. These relate to high injection efficiency, lower turn on voltage and high breakdown voltage. Also, electron mobility of InGaAs is high, meaning therefore that high frequency performance can be achieved.

The measurement of InGaP/GaAs HBT will be shown later. As shown by the analysis above, it is worth achieving and understanding both the DC and the optical performance of this kind of device. Some key fundamental advantages of HBTs against BJT can be summarised as follows [10]:

- Higher doping and lower resistance in the base can be achieved; it is unnecessary to consider the increasing holes reversing the injection to the emitter.

- Due to high base doping, there is minimum change in base width, making the device suitable for high power applications when the base-collector reverse bias increases.

- Improvement of f_t and f_{max}.

- The emitter no longer needs to be more highly doped than the base, therefore emitter-base capacitance becomes lower. This can significantly reduce the noise.

2.3 Optical detector

2.3.1 Fibre optical communication

Since the early 1960's, optical communication in the telecommunications market has showed immense growth. Additionally, although early systems were inefficient, now very low attenuation losses can be achieved easily.

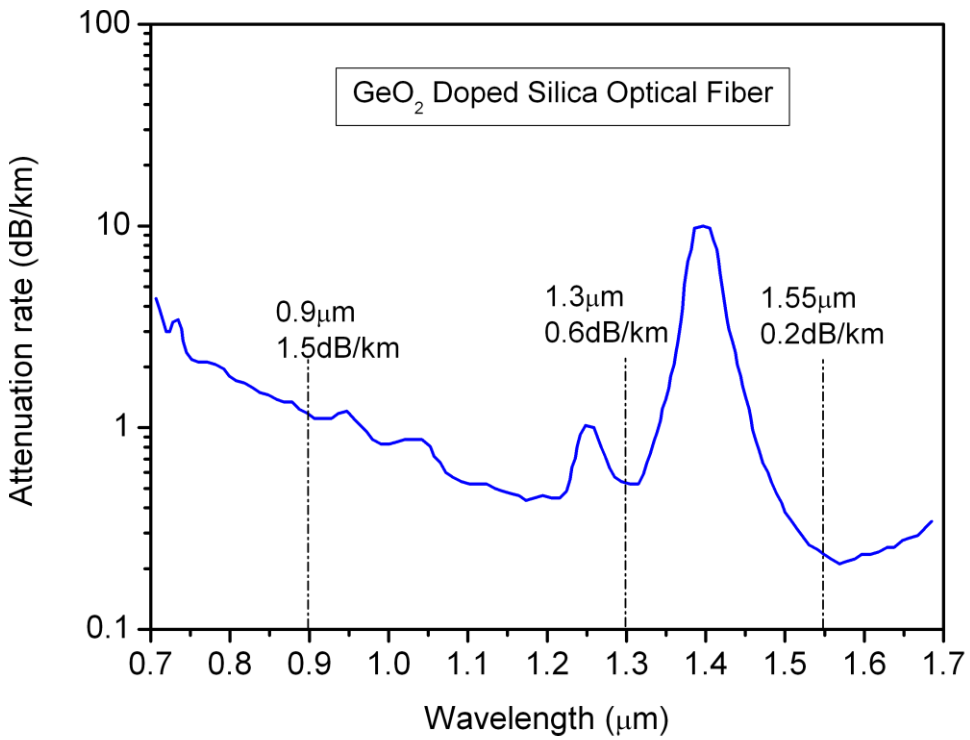

Figure 2.3.1: Loss characteristics of a silica optical fibre [4]

Figure 2.3.1 shows the loss characteristics of a silica optical fibre. There are three interesting wavelengths to point out here, 0.9μm, 1.3μm and 1.55μm. All those wavelengths provide good capacity and low attenuation. Especially from the point of view of telecommunication applications, attenuation at 1.55μm is just 0.2dB/km. This makes it a desirable wavelength for long haul transmission, with the majority of today's long haul optical communication systems being designed to operate at this particular wavelength.

Digital transmission based on an optical fibre communication system is now widely used in intercity systems. Fibre optical communication shows many supreme advantages, such as [11]:

- Enormous bandwidth potential: due to high frequency, the optical fibre communication can offer wider bandwidth than conventional copper cables and microwave radio.

- Low transmission loss: as the figure above shows, the loss of optical fibre communication can descend as low as 0.2dB/km. This feature can reduce repeater numbers and also decrease the cost and complexity of the whole system. These major advantages mean that optical fibre communication occupies an important place in long haul telecommunication applications.

- Small size and weight: compared with copper cable, optical fibre is much smaller and lighter.

- Immunity to cross talk and interference: optical fibre is made from dielectrics; therefore it can be segregated from electromagnetic interference.

- Security: the light signal does not radiate significantly and is not open to effortless interception.

- Reliability: due to the features above, the whole system is reliable and easy to maintain compared with the conventional system.

2.3.2 Basic principles of photodetection

Thermal detectors and photonic detectors are two main types of photodetector. The former type relies on the change in a material's property. Light absorption results in temperature variation and then causes a change in polarisation, resistance or contact potential. This kind of photodetector can operate over a wide wavelength range. However, the drawback is the response time, meaning it is not suitable for high frequency applications. The other type of photodetector relies on free carrier generation, that is, electron excitation from valence band to conduction band. Although this kind of photodetector is sensitive to wavelength, it exhibits a better response time than the thermal detector. Therefore, it is able to work at a high frequency, making it suitable for today's telecommunication systems.

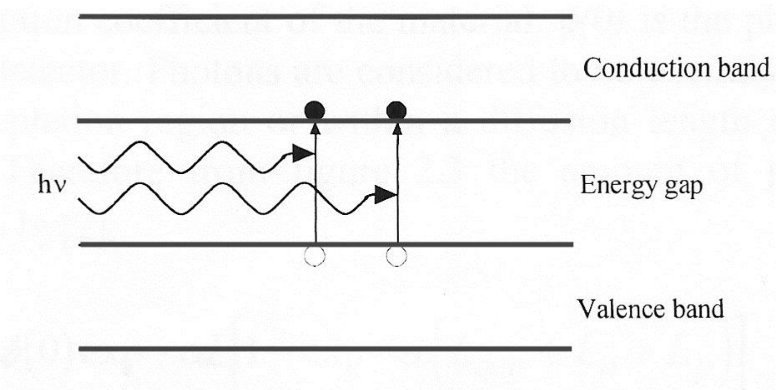

Figure 2.3.2: Photons absorption and electron hole pairs generation [12]

When a photon with enough energy is absorbed by a semiconductor, electron excitation occurs. The excitation electron transits from the valance to the conduction band. The condition is the energy of the photon, which depends on the wavelength, and is larger than the band gap energy of that kind of semiconductor. Where the threshold wavelength is given by:

$$\lambda_{th} = \frac{hc}{E_g} \tag{2.3.1}$$

where λ_{th} is the threshold wavelength, h is Planck's constant, c is the speed of light in the vacuum and E_g is the energy band gap of the material

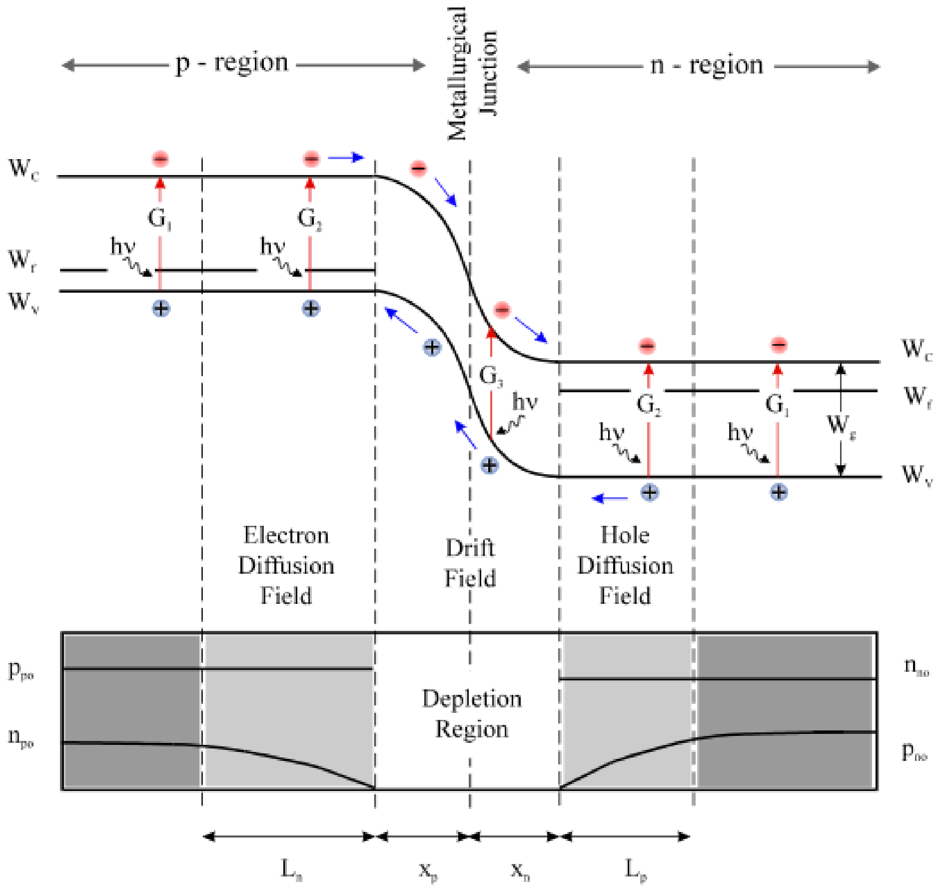

Figure 2.3.3: Electron energy and carrier concentration diagram of reversed p-n junction photo absorption [4]

Here, the basic conception of p-n junction photo detection is discussed. In order to avoid the bias dependent thermionic emission current component and maximise the photon current in the detector external circuit [4], the diode is reverse biased. Assume that the optical signal with the energy is larger than the material's band gap. It illuminates on the diode and the radiation reaches the depletion region. The meaning of the symbols in figure 2.3.3 can be seen below [4]:

x_n = depleted n-region p_{po} = majority carrier concentration in p-region

x_p = depleted p-region n_{no} = majority carrier concentration in n-region

L_n = electron diffusion length n_{po} = minority carrier concentration in p-region

L_p = hole diffusion length p_{no} = minority carrier concentration in n-region

The total absorption area can be divided into three parts. G1 is the bulk of either the p or n region. The electron and hole pairs generated by absorption cannot contribute a current to the external circuit. That means that the optical signal absorbed by this region cannot be detected. Since there is no electric field in this bulk region, electron and hole pairs just scatter randomly until they recombine again. G2 is the region between the depletion region and the bulk, which is called the diffusion field. In the p-region, generated minority carriers, electrons, will diffuse through the diffuse field first and then reach the depletion region boundary. After that, they continue drifting to the n-region. Similarly, the n-region generated minority carriers, holes, will transit in an opposite direction in the same way as the p-region generated electrons. Both of these transitions will contribute current to the external circuit. This means that the absorption in this region is detectable, although it has already been mentioned that the diffusion velocity is much slower than the drift. Therefore, a response delay may be caused by this process. G3 is the depletion region. Photo-generated electrons and holes transit with high speed to the reverse biased n and p region. Also, the contribution of this transition makes the current flow in the external circuit. In fact this is the most desirable process in the detection.

There are more factors affecting the power absorption of a photodetector. When the radiation reaches the surface of the photodetector, not all the power can be absorbed by the semiconductor, rather, some of the power will be reflected by the surface, with even the radiation travelling inside the detector. At different layer surfaces, the power is also reduced due to the reflection. Another factor is when the radiation falls on the photodetector, and the number of photons absorbed does not create a linear relationship with the distance into the material. Instead, an exponential decay is shown between the propagating radiation power density and the radiation travelling distance. This means most of the optical flux is absorbed near the surface of the detector. According to the above analysis, the electron and hole pairs generated in the G1 region can no longer be detected. Therefore, it is desired that the depletion region can be as close to the surface as possible. This can reduce the useless absorption in the neutral G1 region. At the same time, the depletion region is designed to be as wide as possible to absorb more optical power. But this also brings some drawbacks in terms of bandwidth.

2.3.3 Photodetector key parameters

Quantum efficiency and responsivity

These two parameters are interlinked. The responsivity of a detector is defined as the ratio of photo-generated current to the incidence of optical power. It is the amount of photo-current achieved for per unit incident optical power. It shows the optical signal to electrical signal conversion ability of the device. The equation is given as:

$$R_\lambda = \frac{I_{ph}}{P_{opt}} \tag{2.3.2}$$

where I_{ph} is the photogenerated current and P_{opt} is the incidence of optical power.

The quantum efficiency is the ratio of the electrons generated per second and the number of incident photons per second. It shows the efficiency of converting photons into photo-current. It is given as:

$$\eta = \frac{\left(I_{ph} / q\right)}{\left(P_{opt} / E_{ph}\right)} \tag{2.3.3}$$

where $E_{ph} = \dfrac{hc}{\lambda}$ is the energy of a photon.

If we combine these equations and rearrange it, we find that for a given wavelength, quantum efficiency is proportional to the responsivity.

$$\eta = R_\lambda \left(\frac{hc}{q\lambda}\right) \tag{2.3.4}$$

Response time

The response time is affected by the following parameters:

- Diffusion time of carriers
- Drift transit time of carriers through the depletion region
- Junction capacitance charging time

Diffusion time is the slowest process in the three parameters above. So we should try to design the detector absorb light mainly in the depletion region. The equation is given as:

$$\tau_{diff} = \frac{d^2}{2D_n} \tag{2.3.5}$$

where d is the diffuse distance, D_n is the minority carrier diffusion coefficient.

The transit time is the time taken by carriers to drift across the depletion region. Since carriers can transit with saturation velocity in depletion region, the transit time is quite short compared to the diffusion time. It is given as:

$$\tau_R = \frac{W}{V_{sat}} \tag{2.3.6}$$

where V_{sat} is the saturation velocity and W is the depletion region width.

Due to the reverse bias the diode has a capacitance which determines the capacitance charging time constant. It is given as:

$$\tau_{CR} = RC_j \tag{2.3.7}$$

where R is the load resistance and C_j is the junction capacitance.

There is a tradeoff between different parameters. If the depletion region is made thicker, the transit time will increase, although junction capacity can be reduced. On the other hand, if the depletion region is designed thin, the transit time can be reduced, while the junction capacity will be high. Also, the absorption expected will occur in the deletion region to reduce diffusion time. For a detector design all the parameters have to be considered.

2.3.4 p-i-n photodiode

There is an un-doped or slightly doped and wide intrinsic layer between the p and n region in the p-i-n photodiode. This layer acts as the depletion region. It is of an almost constant width and is not reliant on the high reverse bias voltage. So a p-i-n photodiode does not require a high voltage bias to create a depletion region. Many complex structure photodetectors include the p-i-n diode as a part of their construction, like the base-collector junction. Through adjusting the size of intrinsic layer, many characteristics of the photodetector can be optimised.

2.3.5 Heterojunction phototransistors

Figure 2.3.4 above shows how the photo-generated electrons and holes flow in the HBTs under illumination. This reflects the set-up of our HBTs optical measurement experiment. The device is under active common emitter operation, where the B-C junction is reverse biased and the E-B junction is forward biased.

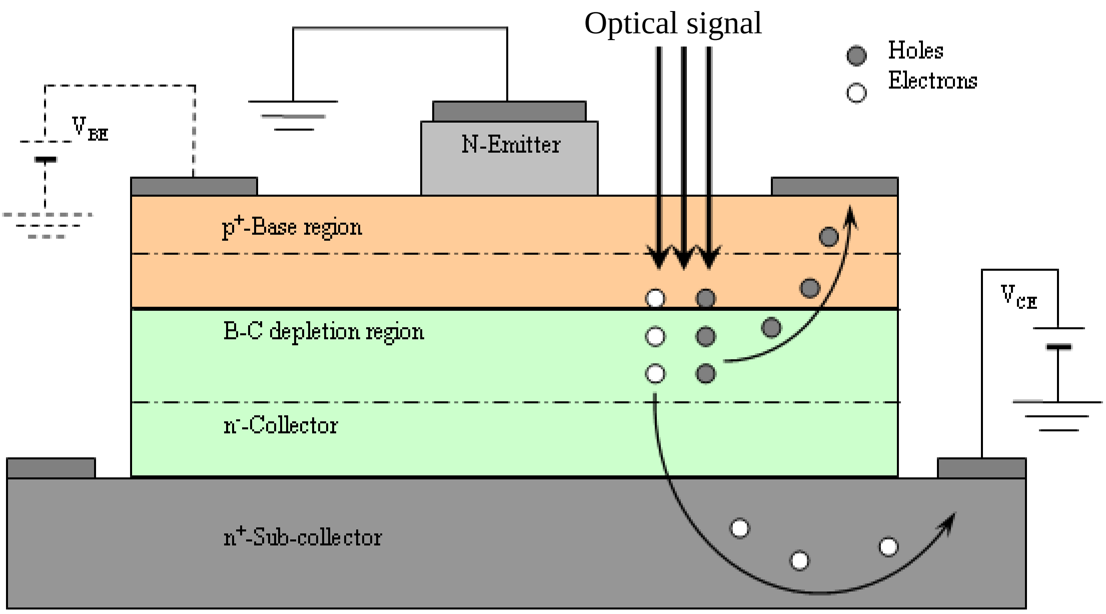

Figure 2.3.4: Cross-section view of the HBT under illumination, showing the flow of photo-generated electrons and holes

An optical signal travels through a wide band gap emitter or directly shines on the base. It is then absorbed in the base and B-C depletion regions. A photocurrent is added to the reverse leakage current I_{CBO} to base [9] and amplified by the transistor's internal gain. Therefore, the whole device works not only as a photo-detector, but as well an amplifier.

2.3.6 InGaP/GaAs DHBTs advantages

InGaP/GaAs HBTs' excellent power handling capability, good linearity and power added efficiency (PAE), means that it has become a candidate for power amplifier designs in the low-to-mid power infrastructure application range, which is currently dominated by Laterally Diffused Metal Oxide Semiconductor (LDMOS) or pseudomorphic High Electron Mobility Transistor (pHEMT) [13-15]. From an application point of view, high voltage operation and high breakdown voltage are the main requirements and technical challenges for InGaP HBTs. DHBTs whose collector are formed by a wide band gap material, offers a good solution to these requirements. This feature offers advantages such as a smaller turn on characteristics (offset voltage), lower B-C leakage current, larger breakdown voltage, and a temperature-insensitive current gain, which make it attractive for power applications [16]. Alternatively, one may compromise the larger breakdown voltage in DHBTs to push the high frequency performance of the device beyond that of SHBTs [17].

Furthermore, according to DHBTs material systems, although GaAs is lattice-matched to AlGaAs in the design of AlGaAs/GaAs, the smaller impact ionisation rates in InGaP compared to those in AlGaAs, with the same band gap, makes the InGaP/GaAs/InGaP material system a much more favourable DHBT choice [17]. To the best of author's knowledge, it is reported [18-19] that InGaAs/GaAs DHBTs have been well studied. However, the literature on the application of $In_{0.49}Ga_{0.51}P$ lattice-matched to GaAs for GaAs-based DHBTs is very limited [17].

High breakdown voltage

Poor collector breakdown characteristic of SHBTs limit their application in many areas. By reducing collector doping and increasing collector thickness, SHBTs can achieve high voltage performance. However, lower collector doping requires higher reverse B-C voltage to pull the potential barrier blew the base conduction band, which results in higher collector current saturation voltage [20]. Also, the Kirk effect is another problem when the device is working under high current density [21]. On the other hand, a thicker collector structure in device topology requires a severe process and causes photo-lithography challenges, potentially, introducing reliability problems [21]. And also, the wider collector layer will greatly enlarge the carriers travelling through time, resulting in reducing the high frequency operation capability of the device.

In order to overcome the above problem, using wide band gap material as the collector becomes a superior solution. Using wide band gap InGaP to replace the thicker GaAs collector layer makes the major part of potential change at high C-E bias voltage occur in the wide band gap collector layer. Very limited potential change in the narrow band gap GaAs base layer is caused [22]. This feature makes the InGaP/GaAs DHBTs increase power handling capability. Also, the topology problems are overcome [23]. Such a material system allows DHBTs to provide higher power without significantly compromising collector transit time [20].

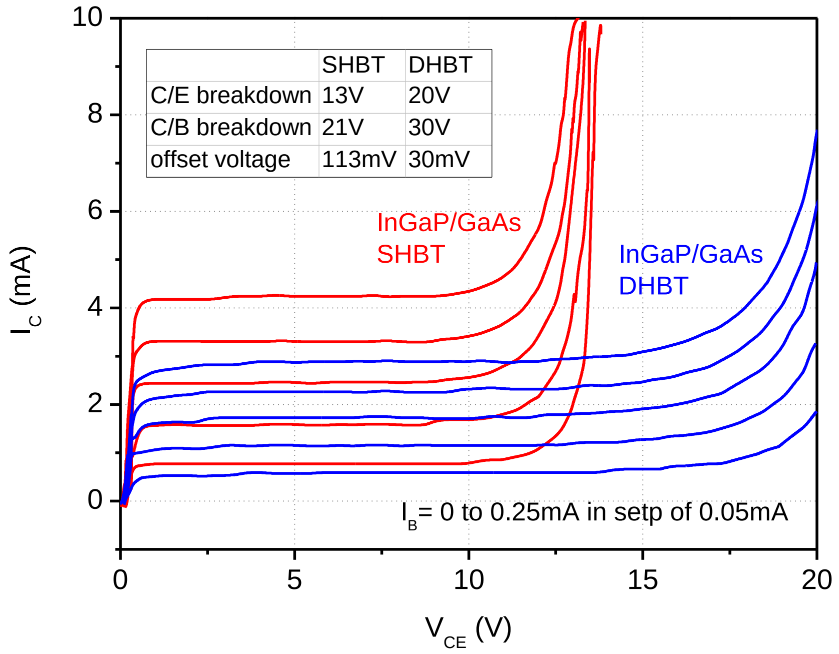

Figure 2.3.5: Measured output characteristic of InGaP/GaAs SHBT and DHBT with the same geometry (6×10μm^2) [16]

In figure 2.3.5 above, a number of advantages for the DHBTs over the SHBTs can be observed. First, C-E breakdown voltage (BV_{CEO}) improved from 13V (InGaP/GaAs SHBT) to 20V (InGaP/GaAs DHBT) whilst the inserted table also shows the value of InGaP/GaAs DHBT C-E offset ΔV_{CEO} (30mV) as much smaller than SHBT (113mV). Furthermore, a higher breakdown voltage allows the device to work under higher level power conditions, helping the device attain better high frequency performance [23].

Temperature insensitivity

From the published work [16], the characteristics of current gain of InGaP/GaAs SHBT, DHBT and AlGaAs/GaAs SHBT at various temperatures are shown.

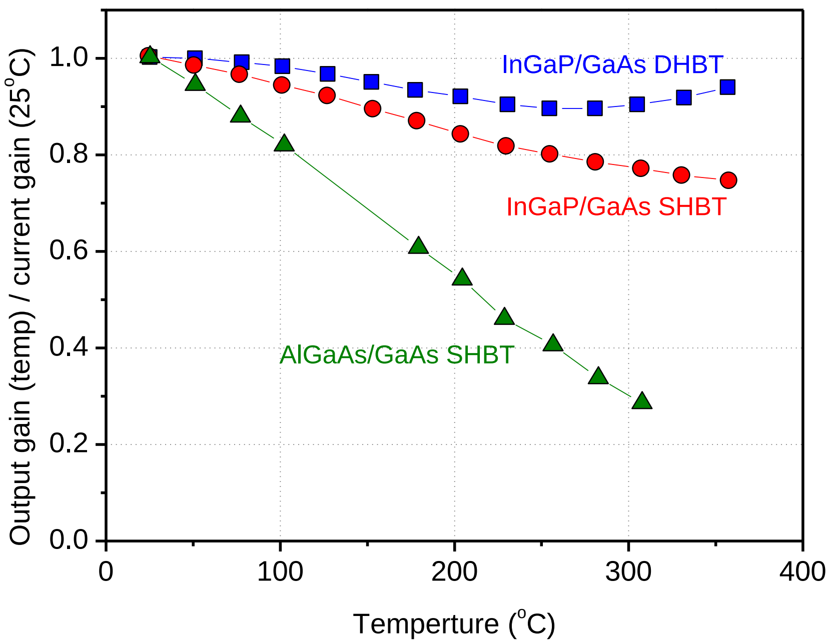

Figure 2.3.6: Measured normalised current gain of InGaP/GaAs SHBT, DHBT and AlGaAs/GaAs SHBT versus temperature [16]

First, in figure 2.3.6, comparing the AlGaAs/GaAs SHBT, both InGaP/GaAs SHBT and DHBT show a relatively flat current gain in relation to temperature. This is attributed to the very large E-B valence band discontinuity (ΔE_v) of this material system. The injection of holes from the base to the emitter could be prevented [24]. Second, the InGaP/GaAs DHBT show even insensitivity to the temperature. The reason is better heat conduction from the collector layer into the emitter contact, which is another motivation for using DHBTs [25]. The conduction band discontinuity (ΔE_c) in the B-C heterojunction of InGaP/GaAs DHBTs enhances the base bulk recombination, which may cause a smaller current gain, although less temperature variation for the current gain, when compared to the SHBT counterparts. Furthermore, technical grading can be used to make the DHBTs own an almost temperature-insensitive current gain. This is since the whole band gap discontinuity

(ΔE_v) effectively exists in the valence band [16].

Lower leakage current

From the published work [16], the characteristics of leakage of InGaP/GaAs SHBT and DHBT at various temperatures are compared.

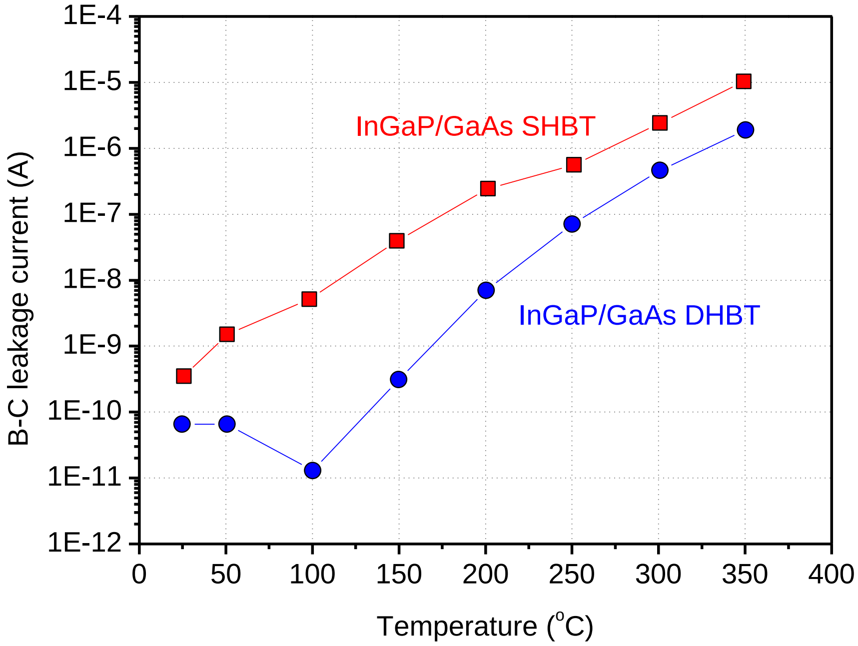

Figure 2.3.7: Measured Base-Collector leakage currents as function of device temperature for InGaP/GaAs SHBT and DHBT [16]

Figure 2.3.7 shows the B-C leakage current versus temperature. The InGaP/GaAs DHBT shows up lower values across the wide temperature region than SHBT, which also benefits from the B-C heterostructure junction, as well as experiencing other advantages. The dip of InGaP/GaAs DHBT leakage current level at 100 degrees Celsius is due to the device under test fabrication defects. The electrons are trapped under this temperature, which can not contribute to the leakage current.

2.3.7 DHBTs as photodetectors

Nowadays, heterojunction Bipolar Transistors (HBTs) are established as a technology suitable for high efficiency amplifiers at microwave frequencies. One of the key trends for HBT power amplifiers used in portable devices such as tablets and smart phones is providing high power-added efficiency to a low bias condition [23]. For devices working as photodetectors, mostly single HPTs (SHPTs) are used, because the relatively thick collector layer results in high responsivity. However, the saturation velocity of holes is one order of magnitude slower than for electrons. Drifting holes generated in the collector and sub-collector limit the overall bandwidth of these devices [26]. The photo-excited holes in the sub-collector layer have little effect on operation speed, and slow down the operation speed of the whole device. These conventionally structured SHPTs with InGaP collector are not suitable for high speed applications.

Due to the superior turn on characteristics and breakdown, DHPTs are potentially a significant improvement over SHPTs [27-28]. Benefiting from these advantages, in optical communication systems, including microwave photonics systems, DHBTs should enable us to build compact, high-performance equipment [29]. It is reported [30] that the developed DHPT/DHBT photo-receiver has already been used to realise compact, high-response and high-sensitivity photo-receiver equipment for optical micro- or millimetre-wave interaction systems such as fibre radio and phased arrays.

2.4 Heterojunction bipolar phototransistors 2-terminal and 3-terminal configurations

The HPTs can offer large optical gain at high incident power without high bias. But at low incident power, for 2-terminal configuration, HPTs' low current gain limits the optical gain. Also at low incident power, recombination at B-E junction results in a small collector current. This can further increase the junction capacitance. The capacitance charging time would affect frequency response.

Using HBT devices as photodetectors can be configured as 2-terminal, 3-terminal with constant base current bias and 3-terminal with constant base voltage bias. In the following section, the equations of optical gain for these three configurations will be respectively discussed.

2.4.1 HPTs 2-teminal configuration

HPTs with 2-terminal configuration are shown in figure 2.4.1. The base of the device is floating.

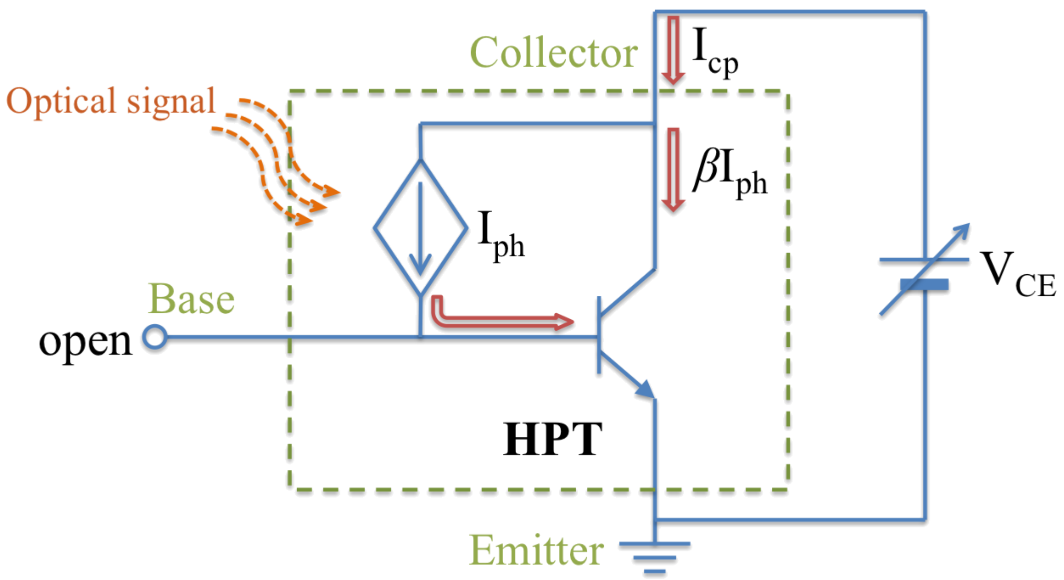

Figure 2.4.1: HPTs with 2-terminal configuration [31]

From figure 2.4.1 the collector current under illumination I_{cp} is given by [31]:

$$I_{Cp} = I_{ph} \times \beta_{(I_B = I_{ph})} + I_{ph} = I_{ph} \times [\beta_{(I_B = I_{ph})} + 1] \tag{2.4.1}$$

where I_{Cp} is the collector current under illumination I_{ph} is photocurrent in base, $\beta_{(I_B = I_{ph})}$ is current gain under illumination.

One can define the optical gain as given below:

$$G = \frac{\Delta I_{Cp}}{I_{ph}} = \frac{\Delta I_{Cp}}{P_{in} / h\nu \times q} = \frac{h\nu}{q} \cdot \frac{\Delta I_{Cp}}{P_{in}} \tag{2.4.2}$$

where ΔI_{Cp} is the induced collector photocurrent resulting from optical injection, P_{in} is the incident optical power, h is Planck's constant, q is unit charge and v is frequency of incident optical signal.

In 2-terminal configuration, since base is floating. ΔI_{Cp} can be replaced by I_{Cp}. The optical gain for 2-terminal configuration is given by [31]:

$$G = \frac{\Delta I_{Cp}}{I_{ph}} = \frac{I_{Cp}}{I_{ph}} = \beta_{(I_B = I_{ph})} + 1 \tag{2.4.3}$$

2.4.2 HPTs 3-terminal configuration with base current bias

HPTs 3-terminal configuration with base current bias is shown in figure 2.4.2. There is a current source connecting the base terminal to supply the bias current $I_{B,DC}$.

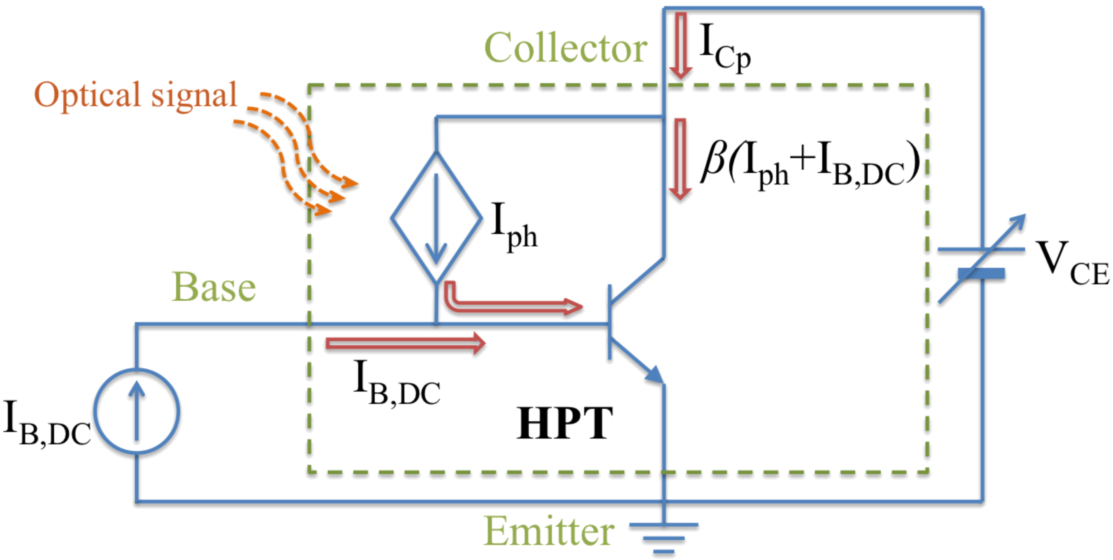

Figure 2.4.2: HPTs with 3-terminal with base constant current bias configuration [31]

From figure 2.4.2 the collector current under illumination I_{cp} is given by [31]:

$$I_{Cp} = (I_{ph} + I_{B,DC}) \times \beta_{(I_{ph}+I_{B,DC})} + I_{ph} \qquad (2.4.4)$$

From above equation (2.4.2) discussion, the optical gain:

$$G = \frac{\Delta I_{Cp}}{I_{ph}} = \frac{I_{Cp} - I_{C,DC}}{I_{ph}} = \frac{(I_{ph} + I_{B,DC}) \times \beta_{(I_{ph}+I_{B,DC})} + I_{ph} - I_{B,DC} \times \beta_{I_{B,DC}}}{I_{ph}} \qquad (2.4.5)$$

Therefore [31]:

$$G = \beta_{(I_{ph}+I_{B,DC})} + 1 + \Delta\beta \times \frac{I_{B,DC}}{I_{ph}} \qquad (2.4.6)$$

where $\Delta\beta = \beta_{(I_{ph}+I_{B,DC})} - \beta_{I_{B,DC}}$, $\beta_{(I_{ph}+I_{B,DC})}$ is the device current gain under illumination with base DC bias, $\beta_{I_{B,DC}}$ is dark current with base DC bias, $I_{C,DC}$ collector current due to base bias and $I_{B,DC}$ is base bias current.

2.4.3 HPTs 3-terminal configuration with base voltage bias

HPTs 3-terminal configuration with base voltage bias is shown in figure 2.4.3. There is a voltage source connecting the base terminal to supply the bias voltage V_{BE}.

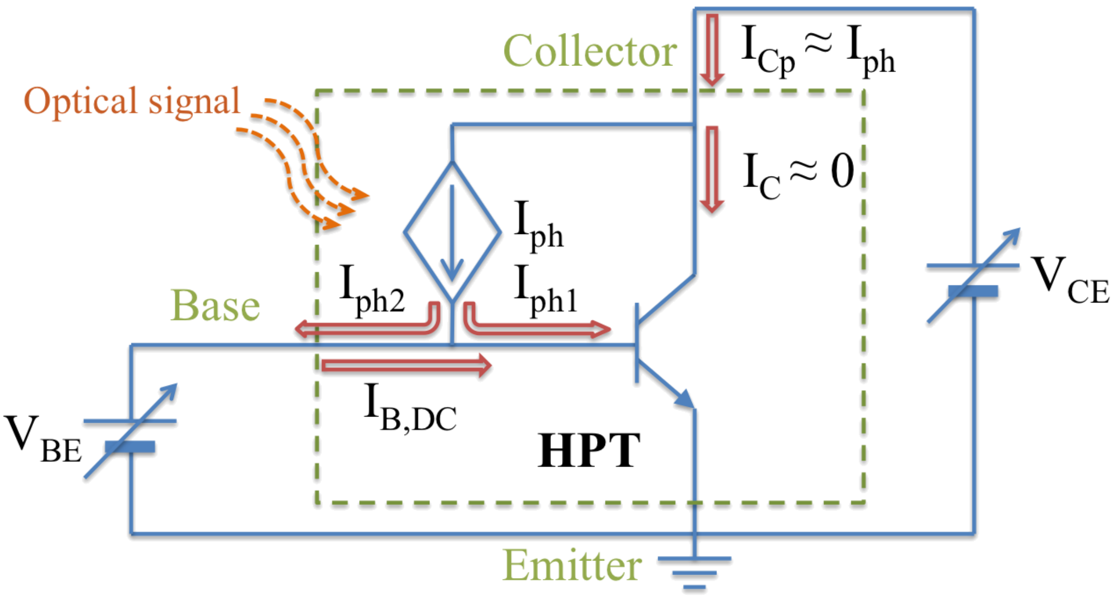

Figure 2.4.3: HPTs with 3-terminal with base constant voltage bias configuration [31]

From figure 2.4.3 the collector current under illumination I_{cp} is given by [31]:

$$I_{Cp} = (I_{ph1} + I_{B,DC}) \times \beta_{(I_{ph1}+I_{B,DC})} + I_{ph} \tag{2.4.7}$$

Therefore [31]:

$$\Delta I_{Cp} = [\beta_{(I_{ph1}+I_{B,DC})} - \beta_{I_{B,DC}}] \times I_{B,DC} + \beta_{(I_{ph1}+I_{B,DC})} \times I_{ph1} + I_{ph} \tag{2.4.8}$$

where $\beta_{(I_{ph1}+I_{B,DC})}$ is the device current gain under illumination with base voltage bias, I_{ph1} is photo-generated current flowing into the transistor.

It is reported [31] that for GaAs-based HPTs $I_{B,DC}$ is very small (<10^{-8}A) at low B-E bias voltage. This results in an extremely large equivalent resistance for B-E junction. Comparing with above B-E equivalent resistance, the parasitic resistance of the voltage source is small. So only a small portion of I_{ph}, which is I_{ph1} (only 2% of I_{ph} at

V_{BE} = 2V), flows into the base to be amplified [31-32]. Therefore the current gain can be given as:

$$G = \frac{\Delta I_{Cp}}{I_{ph}} = \frac{[\beta_{(I_{ph1}+I_{B,DC})} - \beta_{I_{B,DC}}] \times I_{B,DC} + \beta_{(I_{ph1}+I_{B,DC})} \times I_{ph1} + I_{ph}}{I_{ph}} \approx 1 \qquad (2.4.9)$$

The optical gain of HPTs can not be improved by 3-terminal configuration with base voltage bias configuration.

2.5 Eye diagram

An eye diagram, also known as an eye pattern, is widely used in telecommunications, and used extensively in the area of digital communications; this is in order to assess the quality of a system. It has been established as a very powerful tool offering us visual and qualitative evaluations of the performance of any circuit [33] or system. From an eye diagram, an intuitive and quick qualitative analysis of a signal, especially a digital signal, can be achieved. It provides an at-a-glance assessment of a system and a first-order approximation [34], which are highly efficient. It differs from many traditional methods that rely only on S-parameters. With careful analysis of an eye diagram, more parametric information can be obtained, comprehensively, completely and correctly. This information can be related to the physics of the device's operation and assists in optimisation.

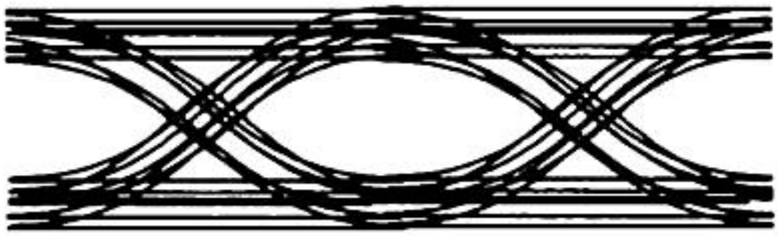

Figure 2.5.1: A simple example of an eye diagram [34]

Figure 2.5.1 shows a simple eye diagram of digital signals. The eye diagram is an oscilloscope display of a series of digital data signals superposition [34]. The reason why it is so named is that for several types of coding, the output diagram looks like a series of eyes set between a pair of rails. It is a very convenient and straightforward technique for evaluating the effects of channel impairments under digital conditions, such as distortion due to noise and inter-symbol interference.

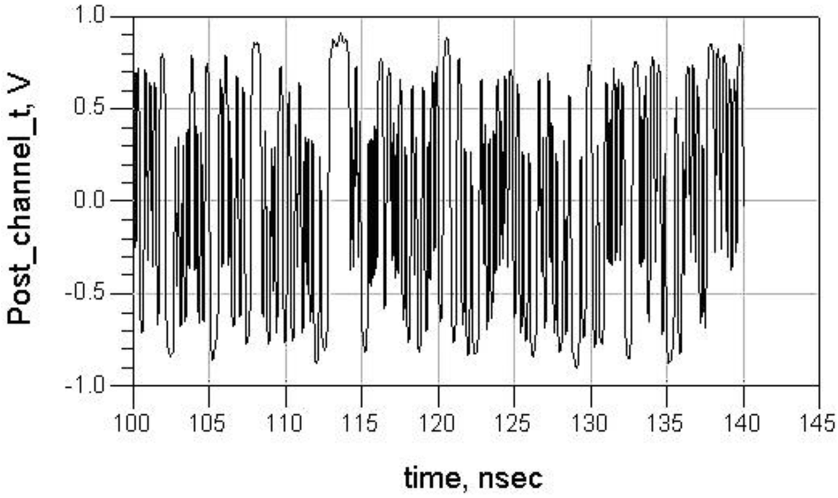

Figure 2.5.2: A simple digital signal waveform which is difficult to understand if there is a distortion [35]

The reason an eye diagram is desired, is that from information in Figure 2.5.2, it is difficult to intuitively describe the performance of this signal and whether or not there is serious distortion and ISI.

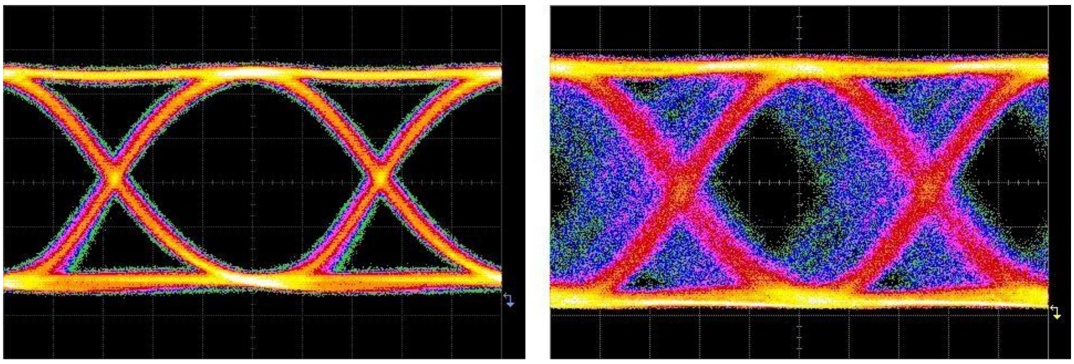

a b

Figure 2.5.3: Comparison of a good quality eye diagram (a) and a distorted eye diagram (b) [35]

However, using figure 2.5.3 we can easily make a judgment. Obviously, the left side eye diagram is extracted from a better quality signal than the right side one. Also, we could, through observing changes to the eye diagram, adjust the design for our device. That is why we needed to include an eye diagram in this project.

The eye diagram is formed simply by overlaying sweeps of different fragments of random patterns of pulses. The long data stream overlaying the results resembles a human eye, which is where its name comes from. Figure 2.5.4 shows an example of four sequential digital bit forming eye diagrams. Considering millions of signals superimposed on one another to generate eye diagrams would establish an effective way of evaluating the device or system under testing.

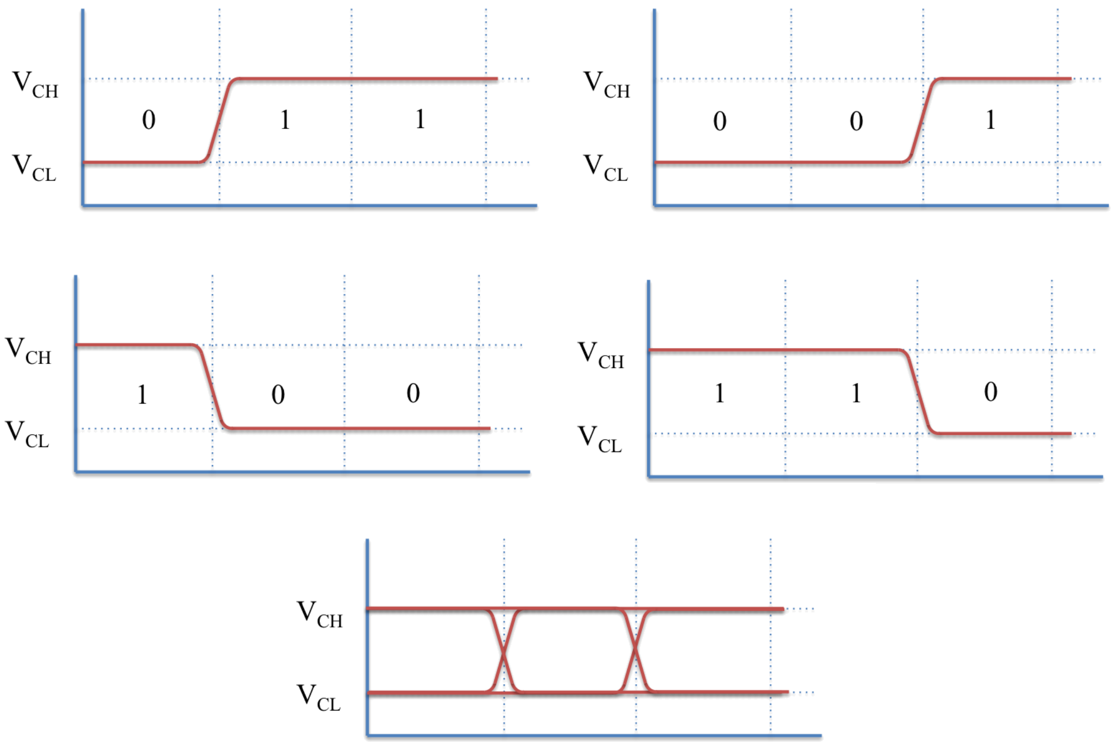

Figure 2.5.4: Eye diagram formation from bit sequences

There are many application areas for the eye diagram. For instance, a common use would be to assess the integrity and quality of the received signal. The whole radio communication system can be composed of many parts, like pre-filtering in the transmitter, amplifiers, frequency converters, propagation path, IF circuits and so on [34]. Each part of the system may cause an impaired signal. Therefore an eye diagram of each part is very useful for troubleshooting.

During the analysis process, various measurements were able to be obtained from eye diagrams. Figure 2.5.5 shows a partial interpretation of an eye pattern measurement.

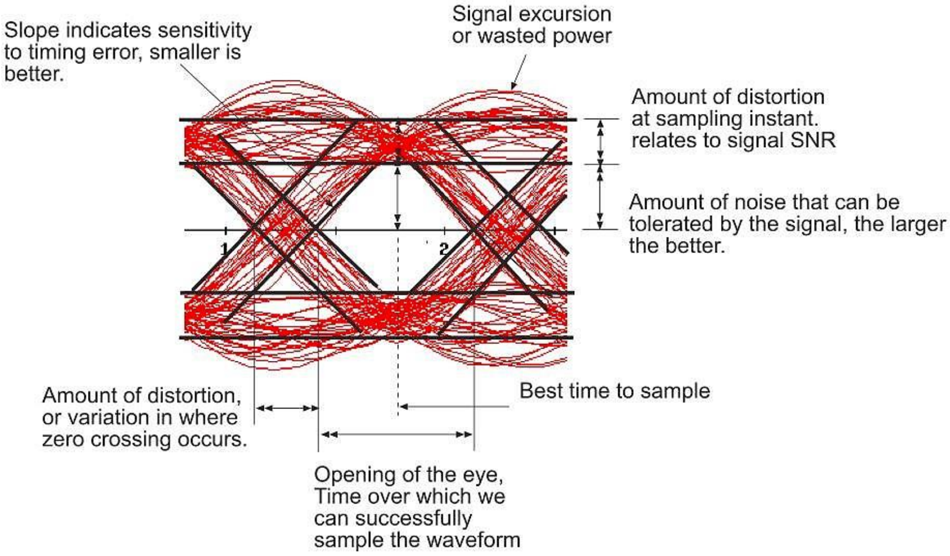

Figure 2.5.5: A partial interpretation of the eye pattern measurement [36]

According to the Matlab help files [37], all of the useful measurements below can be obtained from eye diagrams:

Table 2.5.1: Various eye diagram parameters [37]

Eye Parameters	**Definition**
Eye Amplitude	The distance between two adjoining eye levels.
Eye Height	The three standard deviations' (3σ) distance between two adjoining eye levels.
Eye Level	The amplitude level which is used to stand for data bits.
Eye SNR	The ratio of the eye amplitude to the summation of the standard deviations of the two eye levels.
Vertical Eye Opening	The vertical distance between two vertical histograms.
Horizontal Eye Opening	The horizontal distance between two horizontal histogram points which is equal to the BER value.
Eye Rise Time	The mean time between low and high threshold values.
Eye Fall Time	The mean time between the high and low threshold values.
Eye Width	The horizontal distance between two points where three standard deviations (3σ) are away from the mean eye crossing times.
Peak-to-Peak Jitter	The difference between the histogram extreme data points.

References

[1] Sze, S. M. "Semiconductor Devices, Physics and Technology", Bell Telephone Laboratories. Inc, 1985.

[2] Shockley, W. US Patent no. 2 569 347, 1951.

[3] Kromer, H. "Theory of a Wide-Gap Emitter for Transistors", Proceedings of the IRE, 45, 1957, pp. 1535-1537.

[4] Dr. Bashar, S. A. Ph.D Thesis, "Study of Indium Tin Oxide (ITO) for Novel Optoelectronic Device", Department of Electronic Engineering, University of London, King's Collage London, 1998.

[5] Rezazadeh, A. A. Lecture notes on Optical Communications, University of Manchester, MSc in Communication Engineering, 2006.

[6] Kroemer, H. "Heterostructures Bipolar Transistors and Integrated Circuits", Proc. IEEE, vol. 70, pp.13-25, 1982.

[7] Jalali, B. and Pearton, S. J. "InP HBTs: Artech Housde", 1995.

[8] Dr. Khan, H. First year transfer report, "Electrical and Optical Characterisation of Heterojunction Bipolar Transistors" Microwave and communication systems research group, school of Electrical and Electronics Engineering, University of Manchester, 2007.

[9] Hernandez-Solis, V. Dissertation for MSc, "Electrical and Optical Characterisation of Heterojunction Bipolar Transistors", Department of Electrical Engineering and Electronics, UMIST.

[10] Hughes, W. A., Rezazadeh, A. A., and Wood, C. E. "The Heterojunction Bipolar Transistor (HBT)", GaAs Integrated Circuits, (Editor: J. Mun; Publishers: Blackwell Scientific Publications Ltd, UK), Chapter 7, 1988, pp. 403 – 429.

[11] Miller, S. E., and Kaminow, I. P. "Optical Fiber Telecommunications II", (Publishers: Academic Press Inc., USA), 1988.

[12] Patel, T. Dissertation for MSc, "Electrical and Optical Characterisation of novel HPT's for Optical Telecommunications", Department of Electronic Engineering, University of London, King's College London, 1996.

[13] Hill, D., Kim, T.S. "28-V low thermal-impedance HBT with 20-W CW output power", IEEE Transactions on Microwave Theory and Techniques, vol. 45, no. 12, pp. 2224-2228, 1997.

[14] Kurpas, P., Maaβdorf, A., Doser, W., Heymann, P., Janke, B., Schnieder, F,. Blank, H., Auxemery, P., Pons, D., Heinrich, W., Wurfl, J. "Power GaInP/GaAs HBTs for High Voltage Operation", Digest of the 2002 IEDM

Conference, pp. 681-684, 2002.

[15] Wang, N. L., Dunnrowicz, C., Chen, X., Ma, W., Chau H. F., Sun, X., Chen, Y., Lin, B., Lo, I. L., Huang, C. H., Yang, M. H. T. “High efficiency 28V class AB InGaP/GaAs HBT MMIC amplifier with integrated bias circuit”, IEEE MTT-S International Microwave Symposium Digest, vo1.2, June 2003, pp. 707-710.

[16] Rezazadeh, A.A., Sotoodeh, M., “Design and technology of InGaP/GaAs DHBTs”, Advanced Semiconductor Devices and Microsystems, 2000. ASDAM 2000. The Third International Euro Conference, pp. 119-125, 16-18 Oct. 2000.

[17] Rezazadeh, A.A., Sotoodeh, M., Dharmasiri, N., “Base-Collector Design Optimisation of InGaP/GaAs DHBTs”, High Performance Electron Devices for Microwave and Optoelectronic Applications, 2000 8th IEEE International Symposium, pp. 99 – 104, 2000.

[18] Kurishima, K., H. Nakajima, T. Kobayashi, Y. Matsuoka, and T. Ishibashi, “Fabrication and characterization of high-performance InP/hGaAs double-heterojunction bipolar transistors,” IEEE Transactions on Electron Devices, vol. 41, pp. 1319-1326, 1994.

[19] Chor, E. F. and C. J. Peng. “Composite step-graded collector of InP/hGaAs/InP DHBT for minimised carrier blocking”, Electronics Letters, vol. 32, pp. 1409-1410, 1996.

[20] Lour, W., Chang, W. “Effect of Collector-Base Barrier on GaInP/GaAs Double Heterojunction Bipolar Transistor and Further Improvement by Doping-Spike”, Japanese Journal of Applied Physics, vol. 36, pp. 6210-6214, Part 1, Number 10, October 1997.

[21] Li, J., Cismaru, C., Zampardi, P., Wu, A., Babcock, E., Sun, M., Stevens, K., Ramanathan, R. “Development of High Breakdown Voltage InGaP/GaAs DHBTs”, CSMAN Technology Conference, Austin, Texas, USA, pp.177-180, 2000.

[22] Matsuoka, Y. and, Sano, E. “InP/InGaAs double-heterostructure bipolar transistors for high-speed ICs and OEICs”, Solid State Electronics, 38 9, 1703, Proceedings of the Topical Workshop on Heterostructure Microelectronics, 1995.

[23] Webster, D.R., Rezazadeh, A. Sotoodeh, M. Khalid, A. “Observations on the nonlinear behaviour of single and double InGaP/GaAs HBTs”, High Performance Electron Devices for Microwave and Optoelectronic Applications, London, pp.158-163, 1999.

[24] Liu, W., Fan, S. K., Henderson, T., Davito, D. “Temperature dependences of current gains in GaInP/ GaAs and AlGaAs GaAs heterojunction bipolar transistors,” IEEE Trans. Electron Devices, 1993, vol. 40, pp. 1351-1353.

[25] Cohen Elias, D., Kraus, S., Gavrilov, A., Cohen, S., Buadana, N., Sidorov, V., Ritter, D. "An Abrupt InP–GaInAs–InP DHBT", IEEE Transactions on Electron Devices, vol. 26, no. 1, pp. 14-16, 2005

[26] Leven A., Hill, M., Houtsma V., Kopf R. and Baeyens Y. "InP-based double-heterostructure phototransistors with 135 GHz optical-gain cutoff frequency," Electronics Letters, vol.40, Issue. 13, pp. 833-834, 2004.

[27] Kalid, A., Sotoodeh, H. M., Rezazadeh, A. A. "Planar self-aligned microwave InGaP/GaAs HBT structure using He/O implant isolation", IEEE 5th International Proceedings on Electron Devices for Microwave and Optoelectronic Applications - EDMO97, 24-26th November 1997, London, pp. 279-284.

[28] Sotoodeh, M., Khalid, A.H., Sheng, H., Amin, F. A., Gokdemir, T., Rezazadeh, A. A., Knights, A., Button, C. C. "Direct Extraction and Numercial Simulation of the Base and Collectro Delay Times in Double Hetrojunction Bipolar Transistors", IEEE Trans. Electron Devices, June 1999, vol. 46, No. 6, pp. 1081-1086.

[29] Kamitsuna, H., Matsuoka, Y., Yamahata, S., Shigekawa, N. "Ultrahigh-Speed InP/InGaAs DHPTs for OEMMICs", IEEE Transactions on Microwave Theory and Techniques, vol. 49, no. 10, pp. 1921-1925, 2001.

[30] Kamitsuna, H., Yokosuka, Matsuoka, Y., Yamahata, S., Kurishima, K. "A monolithically integrated photoreceiver realized by InP/InGaAs double-heterostructure bipolar transistor technologies for optical/microwave interaction systems", Gallium Arsenide Integrated Circuit (GaAs IC) Symposium, 1995. Technical Digest 1995. 17th Annual IEEE, pp. 185-188, Oct. 29 1995-Nov. 1 1995.

[31] Tan, S. W., Chen, H. R., Chen, W. T., Hsu, M. K., Lin, A. H., Lour, W. S. "The influence of base bias on the collector photocurrent for InGaP GaAs heterojunction phototransistors", Journal of Applied Physics,vol.97, Issue 3, pp. 034502 - 034502-7, 2009.

[32] Song, C. et al. "Optical characteristics of InGaP/GaAs HPTs", IEEE Electron Device Letters, vol. 22, no. 7, pp. 315-317, 2001.

[33] Selli, G. et al. "Validation of equivalent circuits extracted from S-parameter data for eye-pattern evaluation", Electromagnetic Compatibility, EMC 2004, USA, 9-13, vol.2, Aug. 2004, pp: 666 – 671.

[34] Breed, G. "Analyzing Signals Using the Eye Diagram", pp.50, 2005.

[35] Support of Mathworks, Documentation/Communication Box, http://www.mathworks.com/access/helpdesk/help/toolbox/comm/ref/commscope.eyediagram.html.

[36] Langton, C. Tutorial 15-"How to interpret an eye diagram", pp.1,

www.compextoreal.com, 2002.

[37] “Eye diagram Measurement in Advanced Design System”, pp. 4-5, Agilent Technologies.

Chapter 3. Device Structures and Experimental Setup

3.1 Device structures

3.1.1 $In_{0.49}Ga_{0.51}P$/GaAs single and double heterojuction bipolar transistors

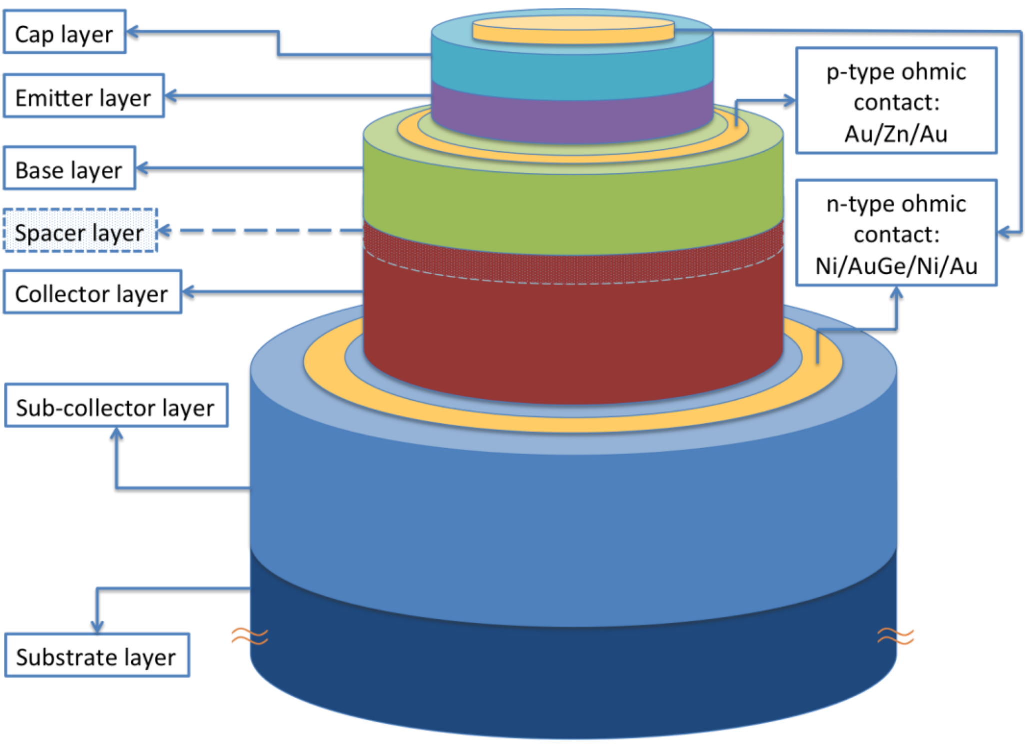

Figure 3.1.1: Schematic device structure of $In_{0.49}Ga_{0.51}P$/GaAs SHBT (on MR873) and DHBT (on MR1095) with emitter contact diameter = 100µm

The device structures of $In_{0.49}Ga_{0.51}P$/GaAs SHBT (on MR873) and DHBT (on MR1095) with 100µm emitter contact diameter are shown in figure 3.1.1 and table 3.1.1. Both device structures were grown using metal organic chemical vapour deposition (MOCVD). Device isolation was achieved by using multiple energy He^+ and O^+ ion implantation [1]. Emitter and base structures in both SHBT and DHBT are similar. As shown in table 3.1.1, both devices own a 100nm thick wide band gap

InGaP emitter layer, with heavy doped cap layers being grown on top of the emitter to reduce the emitter's contact resistance; 100nm GaAs layer which is doped to very high concentrations due to the heterostructure E-B junction; 0.5µm collector layer; and 0.7µm GaAs sub-collector.

Table 3.1.1: Layer structures and doping profiles of $In_{0.49}Ga_{0.51}P$/GaAs SHBT (on MR873) and DHBT (on MR1095) with emitter contact diameter = 100µm

Layer	SHBT	DHBT
Cap Layer	280nm n^+-GaAs 4×10^{18} cm^{-3}	
	20nm n^+-$In_{0.49}Ga_{0.51}P$ 2×10^{18} cm^{-3}	
Emitter	100nm n-$In_{0.49}Ga_{0.51}P$ 5×10^{17} cm^{-3}	
Base	100nm p^+-GaAs 2×10^{19} cm^{-3}	
n^--GaAs spacer 3×10^{16} cm^{-3}	-	20nm
Collector	0.5µm n^--GaAs 1×10^{16} cm^{-3}	0.48µm n^--$In_{0.49}Ga_{0.51}P$ 5-7×10^{16} cm^{-3}
Sub-collector	0.7µm - n^+-GaAs 4×10^{18} cm^{-3}	
Semi-insulating undoped GaAs Substrate		

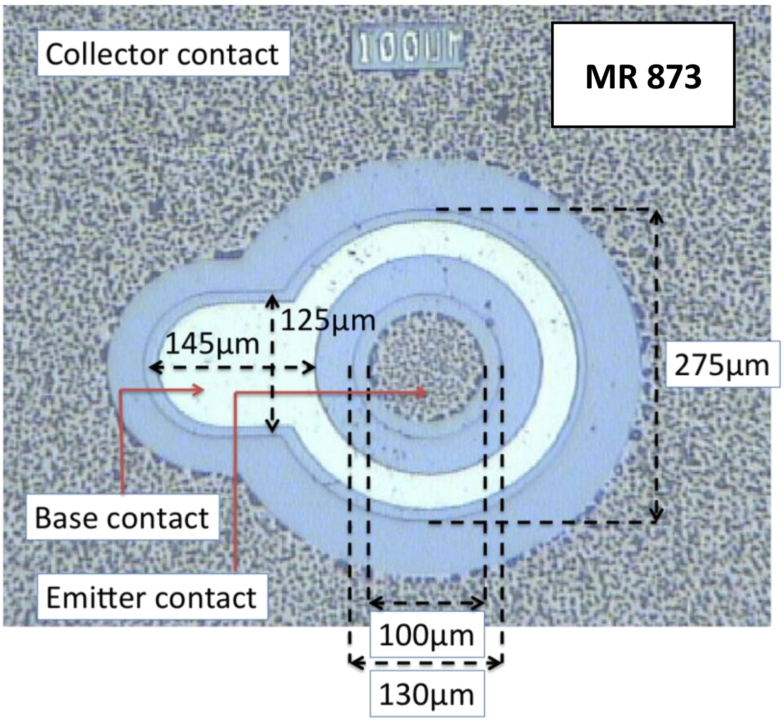

Figure 3.1.2: Micrograph of a fabricated $In_{0.49}Ga_{0.51}P$/GaAs SHBT (on MR873) with emitter contact diameter = 100µm

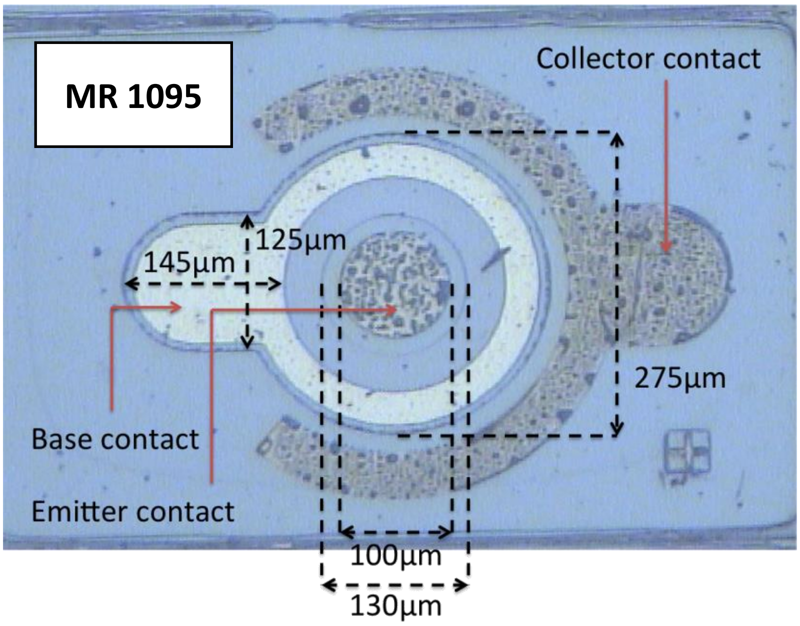

Figure 3.1.3: Micrograph of a fabricated $In_{0.49}Ga_{0.51}P$/GaAs DHBT (on MR1095) with emitter contact diameter = 100µm

The main difference between the $In_{0.49}Ga_{0.51}P$/GaAs SHBT and DHBT is that the collector of the SHBT is simply n^- GaAs, while that of the DHBT is composed of a 20nm undoped GaAs spacer and a 0.48µm InGaP. The presence of the spacer layer can reduce the discontinuity of the B-C junction conduction band which effectively increases the current gain and the cut-off frequency [1]. The micrographs of the fabricated $In_{0.49}Ga_{0.51}P$/GaAs SHBT and DHBT are given in figures 3.1.2 and 3.1.3.

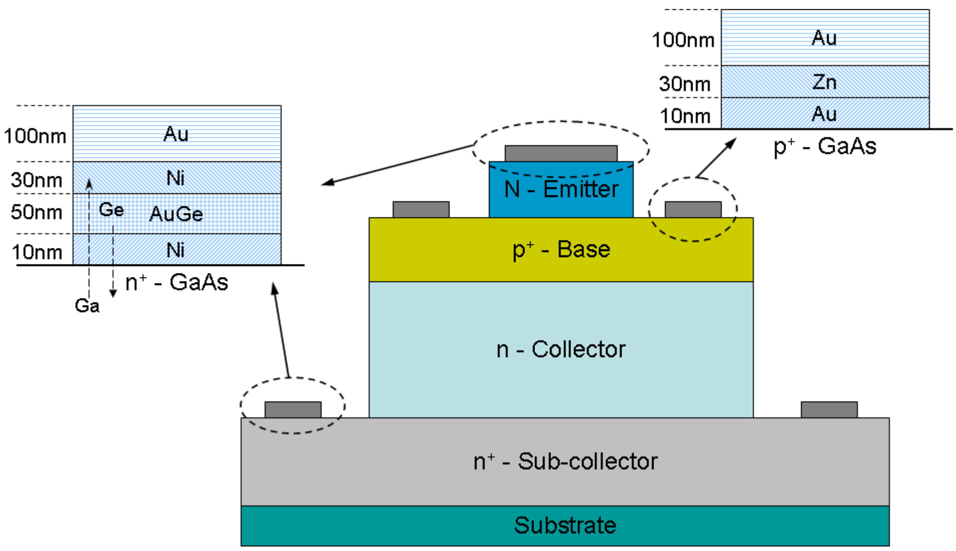

Figure 3.1.4: Metallization structure of contacts for Au/Zn/Au on p-type GaAs and Ni/AuGe/Ni/Au on n-type GaAs with surface protrusion due to thermal alloying

Au/Zn/Au and Ni/AuGe/Ni/Au are commonly used p-type and n-type ohmic contact systems for GaAs HBTs. It is noticed that in both SHBT and DHBT, the emitter and collector contacts metal show protrusion. The texture pattern is caused by alloyed metal from the emitter and collector metal contact fabricating process. The germanium in the emitter and collector contact metal diffuses into n^+ GaAs, acting as n-type doping, producing the surface protrusion. This metal diffusion may reduce contact resistance. While in p-type doped base, no carrier diffusion happens between the metal contact and the p^+ GaAs. So, as shown in figures 3.1.2 and 3.13, the base surfaces are much smoother. As in our test results, the metal contacts of both base and emitter show typical linear ohmic IV characterisations in both directions, indicating that the contacts can supply the required current density with a voltage drop that is very small, compared to the drop across the active region of the device [2]. Additionally, the texture pattern doesn't affect the accuracy of the following measurements.

3.1.2 $Al_{0.3}Ga_{0.7}As$/GaAs single heterojuction bipolar transistor

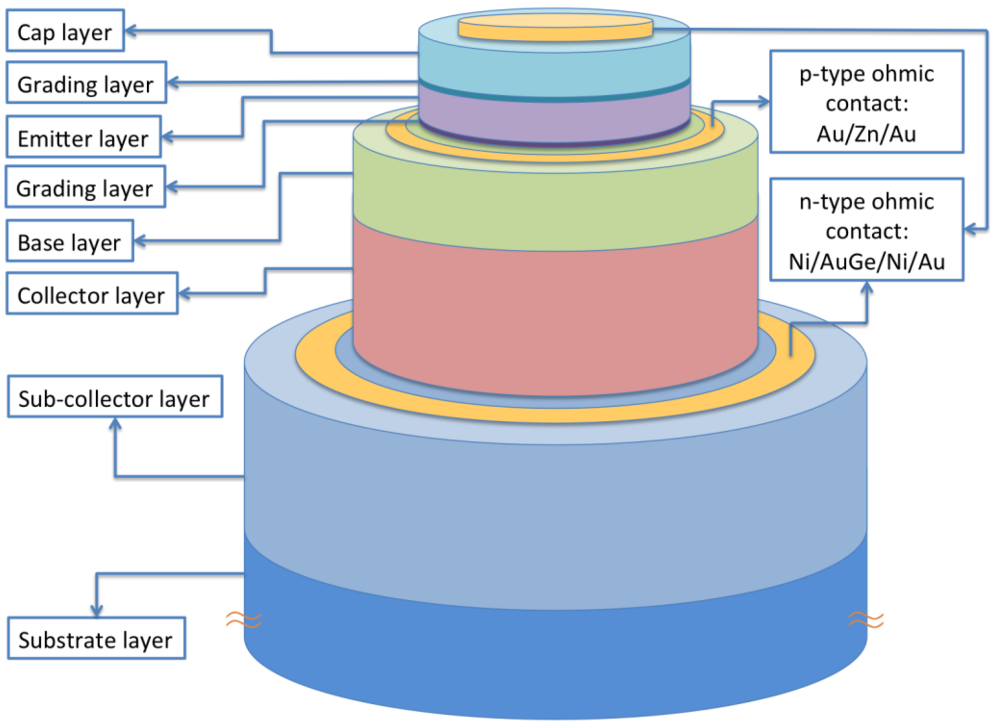

Figure 3.1.5: Schematic device structure of $Al_{0.3}Ga_{0.7}$As/GaAs SHBT (on K15) with emitter contact diameter = 130μm

The $Al_{0.3}Ga_{0.7}As$/GaAs HBT (on K15) is a transistor with a graded B-E junction. The schematic device structure is shown in figure 3.1.5. The layer structure is shown in table 3.1.2, followed by the micrograph in figure 3.1.6.

Table 3.1.2: Layer structures and doping profiles of $Al_{0.3}Ga_{0.7}As$/GaAs SHBT (on K15) with emitter contact diameter = 130μm [2]

Layer	Material	Type	Thickness (μm)	Doping (cm^{-3})	Mole fraction (%)	Dopant
Cap layer	GaAs	n	0.19	5×10^{18}	-	Si
Grading layer	$Al_xGa_{1-x}As$	n	0.02	5×10^{17}	30-0	Si
Emitter	$Al_xGa_{1-x}As$	n	0.15	5×10^{17}	30	Si
Grading layer	$Al_xGa_{1-x}As$	n	0.02	5×10^{17}	0-30	Si
Base	GaAs	p	0.09	2×10^{19}	-	C
Collector	GaAs	n	0.5	2×10^{16}	-	Si
Sub-collector	GaAs	n	1	5×10^{18}	-	Si
Substrate	GaAs	S.I.	400	U/D	-	

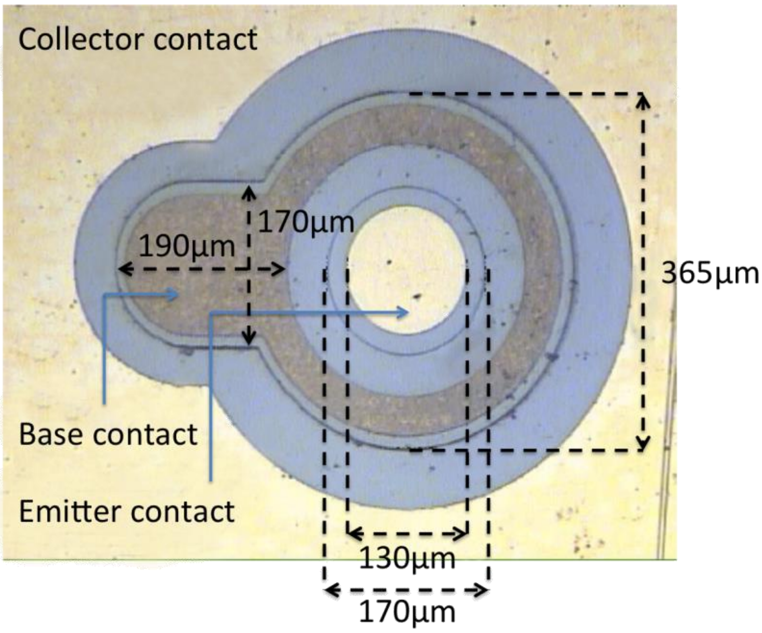

Figure 3.1.6: Micrograph of a fabricated $Al_{0.3}Ga_{0.7}As$/GaAs SHBT (on K15) with emitter contact diameter = 130μm

Similar to the $In_{0.49}Ga_{0.51}P$/GaAs SHBT and DHBT, a heavy doped cap layer was grown on top of the emitter to reduce the emitter's contact resistance. Then, an emitter was formed by a 150nm wide band gap $Al_{0.3}Ga_{0.7}As$. On either side of the emitter, a thin AlGaAs layer was grown for gradual grading of the junction, thus minimising the B-E conduction band discontinuity. A heavily doped GaAs base was present to provide low base resistance and good p-type ohmic contacts [3]; with the 0.5μm lightly doped collector following for a better breakdown voltage performance. In order to archive low resistance n-type ohmic contacts, a highly doped sub-collector was used. The undoped substrate layer was a thick GaAs layer.

3.2 Eye diagram simulation

The simulation setup diagram for eye diagram simulation in this work is shown in figure 3.2.1.

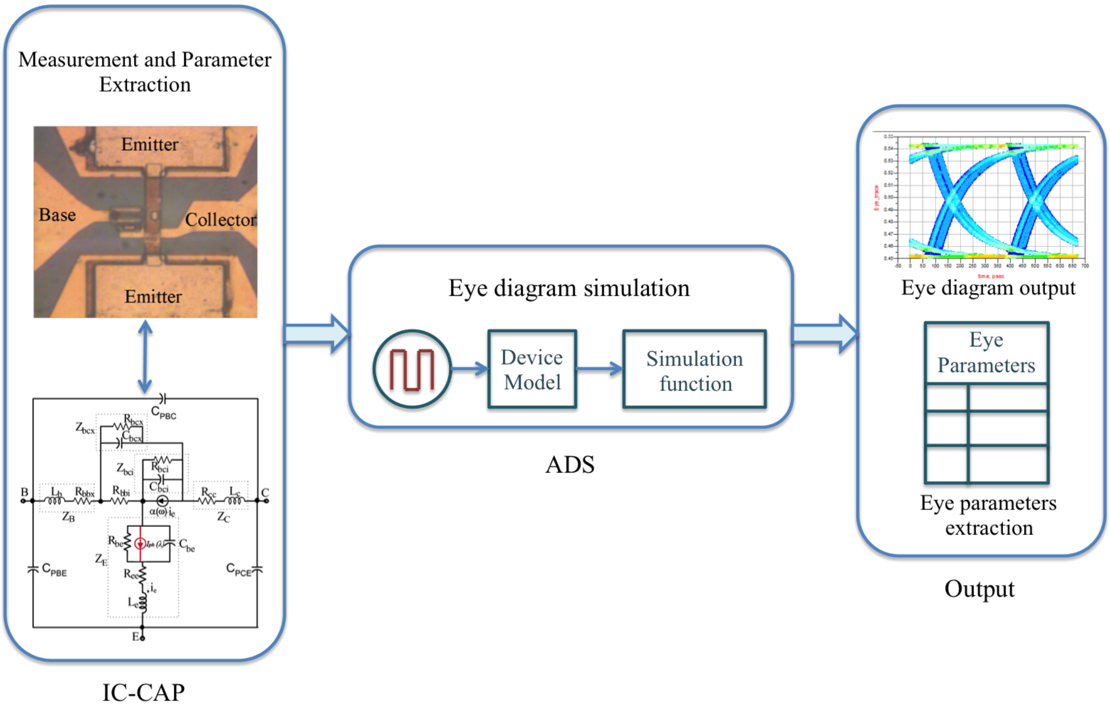

Figure 3.2.1 Simulation setup for generation of eye diagram

On-wafer S-parameters measurements of the device under test were carried out from 45MHz to 30GHz using a HP8510C Network Analyser, controlled by the Integrated Circuit Characterization and Analysis Program (IC-CAP). Before RF measurements were taken, the probes needed to be calibrated in a systematic way, starting from open, short, load and thru, referred to as an LRRM standard. Then accurate S-parameters of DUT were measured under various bias conditions, followed by an automated toolkit for the extraction of small-signal parameters of heterojunction bipolar transistors (HBTs), adopted directly from measured S-parameters using IC-CAP [4-5].

In a T-model small signal equivalent circuit, all model parameters can be directly tied to the physics of the device and maintain backward compatibility with a physics model [6]. Also, T-model fits S-parameters data very well up to mm-wave frequencies. It shows less frequency dependence, than the hybrid-π model, especially at high frequencies [7]. So in this thesis the T-model small signal equivalent circuit is preferred in the following ADS simulation.

The device was given a small signal pseudo random binary sequence (PRBS) RF signal of $25mV_{PP}$ (peak to peak voltage). Such an input level can ensure that the device works in the linear region of operation. Since for long-haul fibre optical communication system, the simplest modulation scheme is a non-return-to-zero (NRZ) format. During the simulation the NRZ signal modulation is adopted. For the NRZ signal modulation baud rate is equal to bitrate. In order to achieve highest bitrate corresponding to the frequency response of the devices, the input signal is coded to switch between “0” and “1” alternately. The bitrate is double values of device operation frequency correspondingly.

Agilent ADS offers a convenient and powerful simulation environment and built-in functions for eye diagram simulation and parameters’ extraction. For instance, the pseudo random digital pulse component in ADS overcomes the many drawbacks of the conventional MATLAB method, and provides a direct option for varying frequency to the desired value without the need for the user to provide a complicated data conversion. After the simulation, the “FrontPanel” function shows the eye diagrams in the data display window as well as the extracted eye parameters, allowing us to carry out further analysis.

3.3 Laser operation and characterisation

3.3.1 Laser diode operation and optical fibre

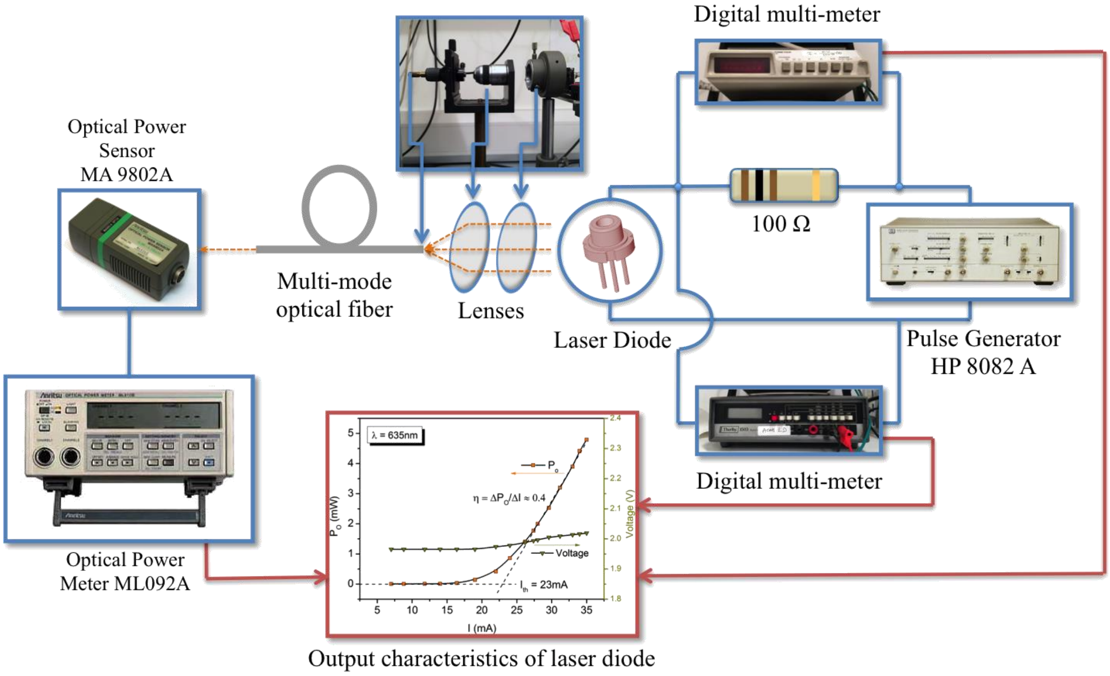

Figure 3.3.1: Block diagram of the setup to characterise laser diodes

In the experiment, 635nm and 850nm laser diodes are adopted as optical input signal sources. Due to the orientation of the set-up, the power falling on the device cannot be measured for every single different value. So a current versus optical power chart for each laser diode needs to be plotted first. As figure 3.3.1 shows, the laser diode was inserted in a case with proper BNC electrical contacts. Since the semiconductor band gap is sensitive to temperature which can affect output wavelength of laser, a pulse generator HP 8082A was used as the bias source of the laser diode, and limited user time was chosen to avoid over heating. The input current was modified by changing the DC offset voltage of the signal from the pulse generator. Two lenses were used to focus the laser on the multi-mode optical fibre (figure 3.3.3). The lens near to the laser diode is a collimating lens, which is adopted to drive a beam in parallel; then the second lens focuses the parallel laser beam on the head of the optical fibre. By adjusting the focal length of the second lens, optimal coupling can be obtained. A 100Ω resistor was connected between the pulse generator and the laser diode, adopted to show the current through the circuit from the digital multi-meter. The other digital multi-meter was connected with the laser diode. Voltage crossing the diode can be monitored from it.

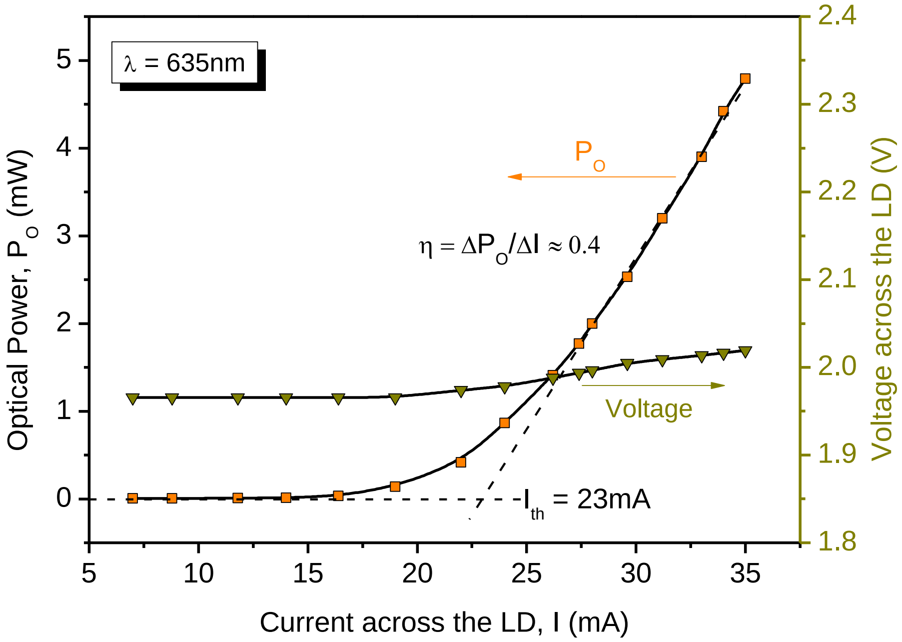

Figure 3.3.2: Measured output characteristics for LD-635-5I 635nm 5mW laser diode

When the laser diode is forward bias high enough, the separation of quasi-Fermi levels, which correspond to the non-equilibrium concentrations of electrons and holes, exceeds the energy of the emitted radiation. A downward transition, known as the negative absorption of an electron from the conduction band, with the emission of a photon of the same energy and phase, occurs. Rather than the upward transition from the valence to conduction band with the absorption of a photon operation take place [8]. This process gives off a spontaneous emitted photon. The cleaved walls at the two borders of the semiconductor structure act as mirrors, resulting in optical feedback. The spontaneous emitted photons can stimulate upwards and downwards transitions, resulting newly stimulated emitted photons [2]. When the rate of such stimulated emission is sufficiently high, gain appears and lasing starts. The current at which the gain exceeds losses within the active region, or spontaneous incoherent emission occurs, is replaced by the stimulated emission of radiation, known as the threshold current I_{th} [9-10].

The amount of power out at the end of the optical fibre was measured by optical power sensor MA 9802A and optical power meter ML092A. The measured output characteristic chart of LD-635-5I, records the amount of current (through), and voltage (across), the laser diode, as well as output power from the end of the optical fibre (figure 3.3.2). The threshold current I_{th} is extracted as 23mA.

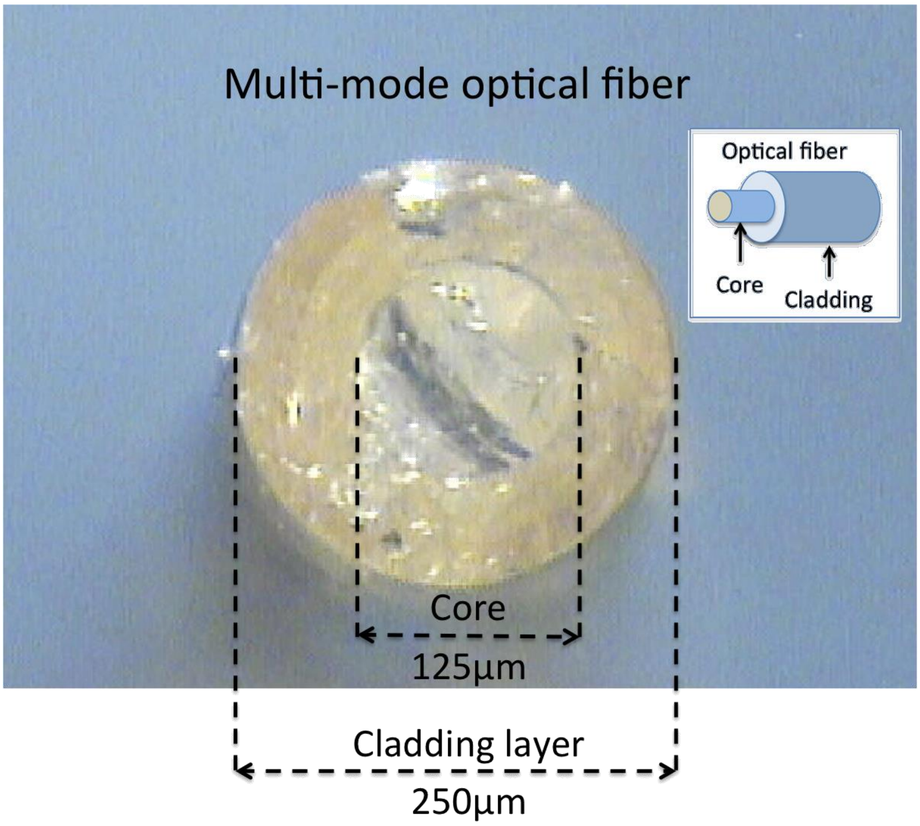

Figure 3.3.3: Micrograph of a 125/250 multi-mode glass optical fibre

3.3.2 Optical measurements setup

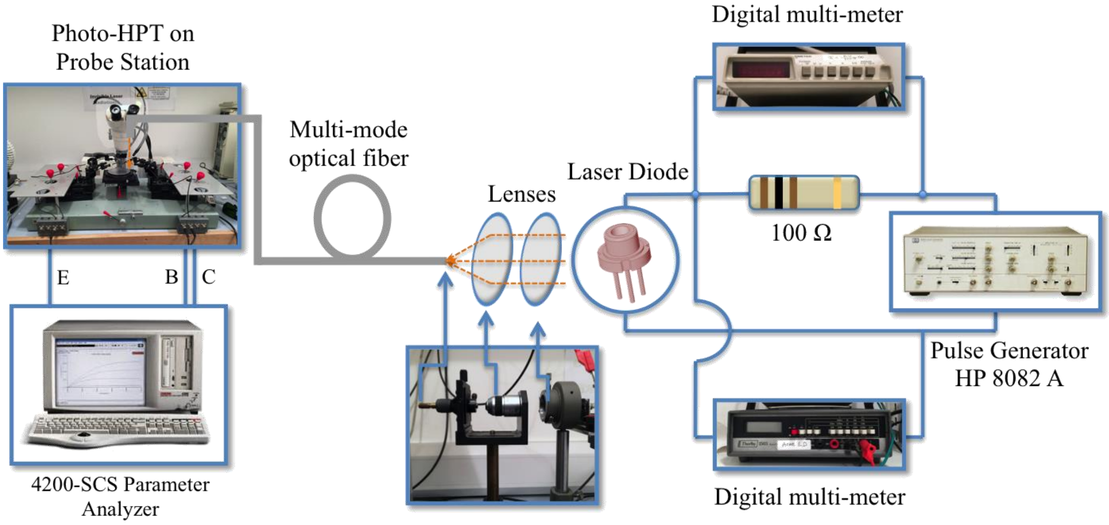

Figure 3.3.4: Block diagram of experimental setup to obtain the DC electrical characteristics and the SR of HPTs

The device under testing was set on a probe station, as shown in figure 3.3.4. There were a total of 4 probes used in this experiment. Three of these were connected to the device emitter, base and collector terminals, respectively. The last probe was used to connect with the multi-mode optical fibre, shining an input optical signal to the base of the device. The probe station then connected with the Keithley 4200 Semiconductor Parameter Analyser (SPA), which provides accurate DC measurements in spreadsheet format and graphical display.

References

[1] Sotoodeh, M., Khalid, A. H., Sheng, H., Amin, F. A., Gokdemir, T., Rezazadeh, A. A., Knights, A. P., Button, C. C. “Direct extraction and numerical simulation of the base and collector delay times in double heterojunction bipolar transistors”, IEEE Transactions on Electron Devices, vol. 46, no. 6, pp.1081-1086, June 1999.

[2] Khan, H. Ph.D thesis, “spectral response modelling and Analysis of Heterojuction bipolar phototransistors”, Microwave and Communication Systems Research Group, School of Electrical and Electronics Engineering, University of Manchester, 2010.

[3] Abernathy, C. R., Pearton, S, J., Ren, F., Hobson, W. S., Fullowan, T. R., Katz, A., Jordan, A. S., Kovalchick, J. “Carbon doping of III-V compounds grown by MOMBE”, Proceedings of the Second International Conference on Chemical Beam Epitaxy and Related Growth Techniques - (ICCBE-2), 11-13 December, 1989.

[4] Ahmad, T., Rezazadeh, A.A., Gill, S.S. “Improved Parameter Extraction Method for Microwave HBTs”, Modelling, Design and Application of MMIC's, IEE Colloquium on, pp. 5/1-5/8, 17 Jun 1994.

[5] Sotoodeh, M., Khalid, A.H., Rezazadeh, A.A. “Bias Dependence Study of the HBT Small-Signal Equivalent Circuit Elements Using a New Parameter Extraction Technique”, High Performance Electron Devices for Microwave and Optoelectronic Applications, pp. 9-14, 1999.

[6] Casey, H. C. J., Sell. D. D. and Wecht, K. W. “Concentration dependence of the absorption coefficient for n- and p-type GaAs between 1.3 and 1.6 eV.”, Journal of Applied Physics, vol. 46, pp. 250-257, 1975.

[7] Lush, G. B., Melloch, M. R. and Lundstrom, M. S. “Concentration-dependent optical-absorption coefficient in n-type GaAs”, Journal of Applied Physics. 74, 4694, 1993.

[8] Casey, H. C. and Panish, M. B. “Part A: Fundamental Principles”, in Heterostructure Lasers: Academic Press, USA 1978.

[9] Sze, S. M. Physics of Semiconductor Devices, 2nd ed. USA: John Wiley & Sons, 2001.

[10] Tyagi, M. S. Introduction to Semiconductor Materials and Devices: John Wiley & Sons, 1991.

Chapter 4 InGaP/GaAs single and double heterojunction bipolar transistors DC and optical characterisations

4.1 Introduction

Equation Chapter 4 Section 1Photonics technology has begun to play an indispensable role in the realisation of various broad-band communication systems, such as high-bit-rate fibre-optic communications systems and fibre-radio wireless communication systems. In these systems, light sources, ultrafast optical modulators, and ultrafast photodetectors are the key components [1]. In recent years, monolithically integrated photo receivers such as optoelectronic integrated circuits (OEICs) have attracted much attention for realising optical/micro- or millimetre-wave interaction systems [2]. Photodiodes such as p-i-n diodes and avalanche photodiodes (APDs) have been widely used as photodetectors, although the p-i-n diode cannot offer any internal gain, making the sensitivity to the weak input optical power inferior. Also, in order to enhance the optical performance of the p-i-n, the layer structure design is severely limited, e.g. i-region thickness increments can degrade the carrier transit time across the intrinsic region as well as increase the capacitance of the p-i-n, thus further limiting the response speed. In the case of APDs, although the avalanche breakdown produces internal gain, excess noise is the result of this process. Among these photo receiver structures, layer- and process-compatible photodetectors based on heterostructure bipolar transistor (HBT) technology are the most promising for high-performance monolithically integrated photo receivers [3]. Heterojuction phototransistors (HPTs) using a III-V compound semiconductor is expected to play a key role in the next generation of microwave and OEICs. The HPT can be thought of as a B-C junction photodiode plus internal amplifier [4]. Their high potential as a high performance photodetector for light wave communications and an alternative to APDs and p-i-n photodiodes is already known. Good RF performance for photodetection amplification of HPTs is fabricated using high-performance HBTs technologies [5]. Integrated circuits using the HPT/HBT combination are the most promising way to realise high-performance photo receivers for micro- or millimetre-wave sub-carrier transmission via optical fibre and optical-microwave signal processing systems [2].

Recently there have been several reports of HPTs operating with a DC bias, and showing enhanced device performance. As we know, 3T-HPT can push the current quiescent bias point to a higher level, resulting in better optical gain, as well as improved frequency response. Although there have been several reports on HPTs operation enhancement with a DC base bias (3T-HPTs) [6-8], no results discuss as to what the differences are between a single and double HPT with a current- and voltage-base bias. Furthermore, the InGaP/GaAs material system HBTs show an enhancement of performance as well as reliability [9-10], although there has been very little study done on using this device as a photodetector [11]. It is therefore worth investigating, comparing and discussing the $In_{0.49}Ga_{0.51}P/GaAs$ SHBT and DHBT in this chapter. This is particularly important in term of applying such devices to the practical circuit of monolithic optical receivers.

In this section, single- and double-$In_{0.49}Ga_{0.51}P/GaAs$ heterojunction bipolar transistors using as HPTs are investigated. DC, 2-terminal and 3-terminal optical characterisations are shown and compared. The advantages of InGaP/GaAs material system DHBT are discussed. Finally, the base band bending effect of the DHBT using as a short wavelength (850nm) photodetector is proved to exist, as will be discussed later.

4.2 InGaP/GaAs material system

For short wavelength applications, such as optical interconnects in multi-chip modules and local area networks, AlGaAs/GaAs system HBTs are widely used and studied [12-14]. However, the Al atoms of the AlGaAs emitter and the exposed surface of the extrinsic base provide the origins of degradation under operation [15]. An alternative to AlGaAs is the aluminium free InGaP which is lattice matched to GaAs substrates and exhibits a number of desirable attributes; these include lower interface and surface recombination, large valence band discontinuity with small conduction discontinuity, low noise and higher efficiency emitter [16].

Table 4.1: Band discontinuities for various HBT material heterostructures [17]

Material structure	ΔE_c (eV)	ΔE_v (eV)
$Al_{0.3}Ga_{0.7}As/GaAs$	0.28	0.19
$In_{0.49}Ga_{0.51}P/GaAs$	0.2	0.29

The lattice matched $In_{0.49}Ga_{0.51}P/GaAs$ heterojuction has a more favourable band line-up for heterojuction bipolar transistor than $Al_{0.3}Ga_{0.7}As/GaAs$ [18]. $In_{0.49}Ga_{0.51}P$ has a small conduction band discontinuity (ΔE_c = 0.2eV) and a larger valence band discontinuity (ΔE_v = 0.29eV) when compared to $Al_{0.3}Ga_{0.7}As$ [17]. Absence of the problems related to DX centres in AlGaAs, existence of highly selective wet and dry etch chemistries for the $In_{0.49}Ga_{0.51}P/GaAs$ material system and low surface recombination velocity are among the other advantages for InGaP over AlGaAs as the emitter of HBTs [16]. These superior physical properties and the easy fabrication of a ledge emitter structure to passivate the surface of the extrinsic base has made the InGaP system attract considerable attention with regard to replacing the AlGaAs [19]. In recent years InGaP/GaAs heterojuction bipolar transistors have been the dominant technology for wireless handset power amplifier (PA) applications due to their excellent performance, reproducibility, reliability and manufacturability [20].

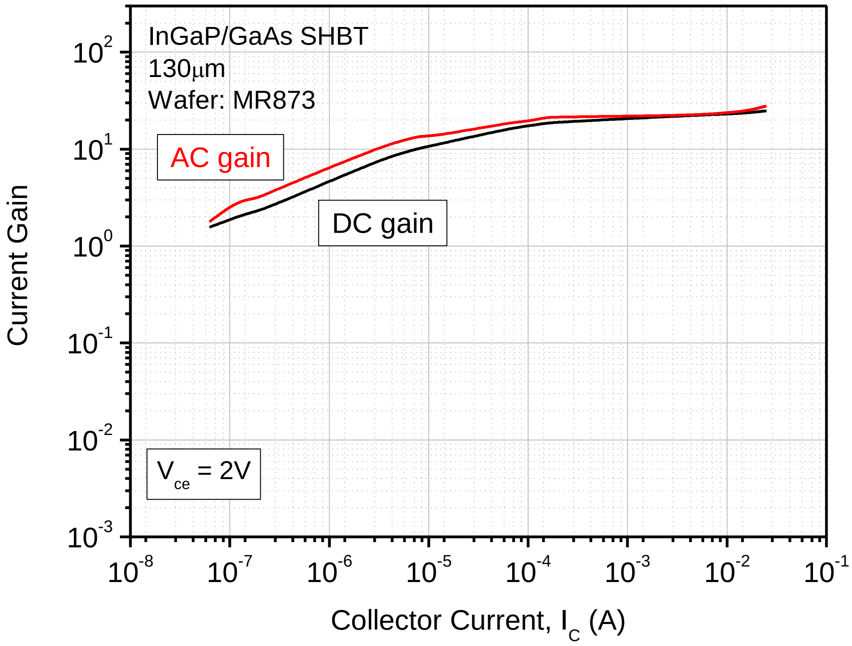

Figure 4.1: Measured current gain from IV characteristics of $In_{0.49}Ga_{0.51}P/GaAs$ SHBT (wafer no. MR873, emitter contact diameter = 100μm)

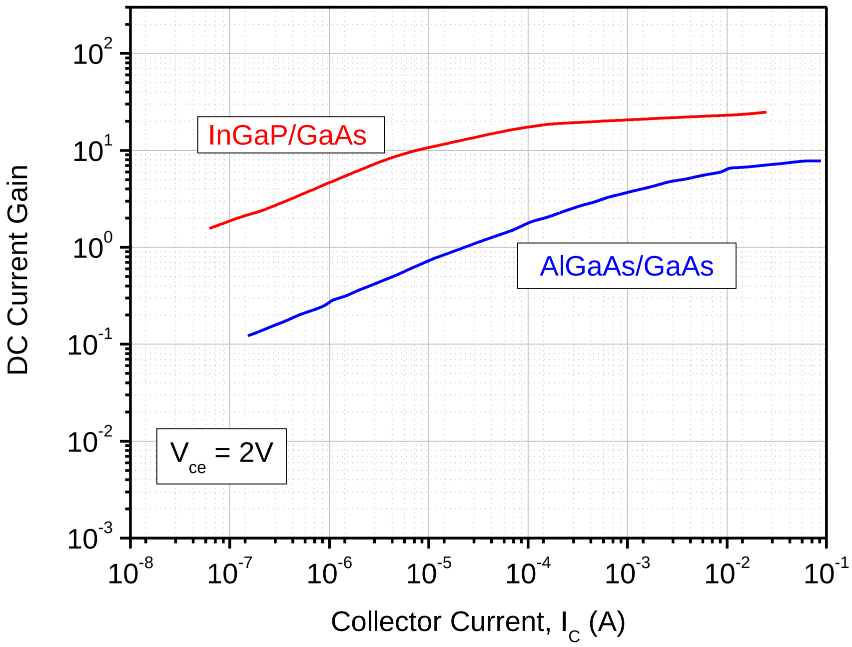

Figure 4.2: Measured current gain from IV characteristics of $In_{0.49}Ga_{0.51}P/GaAs$ (wafer no. MR873) and $Al_{0.3}Ga_{0.7}As/GaAs$ (wafer no. K8) SHBT, both with 130μm emitter diameter

When $In_{0.49}Ga_{0.51}P$ is used as the emitter, most of the energy gap discontinuity occurring within the valence band enables an easier electron injection into the base from the emitter, whilst also preventing holes (electrical and photo-generated) occurring from the base injection into emitter. This results in improved emitter injection efficiency and reduction of the E-B leakage current [17]. Thus, both current gain and optical gain show a considerably enhancement. Moreover, the passivation of the InGaP ledge on the surface of the extrinsic base provides a low surface recombination centre [19]. The current gain of the InGaP emitter HBT is relatively constant over five decades of collector current and useful gain at collector current levels as low as 0.1μA [21] (figure 4.2). This indicates the device's high sensitivity and high linearity, making this system full of potential for low-power operations, and fully compatible with optical devices.

But in InGaP there are also some drawbacks, for example, the reported values of electron saturation velocity, in the ranges of $(4.4\text{-}8.0)\times 10^6$cm/s, and the value in GaAs as $(8.0\text{-}10)\times 10^6$cm/s (either measured or calculated by Monte Carlo methods [22-23]), which can reduce the current gain of the device.

4.3 $In_{0.49}Ga_{0.51}P$/GaAs single heterojuction bipolar transistor

4.3.1 $In_{0.49}Ga_{0.51}P$/GaAs SHBT DC characterisation

Gummel plot and common emitter IV characteristics are two typical measurements for evaluating HBTs performance. Gummel plot is the measurement of collector and base current with a base-emitter voltage variation which simultaneously keeps the base-collector at zero volts bias. In the case of a common-emitter configuration, the collector current is measured as a function of collector-emitter voltage, while a variable base current source is used to provide base bias.

Typical SHBT DC characteristics for the Gummel plot are given in Figure 4.3. The base and collector currents are measured in dark as a function of B-E voltage bias.

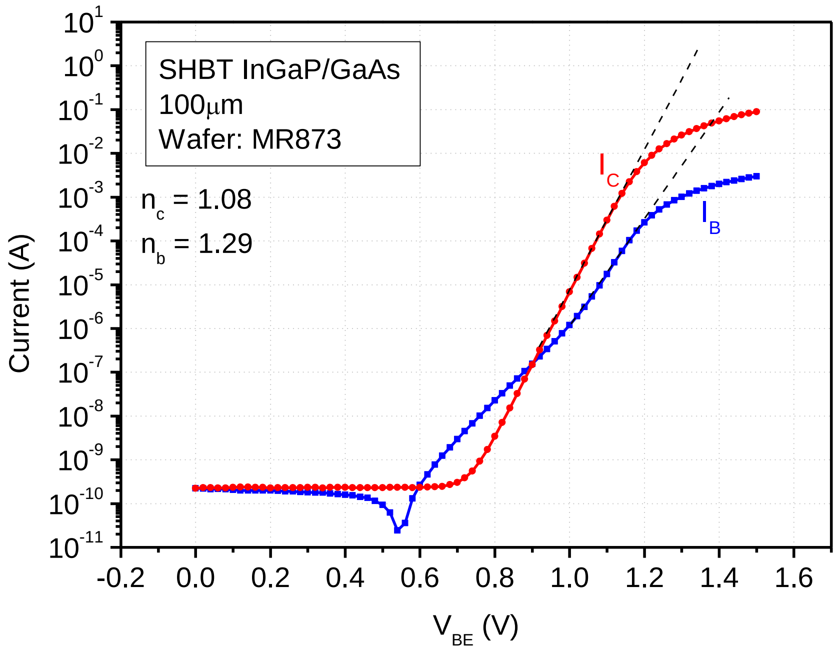

Figure 4.3: Measured Gummel plot of the Npn $In_{0.49}Ga_{0.51}P/GaAs$ SHBT (wafer no. MR873, emitter contact diameter = 100μm)

In the low voltage region the base current is seen as a similar value to the collector current. The gain is unity or even smaller and the total base-emitter junction current is dominated by recombination within the B-E space-charge region. After this voltage (0.9V), the diffusion current component becomes dominant over the generation-recombination process, while the transistor begins to exhibit gain. At an even higher voltage, a high injection effect appears where the number of electrons injected from the emitter into the base becomes comparable with the native holes in the base. This presence of intrinsic series resistances reduces emitter efficiency. One feature of the device data (figure 4.3) can be found is the linear part of I_C which occupies more than six decades. The ideality factor for collector current is $n_C = 1.08$, while for the base current is it $n_B = 1.29$, indicating a high quality E-B interface and low recombination.

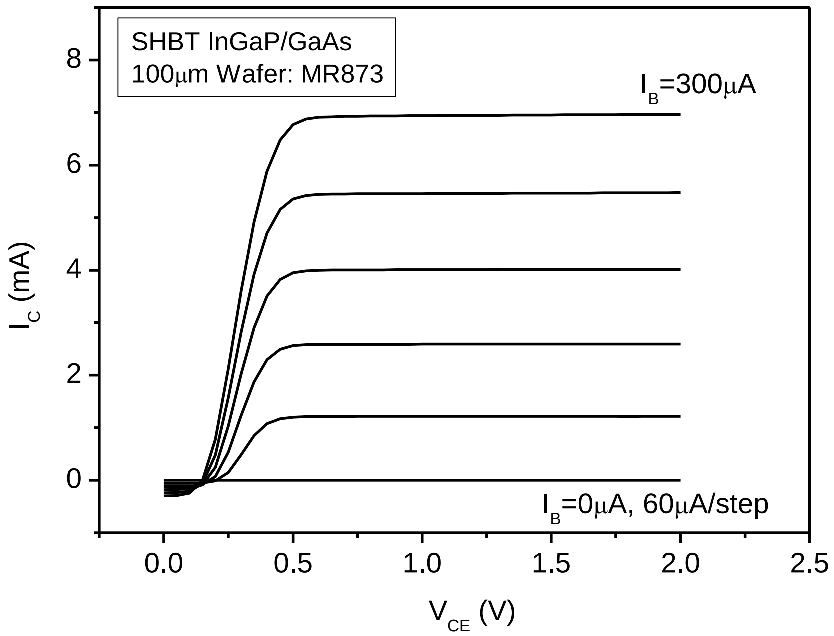

Figure 4.4: Measured IV characteristics of the Npn $In_{0.49}Ga_{0.51}P/GaAs$ SHBT (wafer no. MR873, emitter contact diameter = 100μm)

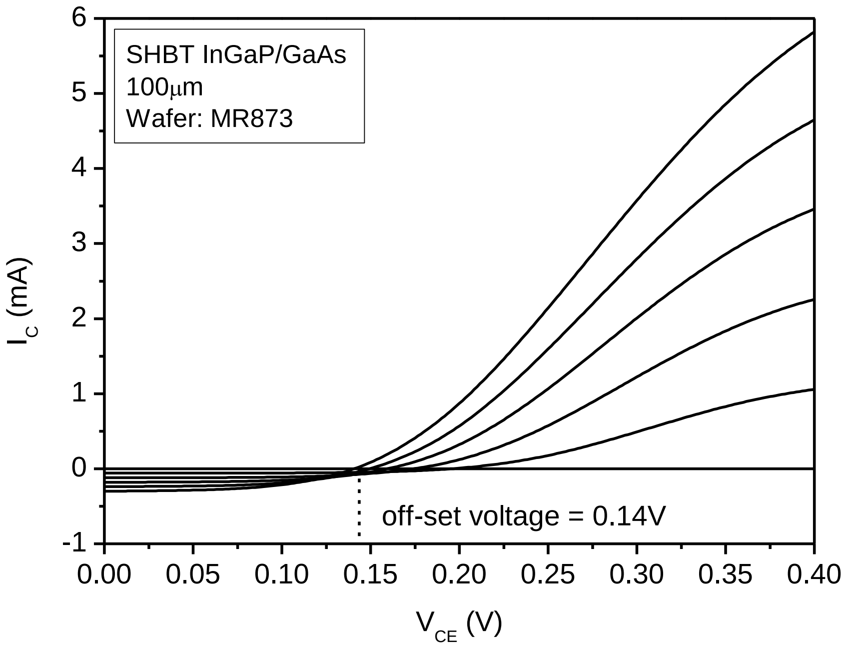

Figure 4.5: Measured off-set voltage of the Npn $In_{0.49}Ga_{0.51}P/GaAs$ SHBT (wafer no. MR873, emitter contact diameter = 100μm)

Figure 4.4 shows common emitter output characteristics of the device, where the output current (I_C) measured as the C-E voltage increases with base current stepped in 60μA increments. The dark current at V_{CE} = 2V is only 1.3×10^{-9} low, which again confirms a high quality E-B junction with low E-B leakage current. Off-set voltage is given in figure 4.5 with the value of 0.14V. This small value benefits from the small conduction band discontinuity of E-B heterojuction.

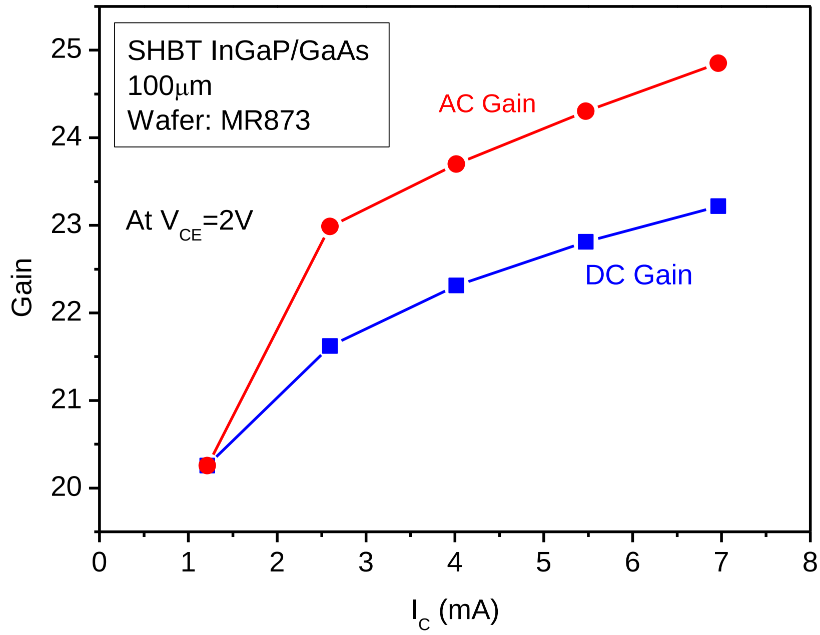

Figure 4.6: Measured DC and AC current gain of the Npn $In_{0.49}Ga_{0.51}P$/GaAs SHBT (wafer no. MR873, emitter contact diameter = 100μm)

DC and AC current gain as a function of collector current is given in figure 4.6. For our measurements, the maximum DC gain can achieve more than 23, which is reasonable for our device. It is noticed that the higher output current level (resulted from higher quiescent bias current (I_B)) the larger the current gain.

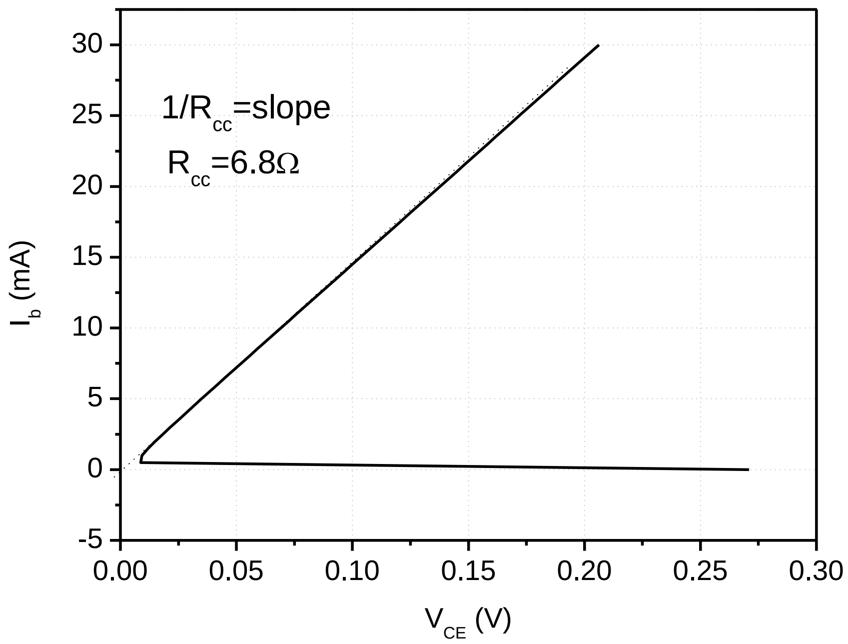

Figure 4.7: Measured collector resistance of the Npn $In_{0.49}Ga_{0.51}P$/GaAs SHBT (wafer no. MR873, emitter contact diameter = 100μm)

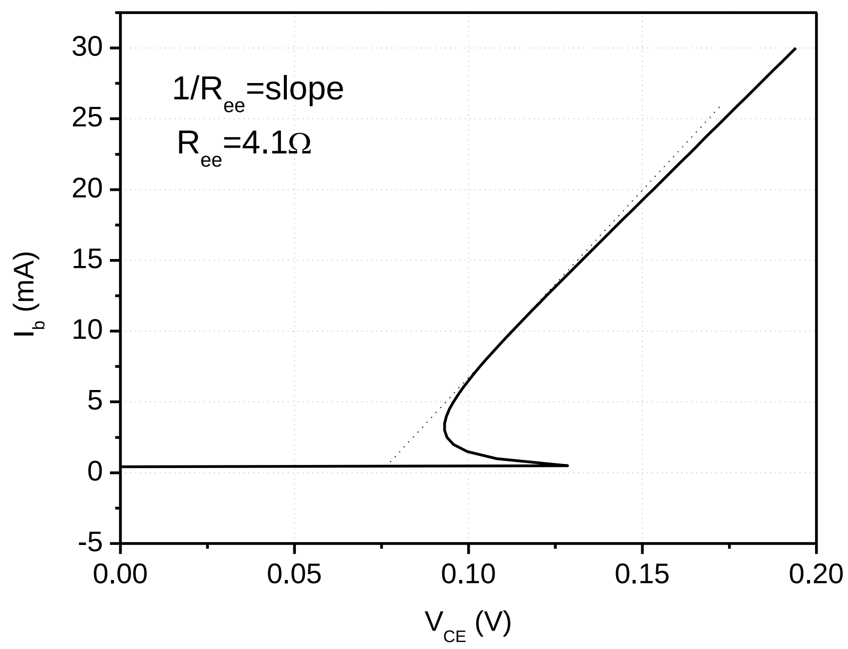

Figure 4.8: Measured emitter resistance of the Npn $In_{0.49}Ga_{0.51}P$/GaAs SHBT (wafer no. MR873, emitter contact diameter = 100μm)

Using the Giacoletto method, the collector and emitter resistances are measured and the results given in the above figures as $R_{cc} = 6.8\ \Omega$ and $R_{ee} = 4.1\Omega$.

Doping concentration for Base and Collector can be achieved by following steps. Firstly, the junction capacitances are measured. Capacitance value is directly proportional to area of the junction and the charge stored and inversely proportional to the width of the depletion region. The equation is given as:

$$C = \varepsilon_0 \varepsilon_s \cdot \frac{A}{d} \qquad (4.3.1)$$

Where d is depletion region thickness and A is the area of the junction. The depletion thickness can be written as,

$$d = [\frac{2\varepsilon_0 \varepsilon_s \Delta V}{qN_D}]^{1/2} \qquad (4.3.2)$$

Where $\Delta V = V_{bi} - V_f$ Forward bias junction

$\Delta V = V_{bi} - V_r$ Reverse bias junction

Insert equation (4.3.2) into (4.3.1),

$$C = A \cdot (\frac{qN_D \varepsilon_0 \varepsilon_s}{2})^{1/2} \cdot (\Delta V)^{-1/2} \qquad (4.3.3)$$

Squaring (4.3.3) and rearranging in the form of *y = (slop)x +C*, gives (4.3.4)

$$\frac{1}{C^2} = \frac{2V_{bi}}{q\varepsilon_0 \varepsilon_s N_D A^2} + \frac{2V_R}{q\varepsilon_0 \varepsilon_s N_D A^2} \qquad (4.3.4)$$

If $1/C^2$ is plotted against V_r and the curve is extrapolated, V_{bi} can be found at $1/C^2$ equal to zero. Bring the values of V_{bi} and V_r back to (4.3.2). Then plot N_D as a function of d. From the figure, the value of $(N_D)_b$ and $(ND)_e$ can be obtained.

Table 4.2: DC measured characteristics of the Npn $In_{0.49}Ga_{0.51}P$/GaAs SHBT (wafer no. MR873, emitter contact diameter = 100μm)

Parameters	Values
$(N_D)_b$	2×10^{19} cm^{-3}
$(N_D)_c$	1×10^{16} cm^{-3}
R_{ee}	4.1Ω
R_{cc}	6.8Ω
off-set voltage	0.14 V
DC gain at V_{ce}=2V, I_b=120μA	22
AC gain at V_{ce}=2V, I_b=120μA	23
Gain from Gummel plot at I_c=10μA	6
Collector ideality factor (n_C)	1.08
Base ideality factor (n_B)	1.29
Collector saturation current (I_{co})	8.2×10^{-22}A
Dark current at V_{ce}=2V	1.3×10^{-9}A
Turn on voltage	0.67 V

4.3.3 $In_{0.49}Ga_{0.51}P$/GaAs SHBT 2-terminal optical characterisation

First, a bias voltage is applied between base and collector. The B-C junction is reverse biased with the emitter floating. The HPT is functioned as a p-i-n photodiode which is formed by base, collector and sub-collector. Various optical powers at wavelengths 635nm is illuminated in the base absorption window. p-i-n photocurrents generated within the B-C junction are shown in figure 4.9.

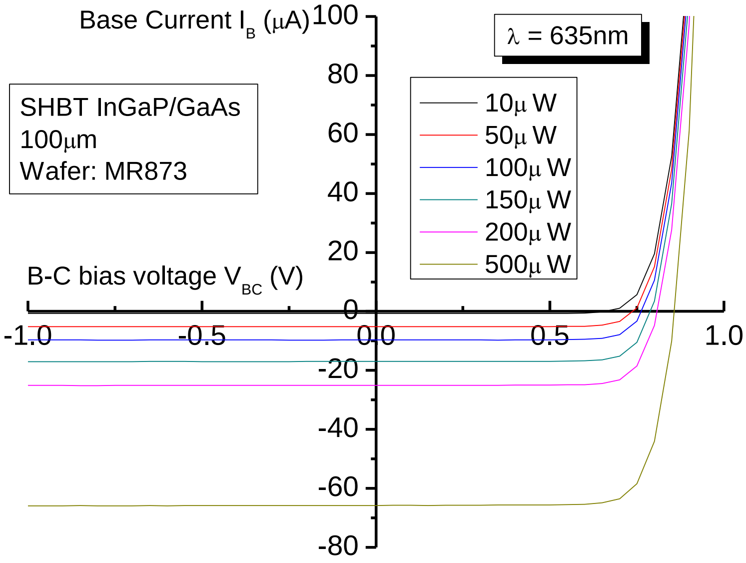

Figure 4.9: Measured B-C junction photocurrent of the Npn $In_{0.49}Ga_{0.51}P$/GaAs SHBT (wafer no. MR873, emitter contact diameter = 100µm) at 635nm

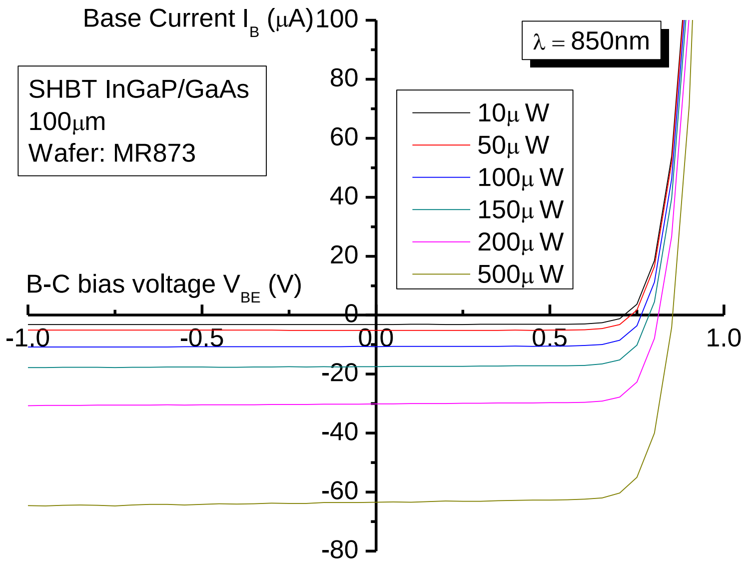

Figure 4.10: Measured B-C junction photocurrent of the Npn $In_{0.49}Ga_{0.51}P$/GaAs SHBT (wafer no. MR873, emitter contact diameter = 100µm) at 850nm

It is noticeable that with the increment of incident optical power, a higher photocurrent is obtained. But the photo-generated current is independent with reverse bias voltage value. Optical responsivity of the B-C junction at -1V B-C reverse bias voltage is given in figure 4.15. A relatively flat trend is observed. Similar measurement results are given in figure 4.10 and figure 4.16, which are the B-C optical currents and optical responsivity at 850nm, respectively.

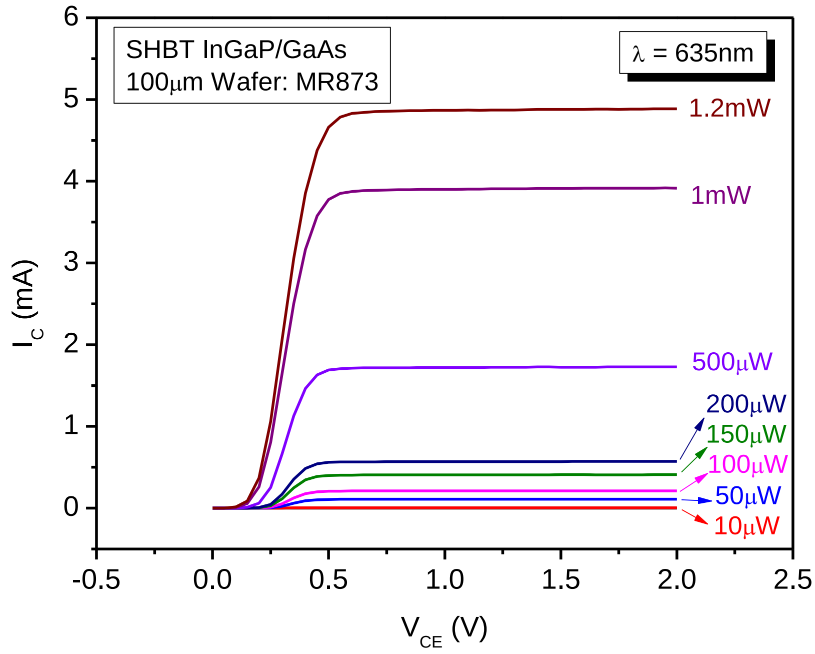

Figure 4.11: Measured 2-terminal photoresponse of the Npn $In_{0.49}Ga_{0.51}P/GaAs$ SHBT (wafer no. MR873, emitter contact diameter = 100μm) at 635nm

Figure 4.11 shows the collector current as a function of C-E bias voltage for a 2T-HPT with a floating base at 635nm wavelength incident light. The photo-generated current in the B-C junction actually provides the bias current for the transistor. The measured collector current versus incident optical power is shown in figure 4.14. Similarly, collector current measurements with incident light at 850nm with various optical powers are given in figures 4.12 and 4.13. Since the 2T-HPT behaves as a transistor, higher optical power produced a higher photo-generated current. Then the current is amplified by the transistor and saturated at high C-E voltage as shown in the figures.

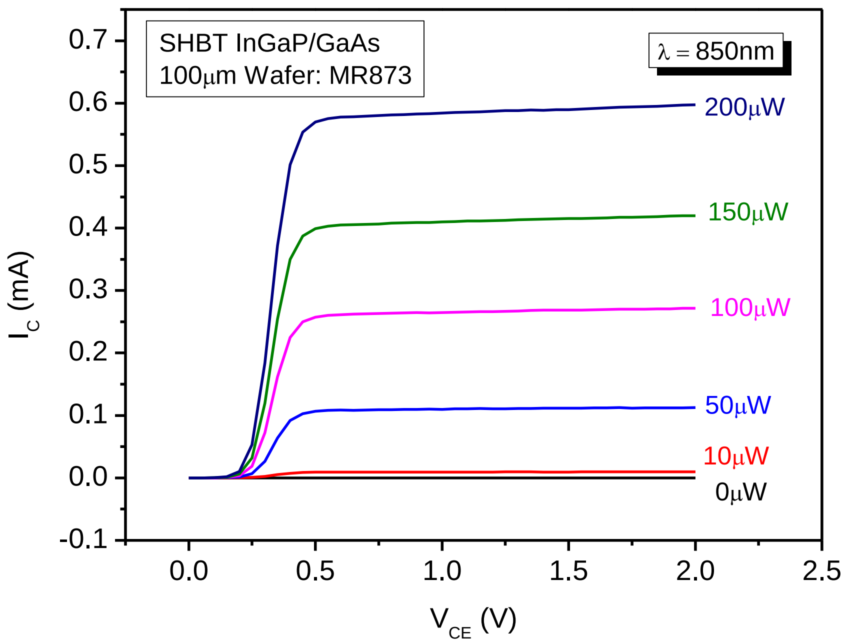

Figure 4.12: Measured 2-terminal photoresponse of the Npn $In_{0.49}Ga_{0.51}P/GaAs$ SHBT (wafer no. MR873, emitter contact diameter = 100μm) at 850nm with optical power up to 200μW

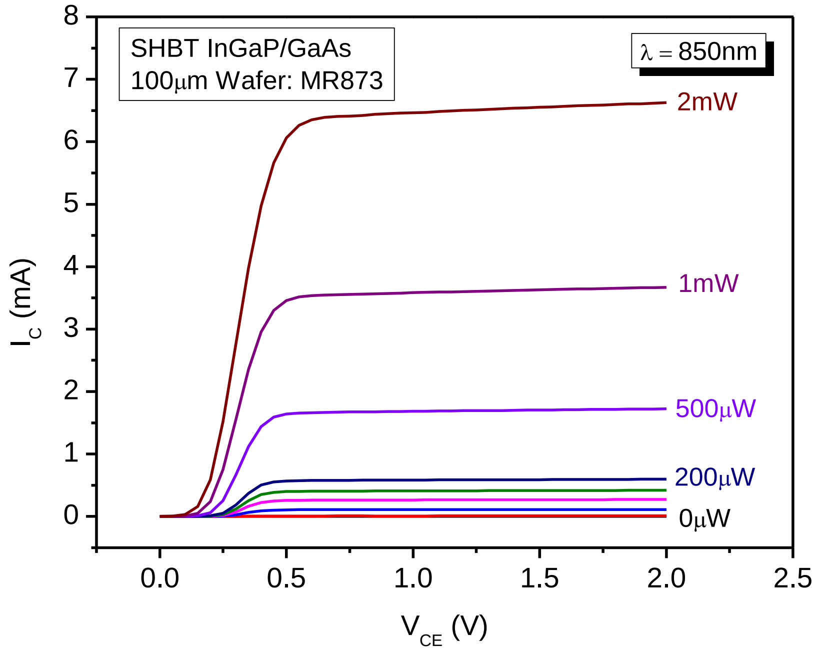

Figure 4.13: Measured 2-terminal photoresponse of the Npn $In_{0.49}Ga_{0.51}P/GaAs$ SHBT (wafer no. MR873, emitter contact diameter = 100μm) at 850nm with optical power up to 2mW

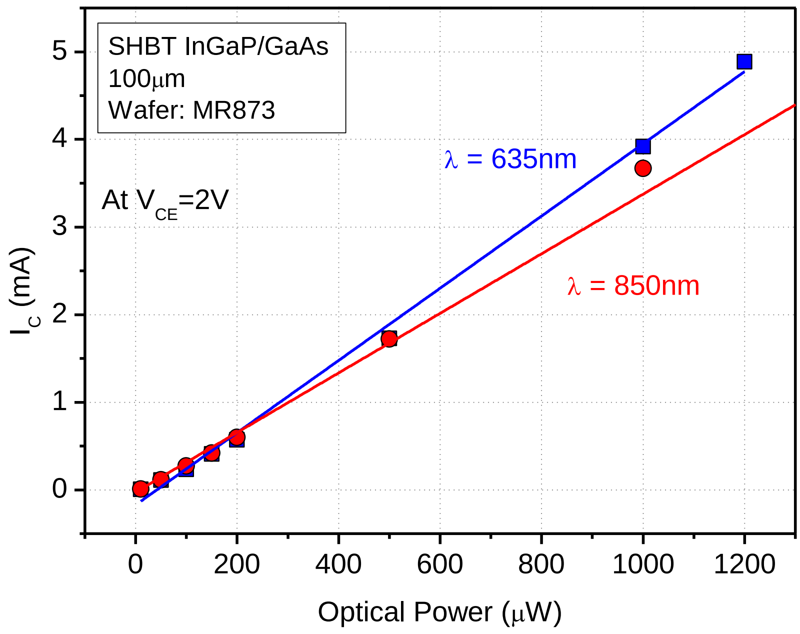

Figure 4.14: Comparison of measured 2-terminal collector current of the Npn $In_{0.49}Ga_{0.51}P$/GaAs SHBT (wafer no. MR873, emitter contact diameter = 100μm) at 635nm and 850nm

Figures 4.15 and 4.16 show the optical responsivity of the 2T-HPT at 635nm and 850nm, which are calculated from figures 4.11, 4.12 and 4.13 respectively. Both results show the responsivity increase rapidly in the low optical power region. This can be attributed to the increment of current gain with the increment of quiescent bias current level (figure 4.6). In the high optical region, the responsivity is saturated at certain values. This can be explained as the absorption limitation of the device. After the certain value of optical power, too many photons incident into the device. The collection efficiency of the device thus begins to reduce, which can further decrease responsivity. The reason why 850nm is beginning to show saturation at lower optical power, when compared with 635nm, is that at a certain incidence optical power level, the longer the wavelength, the more incident photons, meaning that the device is able to reach its limitation earlier.

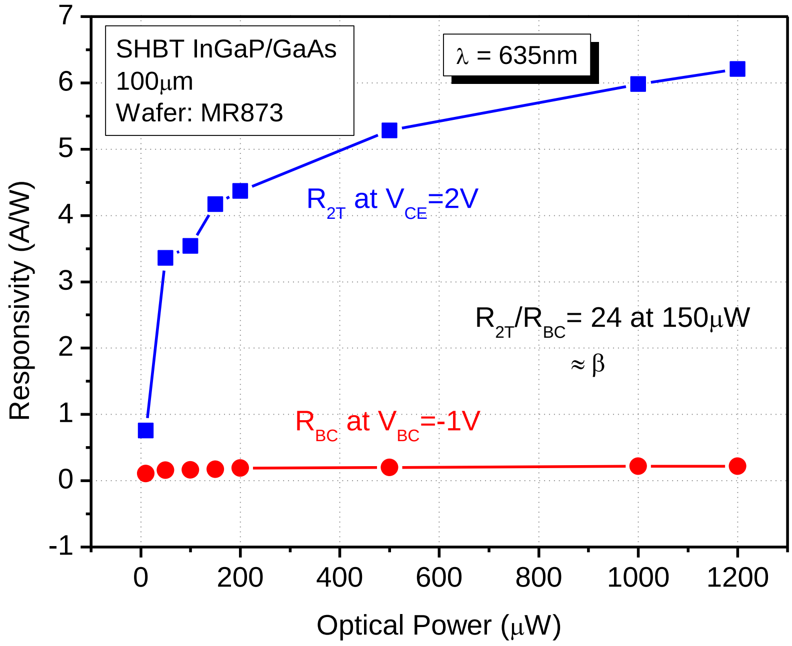

Figure 4.15: Measured 2-terminal and B-C junction - optical responsivity of the Npn $In_{0.49}Ga_{0.51}P$/GaAs SHBT (wafer no. MR873, emitter contact diameter = 100μm) at 635nm

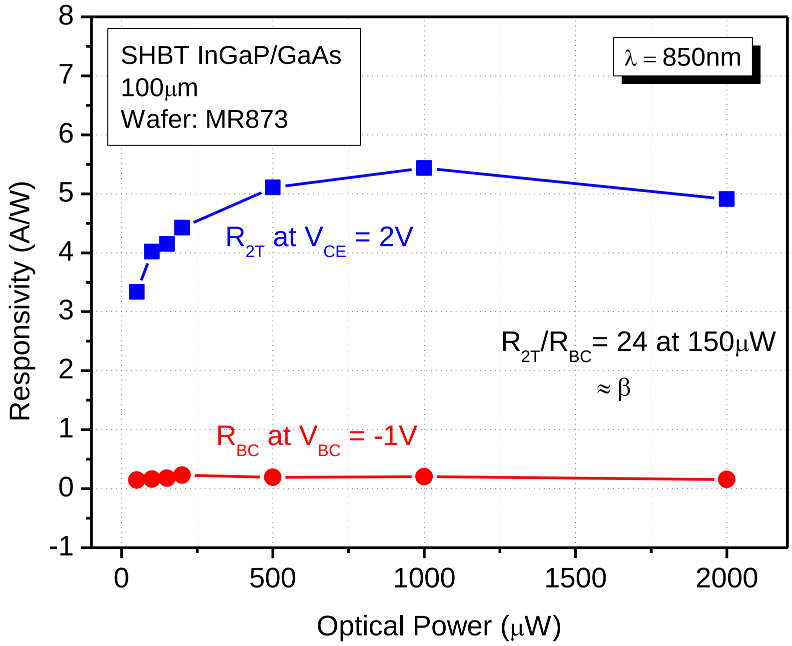

Figure 4.16: Measured 2-terminal and B-C junction - optical responsivity of the Npn $In_{0.49}Ga_{0.51}P$/GaAs SHBT (wafer no. MR873, emitter contact diameter = 100μm) at 850nm

Using equations $R_\lambda = \frac{I_{ph}}{P_{opt}}$ and $I_{Cp} = I_{ph} \times [\beta_{(I_B = I_{ph})} + 1]$ discussed before, from the figures, we could calculate the ratio of 2T's and B-C's responsivity at 635nm and 850nm, both giving us the value of 24 at 150μW, which reasonably equals the value of current gain in figure 4.6. This coincides with the theory.

4.3.4 $In_{0.49}Ga_{0.51}P$ /GaAs SHBT 3-terminal optical characterisation with base current bias

In the early stage of development and application, HPTs were used as 2-terminal devices with a floating base (2T-HPTs). Under such an operating condition, the average incident light provides the quiescent bias current [24-25]. At low incident optical power, the optical current produced by the device is small, and due to recombination at the base emitter heterojuction, the current gain is low resulting in low optical gain. This means the device cannot perform as expectations. Consequently, the lower output current (collector current) increases charging time of junction capacitance, which can further reduce the cut-off frequency. Therefore, it is essential to bias the base terminal with an additional electrical current or voltage, which can push the HBT quiescent bias point to a higher current gain level. Although there have been several reports on HPT operation enhancement with a DC base bias (3T-HPTs) [6-8], none of the results discussed the differences between a single and a double HPT with a current- and voltage-base bias. Furthermore, InGaP/GaAs material system HBTs show enhanced performance as well as reliability [9-10], although very little study has been undertaken on using this device as a photodetector [11].

As discussed previously, at a low incident power level, the low value current gain limits the optical gain of HPT. On other hand, a biased current addition in base can push the HPT operating point to a higher current gain level, thus enhancing the HPT performance. In this section, the 3T-HPT with base current bias configuration will be discussed.

An additional biased current is added to the base terminal. Figure 4.17 shows measured common emitter output characteristics for this configuration operated in the dark (no optical input signals) and under various optical illuminations respectively.

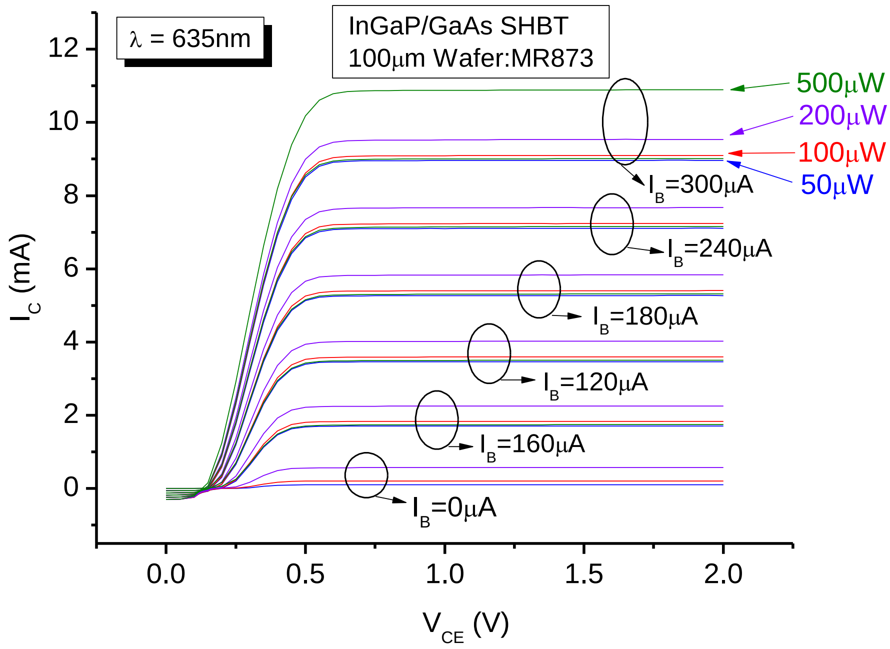

Figure 4.17: Measured 3-terminal photoresponse of the Npn $In_{0.49}Ga_{0.51}P/GaAs$ SHBT (wafer no. MR873, emitter contact diameter = 100μm) at 635nm with constant base current bias

$$\Delta I_C = [\beta_{(I_{ph}+I_{B,DC})} - \beta_{I_{B,DC}}] \times I_{B,DC} + \beta_{(I_{ph}+I_{B,DC})} \times I_{ph} + I_{ph} \qquad (4.3.5)$$

As the equation above shows, the induced collector current ΔI_C should provide additional fraction to the 2T-HPT photocurrent I_{ph}. This can be understood as the addition of the base bias current pushing the device operating point from $I_B = I_{ph}$ to $I_B = I_{ph} + I_{B,DC}$. And the latter higher level current, which is constituted by both photo-generated current and DC electrical current, makes the device work at a larger

DC current gain condition, according to figure 4.17. This is the reason for a 3T-HPT with base current bias to exhibit higher optical gain. Using equation (2.4.6), the optical gain of $In_{0.49}Ga_{0.51}P$/GaAs SHBT with base current bias is shown in figure 4.8

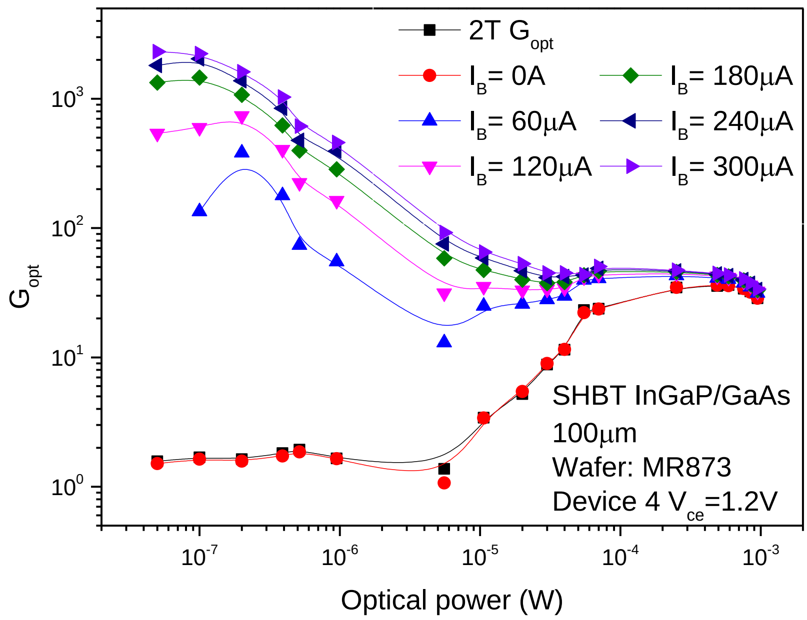

Figure 4.18: Measured 3T and 2T optical gain versus incident optical power for different DC base bias currents of the Npn $In_{0.49}Ga_{0.51}P$/GaAs SHBT (wafer no. MR873, emitter contact diameter = 100μm) at 635nm

Figure 4.1.18 shows 3T-HPT optical gain as a function of optical power for a series of different base current bias levels. At a low optical power level, the optical improvement is great. As the optical incident power increases, the optical absorption degrades the optical gain [26]. The optical gain thus reduces to a lower value. The same trend can be seen for every base bias level. On the one hand, this confirms that the base bias current can improve optical gain. On the other hand, it shows that a higher base bias current level can build up the induced base potential that biases the device into a forward active region faster. So base current biasing is especially significant for a low optical power application. Figure 4.19 shows the 3T-HPT optical gain as a function of base bias current for three optical incident power levels, 50μW, 100μW and 150μW respectively. The transistor action amplifies the photocurrent more effectively as the base current increase [11]. It again demonstrates the same base bias current, with the lower optical power level gaining a higher enhancement.

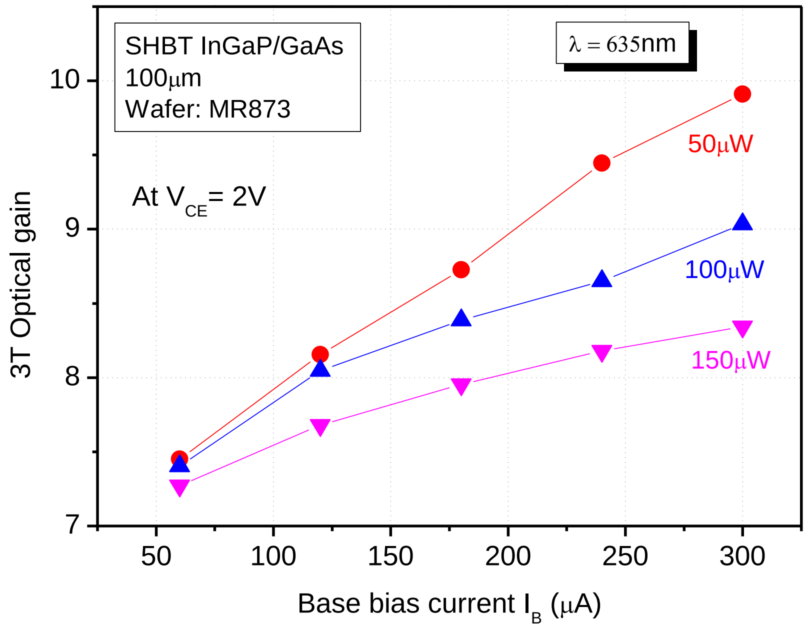

Figure 4.19: Measured 3-terminals optical gain versus DC base bias current for different incident optical power of the Npn $In_{0.49}Ga_{0.51}P$/GaAs SHBT (wafer no. MR873, emitter contact diameter = 100μm) at 635nm

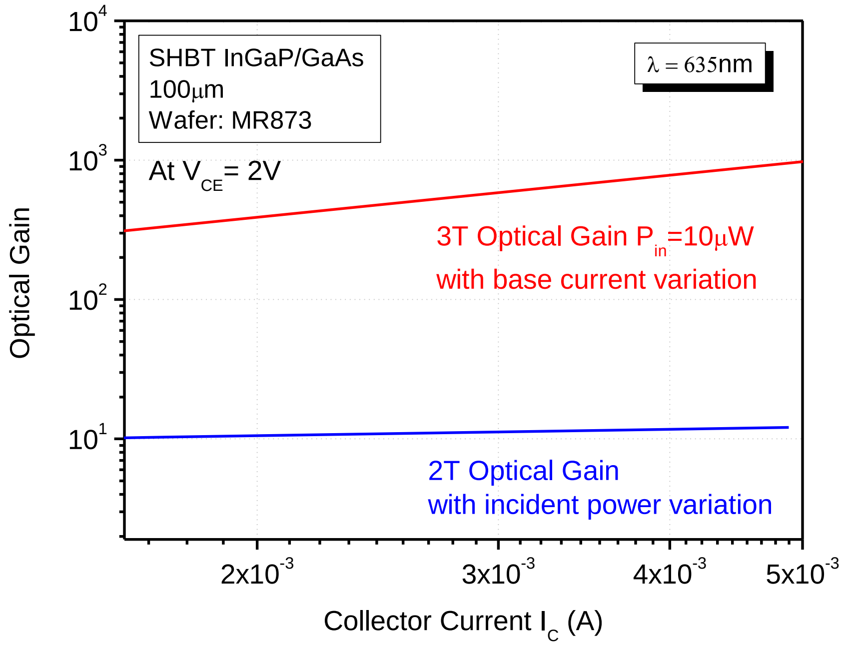

Figure 4.20: The dependence of the optical gain on the collector current for the 2T-HPT and 3T-HPT of the Npn $In_{0.49}Ga_{0.51}P$/GaAs SHBT (wafer no. MR873, emitter contact diameter = 100μm) at 635nm

There is another way to show the base current bias improvement in optical gain at the low input power level. In figure 4.20, optical gain is plotted as the function of the collector current. In the case of 2T-HPT, incident optical power was varied to achieve a range of different collector current values, while in the case of 3T-HPT, incident power was fixed at 10μW with the base current varied to get different collector currents. It is evident from the figure that the optical gain showed obvious improvement at the low optical power level (10μW). This is since, at the low incident optical level, the photo-generated current is small. The electrical base current plays a more important role in saturating the recombination centres in the depletion region. Therefore, more electrons from the emitter can inject and be transported through the space charge region, reaching the collector without recombination [11], and further improving the current gain of the device.

4.3.5 $In_{0.49}Ga_{0.51}P$ /GaAs SHBT 3-terminal optical characterisation with base voltage bias

Figure 4.21 shows the base and collector current as a function of B-E voltage under 100μW illumination at 635nm and 850nm.

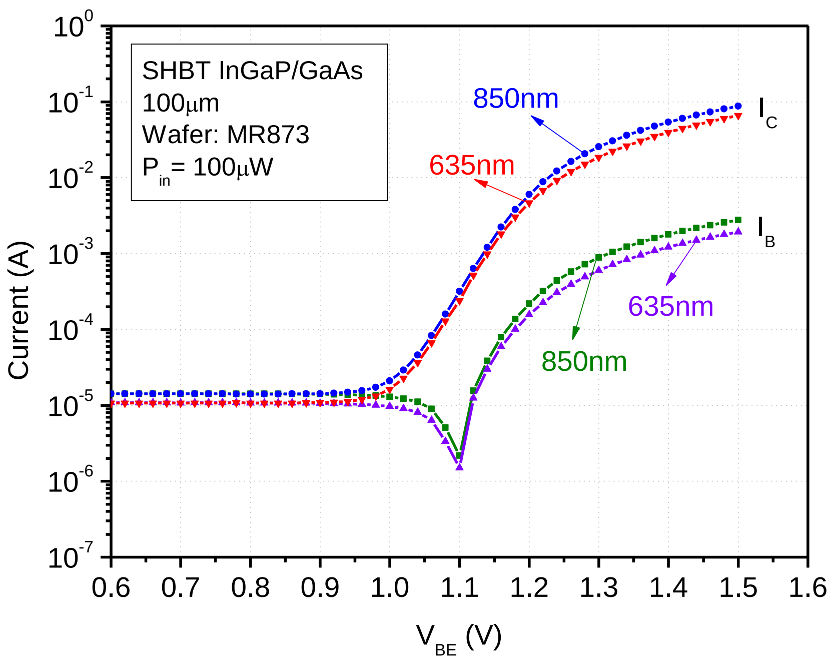

Figure 4.21: Comparison of measured base and collector current as a function of B-E bias with optical illumination at 50μW of the Npn $In_{0.49}Ga_{0.51}P$/GaAs SHBT (wafer no. MR873, emitter contact diameter = 100μm) at 635nm

At low bias, the collector current saturates at a very low value. It is produced from the quasi-neutral base, B-C depletion region and holes diffusion length photo-absorption. Likewise, base current saturates at the same current level as the collector current. The device operates as a p-i-n photodiode when the photo-absorption is at such a low voltage level. At high base bias, due to the current arising from the transistor's operation, the optical absorption effects become negligible. A notch in the base current, due to the reversal in the base current direction, is visible. This reversal in the base current comes from the fact that during absorption, photo-generated holes in the B-C depletion region are injected into the base, reducing the need for hole injections from the base electrical contact [26]. At low bias voltage, with high enough optical incident power, the number of photo-generated holes which inject into the base could exceed the requirement of recombination with emitter injected electrons. Also, due to the high valence band discontinuity of heterojuction, these holes are unable to travel into the emitter. So a flow of holes thus appears in the base contact. The attribution of these photo-generated holes is larger than the electrical current from the external circuit. Therefore, the direction of the net base current reversal turns. However, at high voltage bias, the hole injection arising from the photo-absorption becomes negligible compared to that from the base terminal connection.

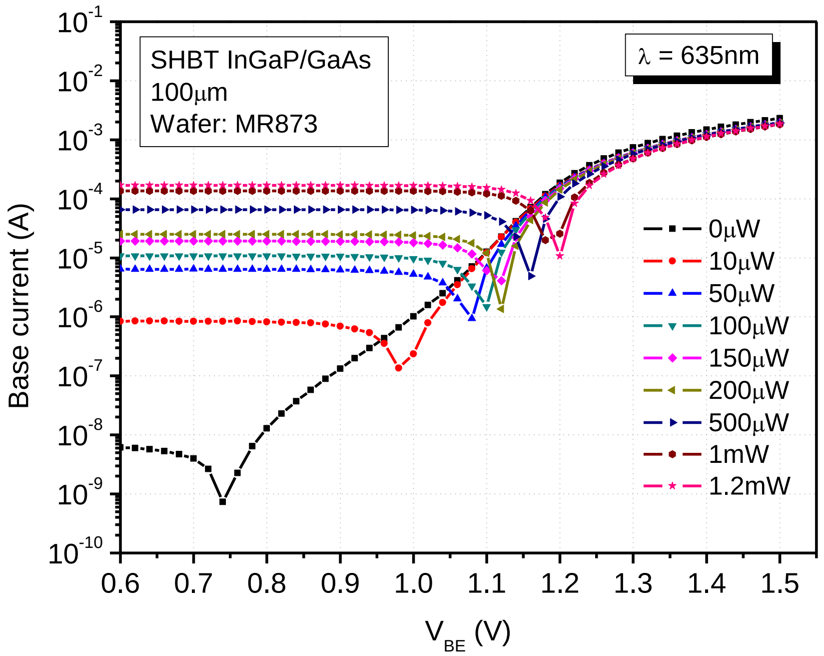

Figure 4.22: Measured base current as a function of B-E bias for various incident optical power of the Npn $In_{0.49}Ga_{0.51}P$/GaAs SHBT (wafer no. MR873, emitter contact diameter = 100μm) at 635nm

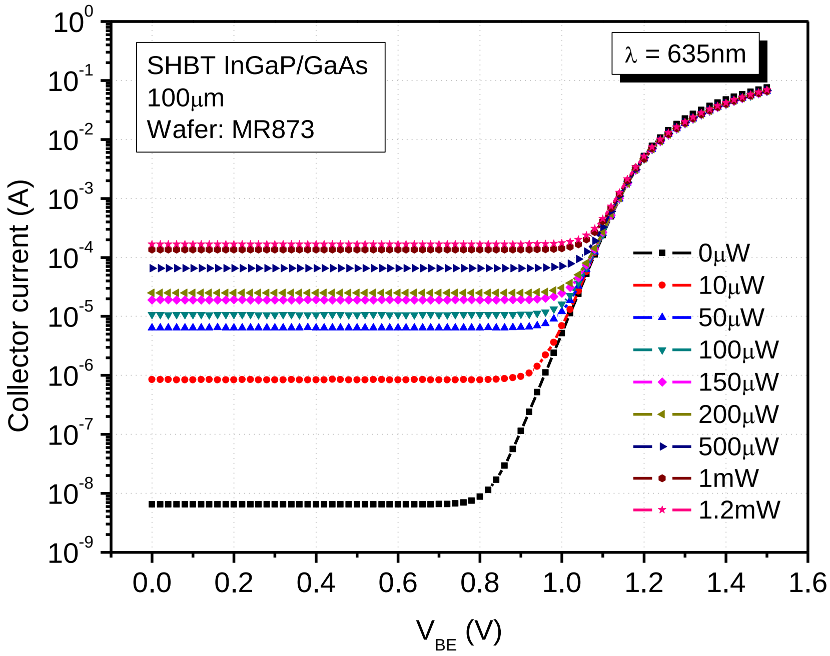

Figure 4.23: Measured collector current as a function of B-E bias for various incident optical power of the Npn $In_{0.49}Ga_{0.51}P/GaAs$ SHBT (wafer no. MR873, emitter contact diameter = 100μm) at 635nm

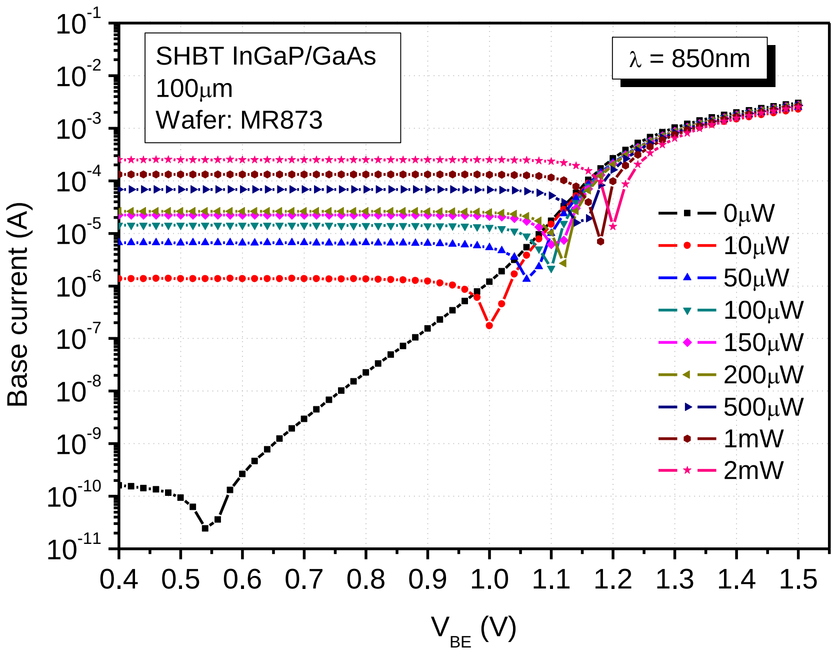

Figure 4.24: Measured base current as a function of B-E bias for various incident optical power of the Npn $In_{0.49}Ga_{0.51}P/GaAs$ SHBT (wafer no. MR873, emitter contact diameter = 100μm) at 850nm

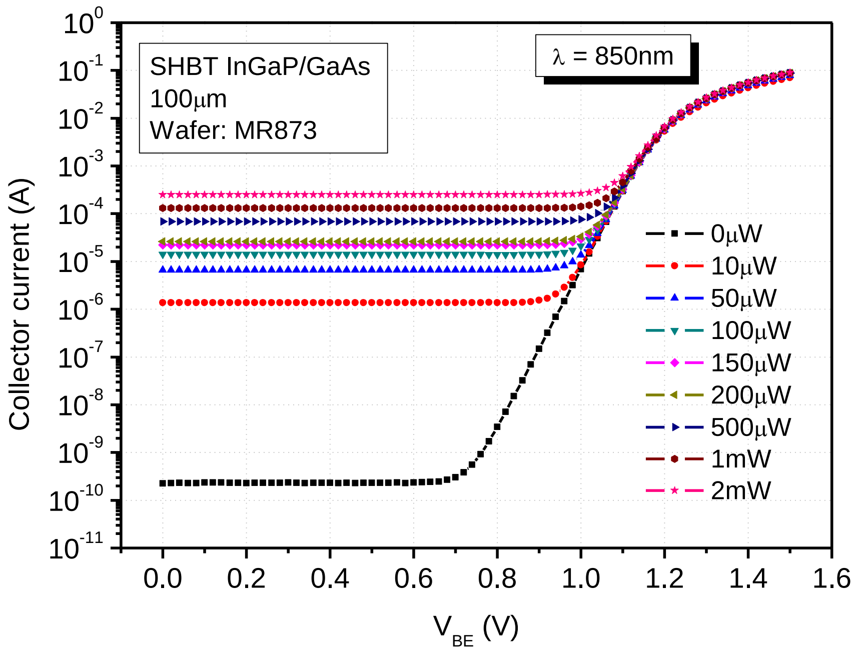

Figure 4.25: Measured collector current as a function of B-E bias for various incident optical power of the Npn $In_{0.49}Ga_{0.51}P/GaAs$ SHBT (wafer no. MR873, emitter contact diameter = 100μm) at 850nm

Figures 4.22 to 4.25 show base and collector current characteristics with different incident optical power levels at 635nm and 850nm respectively. Both incident wavelengths give similar results. First, for base current characteristics (figure 4.22 and 4.24) it is noticed that the notch corresponding to the reversal in the base current moves to a higher B-E bias voltage with the rise in optical power (figure 4.26), which is almost independent of wavelength.

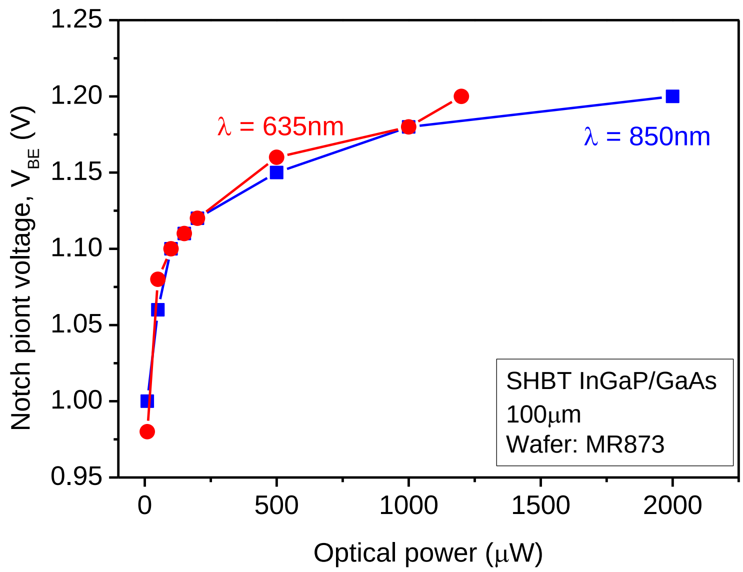

Figure 4.26: Measured base current notch point as a function of incident optical power of the Npn $In_{0.49}Ga_{0.51}P$/GaAs SHBT (wafer no. MR873, emitter contact diameter = 100µm) at 635nm and 850nm

The notch voltage variation is sensitive at a low optical input condition but almost saturated at a high optical input condition. Figures 4.22 and 4.24 also show that base current characteristics at high voltage are independent of incident optical power. The absorption of an incident optical signal only decides the base current level at low bias voltage.

At low bias, the collector current characteristics (figures 4.23 and 4.25) show that the collector current saturation values move gradually to higher levels with increasing optical power. The same as base current at high B-E bias, the collector characteristics at high voltage are unaffected. In summary, with low B-E bias voltage and high optical power, the device operates as a p-i-n photodiode whose photocurrent generation swamps the device's transistor action. The effects of an electron injection into the base from the emitter are negligible. By contrast, at high B-E bias voltage, the device transistor action is established and the photocurrent constitutes a small base current injected into the device, which is then amplified by the device's operation [26].

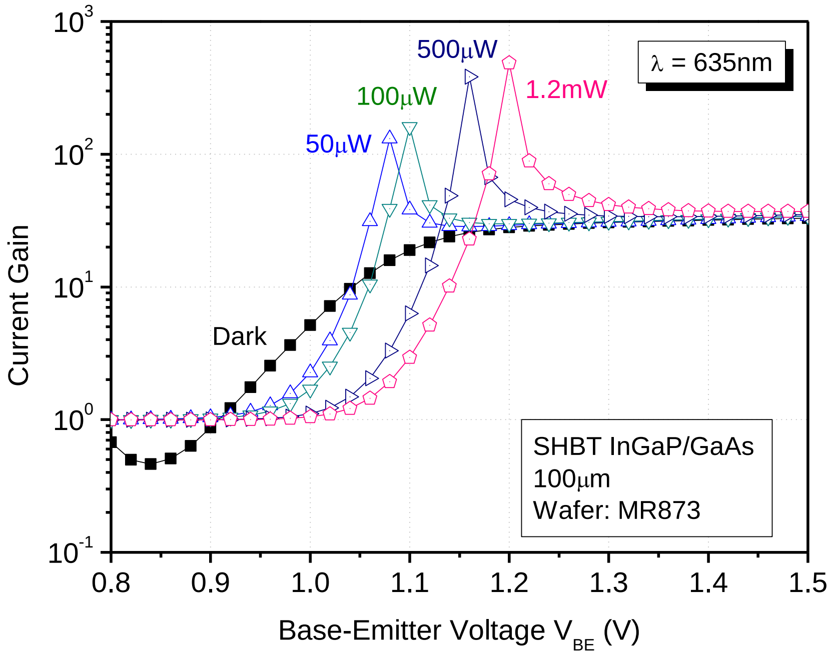

Figure 4.27: Measured DC current gain of the Npn $In_{0.49}Ga_{0.51}P/GaAs$ SHBT (wafer no. MR873, emitter contact diameter = 100µm) in dark and under optical illumination

Figure 4.27 shows a plot of the HPT DC current gain with and without various incident optical power illuminations as a function of B-E voltage. For the device in dark, it can be seen that the current gain at low B-E voltage is lower than unity. This is beneficial for the InGaP large valence band discontinuity, and results in a low leakage current. For device under illumination, the optical absorption interferes with the transistor operation as discussed above. The current gain keeps unity at low B-E voltage. With the bias voltage increasing, a peak appears on each curve and shifts to higher voltage as the optical power increases. Based on the discussion above, the peaks correspond to the reverse base current. As the voltage increases, the optical effects become negligible, and transistor action becomes dominant, so finally, current gain under illumination saturates at the same value as that in dark.

From the figure above, it appears that the 3T-HPT with base voltage bias cannot enhance the optical gain of the device. This can be explained using the following equation [27]:

$$\Delta I_C = [\beta_{(I_{ph1}+I_{B,DC})} - \beta_{I_{B,DC}}] \times I_{B,DC} + \beta_{(I_{ph1}+I_{B,DC})} \times I_{ph1} + I_{ph} \qquad (4.3.6)$$

As shown in figure 2.4.3 at low B-E voltage, the base bias current is very small, which produces large equivalent B-E junction resistance, with almost all of the photocurrent (I_{ph}) flowing as I_{ph2} to the voltage source. At high B-E voltage, although the B-E junction equivalent resistance begins to reduce, it is still very large compared to the smaller resistance from the voltage source. Still, a very small proportion of photocurrent (I_{ph1}) flows into the transistor to be amplified. According to the equation above, since I_{ph1} is very small, the value of the equation on the left hand side is approximately equal to I_{ph}. So no optical gain is produced.

This phenomenon can also be understood via the fixed voltage of the B-E junction bias. At low voltage bias, the emitter electron injection rate and the recombination rate in base are fixed. Additional holes produced by photo-absorption cannot attract more electrons from the emitter. At the same time, these holes cannot travel into the emitter due to the large valance band discontinuity in the B-E heterojunction. The transistor cannot be pushed to a higher operation point to achieve higher current gain. On the other hand, these photo-generated holes have to flow out from the base terminal contact, generating a reversal current. At high B-E voltage, the transistor operation is well established and dominant. The photo-absorption effect becomes negligible. During the whole process, no optical gain is produced.

4.4 $In_{0.49}Ga_{0.51}P/GaAs$ double heterojuction bipolar transistor

4.4.1 $In_{0.49}Ga_{0.51}P/GaAs$ DHBT DC characterisation

As in the SHBT measurements that first used the Giacoletto method, the $In_{0.49}Ga_{0.51}P/GaAs$ DHBT emitter resistance is measured as $R_{cc} = 6\ \Omega$ and $R_{ee} = 6.4\Omega$. The Gummel plot is shown in figure 4.28. The ideality factor for the collector current is $n_C = 1.02$, while for the base current it is $n_B = 1.06$, indicating that DHBT has a high quality E-B interface with low recombination. Two advantages of DHBTs, lower turn on voltage and low leakage current, can be observed.

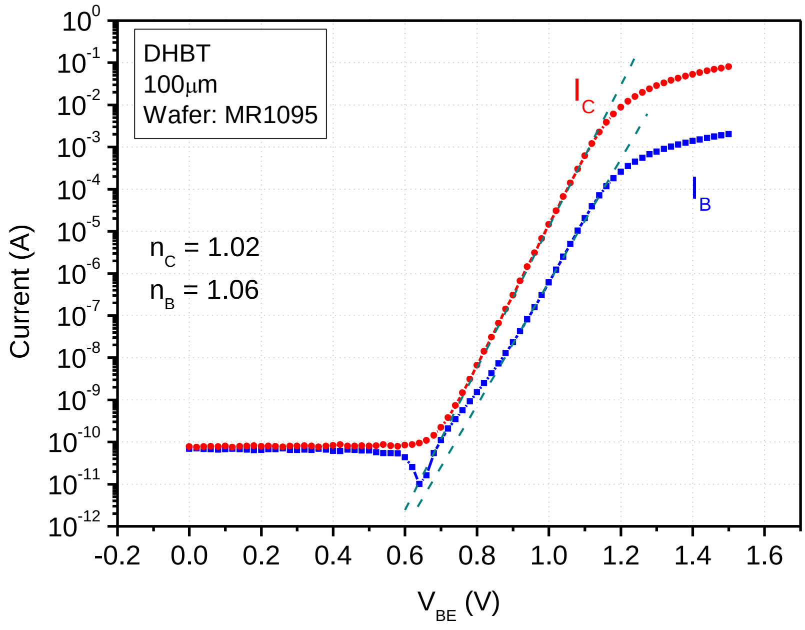

Figure 4.28: Measured Gummel plot of the Npn $In_{0.49}Ga_{0.51}P/GaAs$ DHBT (wafer no. MR1095, emitter contact diameter = 100µm)

Figures 4.29 and 4.30 compare Gummel plots by current densities between the 100µm $In_{0.49}Ga_{0.51}P/GaAs$ SHBT and DHBT as well as a 130µm SHBT.

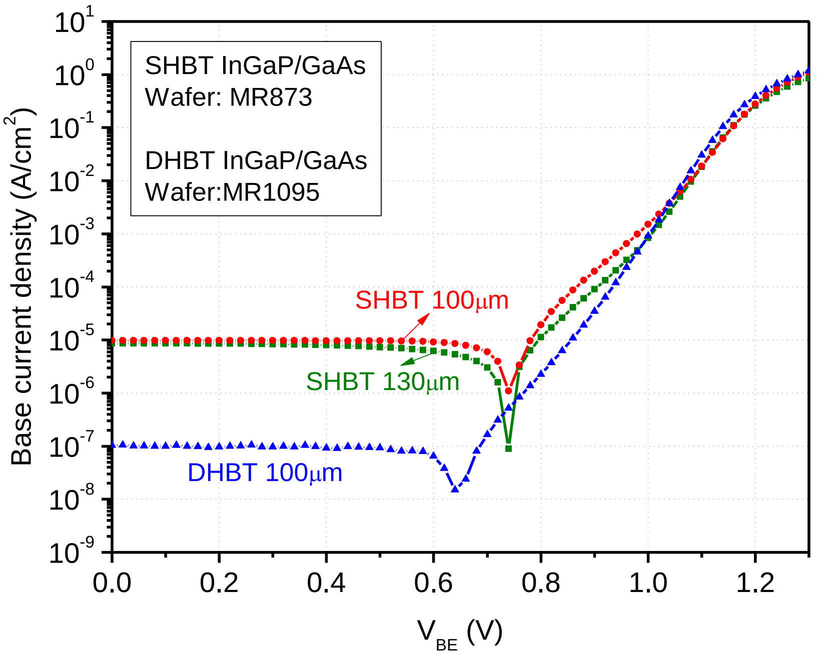

Figure 4.29: Measured Gummel plot I_B of the Npn $In_{0.49}Ga_{0.51}P/GaAs$ DHBT (wafer no. MR1095, emitter contact diameter = 100μm) comparing with 100μm and 130μm $In_{0.49}Ga_{0.51}P/GaAs$ SHBT

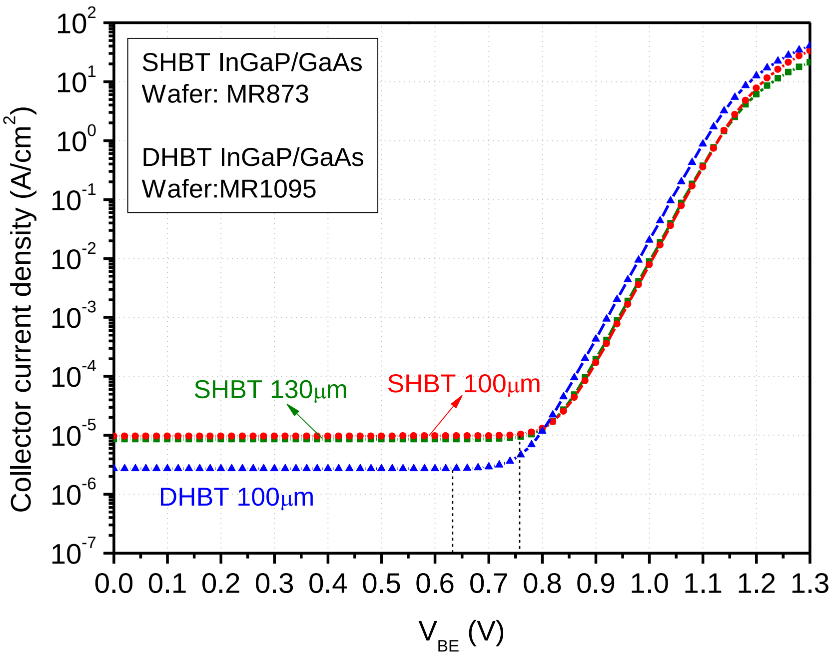

Figure 4.30: Measured Gummel plot I_C of the Npn $In_{0.49}Ga_{0.51}P/GaAs$ DHBT (wafer no. MR1095, emitter contact diameter = 100μm) comparing with 100μm and 130μm $In_{0.49}Ga_{0.51}P/GaAs$ SHBT

First, it is noticed that base and collector current density of two size SHBTs are almost the same, indicating geometry of the device, rather than the key parameter affecting DC performance of the device. Second, figure 4.30 shows that the DHBT base current in a low bias voltage region (lower than 0.7V) is much lower than in the SHBT which proves lower leakage is a current feature of DHBTs. It is noticed that in figure 4.30, the turn on voltage of the DHBT is around 0.63V, which is lower than the value of two SHBTs (0.75V). Also, both in the collector and the base current, the DHBT owns a wider linear region (one more decade) than SHBT, indicating a better performance in applications.

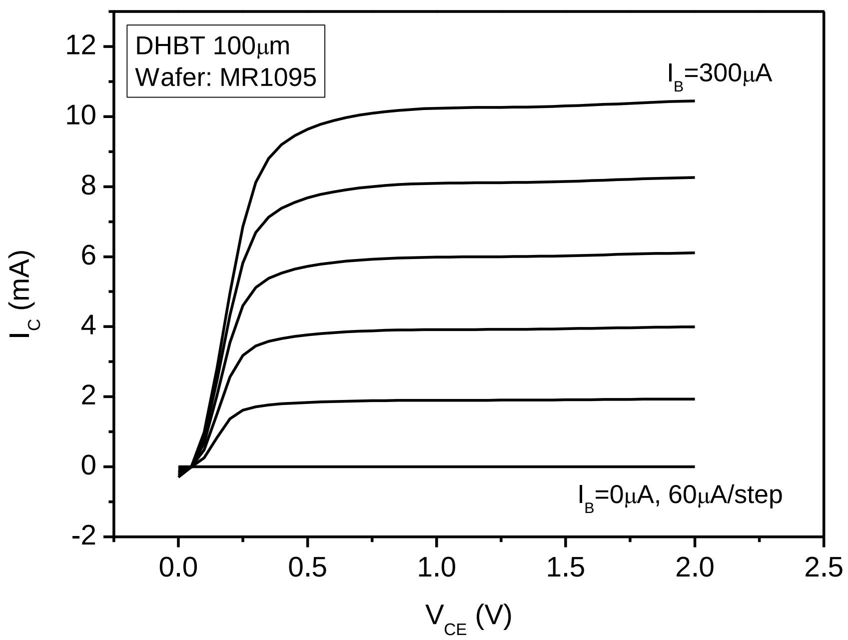

Figure 4.31: Measured IV characteristics of the Npn $In_{0.49}Ga_{0.51}P$/GaAs DHBT (wafer no. MR1095, emitter contact diameter = 100μm)

Figure 4.31 shows common emitter output characteristics of the DHBT device, where the output current (I_C) is measured as the C-E voltage, increasing with base current stepped in 60μA increments. Off-set voltage is given in figure 4.32, with the value as small as 0.04V, which is much lower than our SHBT (0.14).

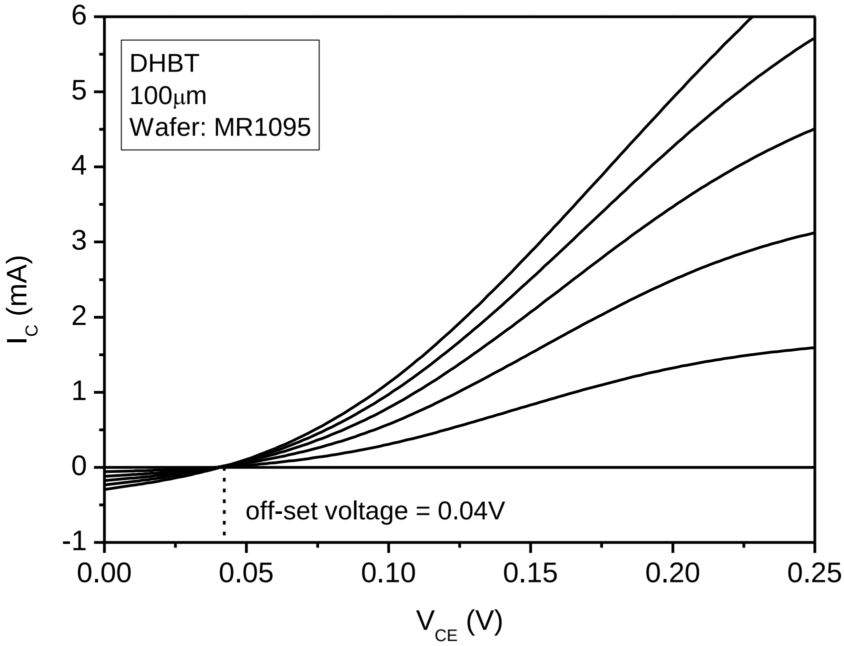

Figure 4.32: Measured off-set voltage of the Npn $In_{0.49}Ga_{0.51}P/GaAs$ DHBT (wafer no. MR1095, emitter contact diameter = 100μm)

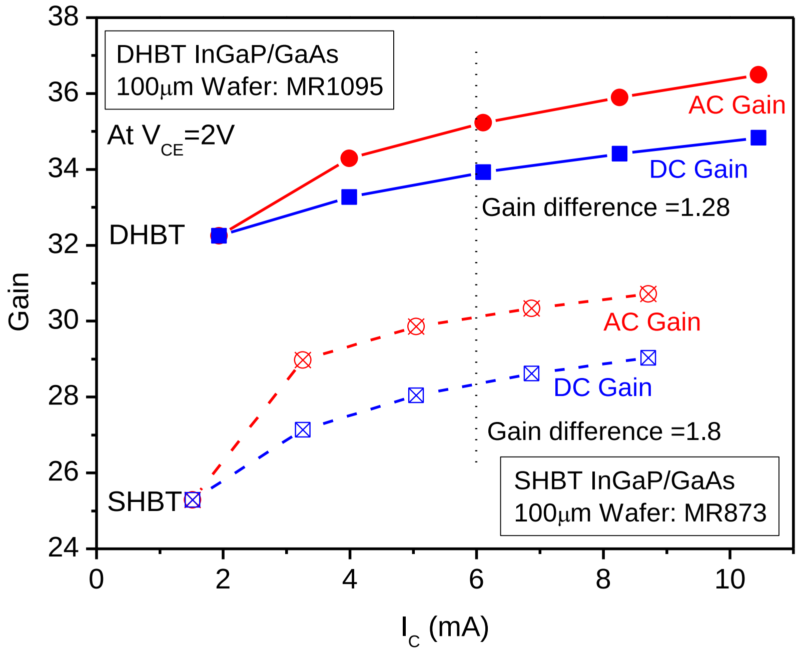

Figure 4.33: Measured DC and AC current gain of the Npn $In_{0.49}Ga_{0.51}P/GaAs$ DHBT (wafer no. MR1095, emitter contact diameter = 100μm)

DC and AC current gain as a function of base current is given in figure 4.33. Also, the SHBT gain in 4.6 is recalled and listed as a comparison. The DC current gain of a transistor is simply the collector current divided by the base current. The AC current gain calculation differs from the DC current gain calculation. The AC gain is calculated in terms of specific increments of base current. This technique gives a more accurate picture of how a transistor reacts to AC signals. First, it is noted that both AC and DC gain of the DHBT is higher than that of the SHBT. For our measurements, the maximum DC gain of the DHBT can achieve 35.5. Second, as we know, the difference between AC gain and DC gain is mainly due to leakage of the current. In the figure above, at the chosen collector current level (6mA), the gain difference of DHBT and SHBT is 1.28 and 1.8, respectively, which again confirms the lower leakage current capability feature of the DHBT. The benefit of this will be clearly shown in our next chapter, looking at the eye diagram simulation results.

Table 4.3: DC measured characteristics of the Npn $In_{0.49}Ga_{0.51}P/GaAs$ DHBT (wafer no. MR1095, emitter contact diameter = 100µm)

Parameters	Values
$(N_D)_b$	2×10^{19} cm^{-3}
$(N_D)_c$	$5\text{-}7\times10^{16}$ cm^{-3}
R_{ee}	6 Ω
R_{cc}	6.4 Ω
Off-set voltage	0.05 V
DC gain at V_{ce}=2V, I_b=120µA	33
AC gain at V_{ce}=2V, I_b=120µA	34
Gain from Gummel plot at I_c=10µA	22
Collector ideality factor (n_c)	1.02
Base ideality factor (n_b)	1.06
Collector saturation current (I_{co})	6.5×10^{-22}A
Dark current at V_{ce}=2V	2×10^{-9}A
Turn on voltage	0.62 V

4.4.2 $In_{0.49}Ga_{0.51}P/GaAs$ DHBT 2-terminal optical characterisation

Figures 4.34 and 4.35 show measured B-C junction responsivity of 100µm InGaP/GaAs DHBT on MR1095 at 635nm and 850nm. A bias voltage is applied between base and collector. The B-C junction is reverse biased and the emitter is floating. The HPT is functioned as a p-i-n photodiode which is formed by base, collector and sub-collector. Various optical powers at wavelength are illuminated on the base absorption window. p-i-n photocurrents are generated within the B-C junction as shown. As in the SHBT, photo-generated currents are independent with reverse B-C bias voltage value.

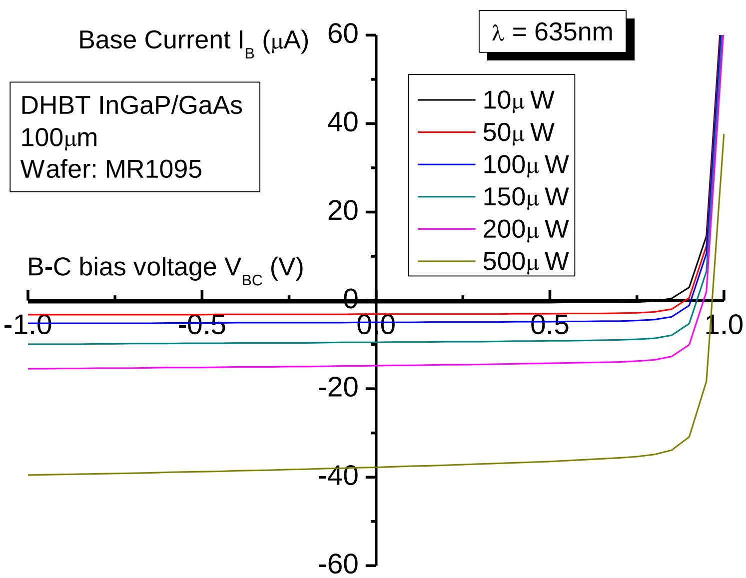

Figure 4.34: Measured B-C junction responsivity of the Npn $In_{0.49}Ga_{0.51}P/GaAs$ DHBT (wafer no. MR1095, emitter contact diameter = 100µm) at 635nm

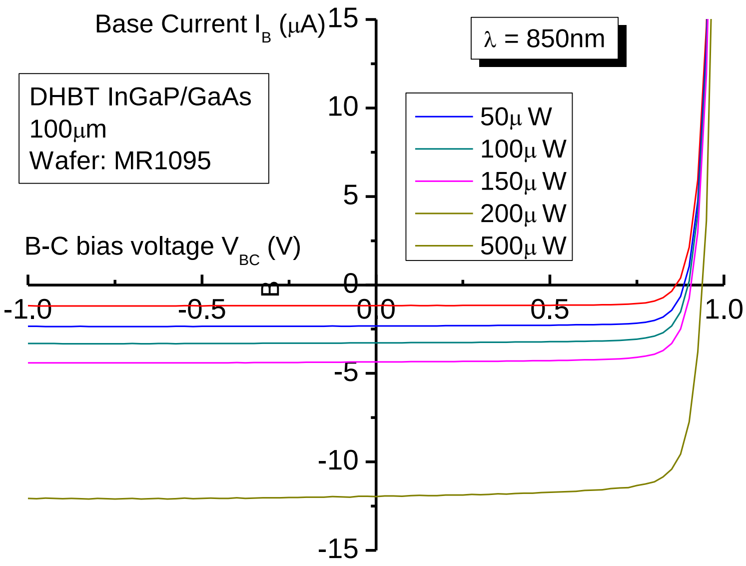

Figure 4.35: Measured B-C junction responsivity of the Npn $In_{0.49}Ga_{0.51}P/GaAs$ DHBT (wafer no. MR1095, emitter contact diameter = 100μm) at 850nm

Figures 4.36 to 4.38 show the DHBT 2-terminal measurements with a floating base at 635nm and 850nm wavelengths incident light. The measured collector current versus incident optical power is shown in figure 4.39. It is noticeable that the DHBT photoresponse of 635nm is much higher than 850nm. This is due to the DHBT collector being made from wide band gap $In_{0.49}Ga_{0.51}P$ (1.9eV). The 850nm incident optical signal (1.46eV) cannot excite e-h pairs, so the collector is “transparent” to this incident signal.

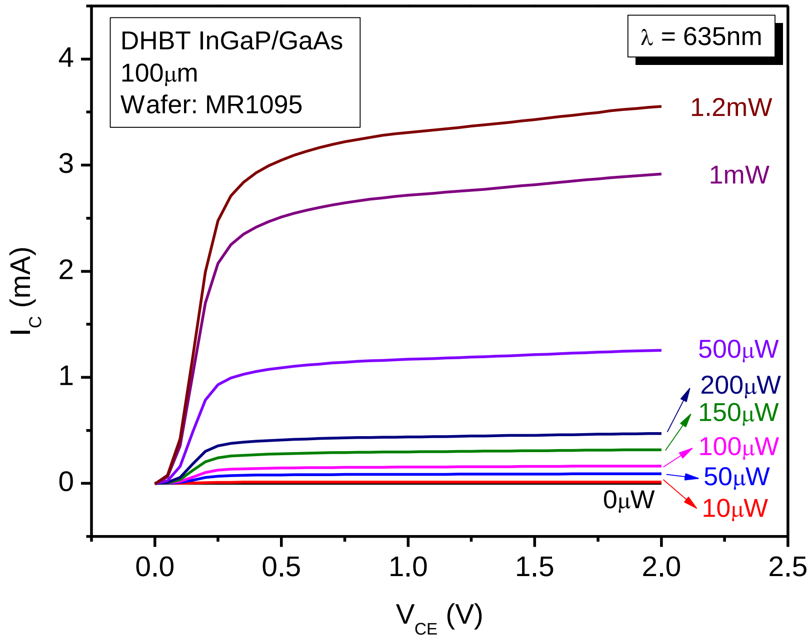

Figure 4.36: Measured 2-terminal photoresponse of the Npn $In_{0.49}Ga_{0.51}P/GaAs$ DHBT (wafer no. MR1095, emitter contact diameter = 100µm) at 635nm

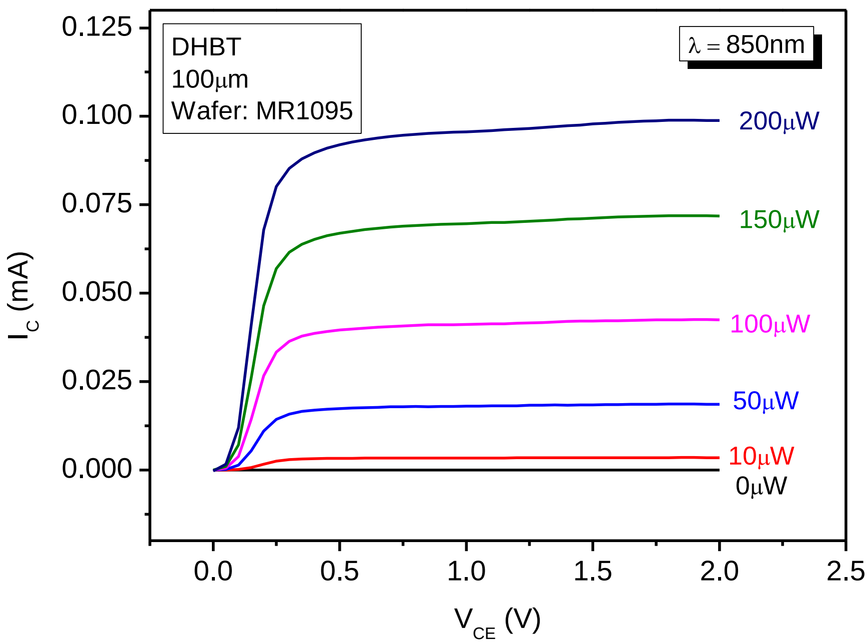

Figure 4.37: Measured 2-terminal photoresponse of the Npn $In_{0.49}Ga_{0.51}P/GaAs$ DHBT (wafer no. MR1095, emitter contact diameter = 100µm) at 850nm with optical power up to 200µW

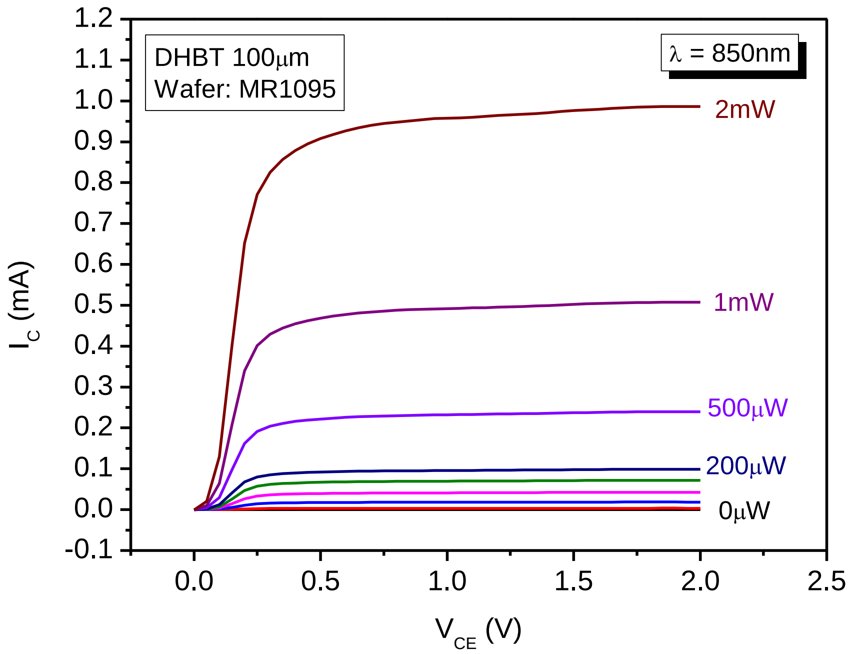

Figure 4.38: Measured 2-terminal photoresponse of the Npn $In_{0.49}Ga_{0.51}P/GaAs$ DHBT (wafer no. MR1095, emitter contact diameter = 100µm) at 850nm with optical power up to 2mW

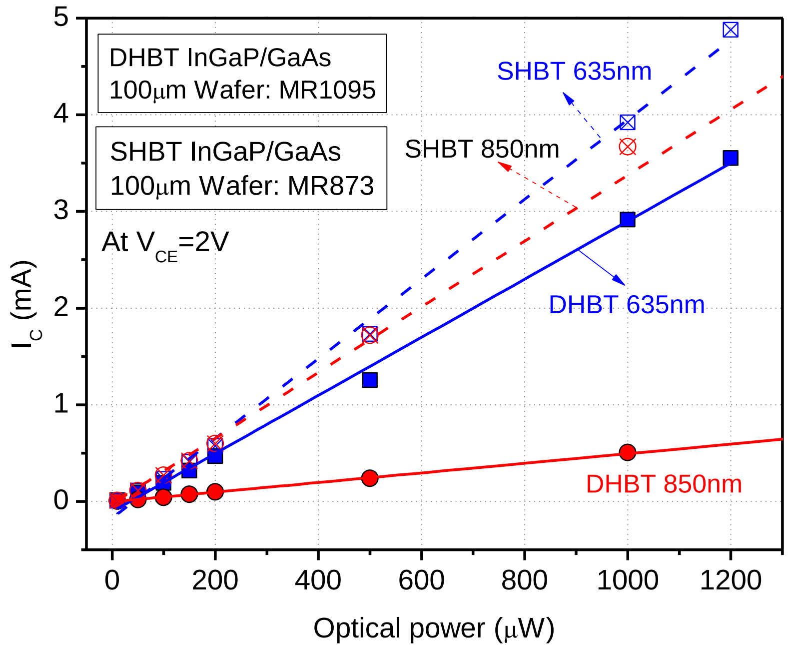

Figure 4.39: Comparison of measured 2-terminal collector current of the Npn $In_{0.49}Ga_{0.51}P/GaAs$ DHBT (wafer no. MR1095) and the Npn $In_{0.49}Ga_{0.51}P/GaAs$ SHBT (wafer no. MR873, emitter contact diameter = 100µm) at 635nm and 850nm

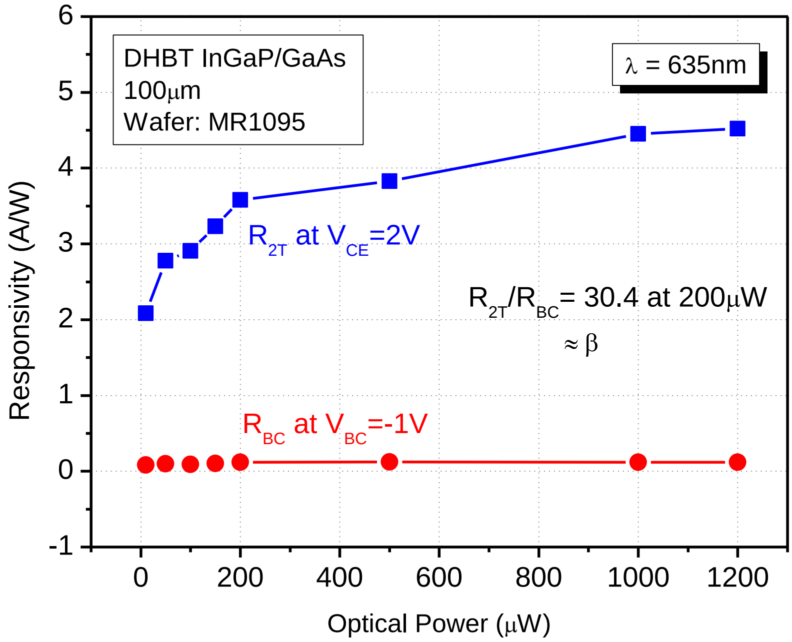

Figure 4.40: Measured 2-terminal and B-C junction optical responsivity of the Npn $In_{0.49}Ga_{0.51}P$/GaAs DHBT (wafer no. MR1095, emitter contact diameter = 100μm) at 635nm

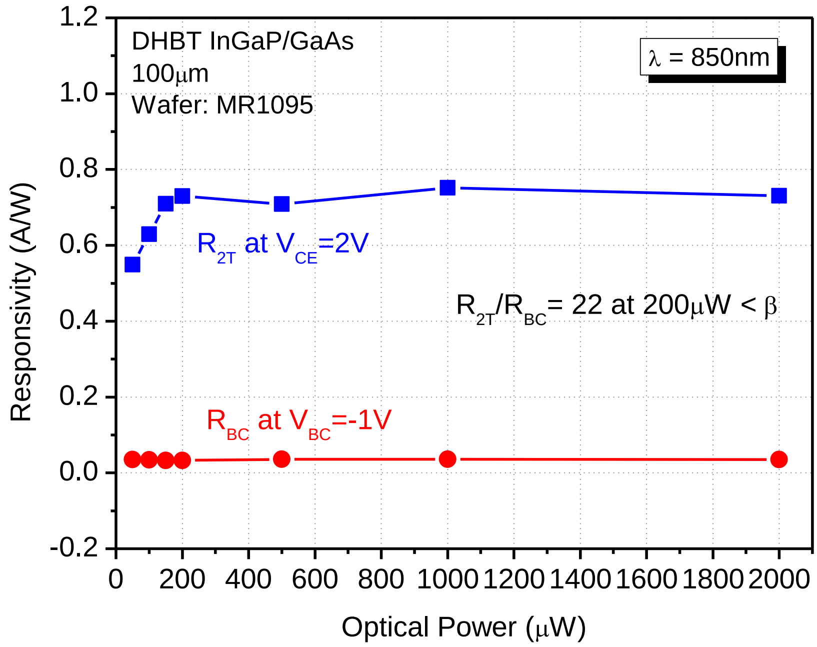

Figure 4.41: Measured 2-terminal and B-C junction optical responsivity of the Npn $In_{0.49}Ga_{0.51}P$/GaAs DHBT (wafer no. MR1095, emitter contact diameter = 100μm) at 850nm

Figures 4.40 and 4.41 show the optical responsivity of the 2T-HPT at 635nm and 850nm, which are calculated from figures 4.36 and 4.38, respectively. Both results show responsivity increasing rapidly at the low optical power region. This can be attributed to the increment of current gain with the increment of quiescent bias current level (figure 4.33). In the high optical region, the responsivity saturated at certain values. This can be explained as the absorption limitation of the device. After a certain value of optical power, too many photons incident into the device; the collection efficiency of the device then begins to reduce, which can further reduce responsivity. The reason why 850nm begins to show saturation at a lower optical power than 635nm is because at a certain incident optical power level, the longer wavelength means more incident photons. Therefore, the device is able to reach the limitation earlier.

The DUT B-C junction optical responsivity R_{BC} 635nm and 850nm are also shown in figures 4.40 and 4.41. The calculation of R_{2T}/R_{BC} at 635nm, for example at 200μW, is 30.4, which is comparable to the value of current gain in figure 4.33. But for 850nm, the value is only 22 which is much smaller than the current gain of the device, due to the transparence of collector to incident signal.

4.4.3 $In_{0.49}Ga_{0.51}P$/GaAs DHPT 3-terminal optical characterisation with base current bias

Figure 4.42 shows the measured common emitter output characteristics of the DHPT for a 3-terminal configuration operated in the dark and under various optical illuminations. As discussed for the SHPT, the optical gain under such a configuration is expected to be improved by application of base current bias.

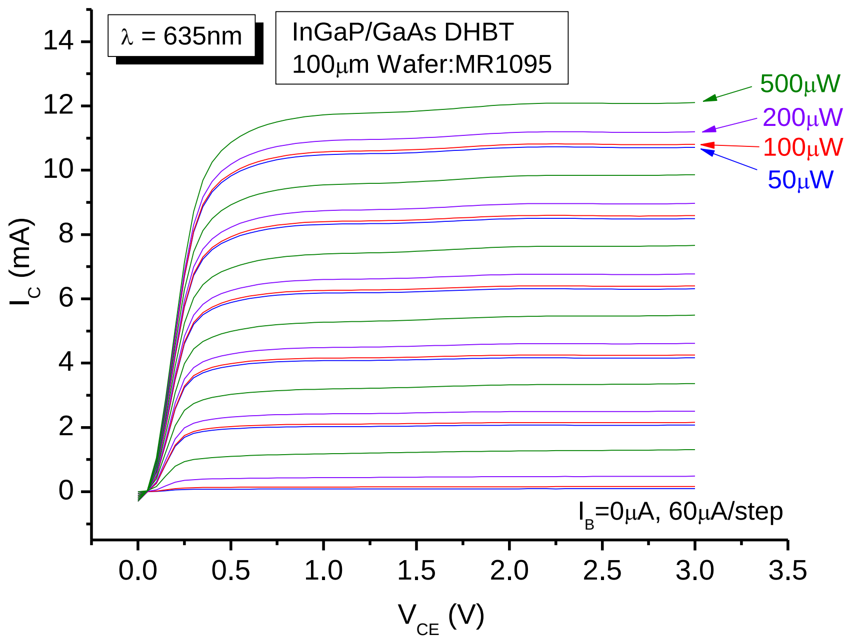

Figure 4.42: Measured 3-terminal photoresponse of the Npn $In_{0.49}Ga_{0.51}P/GaAs$ DHBT (wafer no. MR1095, emitter contact diameter = 100μm) at 635nm with constant base current bias

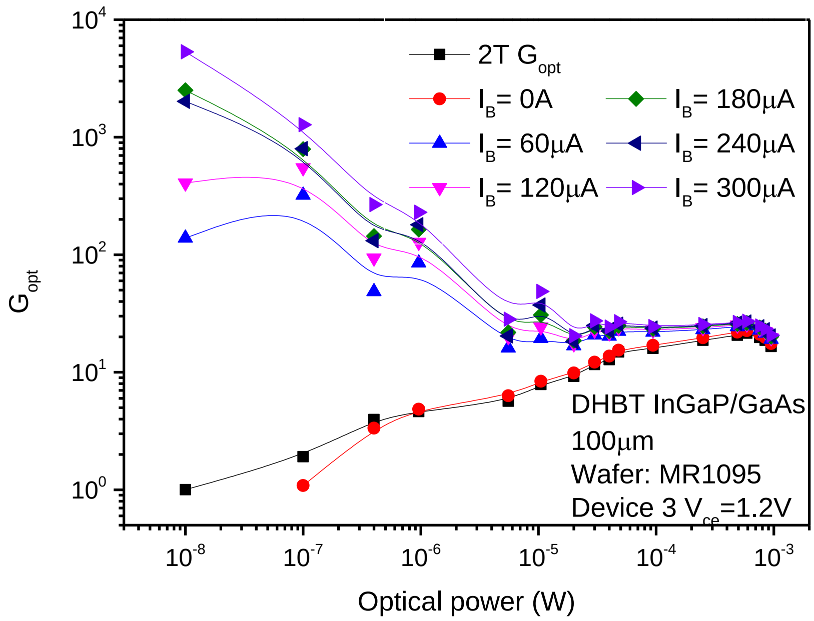

Figure 4.43: Measured 3T and 2T optical gain versus incident optical power for different DC base bias currents of the Npn $In_{0.49}Ga_{0.51}P/GaAs$ DHBT (wafer no. MR1095, emitter contact diameter = 100μm) at 635nm

But the results for the DHPT (figure 4.43) show that 2T responsivity is always higher than 3T responsivity. This is very different to the data for the SHPT (see figure 4.18). To explain this effect, one can consider the effect of base current on the energy band diagram of DHBTs. The I_B will diminish the induced base electric field. Higher I_B can 'flatten' the base band from bending easier and earlier. This can reduce the device's performance under illumination, which will be discussed in a later section.

4.4.4 $In_{0.49}Ga_{0.51}P$/GaAs DHPT 3-terminal optical characterisation with base voltage bias

The characteristics of the SHBT under optical illumination with voltage base bias are discussed in section 4.3.5. It is also important to investigate the effect of base voltage bias on the characteristics of the DHPT.

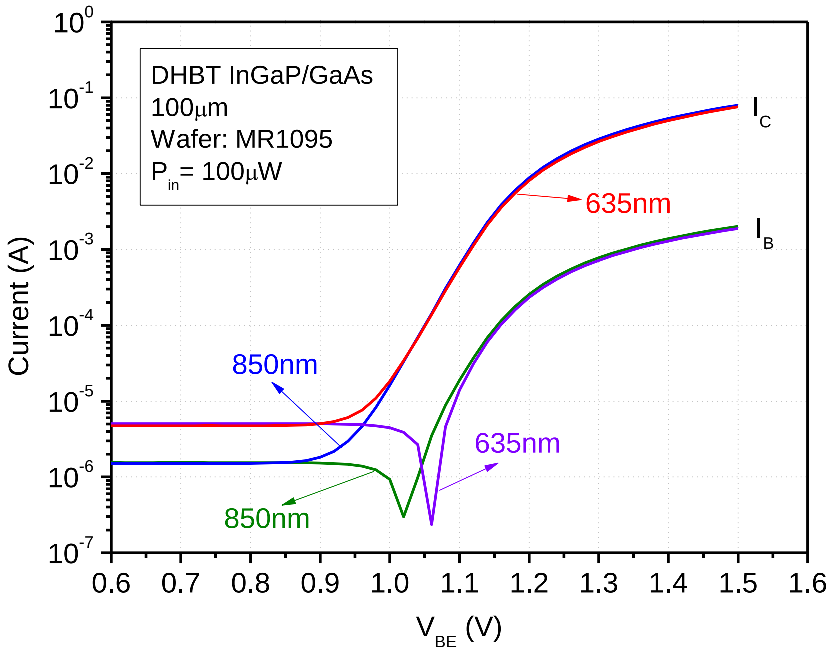

Figure 4.44: Measured base and collector current as a function of B-E bias with optical illumination at 100μW of the Npn $In_{0.49}Ga_{0.51}P$/GaAs DHBT (wafer no. MR1095, emitter contact diameter = 100μm) at 635nm and 850nm

Figure 4.44 gives the base and collector current as a function of B-E voltage under a 100µW optical power illumination at both 635nm and 850nm radiations. It is seen that below V_{BE} = 0.8V, at both 850 and 635nm, the I_B and I_C have similar magnitudes, since the device at this lower V_{BE} acts as a p-i-n diode. When V_{BE} is higher than that value, the HPT starts to operate as a transistor.

For 635nm, the DHPT behaves similarly to the SHPT. However, it is seen that DHPTs shows much lower leakage current and a lower turn on voltage. For 635nm at V_{BE} = 0.7V the leakage currents in DHPTs are: $I_C = 5\times10^{-6}$A. This is much lower than for the SHPT ($I_C = 1.1\times10^{-5}$A). This shows the advantages of DHPTs for optical detection, for example, they are more sensitive to small signals. At 635nm radiation, both I_B and I_C have a higher magnitude in the case of low V_{BE}.

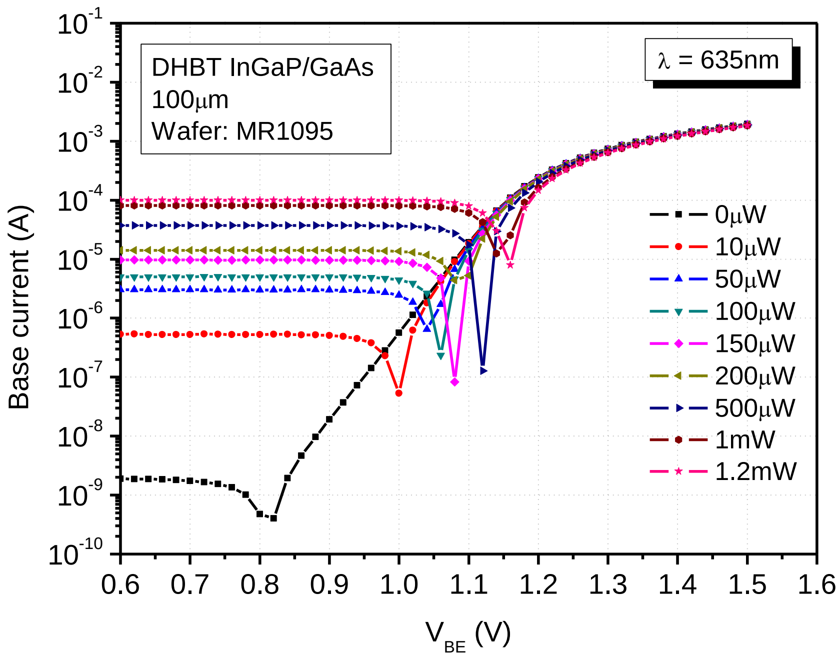

Figure 4.45: Measured base current as a function of B-E bias for various incident optical power of the Npn $In_{0.49}Ga_{0.51}P$/GaAs DHBT (wafer no. MR1095, emitter contact diameter = 100µm) at 635nm

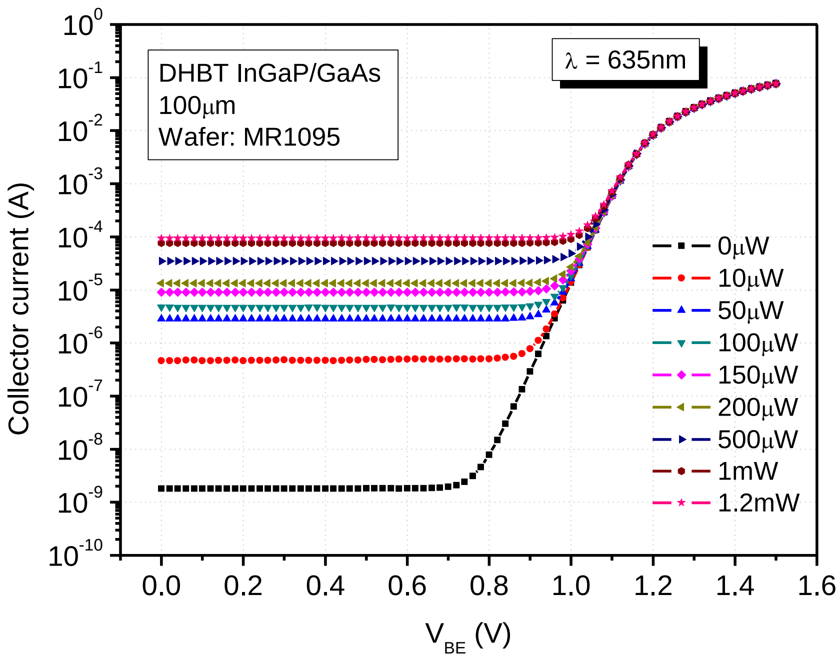

Figure 4.46: Measured collector current as a function of B-E bias for various incident optical power of the Npn $In_{0.49}Ga_{0.51}P$/GaAs DHBT (wafer no. MR1095, emitter contact diameter = 100µm) at 635nm

Figures 4.45 and 4.46 show base and collector current characteristics with different incident optical power level at 635nm. Similar device behaviour is observed as in the SHPT. First, for base current characteristics (figure 4.45) it is noticed that the notch corresponding to the reversal in the base current moves to a higher B-E bias voltage, with a rise in optical power. But the characteristics at high voltage are independent of incident optical power. Secondly, at low V_{BE}, the collector current (figure 4.46) responds to optical power i.e. it increases with optical radiation. A similar case is also observed in terms of the base current, and at higher V_{BE}, the I_B is unaffected. At low V_{BE}, and high enough optical power, the base, collector and sub-collector operate together as a p-i-n photodiode, and with high base-emitter bias, the transistor action is well established.

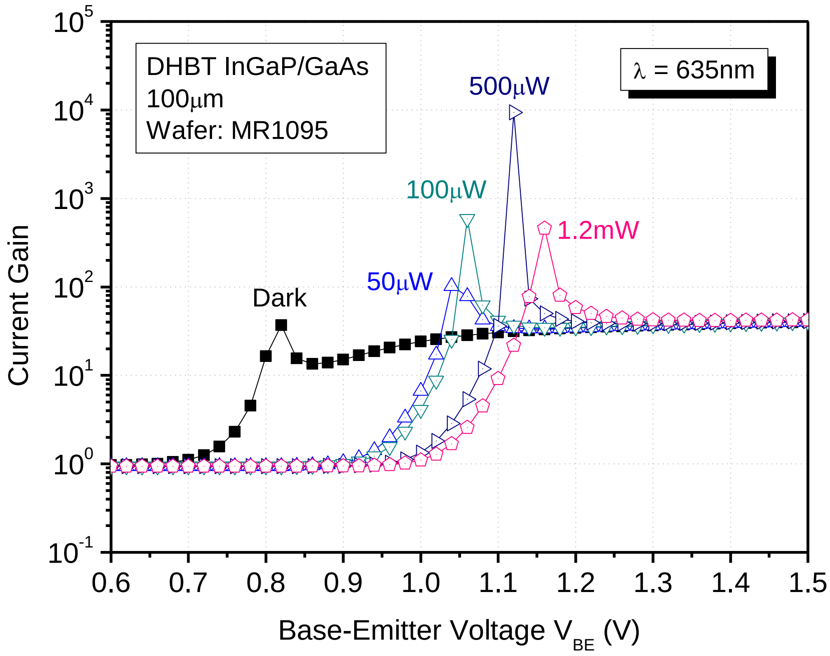

Figure 4.47: Measured DC current gain (from Gummel plot) of the Npn $In_{0.49}Ga_{0.51}P$/GaAs DHBT (wafer no. MR1095, emitter contact diameter = 100μm) in dark and under optical illumination

Figure 4.47 shows a plot of the HPT DC current gains (from Gummel plot) at dark and under optical powers. The current gain remains constant at unity with a low V_{BE}. However, with the increase in the V_{BE} a peak appears on each curve and shifts to higher voltage as the optical power increases. Similar to the discussions on the SHPT, the peaks correspond to the reverse base current. As the V_{BE} increases, the optical effects become negligible and the transistor action becomes dominant, so finally current gain under illumination saturates at the same value as that produced in the dark. It is seen that 3T-HPT with base voltage bias cannot enhance the optical gain of the device, which is the same as the SHPT.

4.5 $In_{0.49}Ga_{0.51}P$ /GaAs DHPT base band bending

4.5.1 Band diagram of InGaP/GaAs DHBTs

Figure 4.48 shows the band diagram of InGaP/GaAs/InGaP DHBTs, while the InGaP/GaAs for SHBTs is indicated in figure 4.49. The valence band discontinuity at the interface between the InGaP collector layer and the GaAs sub-collector layer of the DHBT, acts as a potential barrier for the photo-generated low-speed holes in the sub-collector [28]. This extra barrier will confine the photo-generated holes and stop them flowing towards the base region, unlike in the SHBT. Preventing the flow of slow holes would improve the performance of detectors for high-speed photo-response. It has been reported [29] that a large partition of energy gap discontinuity to the valence band in the B-C heterojunction within DHBTs would be highly desirable.

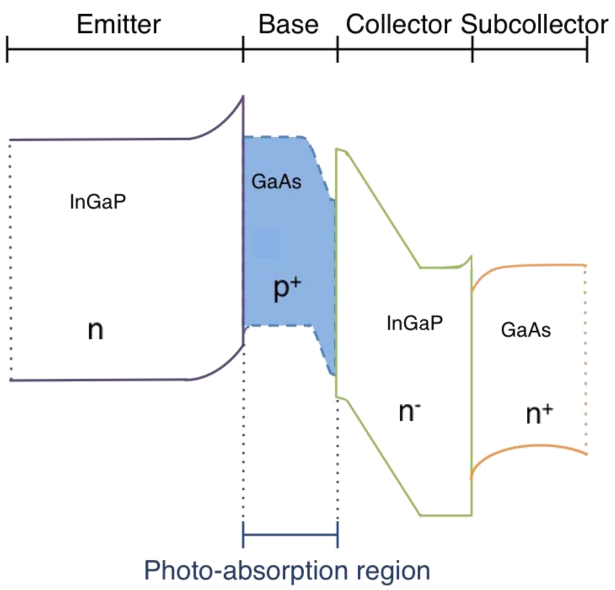

Figure 4.48: Band diagram of InGaP/GaAs/InGaP DHBTs under zero bias condition

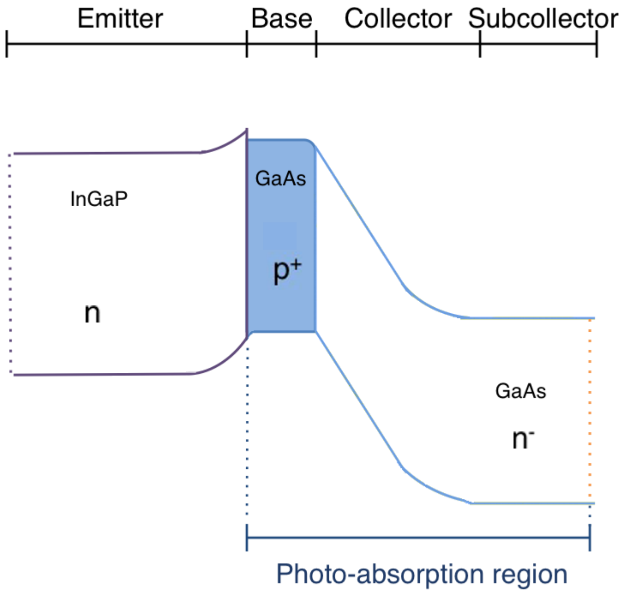

Figure 4.49: Band diagram of InGaP/GaAs SHBTs under zero bias condition

As can be seen in figure 4.49 in SHBTs photo-generated holes in the subcollector will still drift through the collector layer and finally reach the base region; so the photo-absorption region consist of collector and sub-collector plus the base. For the InGaP/GaAs DHBTs, if the device is used at a certain wavelength input signal, for example at 850nm (1.46 eV), where the photo energy is larger than the band energy of GaAs base (E_g = 1.43eV) and smaller than the InGaP (E_g = 1.9eV). The photo-absorption takes place only within the base layer and the sub-collector layer. Both the wide band gap InGaP emitter and the collector layers are 'transparent' to the optical signal of 850nm. The optical signal can only be absorbed by the GaAs material. During the design of the InGaP/GaAs DHPT detector, if only the highly p-doped base is used as an absorption layer, the photo-generated holes will vanish within the dielectric relaxation time since the holes are the majority carriers in the base [30]. At the same time, sub-collector photo-generated holes are blocked by the B-C valence band discontinuity. So only electrons in the DHPT are active carriers, and therefore their transport will determine the device speed. This resembles the carrier transport in a uni-travelling-carrier photodiode (UTC-PD) [1].

4.5.2 Uni-travelling-carrier photodiode

Uni-travelling-carrier photodiodes (UTC-PDs) architecture is an interesting area for the development of high performance photodetectors. In a conventional B-C junction, both electrons and holes in the depleted absorption layer (collector layer) contribute to the photoresponse. The output response is the sum of electron and hole current components. Due to much lower drift velocity of holes (400 cm^2/Vs) when compared to electrons (8500 cm^2/Vs), hole transport dominates the space charge effect and saturation behaviour [31]. In this work, the B-C junction formed a UTC-PD structure in our DHBT device, in contrast to the conventional B-C junction formed p-i-n photodiode structure. The photo-generated holes in the sub-collector are blocked by the potential barrier of the valence (figure 4.48) in the collector-sub-collector layer interface. Only high-speed electrons are allowed to be injected in the wide band gap collector layer [32], therefore, their transport determines the device's operation speed. The transport of holes will not directly affect the device response and output saturation current [31]. The electron velocity at overshoot is about one order of magnitude larger than the hole saturation velocity, so the carrier transit time in the depleted collector layer can be much shorter, and the space charge effect much smaller, than a conventional B-C junction [33]. Under such a mechanism, the device is expected to provide a higher saturation output current, whilst maintaining a faster response. Therefore, at a given optical input, both a higher 3dB bandwidth and higher output saturation current can be achieved.

4.5.3 Base self-induced field (band bending)

Photo-generated holes contribute a delay to the order of dielectric relaxation time in the absorbing base layer. So electron diffusion through the narrow-gap optical absorbing base layer of the device becomes the determinant factor for bandwidth in a

UTC-PD [34-35]. The experimental result shows that electron transport in the p-type photo-absorption layer is of prime importance in maximising the operation speed [36].

It is well known that the high electron velocity that appears in unsteady conditions is usually called velocity overshoot or ballistic transport, and should permit improvement in the high-speed performance of electron devices fabricated with GaAs or other high-mobility III-V materials [34-35]. A recent study on AlGaAs/GaAs HPTs with a conventional collector revealed that the overshoot phenomenon exists in the collector depletion layer on the base side, which can reduce collector transit time [37].

The DHPT under our investigation is working under high optical inputs (large signal outputs). One would expect a self-induced electric field (E_{ind}) in the base absorption layer to produce a potential gradient band bending effect ($\Delta\phi_{eff}$) as shown in figure 4.50. This band bending could further enhance the saturation output current and high-speed performance.

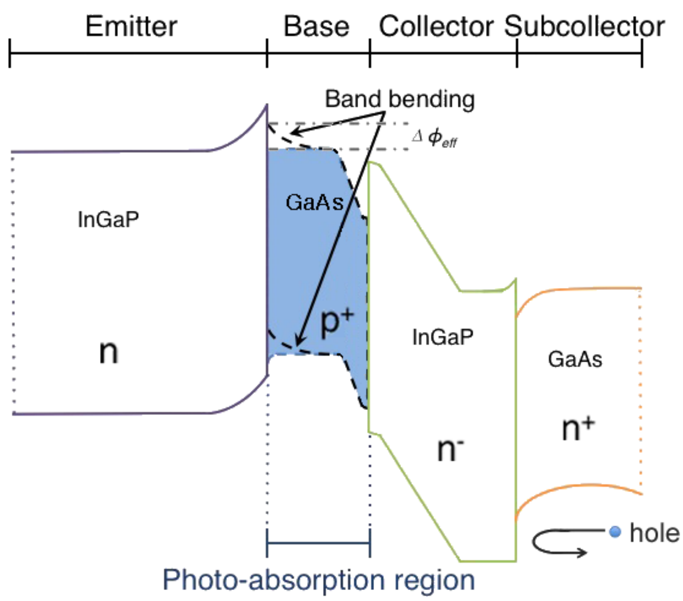

Figure 4.50: Band bending in the base region of the InGaP/GaAs DHPT

The origin of the self-induced electric field, E_{ind}, is the drift current of the majority of holes in the base layer that must flow to maintain the current continuity [31]. As the photo-excited electrons flow toward the collector due to the reverse biased B-C junction, a compensatory hole current is induced in the photo-absorption base layer. In the low output region, the photo-excited hole distribution is close to the electron distribution under the quasi-neutral condition. This situation and the small hole diffusion coefficient ($10cm^2/s$) imply that the hole diffusion current is much smaller than the total photo-current. Then it is possible to regard the hole current as dominated by the drift component [36]. The hole drift current density J_h in the photo-absorption layer at a low electric field is given as:

$$J_h = qp\mu_h E_{ind} \tag{4.5.1}$$

where q is the elemental charge, μ_h is the hole mobility in the photo-absorption layer, E_{ind} is the electric field and p is the concentration of holes.

In equation 4.1.3, the electric field E_{ind} is induced in the photo-absorption layer and as a result causes band bending to occur. The shape of the bended band is parabolic as shown in figure 4.50. The field that has been set up in the base layer can effectively accelerate the photo-excited electrons in the base layer flowing towards the collector layer.

Here, the relations between doping level and potential gradient in the photo-absorption layer $\Delta\phi_{eff}$ will be discussed. Assuming that the photo-excited carriers are generated uniformly, DC electron current distribution, $J_e(x)$ due to the electron current continuity in the photo-absorption layer is [36]:

$$J_e(x) \approx J_0 \frac{x}{W_a} \tag{4.5.2}$$

where J_0 is total current density, W_a is thickness of the photo-absorption layer, and x is the distance from the E-B interface.

By the law of conservation of current in the photo-absorption base layer, hole current density is given as:

$$J_h(x) = J_0(1 - \frac{x}{W_a}) \tag{4.5.3}$$

Given the boundary condition, drift current of the majority of holes is zero at the B-C layer interface, and linearly increases (under uniform carrier generation) toward the p-contact layer, side up to the device operation current [31]. It is found that current density and E_{ind} change linearly with x. So the band bending is in a parabolic shape. Then the potential gradient $\Delta\phi_{eff}$ caused by the self-induced electric field E_{ind} can be calculated as:

$$\begin{aligned}
\Delta\phi_{eff} &\propto \int E_{ind}\,dx \\
&= \int_0^{W_a} \frac{J_0(1-\frac{x}{W_a})}{qp\mu_h}\,dx \\
&= \frac{J_0}{qp\mu_h}[\int_0^{W_a} 1dx - \int_0^{W_a} (\frac{x}{W_a})dx \\
&= \frac{J_0}{qp\mu_h}\cdot\frac{W_a}{2}
\end{aligned} \tag{4.5.4}$$

The final equation for the potential gradient is given as:

$$\Delta\phi_{eff} \propto \frac{W_a J_0}{2qp\mu_h} \tag{4.5.5}$$

The potential gradient $\Delta\phi_{eff}$ attributes the enhanced electron speed towards the sub-collector as due to the self-induced electric field E_{ind} in the photo-absorption base layer associated with the hole current [36]. Although the E_{ind} does not depend on the thickness of the absorption layer, the diffusive velocity drops with an increase in the absorption layer thickness. Thus this effect is more intense for the wider absorption base layer. Also, the effect can be suppressed by higher absorption layer doping, as the induced potential gradient is proportional to the reciprocal of the hole density [31]. Also, although the self-induced field may bring about a kind of nonlinear effect peculiar to the device, no disadvantages are presented that provide higher 3dB bandwidth.

Figure 4.51 shows that variation in the electron density over the absorption layer is changed as a parameter for different potential gradients ($\Delta\phi_{eff} \propto \int_0^{W_a} E_{ind} dx$). The lower electron density means higher electron velocity and shorter travel time [31]. At $\Delta\phi_{eff} = 0mV$, where electron density has a parabolic shape, only diffusion transport exists. As $\Delta\phi_{eff}$ increases, the electron density is significantly reduced and the distribution shifts to the collection layer. Electrons can be ballistically launched to diffuse/drift towards the collector layer by higher $\Delta\phi_{eff}$. As in the case of the DHPT, electrons represent velocity overshoot in the collector layer [38], where the velocity is far greater than hole saturation velocity [31]. So the above features synchronously result in a higher saturation output current and a faster response.

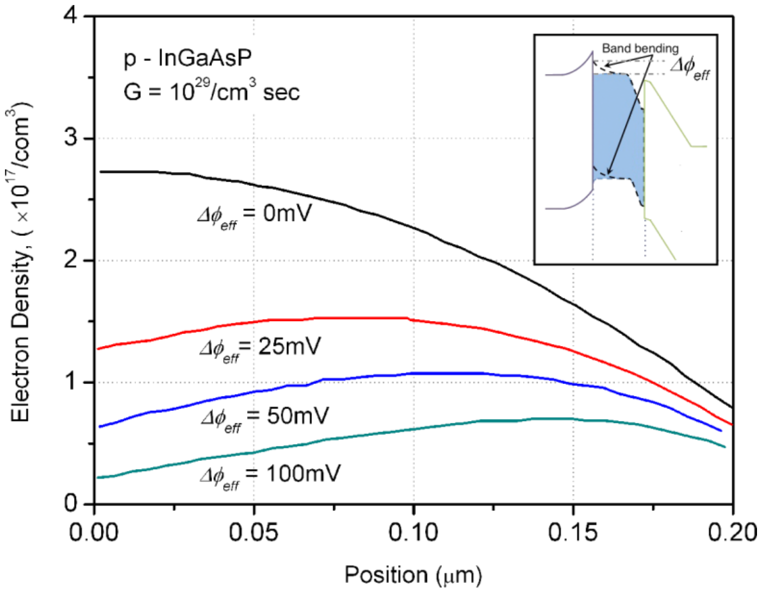

Figure 4.51: Electron density distribution in the absorption layer of a UTC-PD with absorption layer thickness of 0.2μm. Minority electron mobility of 4000 cm^2/Vs is assumed [31]

In the following section, both DC and optical measurements of the $In_{0.49}Ga_{0.51}P/GaAs$ SHPT and DHPT are shown to prove the optical absorption base layer band bending effect.

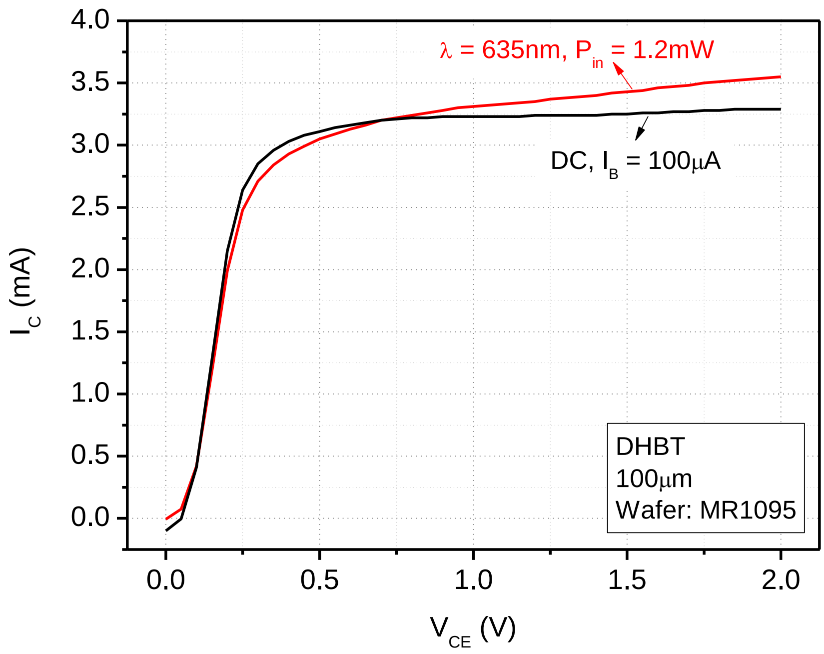

Figure 4.52: Measured IV characteristics (I_B = 100μA) and 2-terminal photoresponse (λ = 635nm, P_{in} = 1.2mV) of the Npn $In_{0.49}Ga_{0.51}P$/GaAs DHPT (wafer no. MR1095, emitter contact diameter = 100μm)

From equation (4.1.7), the origin of the photo absorption base layer band bending is the holes' drift current. In this work, in order to investigate the effect of band bending in the base layer, we have studied the characteristics of the DHPT under both DC and optical conditions. Figures 4.52 and 4.53 show comparison between the measured DC IV characteristics and 2-terminal photoresponse of the $In_{0.49}Ga_{0.51}P$/GaAs DHPT for different optical power at similar I_B input current levels with I_{ph} = 92mA, the I_C at higher V_{CE} (larger than 0.75V) of I_{ph} is larger than I_C (DC condition). First, from figure 4.52, it is noticed that for a 635nm photoresponse, the device current level in the active region is not flat but increases with an increase in the C-E bias voltage. This behaviour is different with the device under DC condition. For a normal bipolar transistor, this phenomenon may result from base width modulation [39]. However, in HBTs, especially DHBTs, since the base layer is highly doped, the recombination rate of the carriers is very high; therefore, base width modulation is not expected. Another explanation may be that with the increase in C-E bias voltage, B-C reverse bias voltage increases, causing the energy spike in the B-C conduction band to be suppressed. This can raise the current gain of the device by allowing more electron carriers to flow towards the collector contact. But the data in figure 4.52 clearly shows that the DC collector current in the active region does not increase with an increase in the V_{CE}. So base band bending is the only cause of the increase in the collector current under illumination.

As a device with 2-terminal operation, the base terminal is floating. Photo-excited holes in the GaAs base layer cannot flow out through base contact as a DC 3-terminal measurement. By the description in equation 4.1.7, the hole current flowing generates band bending in the base region and produces the potential gradient $\Delta\phi_{eff}$: this ballistically launches electrons which flow into the collector layer. This progress results in high saturation current level, as discussed previously. With higher C-E bias voltage, a higher potential gradient $\Delta\phi_{eff}$ is produced, as shown in figure 4.51, with further higher electron velocity induced. So a higher output current level is observed:

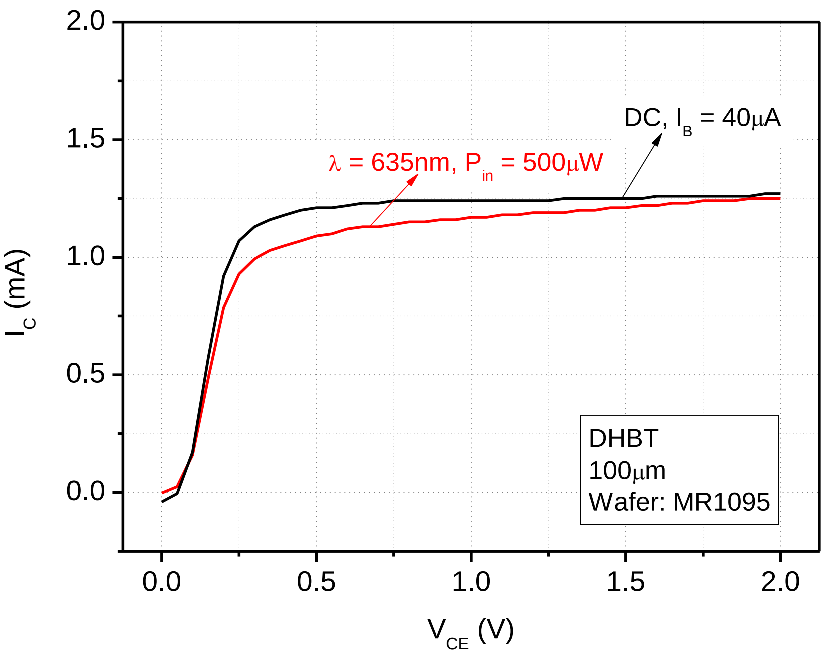

Figure 4.53: Measured IV characteristics (I_B = 40μA) and 2-terminal photoresponse (λ = 635nm, P_{in} = 500μW and λ = 850nm, P_{in} = 2mW) of the Npn $In_{0.49}Ga_{0.51}P/GaAs$ DHPT (wafer no. MR1095, emitter contact diameter = 100μm)

The same phenomenon can be found in figure 4.53. Due to lower current level in active region, the variation of the current in the active region produced by 850nm wavelength is not obviously as 635nm. This also accord with our equations and principle deduction.

In order to verify our explanation, figure 4.54 and figure 4.55 are shown. In figure 4.54, under similar measurement conditions as figures 4.52 and 4.53, DC and optical measurements are plotted for $In_{0.49}Ga_{0.51}P$/GaAs SHPT; since the B-C junction of our SHPT involves the conventional structure (p-i-n PD structure). Even at a high output current level (4mA), no band bending effects are evident (I_{ph} in active region is relatively flat and the value is not bigger than DC bias condition). This, again, proves our UTC-PD structure DHPT device operation mechanism. Finally, under the same optical input power level, 2-terminal photoresponse of the In0.49Ga0.51P/GaAs DHPT and SHPT with 635nm and 850nm, respectively, are plotted in figure 4.55. The figure clearly shows the band bending phenomenon takes place only in the DHPT, and shows how the device saturation current benefits from the mechanism.

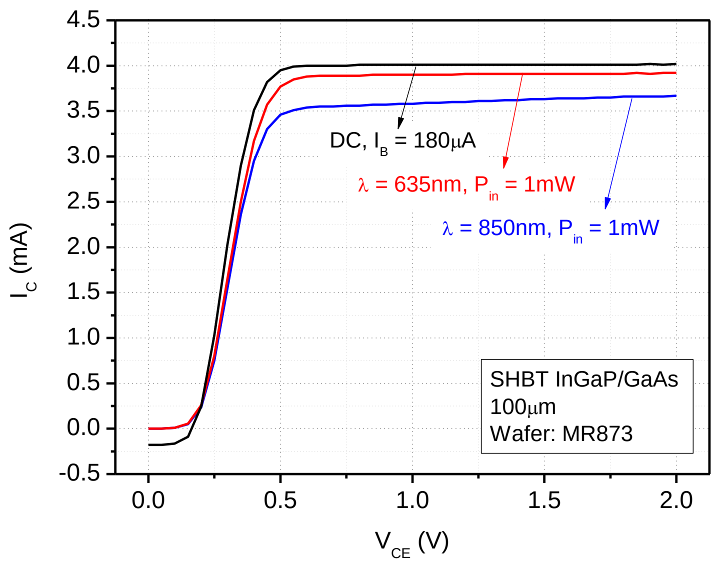

Figure 4.54: Measured IV characteristics (I_B = 180μA) and 2-terminal photoresponse (λ = 635nm and λ = 850nm, P_{in} = 1mW) of the Npn $In_{0.49}Ga_{0.51}P$/GaAs SHPT (wafer no. MR873, emitter contact diameter = 100μm)

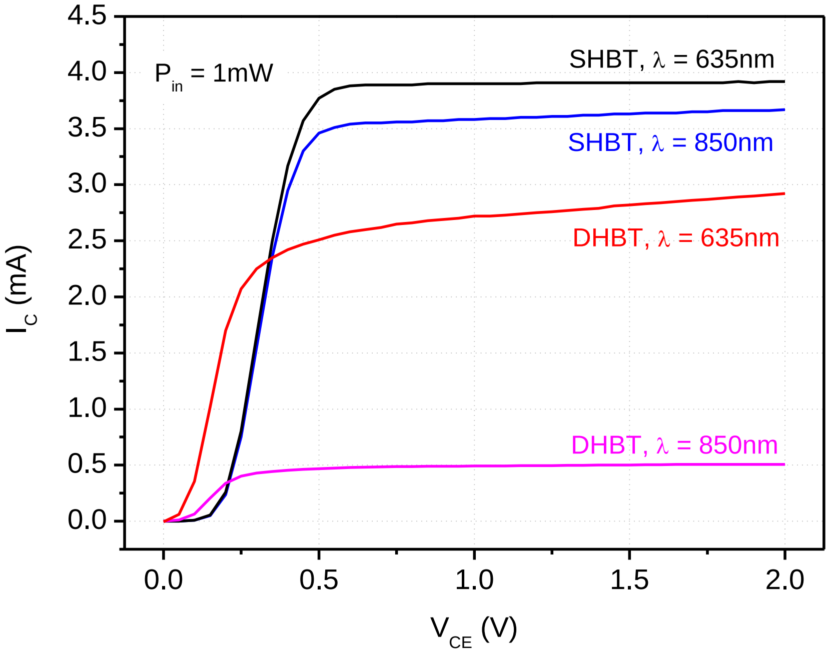

Figure 4.55: Measured IV characteristics (I_B = 40μA) and 2-terminal photoresponse (λ = 635nm and λ = 850nm, P_{in} = 1mW) of the Npn $In_{0.49}Ga_{0.51}P$/GaAs DHPT on MR1095 and SHPT on MR873 (emitter contact diameter = 100μm)

Through the discussion above, the $In_{0.49}Ga_{0.51}P$/GaAs DHBT, working as a photodetector, is analysed. The benefit of a second heterojuction in the DHPT, which located at the B-C interface, is clearly shown. The UTC-PD operation mechanism and the base band effect are verified both by equations and measurement results. It is believed that by undertaking good design of InGaP/GaAs DHPTs, an excellent short wavelength photodetector with high speed and high saturation output capabilities for various high frequency and high performance optical communication systems, is expected.

References

[1] Ito, H., Nagatsuma, T. Ishibashi, T. “Recent development on uni-traveling-carrier photodiodes and their applications”, Proc. LEOS, San Diego, CA , vol.1, pp. 386-387, 2001.

[2] Ogawa, H. “Microwave and millimeter-wave fibre optic technologies for subcarrier transmission systems”, IEICE Trans. Commun., vol. E76-B, pp.1078-1090, Sept. 1993.

[3] Kamitsuna, H., Yokosuka, Matsuoka, Y., Yamahata, S., Kurishima, K. “A monolithically integrated photoreceiver realized by InP/InGaAs double-heterostructure bipolar transistor technologies for optical/microwave interaction systems”, Gallium Arsenide Integrated Circuit (GaAs IC) Symposium, 1995. Technical Digest 1995. 17th Annual IEEE, pp. 185-188, Oct. 29 1995-Nov. 1 1995.

[4] Y. Chin, Lin, H., Huang, C. “InGaP/$GaAs_{0.57}P_{0.28}Sb_{0.15}$/GaAs Double HBT with Weakly Type-II Base/Collector Junction”, Electron Device Letters, IEEE, vol. 33, Issue 4, pp. 489 -491, 2012.

[5] Kamitsuna, H., Y. Matsuoka, S. Yamahata, H. Nakajima and H. Ogawa, “Photodetection characteristics of InP/InGaAs HBTs and their process compatible pin-photodiode”,,in 19th Int. Conf. on Infrared and Millimetre Waves Dig., pp. 325-326, Oct. 1994.

[6] H. Fukano, Y. Takahashi and M. Fugimoto, “High-Speed InP-lnGaAs Heterojunction Phototransistors Employing a Nonalloyed Electrode Metal as a Reflector”, IEEE Journal of Quantum Electronics, Vol.30, No.12, pp.2889-2895, December 1994.

[7] R. Sridhara, S. M. Frimel, K. P. Roenker, N. Pan, J. Elliott, “Performance enhancement of GaInP/GaAs heterojunction bipolar phototransistors using DC base bias”, J Lightwave Technology., vol. 16, pp. 1101–1106, 1998.

[8] Song, C. K., Lee, S. H., Kim, K. D., Park, J. H., Koo, B. W., Kim, D. H., Hong, C. H., Kim, Y. K., Hwang, S. B. “Optical characteristics of InGaP/GaAs HPTs”, IEEE Electron Device Letter.., vol. 22, pp. 315–317, 2001.

[9] Yang, Y. F., Hsu, C. C., Yang, E. S., Chen, Y. K. “Comparison of GaInP/GaAs heterostructure-emitter bipolar transistors and heterojunction bipolar transistors”, IEEE Trans. Electron Devices, vol. 42, pp. 1210–1215, 1995.

[10] Sridhara, R., Frimel, S. M., Roenker, K. P., Pan, N., Elliott, J. “Performance enhancement of GaInP/GaAs heterojunction bipolar phototransistors using DC base bias,” J. Lightwave Technol., vol. 16, pp. 1101–1106, 1998.

[11] Song, C., Lee, S., Kim, K., Park, J., Koo, B., Kim, D., Hong, C., Kim, Y.,

Hwang, S. “Optical Characteristics of InGaP/GaAs HPTs”, IEEE Electron Device Letters, vol. 22, no. 7, pp. 315-317, 2001.

[12] Pedrotti, K. D., Pierson, R. L., Sheng, N. H., Nubling, R. B., Farley, C. W., Chang, M. F. “High-bandwidth OEIC receivers using heterojunction bipolar transistors: Design and demonstration”, J. Lightwave Technology, vol. 11, pp.1601 -1614 1992.

[13] Kamitsuna, H. “Ultra-wideband monolithic photoreceivers using HBT-compatible HPT',s with novel base circuits, and simultaneously integrated with an HBT amplifier”, J. Lightwave Technology, vol. 13, pp.2301 -2307 1995.

[14] Nagano, N., Suzaki, T., Soda, M., Kasahara, K., Takeuchi, T., Honjo, K. “Monolithic ultra-broadband transimpedance amplifiers using AlGaAs/GaAs heterojunction bipolar transistors”, IEEE Trans. Microwave Theory Tech, vol. 43, pp.2-9, 1994.

[15] Song, C. K., Choi, P. J. “Effect of InGaP heteropassivation on reliability of GaAs HBTs”, Microelectronics Reliability, vol. 39, pp. 1817–1822, 1999.

[16] Rezazadeh, A. A., Sotoodeh, M., Dharmasiri, N. “Base-Collector Design Optimisation of InGaP/GaAs DHBTs”, High Performance Electron Devices for Microwave and Optoelectronic Applications, 2000 8th IEEE International Symposium, pp. 99 – 104, 2000.

[17] Rezazadeh, A. A., Sotoodeh, M. “Design and technology of InGaP/GaAs DHBTs”, Advanced Semiconductor Devices and Microsystems, 2000. ASDAM 2000. The Third International Euro Conference, pp. 119-125, 16-18 Oct. 2000.

[18] Lour, W., Chang, W. “Effect of Collector-Base Barrier on GaInP/GaAs Double Heterojunction Bipolar Transistor and Further Improvement by Doping-Spike”, Japanese Journal of Applied Physics, vol. 36, pp. 6210-6214, Part 1, Number 10, October 1997.

[19] Liu, W., Bean, E., Henderson, T., Fan, S. “Extrinsic base surface pas- sivation in GaInP/GaAs heterojunction bipolar transistors”, IEEE Electron Device Letter., vol. 14, pp. 301–303, 1993.

[20] J. Li, Cismaru, C., Zampardi, P., Wu, A., Babcock, E., Sun, M., Stevens, K., Ramanathan, R. “Development of High Breakdown Voltage InGaP/GaAs DHBTs”, CSMAN TECH Conference, Austin, Texas, USA pp.177-180, 2000.

[21] Kren, D.E., Rezazadeh, A. A., Rees, P. K., Tothill, J. N. “High C-doped base InGaP/GaAs HBTs with improved characteristics grown by MOCVD”, Electronics Letters, vol.29 , Issue 11, pp.961-963, 2002.

[22] Liu, W., Henderson, T., Beam III, E., Fan, S. K. “Electron saturation velocity in $Ga_{0.5}In_{0.5}P$ measured in a GaInP/GaAs/GalnP double-heterojunction bipolar

transistor", Electron. Letter, vol. 29. pp. 1885-1887. 1993.

[23] Fischetti, M. V. "Monte Carlo simulation of transport in technologically significant semiconductors of the diamond and zinc-blende structures- Part I: Homogeneous transport," IEEE Trans. ElectroM Devices, vol. 38, pp. 634-649, 1991.

[24] Chen, H. R., Tan, S. W., Chen W. T., Lin, T. S. "The Effect on Base Bias for InGaP/GaAs Heterojunction Phototransistors", Optoelectronic and Microelectronic Materials and Devices, pp. 241-244, 2004.

[25] Chandrasekhar S., Hoppe M. K., Dentai A. G., Joyner C. H. "Demonstration of enhanced performance of an InP/InGaAs heterojunction phototransistor with a base terminal", IEEE Electron Device Letters, vol.12, Issue: 10, pp. 550-552, 1991.

[26] Sridhara, S., Frimel, S. M., Roenker, P. K, Elliot, J. "Performance Enhancement of GaInP/GaAs Heterojunction Bipolar Phototransistors Using DC Base Bias", Journal of Lightwave Technology, Vol. 16, No. 6, pp. 1101-1106, June, 1998.

[27] Tan, S. W., Chen, H. R., Chen, W. T., Hsu, M. K., Lin, A. H., Lour, W. S. "The influence of base bias on the collector photocurrent for InGaP GaAs heterojunction phototransistors", Journal of Applied Physics,vol.97, Issue 3, pp. 034502 - 034502-7, 2009.

[28] Matsuoka, Y., Sano, E. "InP/InGaAs double-heterostructure bipolar transistors for high-speed ICs and OEICs", Solid State Electronics, 38 9, 1703, Proceedings of the Topical Workshop on Heterostructure Microelectronics, 1995.

[29] Lour, W., Chang, W. "Effect of Collector-Base Barrier on GaInP/GaAs Double Heterojunction Bipolar Transistor and Further Improvement by Doping-Spike", Japanese Journal of Applied Physics, 36 6210,1997.

[30] Leven, A., Lucent, T., Hill, M., Houtsma, V., Kopf, R., Baeyens, Y. "InP-based double-heterostructure phototransistors with 135 GHz optical-gain cutoff frequency", Electronics Letters, vol.40, Issue. 13, pp. 833-834, 2004.

[31] Ishibashi, T., Furuta, T., Kodama, S., Nagatsuma, T., Shimizu, N., Miyamoto, Y. "InP/InGaAs Uni-Traveling-Carrier Photodiodes", IEICE Transactions on Electronics, vol. E83–C, no.6, 2000.

[32] Ito, H., Furuta T., Ishibashi, T. "High-speed and high-output unitraveling-carrier photodiodes", IEICE Transactions on Electronics, vol. 84, pp. 1448-1454, 2001.

[33] Ito, H., K. Satoshi, Muramoto, Y., Furuta, T. "High-speed and high-output InP-InGaAs unitraveling-carrier photodiodes", IEEE Journal of Selected Topics in Quantum Electronics, vol.10, issue 4, pp.709-727, 2004.

[34] Ruch, J. G.. “Electron dynamics in short channel field-effect transistors”, IEEE Transactions on Electron Devices, vol. ED-19, pp.652 -654, 1972.

[35] Shur, M. S., Eastman, L. F. “Ballistic transport in semiconductor at low temperatures for low-power high-speed logic”, IEEE Transactions on Electron Devices, vol. ED-26, pp.1677 -1683, 1979.

[36] Shimizu, N., Watanabe, N., Furuta T., Ishibashi, T. “Improved Response of Uni-Traveling-Carrier Photodiodes by Carrier Injection”, Japanese Journal of Applied Physics, vol. 37, pp.1424-1426, 1998.

[37] Yamauchi, Y., Ishibashi, T. “Electron velocity overshoot in the collector depletion layer of AlGaAs/GaAs HBT\'s”, IEEE Electron Device Letter., vol. EDL-7, pp.655 -657, 1986.

[38] Kurishima, K., Nakajima, H., Kobayashi, T., Matsuoka, Y., Ishibashi, T. “Fabrication and characterisation of high-performance InP/InGaAs double-heterojunction bipolar transistors”, IEEE Transactions on Electron Devices, vol.41, pp.1319–1326, 1994.

[39] Sze, S. M. Physics of Semiconductor Devices, 2nd ed. USA: John Wiley & Sons, 2001.

Chapter 5 Small signal analysis and eye diagram simulations

5.1 Eye diagram analysis methodology

The main idea of this chapter is to check performance of the $In_{0.49}Ga_{0.51}P/GaAs$ DHBT, both as an amplifier and a photodetector, using an eye diagram as a tool. So often in device design and optimisation processes, the output response turns out to be different than expected. Traditional procedures like S-parameters and trial and error methods were used to try and minimise the impairments in the design. However, the results either did not provide enough information or were too problematic, in terms of time and cost. However, as reported [1] an eye diagram can be used as a visual tool to depict the output response of any circuit and device. Additionally, it offers additional visual information, both in amplitude and timing, like noise, jitter and inter-symbol interference (ISI) [2], which can help the designer to optimise the design.

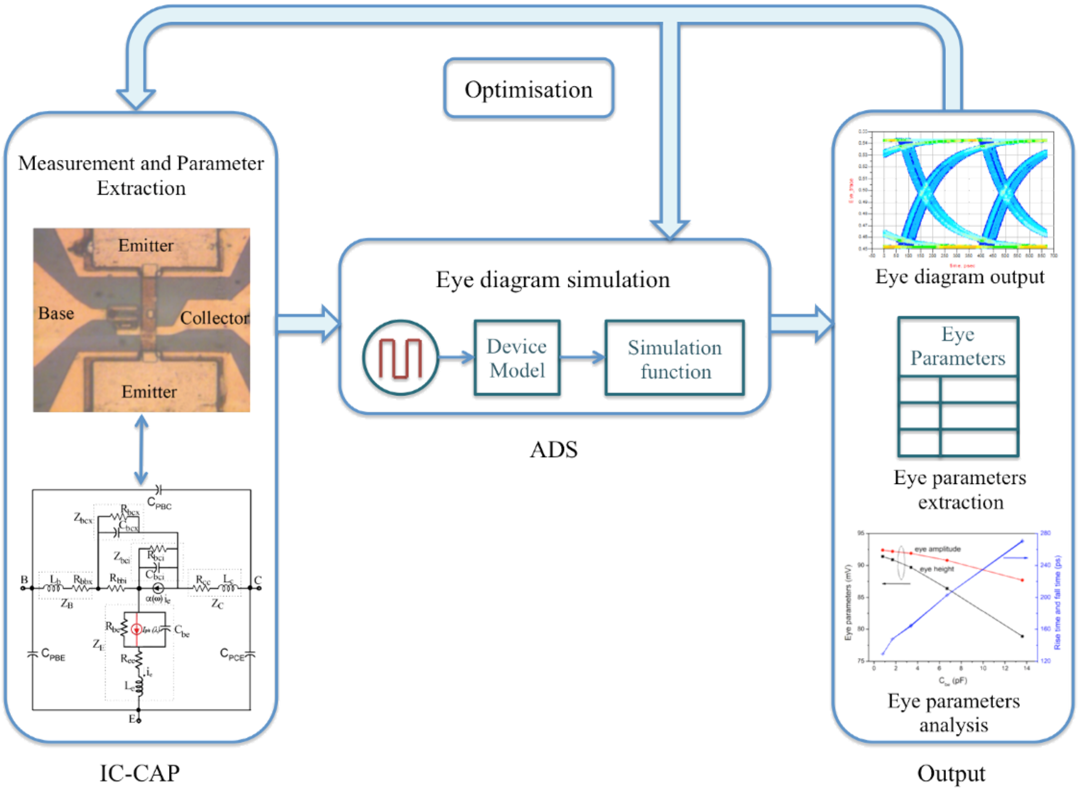

Figure 5.1: Methodology of eye diagram to optimise device performance

Figure 5.1 shows the main set-up for using an eye diagram in this project to check the performance of the $In_{0.49}Ga_{0.51}P$/GaAs DHBT working as an amplifier and short wavelength photodetector (850nm). The small signal parameters of the device are extracted for a T-equivalent circuit model using Integrated Circuit Characterization and Analysis Program (IC-CAP). IC-CAP is the world's leading electronic design automation software for RF, microwave, and high speed digital applications. It is a device modelling software which is employed as the primary tool for controlling measurements, and also used to extract small signal parameters. IC-CAP is pre-programmed by the university of Manchester microwave research group. The only data is required is measured S-parameters. So the small signal parameters extraction progress is called "automatically". A T-equivalent circuit model is then built using these parameters. A T-equivalent circuit model is known to more accurately model the device than a hybrid π-model, especially for high frequency simulation, Further, a T-model is more physically related to the DUT [3], and makes it easier for us to carry out a physical investigation of the device. Advanced Design

System (ADS) is the world's leading electronic design automation software for RF, microwave, and high speed digital applications. After conducting the above process in ADS, a small signal pseudo-random signal, which is provided by the data component in the ADS Ptolemy environment, is used as input a signal to the circuit. The output eye diagram is collected by a data display window. After this, the inbuilt function "FrontPanel" in ADS calculates and extracts the eye parameters. Using these eye parameters, careful analysis can be done. The feedback is then used to allow us to return to the T-equivalent model and vary the small signal parameters, as well as check whether the variation influences the eye diagram.

For HPT performance checking, an additional current source is added between the emitter and base terminals on the T-equivalent circuit. Optical affected components (small signal parameters) are discussed both by equations and eye diagram simulations. Then, a similar process to amplifier performance checking is carried out. Combined with the conventional method, by relating the eye diagram to S-parameters, and then small signal parameters of the device, the interrelation offers us a powerful new method for optimising a device for a desired output. This data from the eye diagram could also be used in the fabrication process to identify the effect of device layer structure and fabrication [4].

In this section, a $16\times20\mu m^2$ $In_{0.49}Ga_{0.51}P$/GaAs DHPT biased in a common emitter with V_{ce} = 3V, V_{be} = 1.2V and I_c = 20mA is simulated as the small signal T-model equivalent circuit. As compared with the same geometry, $8\times10\mu m^2$ InGaP/GaAs SHBT and DHBT device simulations are also shown to indicate the influence of carrier transit time in the B-C junction. A data rate was chosen from low to high, with the inclusion of some typical data rates, like -3dB point and the cut-off frequency (half corresponding value). The data rate variety is only focused on a single eye in order to allow for intuitionistic analysis. All eye diagrams in this report are plotted with picoseconds or nanoseconds of X-axis and millivolts of Y-axis. After the eyes are plotted, the parameters of the eye diagrams are also plotted in figures, and then intuitionistic analysis is given.

5.2 Small signal model

In order to analyse device behaviour, there are two commonly used equivalent circuit topologies for developing an accurate small signal linear equivalent circuit, known as T and hybrid-π topologies [5-9]. Most techniques reported in the literature dealing with small signal HBT device performance make use of the T model topology [10]. The T model is preferred because all the model parameters can be directly tied to the physics of the device. It can maintain backward compatibility with a physics model [11] and fit S-parameter data well up to mm-wave frequencies [10]. On the other hand, the hybrid-π model parameters show noticeable frequency dependence, especially at high frequencies [10].

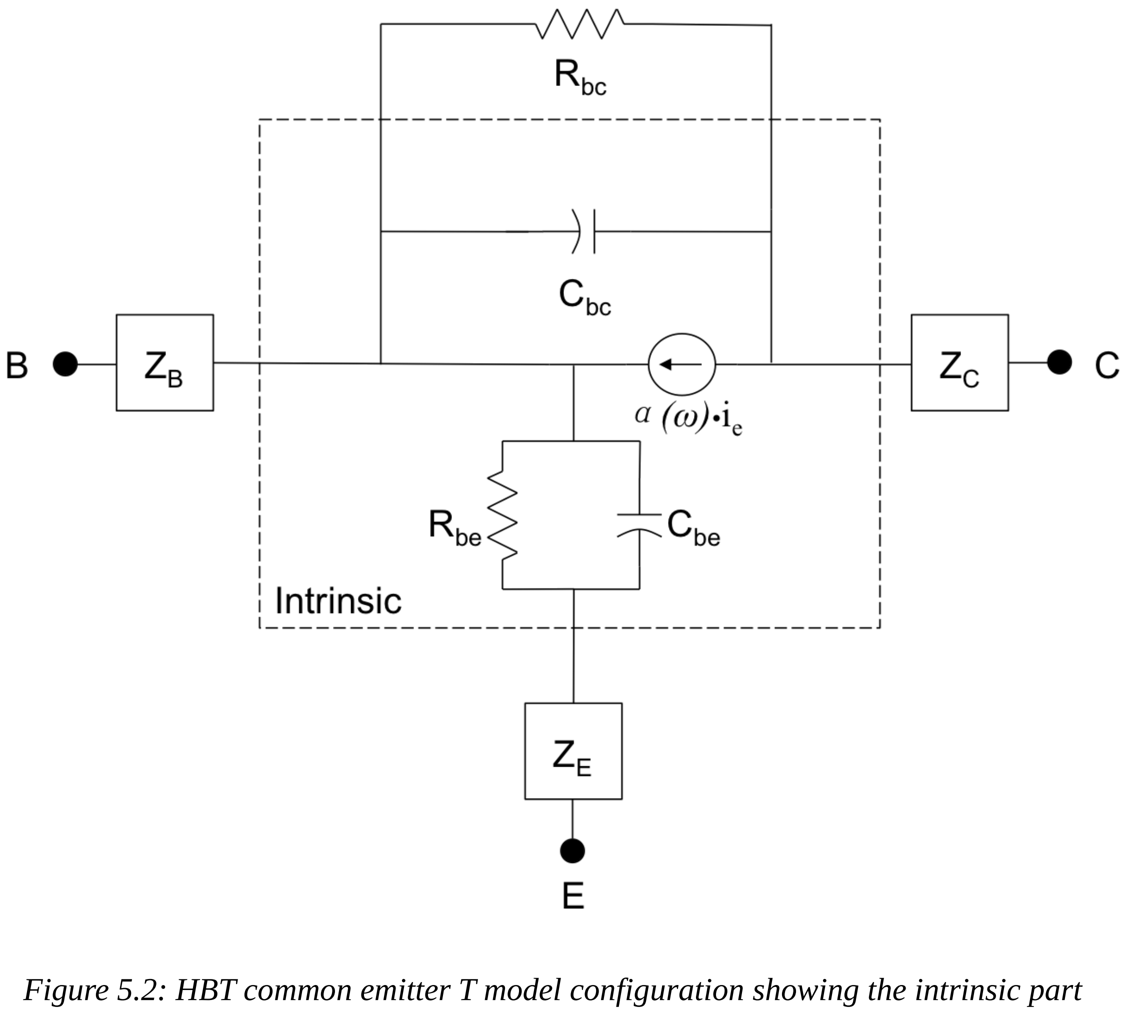

Figure 5.2: HBT common emitter T model configuration showing the intrinsic part

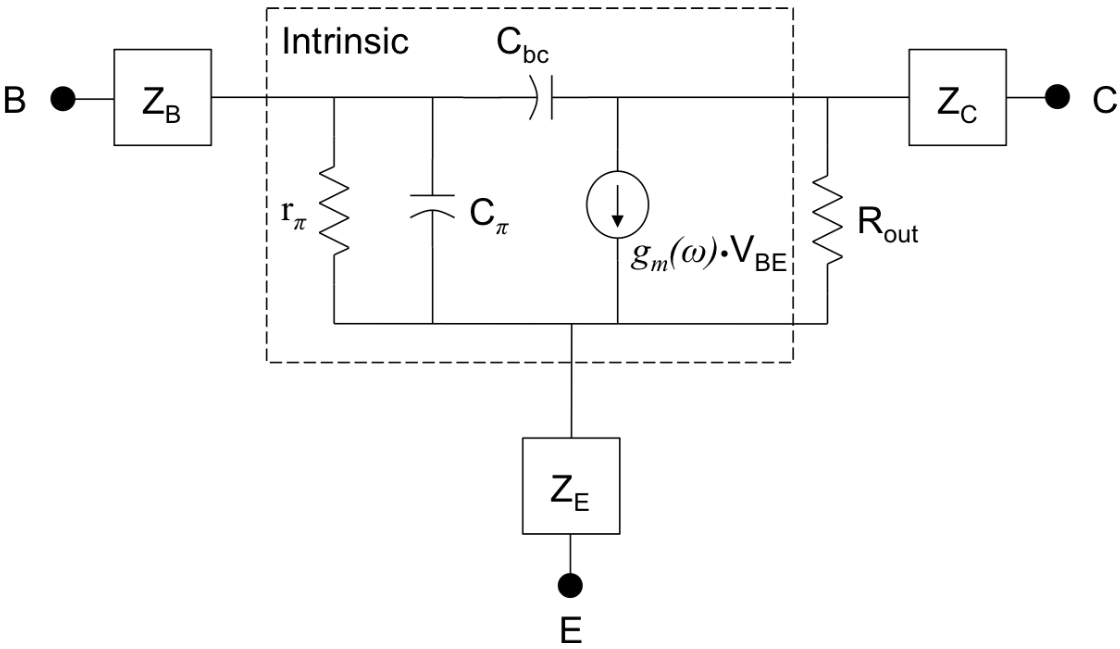

Figure 5.3: HBT common emitter intrinsic hybrid-π model configuration

The T and hybrid-π topologies are shown in figures 5.2 and 5.3, respectively. Since the extrinsic circuit is the same between the two topologies, it will therefore have the same parameter values [10]. So here we only focus on the only difference existing between the intrinsic equivalent circuits by figures. The circuit in the figure 5.2 dashed box is the intrinsic T equivalent circuit. Correspondingly, the dashed box in figure 5.3 is the intrinsic hybrid-π equivalent circuit. Using the Y-parameter, the two topology circuits can be described as:

$$[Y_T] = \begin{bmatrix} (1-\alpha(\omega)\cdot\dfrac{1}{R_{be}} + j\omega(C_{be}+C_{bc}) & -j\omega C_{bc} \\ \dfrac{\alpha(\omega)}{R_{be}} - j\omega C_{bc} & j\omega C_{bc} \end{bmatrix} \tag{5.2.1}$$

$$[Y_\pi] = \begin{bmatrix} \dfrac{1}{r_\pi} + j\omega(C_\pi + C_{bc}) & -j\omega C_{bc} \\ g_m - j\omega C_{bc} & j\omega C_{bc} \end{bmatrix} \tag{5.2.2}$$

In equation 4.2.1, the parameter $\alpha(\omega)$ consists of various carrier transit delay terms, and the DC common base current gain α_0. g_m in equation 4.2.2 is the transconductance of the device. Z_E, Z_B and Z_C which consist of a resistor and an inductor in series are the impedances of extrinsic circuit.

Comparing the two equations, it is notable that T and hybrid π model equations can be converted by:

$$r_{\pi} = \frac{R_{be}}{1-\alpha(\omega)},\ g_m = \frac{\alpha(\omega)}{R_{be}} \text{ and } C_{\pi} = C_{be} \tag{5.2.3}$$

All other parameters are equivalent. Although both T and hybrid-π topology formulations are not equivalent to the device in all cases. Profiting from the relative high frequency independent, and being more closely related to the original derivation of the common base Y-parameters of the HBT [12-13], in this work, the T model equivalent circuit is adopted to characterise the small signal behaviour of HBTs.

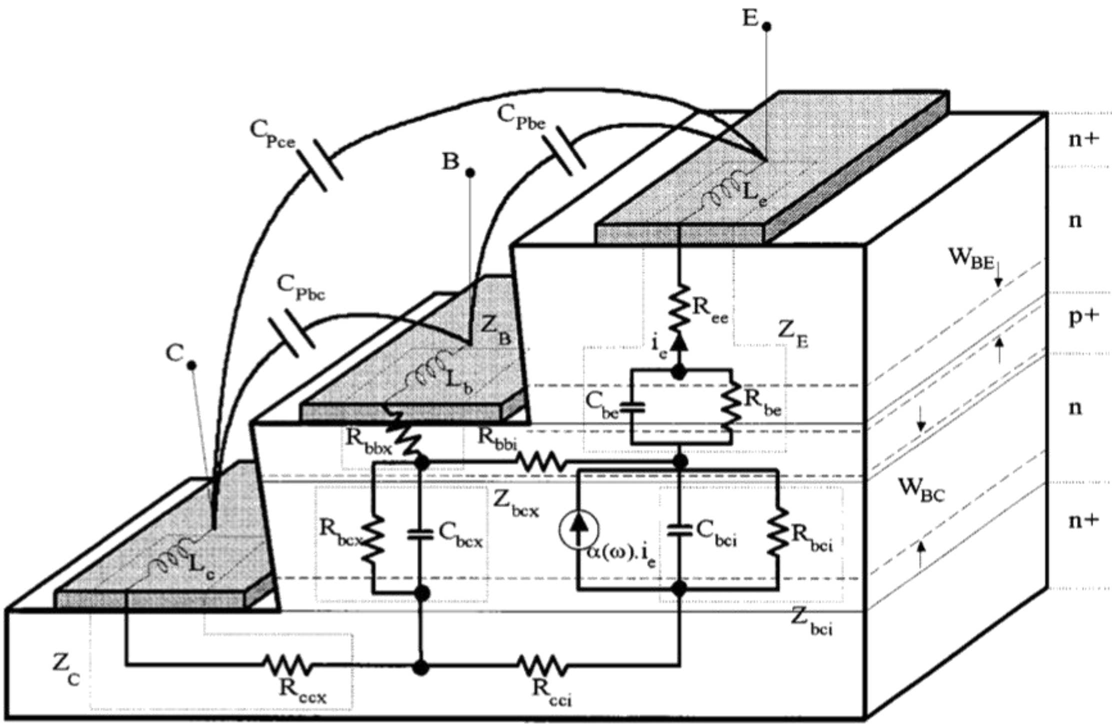

Figure 5.4: Schematic cross-section of a small-geometry Npn HBT, together with its lumped element T-shape small-signal equivalent circuit [14]

Figure 5.4 shows the cross-sectional view of an Npn HBT, along with its associated small-signal lumped-elements, which is very useful in interpreting the small-signal parameters. In the figure, three parallel capacitances are added to a T-shaped equivalent circuit due to the contact pads. The base resistance and the base-collector capacitance are modelled by dividing them into the distributed nature of intrinsic and extrinsic parts, respectively.

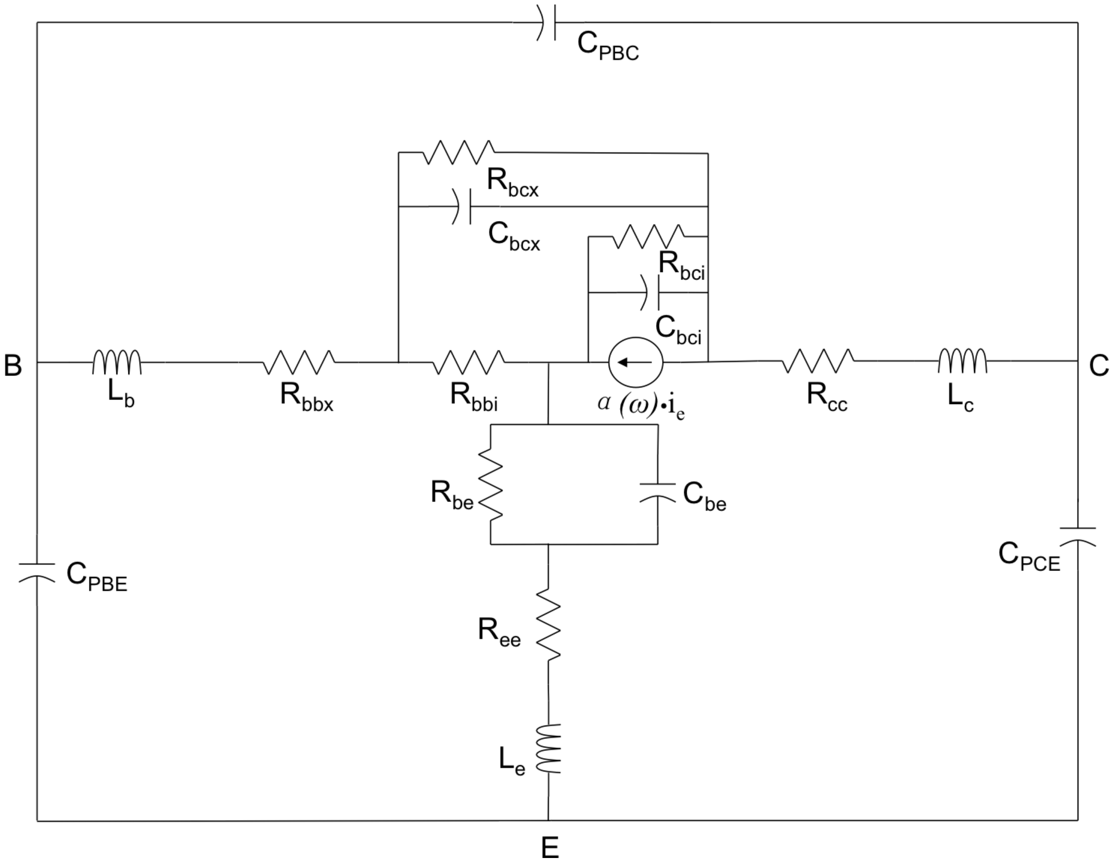

Figure 5.5: T-shaped small signal equivalent circuit of HBT

The complete conventional T-shaped small signal equivalent circuit model used for this work is shown in figure 5.5. The lumped elements and extracted small signal parameters for $In_{0.49}Ga_{0.51}P$/GaAs DHBT (16×20μm^2) with bias condition V_{ce} = 3V, V_{be} =1.2V and I_c = 20mA summarised in table 5.1 [14-15] are used in the following eye diagram simulation. Small signal parameters in table 5.1 are extracted by using the direct extraction technique, also known the most accurate method for determining the linear equivalent circuit of HBTs [5-6, 16].

Table 5.1: Extracted parameters for $In_{0.49}Ga_{0.51}P$/GaAs DHBT (16×20 μm^2), V_{ce} = 3V, V_{be} =1.2V and I_c = 20mA [14-15]

Parameters	**Description**	**Value**	**Parameters**	**Description**	**Value**
L_b (pH)	Parasitic base Inductance	51.7	C_{be} (pF)	BE diffusion capacitance	3.39
L_c (pH)	Parasitic collector inductance	75.8	C_{jbe} (pF)	BE junction capacitance	0.56
L_e (pH)	Parasitic emitter inductance	55.7	R_{ee} (Ω)	Emitter resistance	8.56
τ_b (psec)	Base transit time	4.63	R_{cc} (Ω)	Collector resistance	17
τ_c (psec)	Collector transit time	2.75	R_{bbi} (Ω)	Intrinsic series base resistance	31
C_{pbe} (fF)	Parasitic BE capacitance	24.4	R_{bbx} (Ω)	Extrinsic series base resistance	1.19
C_{pbc} (fF)	Parasitic BC capacitance	5.85	R_{be} (Ω)	BE junction resistance	1.36
C_{pce} (fF)	Parasitic CE capacitance	38.9	R_{bc} (kΩ)	BC junction resistance	20.77
C_{bc} (fF)	BC junction capacitance	189.5	R_{bci} (kΩ)	Intrinsic BC junction resistance	36.43
C_{bci} (fF)	Intrinsic BC junction capacitance	108	R_{bcx} (kΩ)	Extrinsic BC junction resistance	48.3
C_{bcx} (fF)	Extrinsic BC junction capacitance	81.5	r	Ratio of BE area to BC area	0.62

5.3 $In_{0.49}Ga_{0.51}P$/GaAs RF characterisation simulation and validation

The device is first DC characterised with bias V_{ce} = 3V V_{be} = 1.2V and I_c = 20mA. The results confirm that the device works in the linear operating region, and is not affected by any high/low current effect, with above bias condition [4]. Then on-wafer S-parameters measurements were carried out. Figures 5.6 to 5.11 show both S-parameters measurement results and simulation results using a T-shaped equivalent circuit, with table 5.1 showing small signal parameters in Agilent ADS. From figure 5.6, S_{21}, -3dB bandwidth frequency is extracted as 1.1GHz.

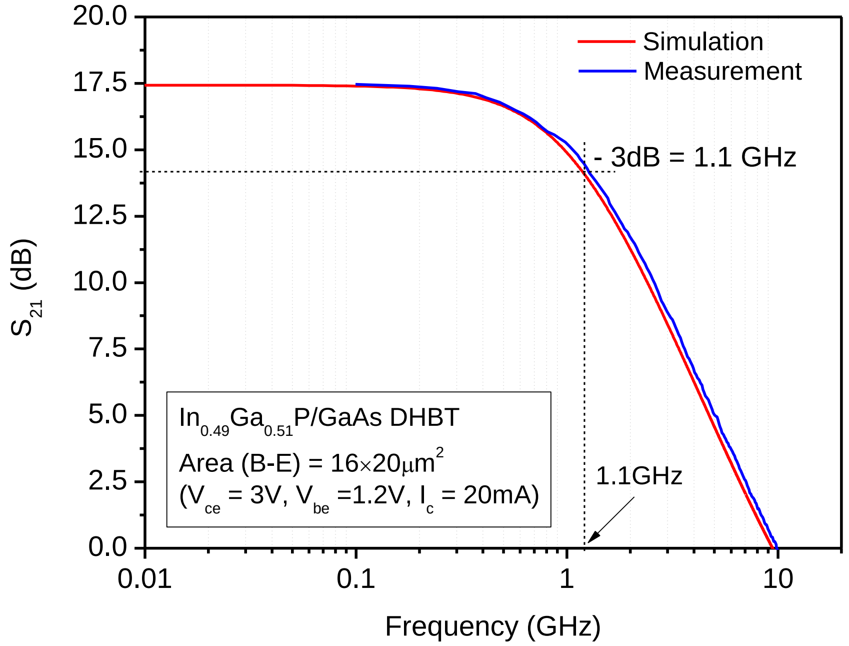

Figure 5.6: Simulated and measured S_{21} of $In_{0.49}Ga_{0.51}P$/GaAs DHBT (16×20 μm^2)

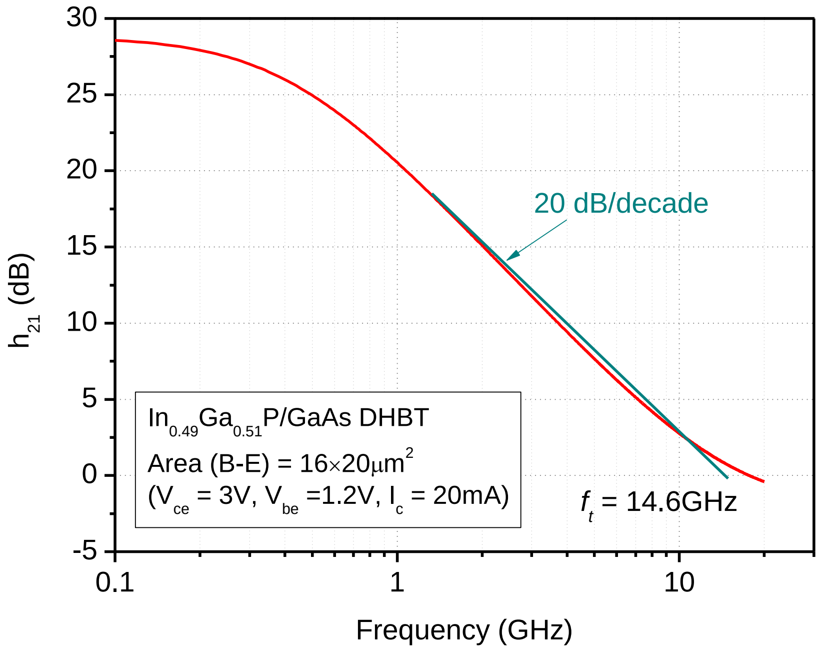

Figure 5.7: Simulated h_{21} of $In_{0.49}Ga_{0.51}P/GaAs$ DHBT (16×20 μm^2)

h_{21} is defined as short circuit current gain, current-off frequency and f_t is defined as the frequency when this current gain drops to unity (0dB). Figure 5.7 shows the simulated result of h_{21} with the f_t extracted as 14.6GHz. The theoretical values of the cut-off frequency can be calculated by using the transit times of the carriers [17]:

$$f_t = \frac{1}{2\pi\tau_{ec}} \tag{5.3.1}$$

where:

$$\tau_{ec} = \tau_{eb} + \tau_{bc} + \tau_b + \tau_c \tag{5.3.2}$$

$$\tau_{eb} = C_{be}R_{be},\ \tau_{bc} = C_{bc}(R_{be} + R_{ee} + R_{cc}) \tag{5.3.3}$$

So, τ_{eb} = 11.01ps and the f_t = 14.45GHz. The simulation result (14.6GHz) is close to the theoretical calculation value.

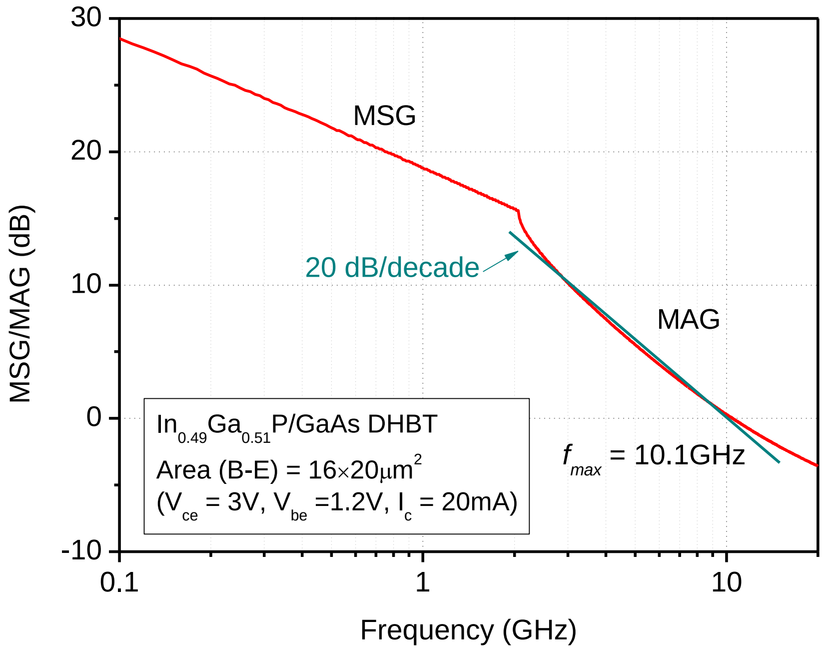

Figure 5.8: Simulated MSG/MAG of $In_{0.49}Ga_{0.51}P$/GaAs DHBT (16×20 μm²)

The maximum frequency f_{max} is defined as the frequency at which the power gain of the transistor falls to unity (0dB). The calculation equations of maximum stable gain (MSG) and maximum available gain (MAG) depend on Rollet's stability factor, also known as K-factor, given as:

$$K = \frac{1-|S_{11}|^2 - |S_{12}|^2 + |S_{11}S_{22} - S_{12}S_{21}|^2}{2|S_{21}S_{12}|} \qquad (5.3.4)$$

When $K < 1, MSG = \frac{|S_{21}|}{|S_{12}|}$ (5.3.5). When $K > 1, MAG = \frac{|S_{21}|}{|S_{12}|} \cdot (K - \sqrt{K^2 - 1})$ (5.3.6).

The maximum frequency can be calculated by:

$$f_{\max} = \left[\frac{f_t}{8\pi (R_{bbi} + R_{bbx}) C_{jc}} \right]^{1/2} \qquad (5.3.7)$$

The theoretical value of our $In_{0.49}Ga_{0.51}P$/GaAs DHBT is 9.71GHz, which is less than 10% different from the simulation extracted value of 10.1GHz.

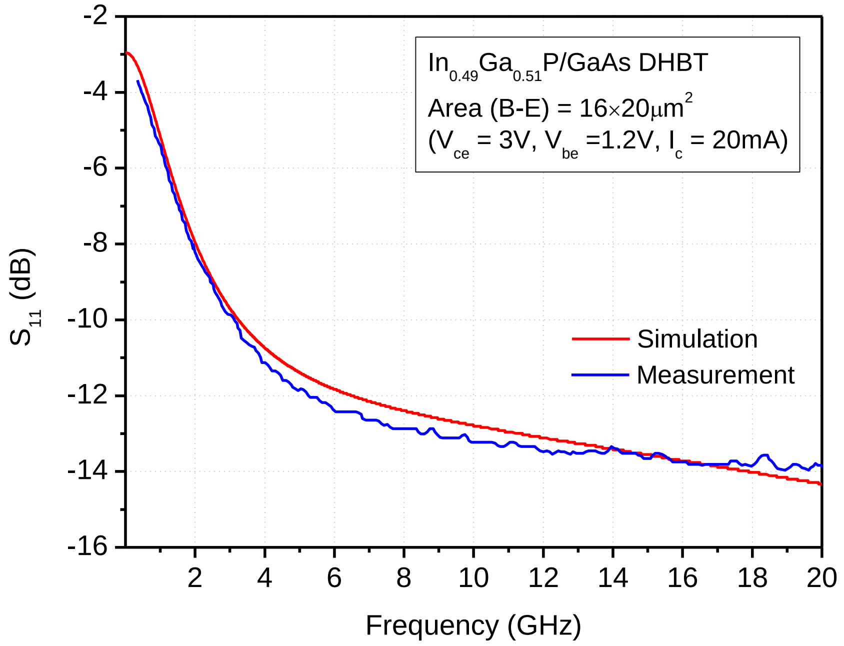

Figure 5.9: Simulated and measured S_{11} of $In_{0.49}Ga_{0.51}P/GaAs$ DHBT (16×20 μm^2)

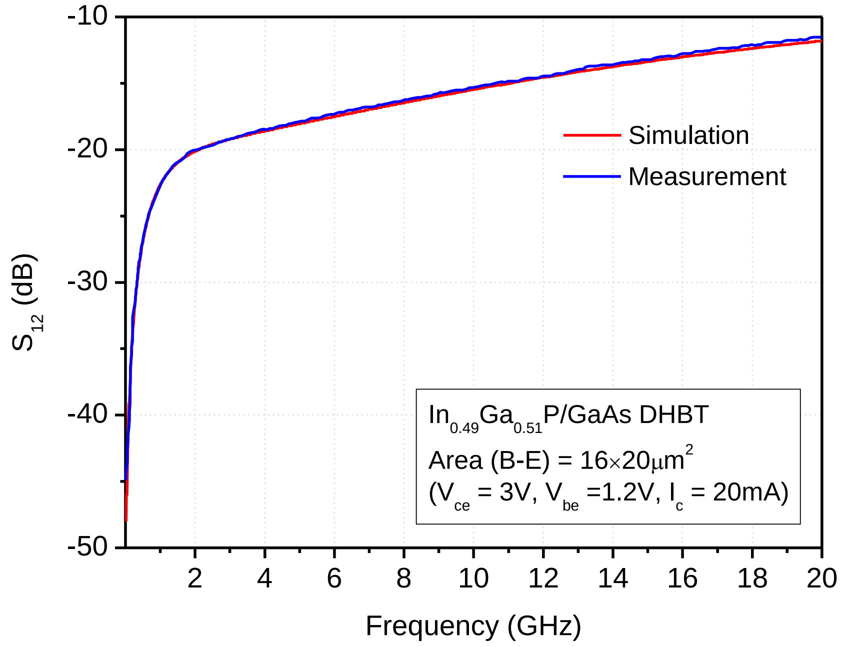

Figure 5.10: Simulated and measured S_{12} of $In_{0.49}Ga_{0.51}P/GaAs$ DHBT (16×20 μm^2)

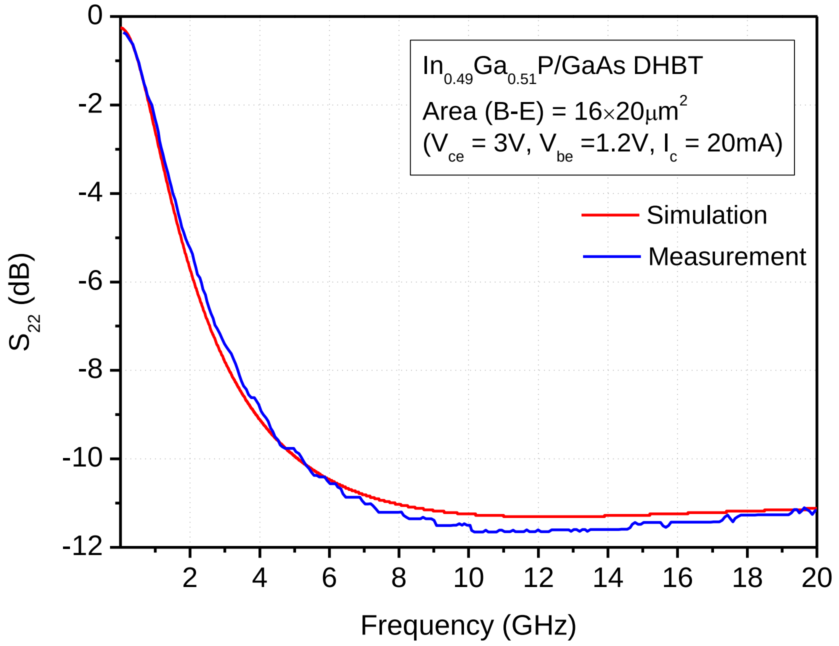

Figure 5.11: Simulated and measured S_{22} of $In_{0.49}Ga_{0.51}P/GaAs$ DHBT (16×20 μm^2)

Figures 5.9, 5.10 and 5.11 show the measured and simulated S_{11}, S_{12} and S_{12} of $In_{0.49}Ga_{0.51}P/GaAs$ DHBT (16×20 μm^2), respectively. The result curves are fairly close, which validates the correction and accuracy both of our small signal parameters and simulation.

5.4 $In_{0.49}Ga_{0.51}P/GaAs$ DHBT eye diagram simulation

In this section the simulation and measurement [4] results of the eye diagram showing varying frequencies are shown. Then some of the key eye parameters are recorded over the entire range. During the simulation the NRZ signal modulation is adopted. For the NRZ signal modulation baud rate is equal to bitrate. In order to achieve highest bitrate corresponding to the frequency response of the devices, the input signal is coded to switch between “0” and “1” alternately. The bitrate is double value of device operation frequency correspondingly.

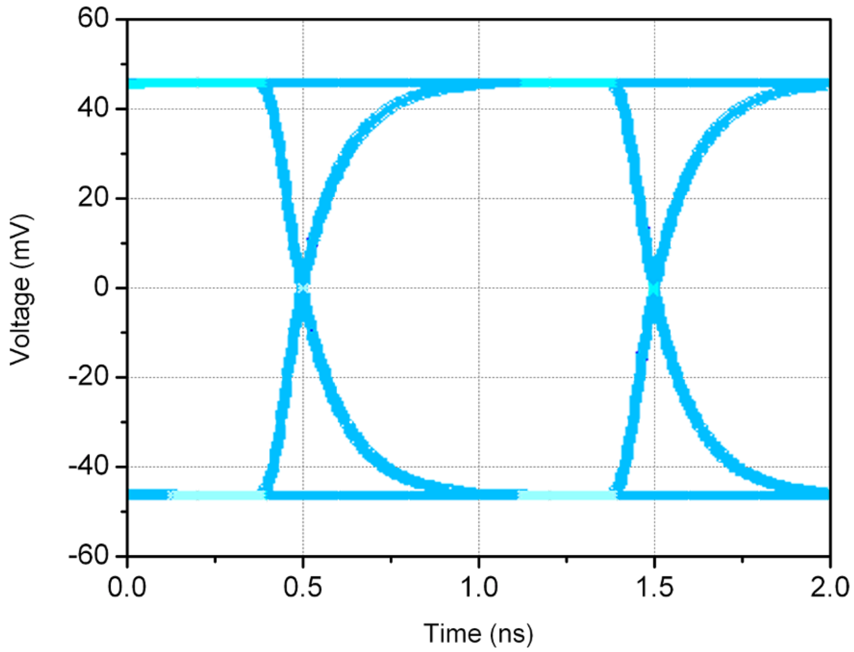

Figure 5.12: Simulation of eye diagram of the $In_{0.49}Ga_{0.51}P/GaAs$ DHBT ($16\times20\ \mu m^2$) with 1Gbps input signal

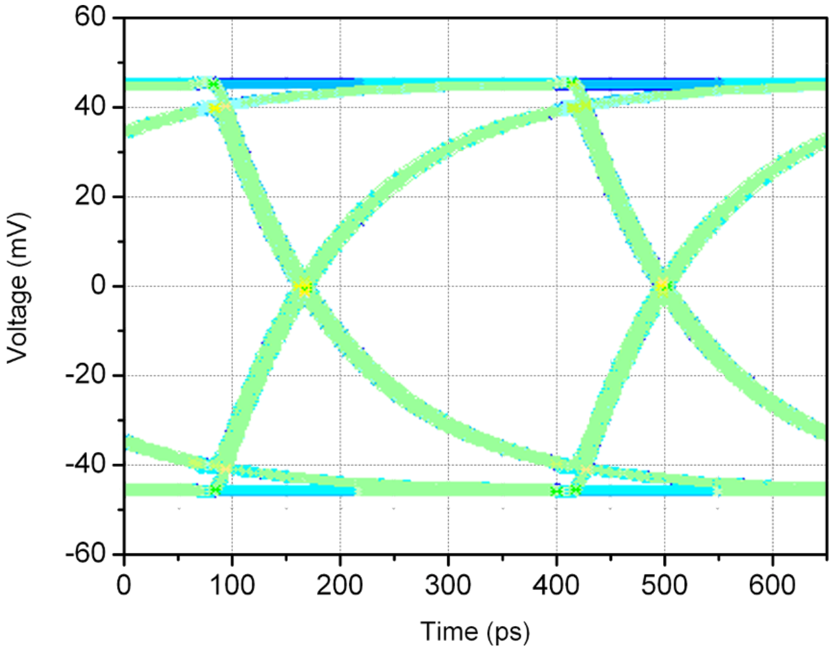

Figure 5.13: Simulation of eye diagram of the $In_{0.49}Ga_{0.51}P/GaAs$ s DHBT (16×20 μm^2) with 3Gbps input signal

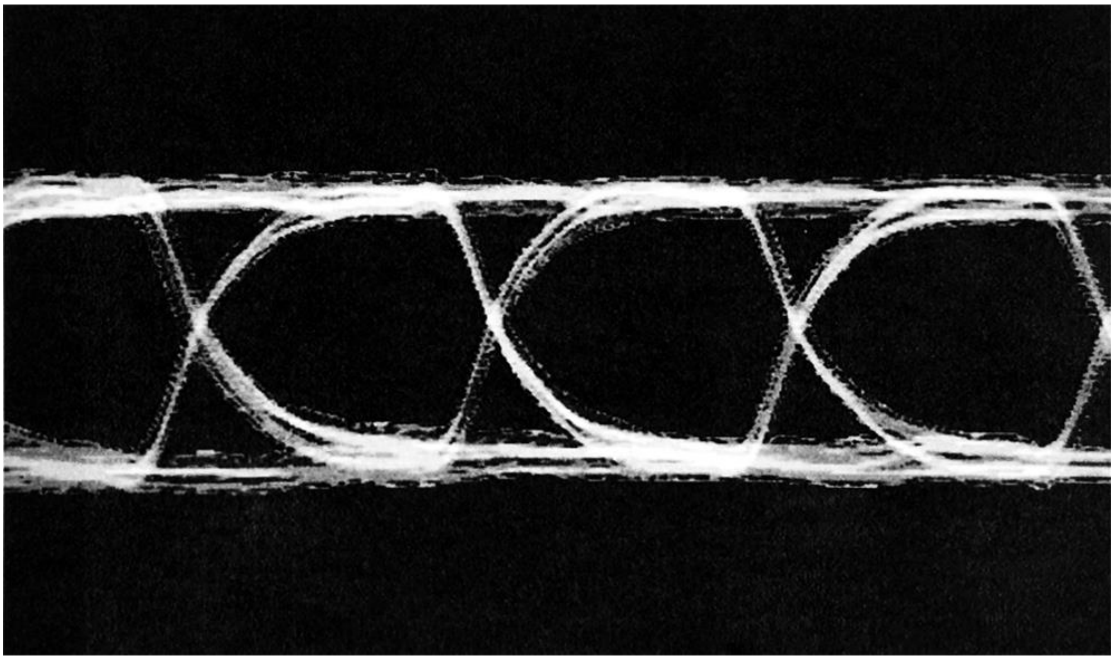

Horizontal Scale: 0.5Gbps
Vertical Scale: -200mV to 200mV

Figure 5.14: Snapshot of measured eye diagram of the $In_{0.49}Ga_{0.51}P/GaAs$ DHBT (16×20 μm^2, V_{BE} = 1.5V, V_{CE} = 3V, I_c = 21mA) at 1Gbps input signal [4]

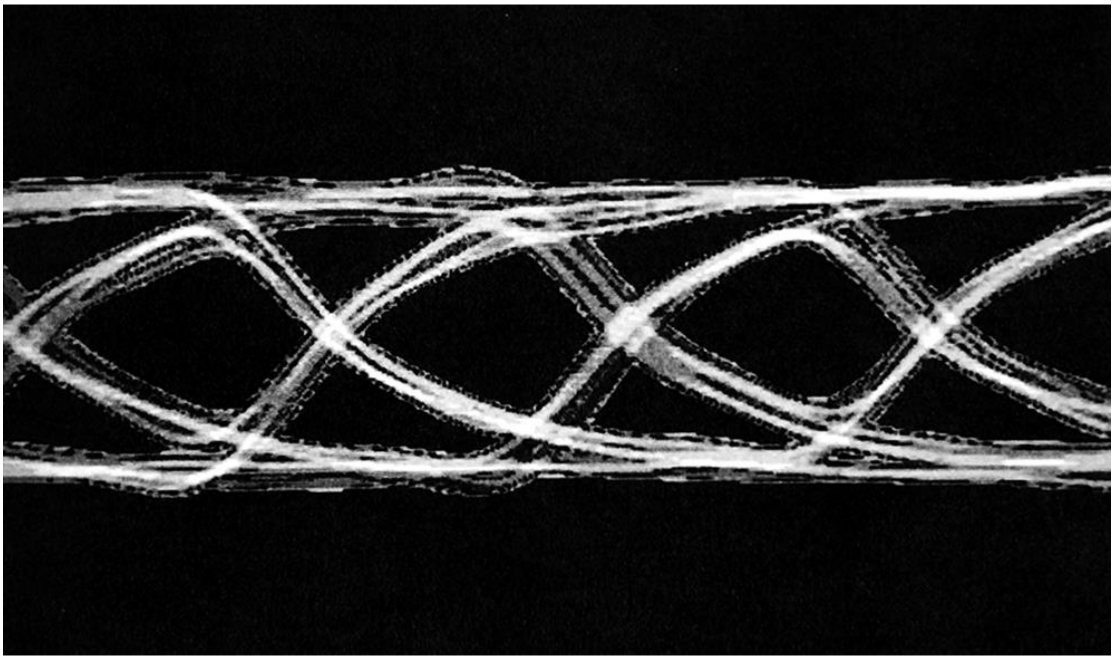

Horizontal Scale: 3Gbps
Vertical Scale: -200mV to 200mV

Figure 5.15: Snapshot of measured eye diagram of the $In_{0.49}Ga_{0.51}P/GaAs$ DHBT ($16\times20\ \mu m^2$, V_{BE} = 1.5V, V_{CE} = 3V, I_c = 21mA) at 3Gbps input signal [4]

Figures 5.12 and 5.13 show the simulated eye diagram of the $In_{0.49}Ga_{0.51}P/GaAs$ DHBT at 1Gbps and 3Gbps, respectively. Accordingly, the measured results [4] are shown in figures 5.14 and 5.15, and these can be used to verify the simulation data. The different eye parameters were measured and analysed at varying bitrate. Both in simulation and measurement, DC bias is set at V_{be} = 1.5V, V_{ce} = 3V and I_c = 20mA. The device was given a small signal PRBS RF signal of 25mV$_{PP}$. Such an input level can ensure that the device works in the linear region of operation. The bitrate was varied between 0.5Gbps and 3Gbps and the amplitude of the signal maintained at 25mV$_{pp}$ throughout the experiment. An Infiniium oscilloscope 54854A was used to observe the output [18].

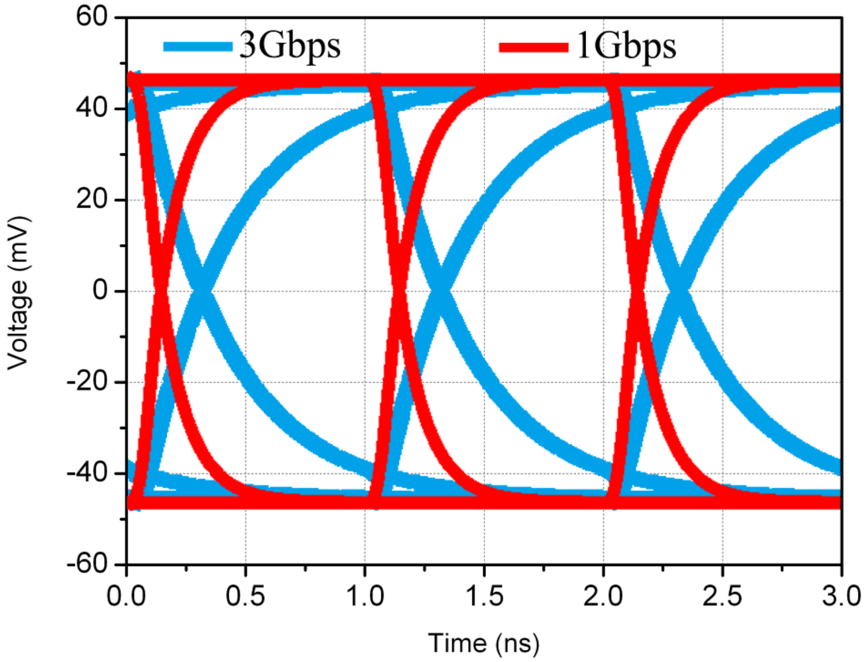

Figure 5.16: Simulated eye diagram response of the $In_{0.49}Ga_{0.51}P/GaAs$ DHBT ($16\times20\ \mu m^2$) at 1Gbps and 3Gbps

It is visible, from both the simulation and the measurements, that although the DUT was kept functional under the two bitrates (figure 5.16), eye quality did deteriorate at 3Gbps. For device design optimisation, the analysis of the eye diagram parameters and subsequent relating of these to the devices' small signal parameters is necessary.

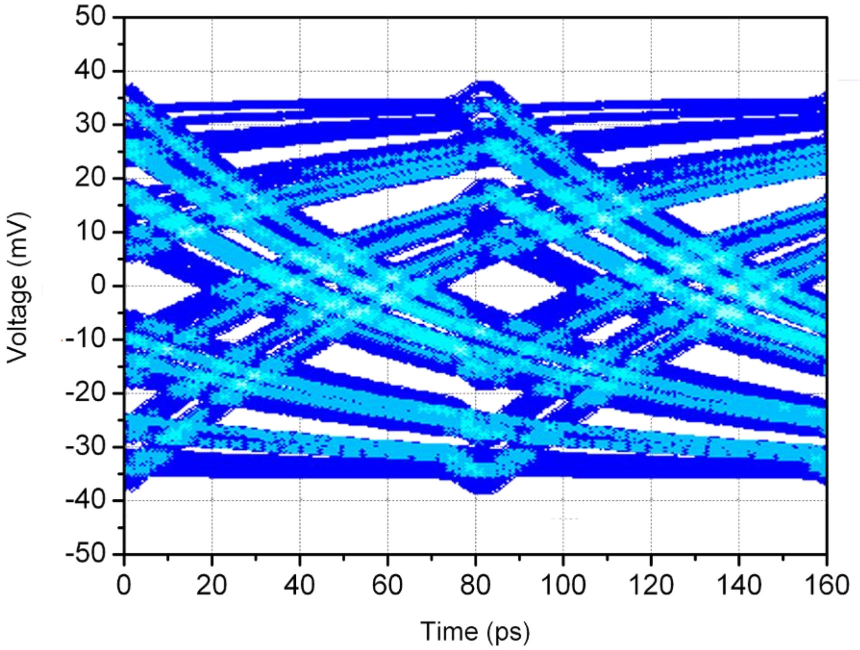

Figure 5.17: Simulation of eye diagram of $In_{0.49}Ga_{0.51}P/GaAs$ DHBT ($16\times20\ \mu m^2$) with 10.1Gbps input signal

When the device works up to half of cut-off frequency (10.1Gbps correspond to 5.05GHz), almost total eye closure is shown (figure 5.17), which means that at such a high input bitrate, the device cannot remain functional. From the application point of view, such a high speed is beyond the device's capability, and should be avoided. This diagram provides valuable information for circuit designers, assisting them in the proper use of the device to optimise the whole circuit performance.

There are two imperative eye parameters that now need to be discussed. Eye amplitude is defined as the difference between one and zero levels histogram mean value of all the data samples [18]. It represents all information that a signal is carrying, which accounts for noise. The second parameter is at eye height and defined as the vertical opening of the eye pattern, however, it is different from the eye amplitude. Since the former depicts the actual output, which is unaffected by any voltage or noise error, the height is more dependent on the noise or any other distortion in the data signal [19].

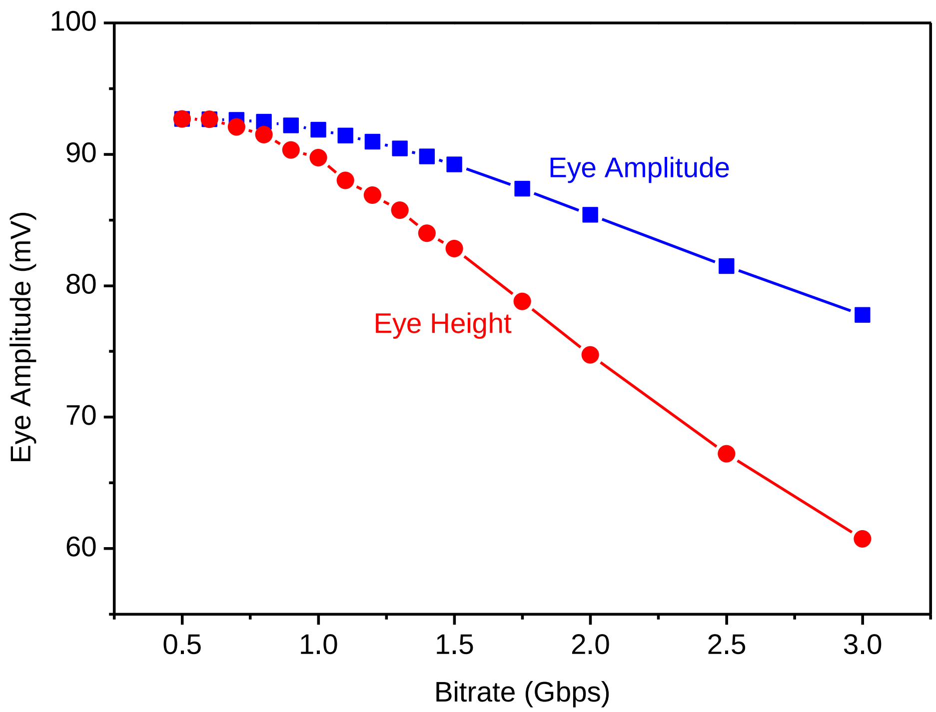

Figure 5.18: Simulated eye amplitude and eye height versus bitrate for the $In_{0.49}Ga_{0.51}P/GaAs$ ($16\times20\ \mu m^2$) DHPT

In figure 5.18, it is noticeable that both eye amplitude and eye height reduce with the increase in bitrate. This is explainable, as since the bitrate increases, the device gain reduces. It can easily be seen in the S_{21} of the device. Both in the eye amplitude and eye height, the reduce rates appear to reach maximum around 2Gbps which is just around the -3dB bandwidth frequency (1.1GHz correspond to 2.2Gbps). This indicates that the -3dB bandwidth frequency plays a key role in device optimisation, like setting up the voltage threshold levels at the receiver end. Furthermore, it is seen that the decline rate of the eye height is faster than the eye amplitude, due to generating a noisier signal at the high input data rate. This information cannot be easily explained just by pointing to the decline of the device gain, as above. It is worth identifying which specific small signal parameters are most affected.

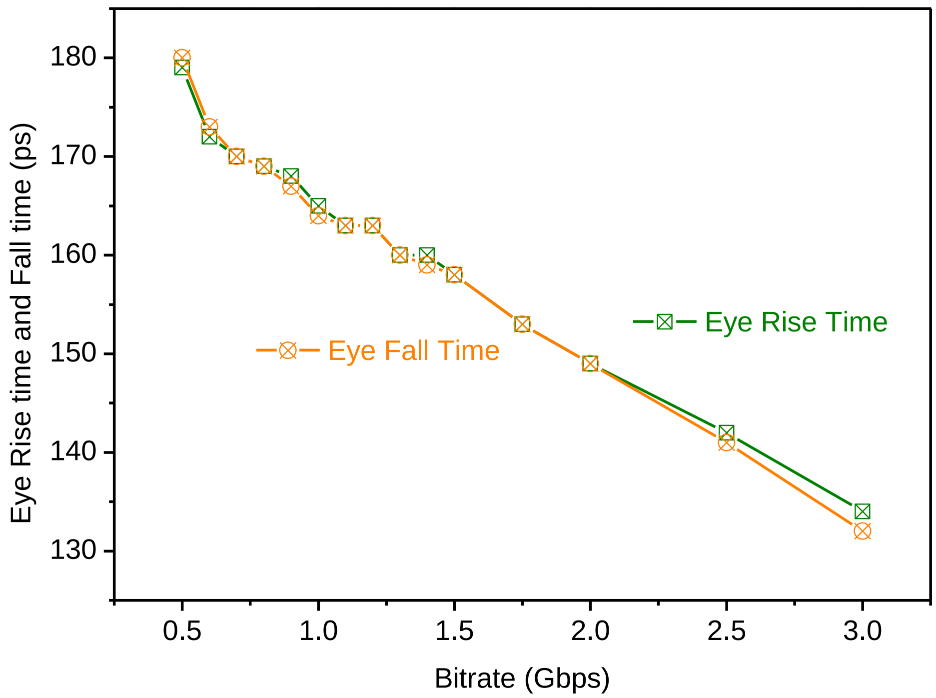

Figure 5.19: Simulated eye rise and fall time versus bitrate for the $In_{0.49}Ga_{0.51}P/GaAs$ ($16\times20\ \mu m^2$) DHPT

Eye rise and fall time reduce fairly linearly with the bitrate increase. This is mainly due to the reduction of time in signal pulse duration. It means that here these two eye parameters cannot show the frequency dependent deterioration of the signals clearly.

The eye diagram can also give information on the signal to noise ratio (SNR) in figure 5.20. It is defined as:

$$SNR = 20 \cdot \log\left(\frac{Amp_{signal}}{Amp_{noise}}\right) \tag{5.4.1}$$

where *Amp* is the root mean square (RMS) amplitude of signal and noise level measured at the same or equivalent points in a system [18]. A reduction of SNR at higher data rate is expected due to lower current gain and more random noise. It seems to prove our deduction for faster reduction of eye height in figure 5.18

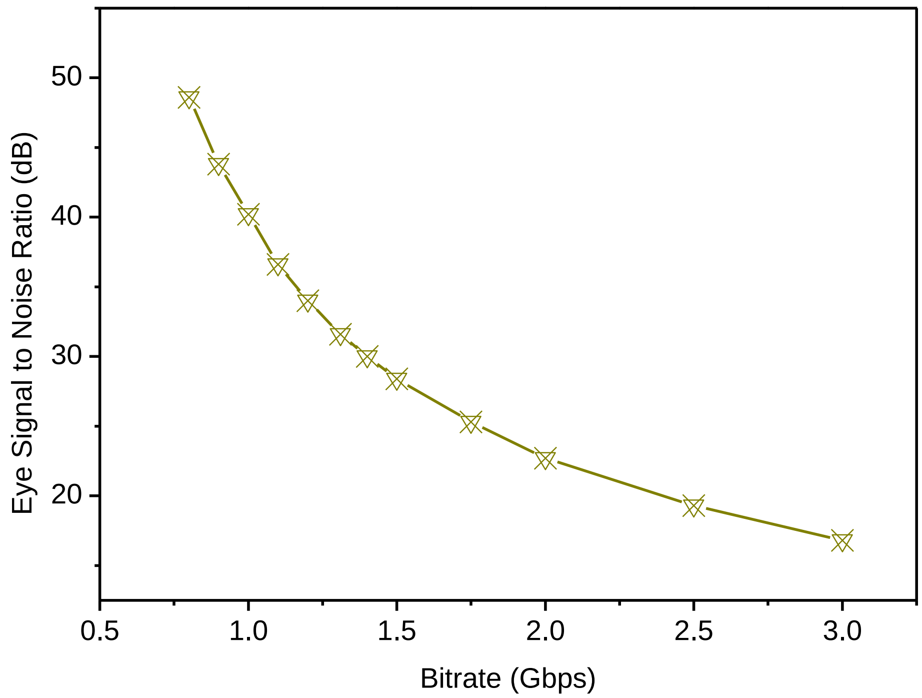

Figure 5.20: Simulated eye signal to noise ratio versus bitrate for the $In_{0.49}Ga_{0.51}P/GaAs$ ($16\times20\ \mu m^2$) DHPT

5.5 Relating eye parameters to the bias dependent device parameters

Eye diagrams reflect the behaviour of the DUT in relation to a digital input signal. The quality of eye diagrams is influenced by minute deviations in device parameters. The degradation of the eye parameters with the bitrate seen in the above section can be related to the characteristics of the DUT. Utilising the simulation, one can isolate the effects of individual small signal parameters, and subsequently investigate how each of the transistor parameters modify the eye pattern. Since some small signal parameters show bias dependent property, this feature of small signal parameters enables us to utilise eye parameter analysis to investigate the bias effect and help us optimise the biasing conditions.

The eye parameters variations with bitrate discussed in the last section can be addressed by studying the variation of base transport factor *α(ω)*. The extracted frequency dependence of the parameter |*α(ω)*| from the $In_{0.49}Ga_{0.51}P$/GaAs DHPT measurements are shown in figure 4.2.21 [11, 14].

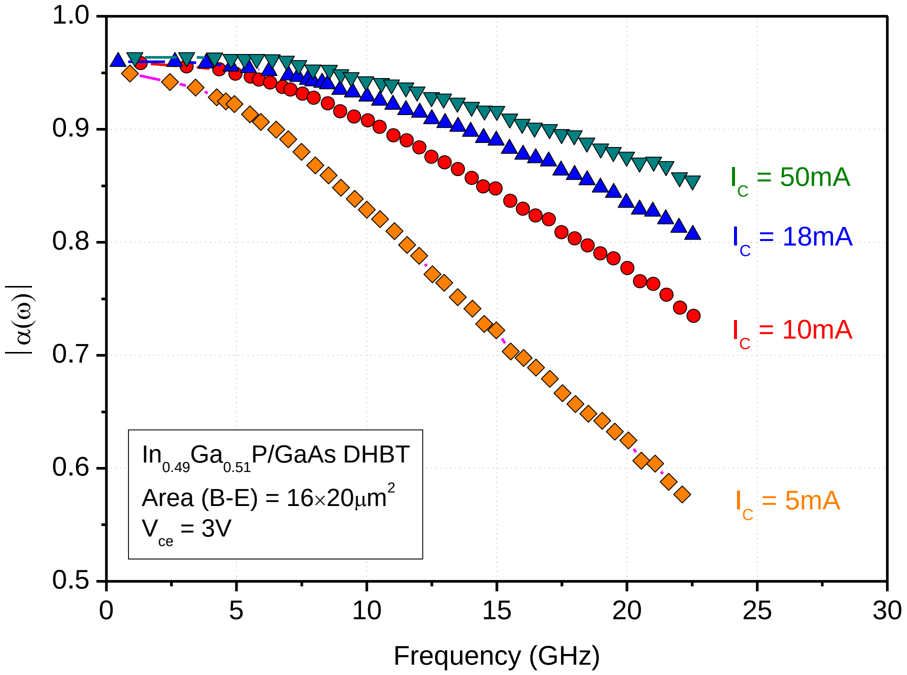

Figure 5.21: Measured variation of |*α(ω)*| *with frequency under various* I_C *and constant* V_{CE} *= 3V of* $In_{0.49}Ga_{0.51}P$*/GaAs (16×20 μm*^{2}*) DHPT [11, 14]*

Figure 5.21 shows that $\alpha(\omega)$ is frequency dependent as well as current bias dependency. The decrease of $\alpha(\omega)$ over frequency can be attributed to the dominating effect of recombination as the frequency increases. At high frequencies the injected minority carriers (electrons here, since npn device) from the emitter into the base are modulated fast. This rapid modulation leads to a recombination increase which causes $\alpha(\omega)$ decrease [18].

The increase of $\alpha(\omega)$ with higher bias current can be attributed to the enlargement of the emitter minority carriers' (electrons) injection rate. Higher bias current enlarges the B-E forward bias voltage which has an exponential relationship with current flowing through the device. The increased emitter carriers' injection rate (electrons) further increases the base transport factor $\alpha(\omega)$ as clearly seen in figure 5.21. Also this can be simply explained where the higher current bias pushes the common emitter current gain $\beta(\omega)$ to a higher current level.

$$\beta(\omega) = \frac{\alpha(\omega)}{1-\alpha(\omega)} \tag{5.5.1}$$

$\alpha(\omega)$ is a very sensitive parameter a small change in its magnitude would have a large change in the magnitude of the common emitter current gain $\beta(\omega)$.

Since $\alpha(\omega)$ is frequency dependent parameter, it is very difficult to analyse the individual effect of only $\alpha(\omega)$ on eye parameters. For a better understanding of the influence of small signal parameters on the eye diagram, here we fixed the input signal bitrate at 1Gbps but varied other bias dependent small signal parameters over a range of values to carry out simulation. Then the effects of these parameters on the eye parameters can be studied.

The first parameter to be considered for analysis is α_0 (DC common base current gain). The base transport factor $\alpha(\omega)$ in a small signal model can be represented by [14]:

$$\alpha(\omega) = \frac{\alpha_0 \exp(-j\omega(1-m)\tau_b + \tau_c)}{1 + j\omega C_{be} R_{be}} \cdot \frac{\sin(\omega\tau_c)}{\omega\tau_c} \quad (5.5.2)$$

where τ_b and τ_c are base and collector transit times, respectively, m is the grading factor.

It is seen in the equation (5.5.2) that DC common base current gain α_0 directly decides the value of $\alpha(\omega)$. At a certain frequency, α_0 is a bias dependent small signal parameter. For the purpose of this analysis, a very small variation in α_0, between 0.98 and 0.94, is chosen for the simulation purposes. During the simulation, all the other small signal parameters are maintained constant in order to isolate the effect of α_0 on eye parameters. Therefore when one changes the magnitude of α_0 in the ADS simulator one can determine various eye parameters, for example in figure 5.22 two vital eye parameters are affected, which are eye amplitude and eye height.

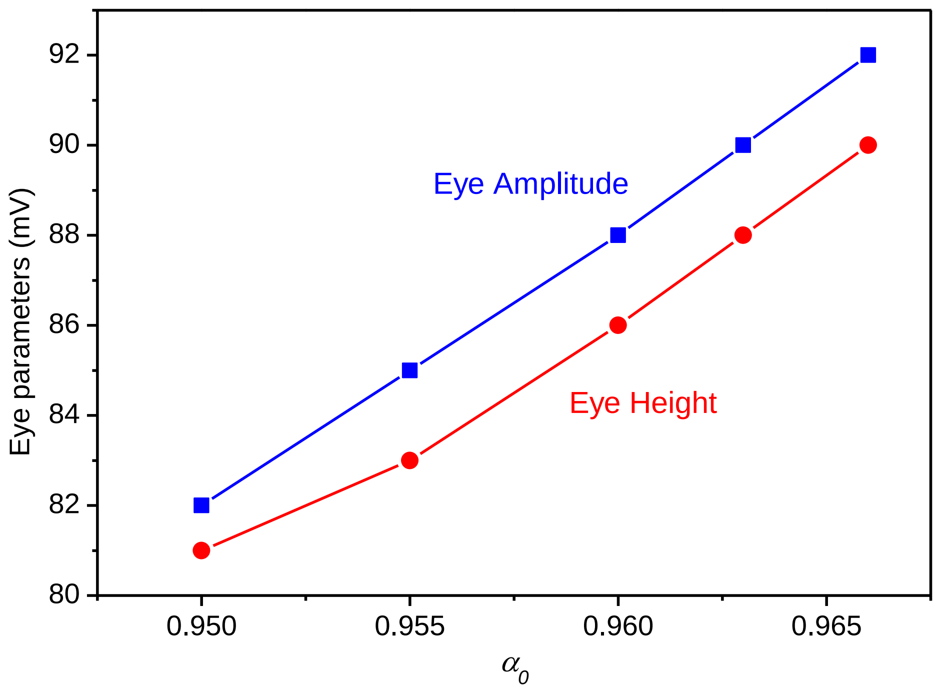

Figure 5.22: Simulated eye parameters for the $In_{0.49}Ga_{0.51}P/GaAs$ (16×20 μm^2) DHPT with the common base current gain α_0 at 1Gbps

Figure 5.22 sees a minute increase in the α_0 which increases both eye height and eye amplitude. This is justified because eye amplitude and height mainly depend on the common emitter, β and common base current gains α of the device [4]. Also, it is noticeable that for both eye height and eye amplitude, the increase rate is relatively similar. This confirms that simply the increasing α_0 would not degrade the signal by introducing more noise into the device.

From a small signal point of view, intrinsic base-collector capacitance C_{bci} describes the region of the B-C junction with current flowing through it, while extrinsic base-collector capacitance C_{bcx} describes the region without significant current flowing [11]. So the injection of electrons results in the current dependent phenomena occurring in the intrinsic part of the device only. The extrinsic base-collector capacitance C_{bcx} is expected to stay constant; as a result of the variations of base-collector capacitance C_{bc} mainly comes from C_{bci} [20-21]. Figure 5.23 shows the extracted $In_{0.49}Ga_{0.51}P$/GaAs DHBT C_{bc} versus I_C plots for I_B feed from 0 to 2.2mA and V_{CE} keeping constant at 2.8 and 3.2V, respectively. Similar behaviour is noticed for both 2.8 and 3.2 bias conditions. With the initial reduction of I_C (equivalently known as I_B bias current), C_{bc} then suddenly increases after a certain I_C (I_B) current level.

As we know, in order to keep the value of base-collector capacitance low and to increase breakdown voltage, it is usual for low doping levels to be chosen by collectors of HBTs. This brings drawbacks, however, as, even at low current density levels, high current injection phenomena occur. As I_C (I_B) increases, more electrons are injected into the base-collector depletion region. The total space charge density is reduced by the injection. Since the total space charge of the base-collector depletion region is decided by reverse bias across the junction. In order to compensate for the reduction of space charge density, a broader depletion region is required in order to keep the fixed total space charge. This wider depletion region results in the reduction in depletion capacitance, which is C_{bc}. With increasing current level, the base-collector space charge region keeps widening, until the whole collector is fully depleted. Then the depletion region stops to increase at the interface of the InGaP collector and the GaAs sub-collector. Now the electron concentration in fully depleted collector is comparable to the doping concentration [22]. As shown in figure 5.23, this is noticed in the middle region of the collector current level, although C_{bc} still decreases with I_C increasing, a much weaker dependence is observed. In summary, the reduction of collector-base capacitance with current I_C (I_B) is attributed to the current-induced broadening of the base-collector depletion layer [11].

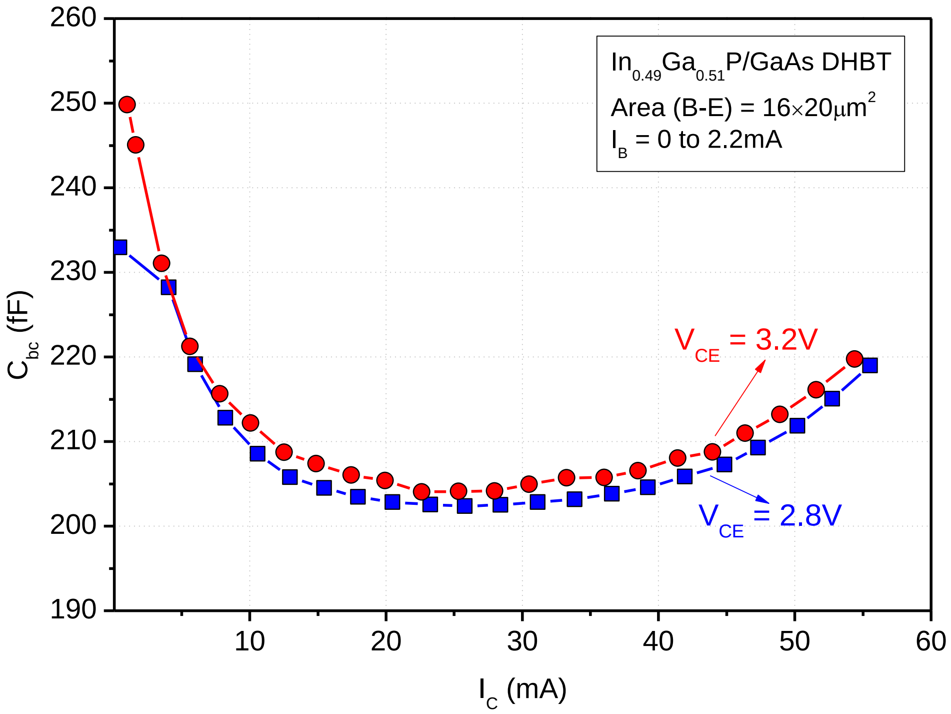

Figure: 5.23: Extracted measurement of C_{bc} versus collector current for the $In_{0.49}Ga_{0.51}P/GaAs$ (16×20 μm²) DHPT at V_{CE} = 3.2V and 2.8V with I_B feed from 0 to 2.2mA [11]

As shown in figure 5.23, after I_C (I_B) is beyond a certain critical current value, the magnitude of the electric field at the base edge of the junction continues to decrease and may even become zero [23]. In order to maintain a constant voltage across the base-collector junction, the base majority carriers spill over into part of the collector; this is known as base push-out, so that the field there remains zero to prevent the field from becoming positive [11]. After that, continuing the increased bias current, base push-out reduces the size of the base-collector depletion region, resulting in a sudden increase in base-collector capacitance.

In the ADS simulator one can study the effects of C_{bc} on the eye parameters. An example is given in figure 5.24

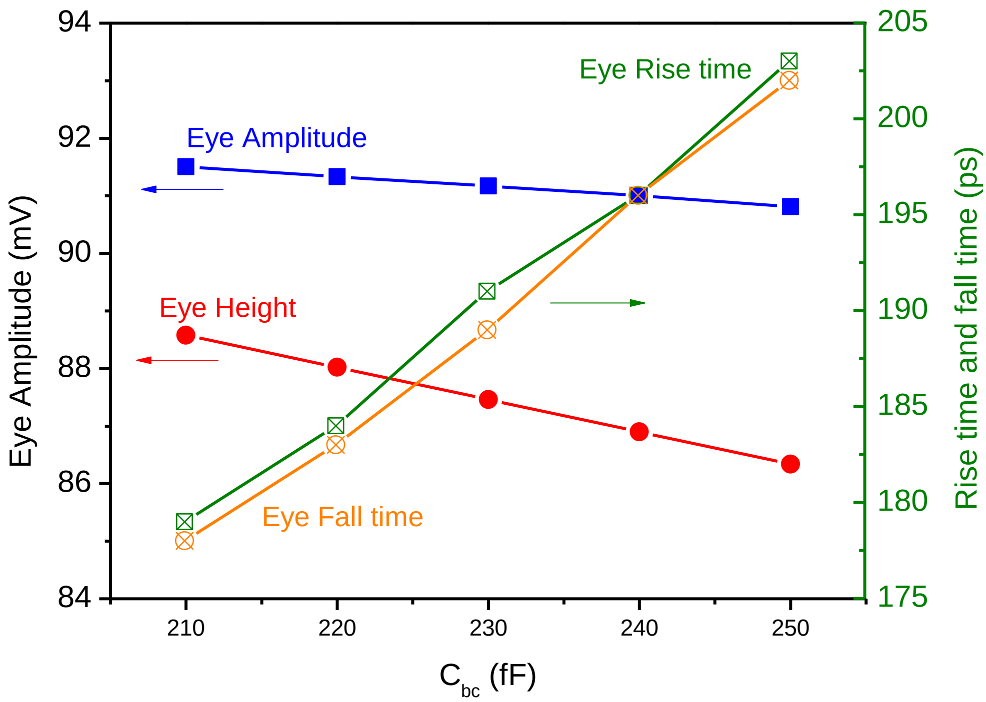

Figure 5.24: Simulated eye parameters with base emitter capacitance variations at 1Gbps for the $In_{0.49}Ga_{0.51}P/GaAs$ (16×20 μm^2) DHPT

Figure 5.24 shows the extracted eye parameters over varying C_{bc} for the device under test. C_{bc} was varied between 210fF to 250fF, which is the range of extracted values from the measurements in figure 5.23. During the simulation, the varying AC signal with magnitude 25mV is sufficient to change the charge density at the outer edges of the depletion region [4], where mobile charge carriers reside, leading to a change in depletion region width [24].

It is noticed that an increase in C_{bc} gives a negative influence on all eye parameters in figure 5.24, which results in undesired eye closure. The effect can be explained as the base-collector capacitance variation modulating charging times as reported in [3]. This influences the RF behaviour and especially has a negative impact on linearity [25]. The increase in eye rise and fall time clearly shows the effect of the charging times increase. Using equation [32]:

$$\tau_{rc} = \left(R_{be} + R_{cc} + R_{ee}\right) C_{bc} \tag{5.5.3}$$

The influences of C_{bc} variation on charging time can be calculated in a straight-forward manner; again, from the SNR point of view, figure 5.25, can be used to explain the deterioration of eye parameters.

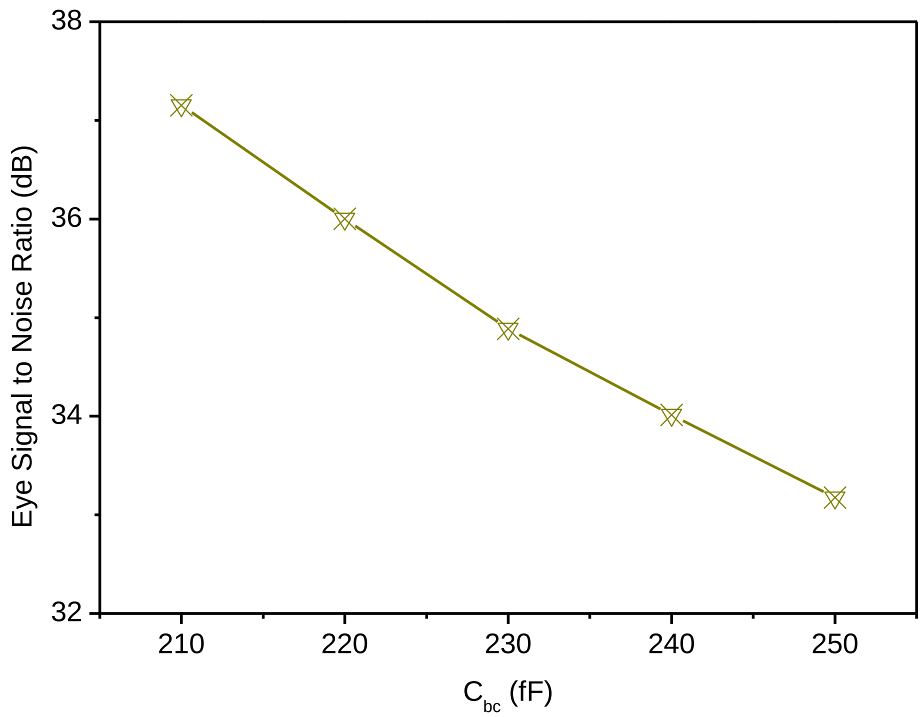

Figure 5.25: Simulated eye signal to noise ratio with base emitter capacitance variations at 1Gbps for the $In_{0.49}Ga_{0.51}P/GaAs$ (16×20 μm^2) DHPT

The above discussion implies that bias dependent small signal parameters can significantly affect the eye opening. This kind of study offers extra information which is a step forward for designers aiming to obtain the desired circuit bias point. Such a prior estimation of eye characteristics of discrete components is very valuable in circuit design and optimisation.

5.6 Optical effect of $In_{0.49}Ga_{0.51}P/GaAs$ DHBT on eye diagram

In this section, GaAs-based double heterojunction phototransistors (DHPTs) in surface-illuminated orientation have been analysed with a modified small-signal model using an eye diagram. Since the primary detecting material is GaAs, the device is optimised to detect short wavelengths (850nm). The DUT works as a short wavelength photodetector, while the photo-absorption in the base region influences associated intrinsic elements that can further affect the eye diagrams. From an optical point of view, a detailed analysis is necessary. The effect of incident optical illumination on various intrinsic parameters has already been discussed for $In_{0.49}Ga_{0.51}P/GaAs$ $16\times20\mu m^2$ DHPT.

The analysis of DHPTs presented in this work can be utilised for performance enhancement through device optimisation in sensors, photoreceivers in optical networks and remote sensing applications employing integrated circuits. Parameter evolution in the design of optical receivers can have a contradictory effect on various figures of merit for HPTs. For example, improved cut-off frequency, due to a reduced absorbing layer width for surface illuminated HPTs, can be accompanied by lower conversion or collection efficiency, resulting in low responsivity. In order to achieve efficient photoresponse and high speed operation of these devices, a detailed analysis of the device's parameters is of paramount importance. As we know, the photoresponse for SHPTs has been widely discussed in the literature [14-15, 26-28], however, research on DHPTs remains rather limited.

It is reported [29-30], as figure 5.26 and table 5.2 show, that photo-generated carriers can affect certain inherent parameters for optical devices. So a careful analysis of these optical dependent parameters is vital for achieving optimal performance.

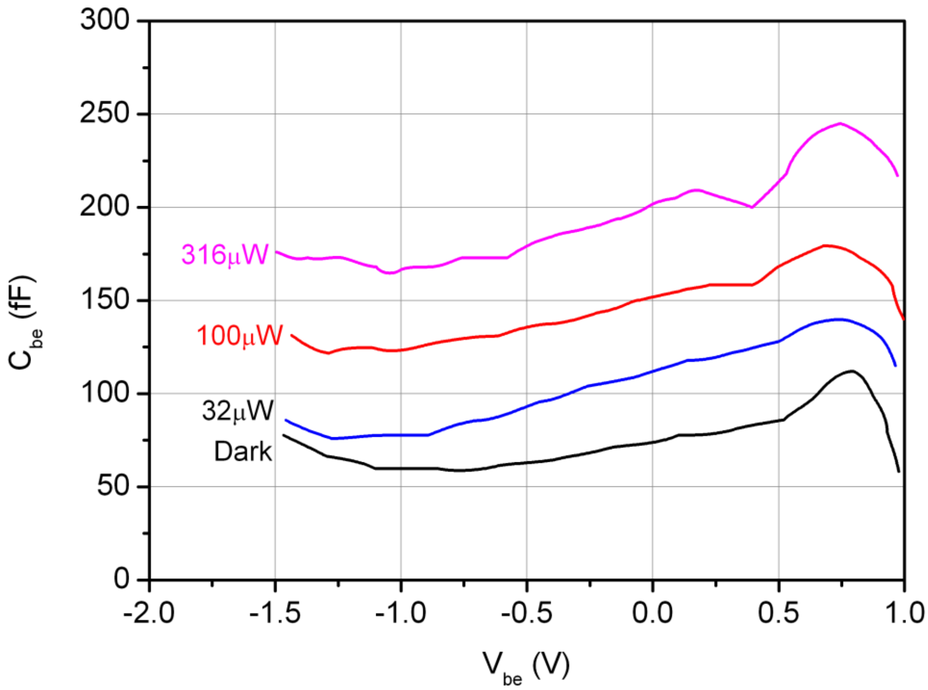

Figure 5.26: CV characteristics of the illuminated base-emitter junction [29]

Table 5.2: Optical power dependencies of AC small-signal model parameters biased at I_B = 100μA and V_{CE} = 1.0V [30]

	Dark	**63μW**	**159μW**	**316μW**	**631μW**
R_{BB} (Ω)	350	315	290	262	225
R_{BE} (Ω)	475	434	388	320	103
R_O (Ω)	7.5 K	5.3 K	4.4 K	2.2 K	1.6 K
C_{BE} (fF)	212	261	303	375	953
C_{BC_int} (fF)	5.3	6.15	6.8	7	9.1

In order to relate the eye diagram to the device's optical performance, we have investigated several analyses, and have found that the optical signal propagation through the base of the DHPT device towards the collector and the sub-collector regions will mainly affect the associated intrinsic capacitance and resistances. These two parameters, namely the device's intrinsic B-E resistance (R_{be}), and capacitance (C_{be}), are studied here.

Variations in the optical signal will modify the intrinsic elements of the device which, in turn, will affect the photoresponse. Since the collector of the device is $In_{0.49}Ga_{0.51}P$, which is largely transparent to an incoming optical signal of 850 nm, the B-C resistances and capacitances will remain unaffected [31]. However, B-E resistance and capacitance will nevertheless be affected with the change in optical intensity, which may affect the photoresponse and result in cut-off frequency variation for the device. R_{be} is related to the photo-generated current, I_{ph}.

$$R_{be} = \frac{\text{Thermal voltage}}{\text{Current flowing through B-E junction}} \tag{5.6.1}$$

The thermal voltage is kT/q. When the device is under optical illumination the current flowing through B-E junction is equal to photo-generated current which is amplified by the device current gain β, ie βI_{ph}. The photo-generated current can be written as unit charge (q) multiplied by incident photon numbers ($P_{in}/h\nu$). Here it is assumed all incident photons are absorbed by the device. Then $I_{ph} = q \cdot P_{in}/h\nu \cdot \eta$. The B-E resistance R_{be} can be given as:

$$R_{be} = \frac{kTh\nu}{q^2 \beta \eta P_{in}} \tag{5.6.2}$$

where T is absolute temperature, k is Boltzmann constant, q is unit charge, h is Planck's constant, β is the current gain of the transistor and η is quantum efficiency defined by the ratio of incident photons to the converted electrons.

Similar to resistance, the C_{bc} will remain independent of incident optical signal at 850nm. However, C_{be} will be affected by the generation of photo-generated carriers in the base region because the base layer is made up of GaAs and is sensitive to 850nm radiation. Since the B-E junction is forward biased, diffusion capacitance dominates and will increase with the increase in incident signal intensity. This rise in capacitance lowers the photoresponse and output signal quality, since it increases the transistor junction charging time. The diffusion capacitance, C_{be} can be given by [32]:

$$C_{be} = \frac{I_E}{V_T} \cdot \tau_B \tag{5.6.3}$$

where I_E , V_T, τ_B are given as [32]:

$$I_E = A \cdot \frac{q\beta\eta P_{in}}{h\nu} \tag{5.6.4}$$

$$V_T = \frac{kT}{q} \tag{5.6.5}$$

$$\tau_B = \frac{L_n^{\ 2}}{D_n} \tag{5.6.6}$$

Insert equation (5.6.4), (5.6.5) and (5.6.6) into (5.6.3):

$$C_{be} = \frac{Aq^2 L_n^{\ 2} \beta\eta P_{in}}{kTD_n h\nu} \tag{5.6.7}$$

where D_n is the diffusion coefficient of the electrons.

We know that the intrinsic B-E resistance, R_{be}, will be lowered by the increase in the photo-generated carriers within the base region (R_{be} inversely proportional to P_{in}). Thus, the increase in the diffusion capacitance is accompanied by the reduction of intrinsic resistance. One can use the above equations (5.6.2) and (5.6.7) to plot figure 5.27. Resistance variation along with the capacitance variation with optical power is shown.

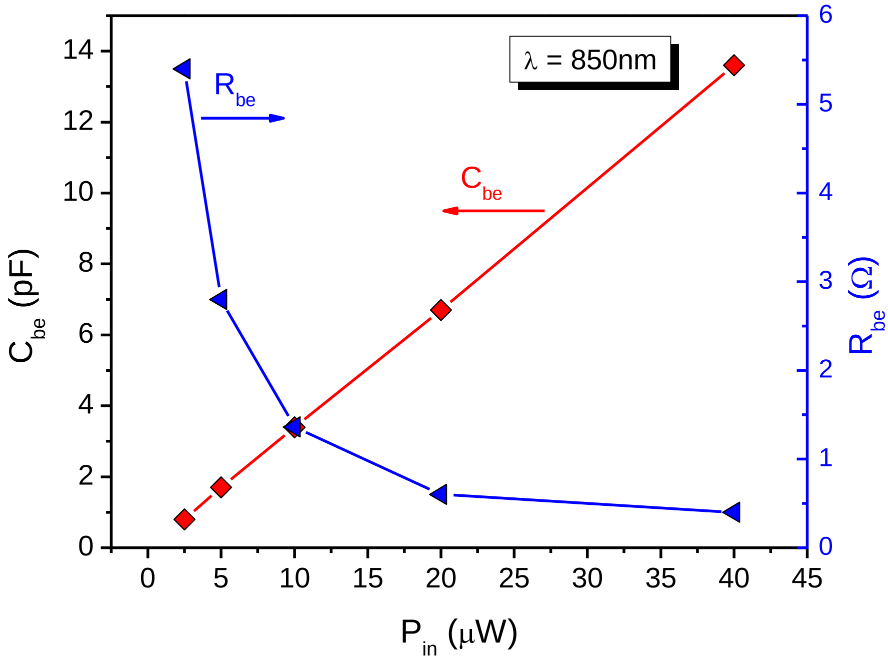

Figure 5.27: Simulated variation of base emitter diffusion capacitance with input optical power for the $In_{0.49}Ga_{0.51}P$/GaAs (16×20 μm^2) DHPT at 850 nm incident radiation

The photo-absorption in the $In_{0.49}Ga_{0.51}P$/GaAs/InGaP DHPT differs to that of the InGaP/GaAs/GaAs SHPT for 850nm as the base region (GaAs) primarily influences the device's response to optical illumination. The associated intrinsic capacitances and resistances change accordingly, and affect the device's characteristics. Therefore, a careful analysis of this phenomenon is important for determining the accurate DHPT photoresponse modelling and optimisation. To the best of the author's knowledge, this variation of intrinsic parameters with optical illumination using an eye diagram is discussed here for the first time.

A small-signal modelling for surface-illuminated HPTs is shown in figure 5.28.

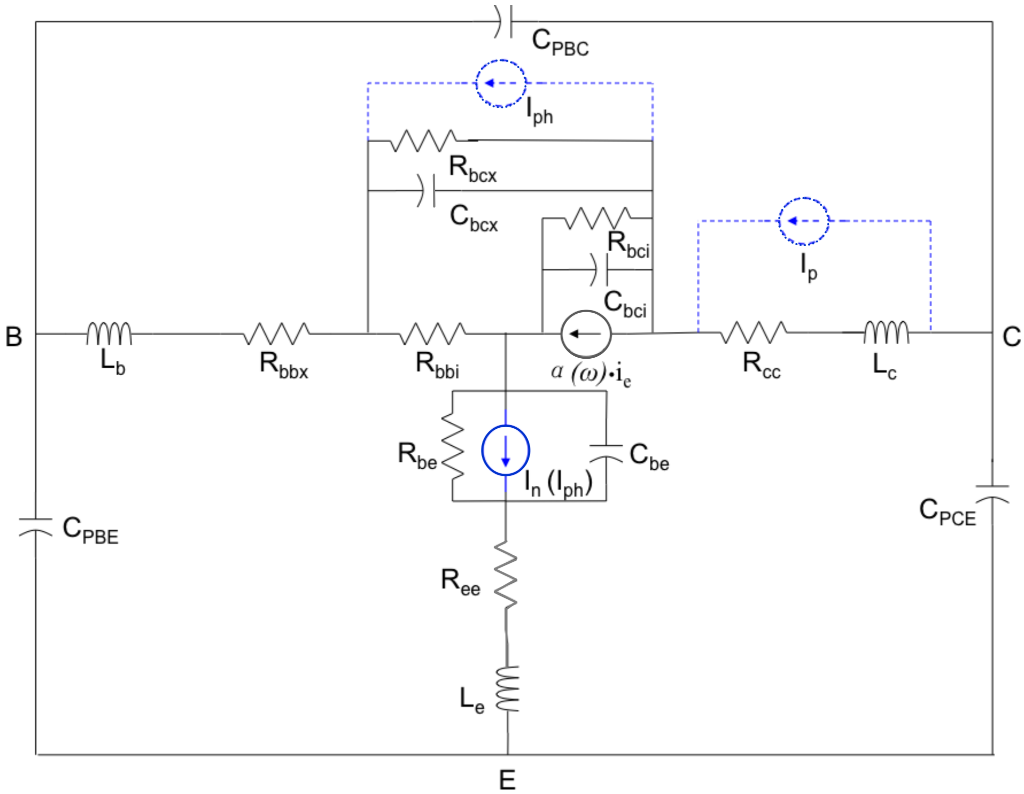

Figure 5.28: Small signal equivalent circuit of the $In_{0.49}Ga_{0.51}P/GaAs$ (16×20 μm^2 B-E) SHPTs with three optical current sources

A significant modification in small-signal modelling for surface-illuminated HPTs, compared to that of HBTs, is the introduction of optically-controlled current sources in the small signal equivalent circuit. In the SHPTs, as shown in figure 5.28, three photocurrent sources (I_c generated in the collector region, I_{ph} generated in the B-C depletion region and $I_{n(ph)}$ generated in the base region) are introduced, and all of them will affect the device's output.

In the DHPT, however, since the analysis is performed for a short wavelength (850 nm corresponding to 1.46eV), in the current device under investigation, the wide band gap $In_{0.49}Ga_{0.51}P$ (E_g = 1.9eV [33]) emitter and collector will be transparent as the incident signal goes through un-attenuated. The absorption only takes place at the GaAs base layer, represented by $I_n(I_{ph})$ in figure 5.29, and contributes towards the photoresponse. In addition, neither does the signal absorbed in the sub-collector region (GaAs) contribute towards transistor action (current gain). This is because, in principle, although the optical signal can propagate through the base and the collector of the device, and arrive at the sub-collector, the photo-generated holes in the sub-collector will not drift towards the base region due to the additional heterostructure (B-C) in the DHPT (figure 5.29).

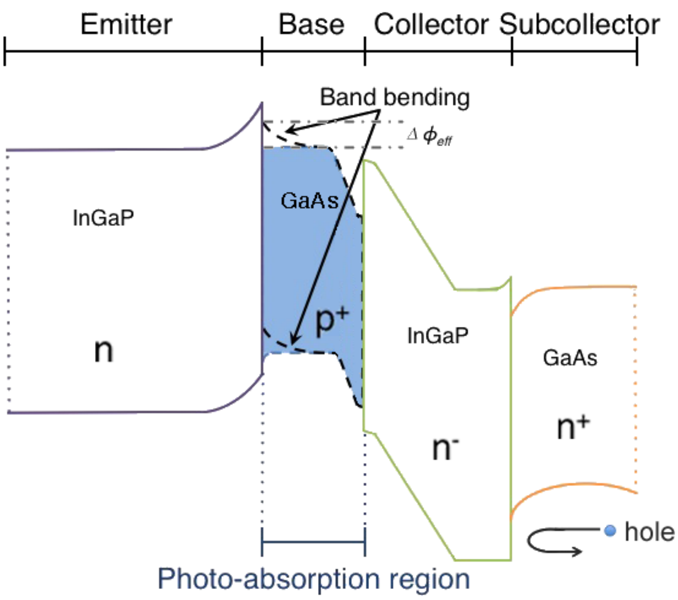

Figure 5.29: Band bending in the base region of the InGaP/GaAs DHPT

This additional heterojunction between the base and the collector blocks the photo-generated carriers in the sub-collector from drifting towards the base region, preventing frequency degradation of the device from these slow moving hole carriers. Finally, only the optical flux absorbed in the base region can contribute towards the photoresponse. Moreover, no flux is absorbed in the emitter or the collector, and therefore I_{ph} and I_c can be removed. As shown in figure 5.30, a small signal T-model of DHBT with only one additional optical generated current source is used in the simulation.

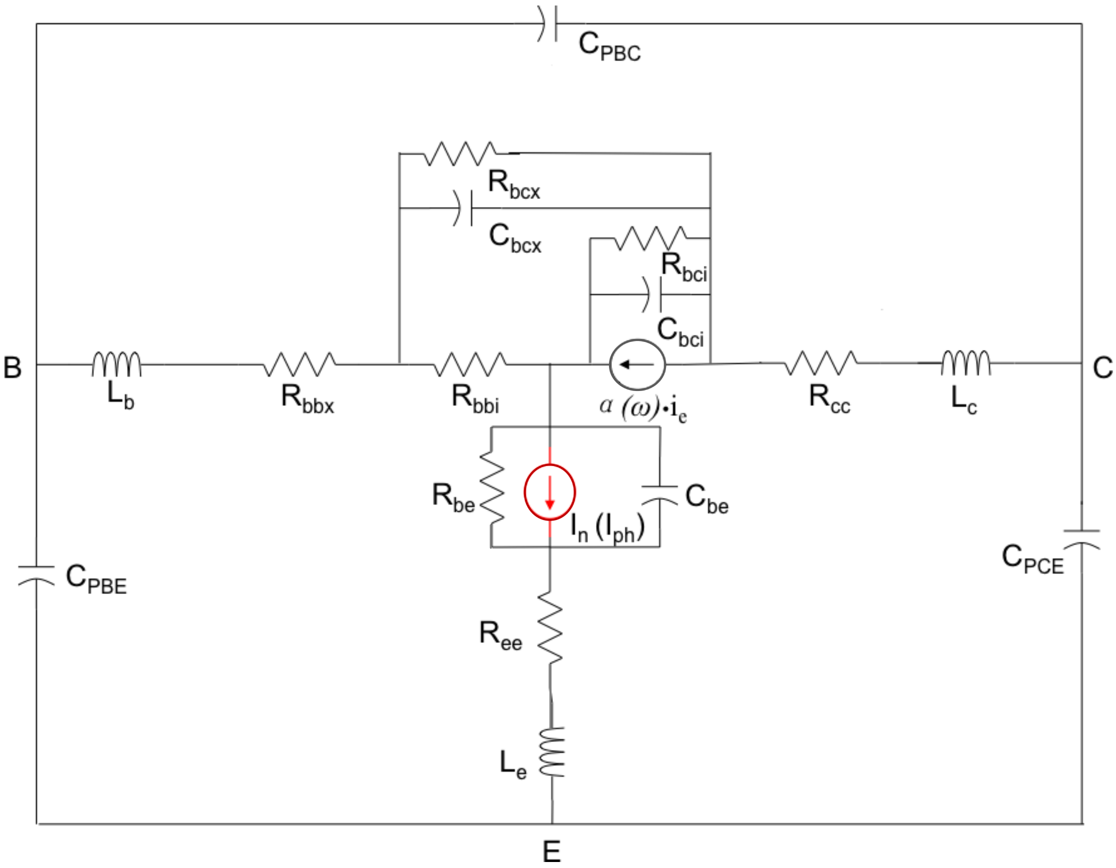

Figure 5.30: Small signal equivalent circuit of the $In_{0.49}Ga_{0.51}P/GaAs$ ($16\times20\ \mu m^2$) DHPTs with optical current source at 850 nm incident radiation

As shown in figure 5.27, the rise in optical incident power leads to an increase in diffusion capacitance, C_{be}. By changing the values of C_{be} according to figure 5.27, ADS simulation eye parameters are extracted.

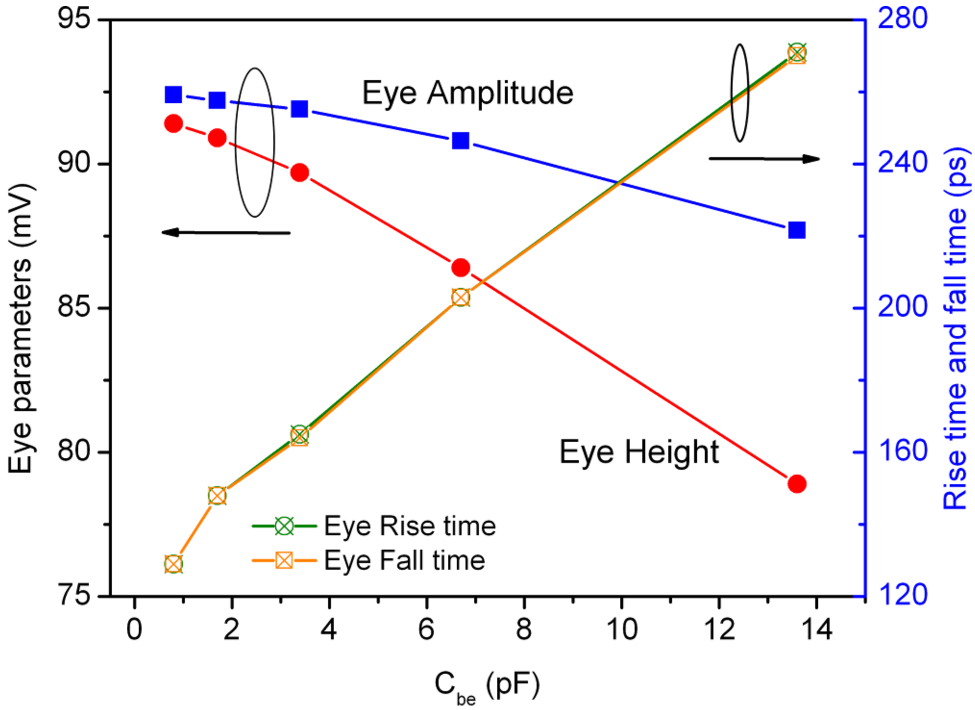

Figure 5.31: Simulated eye parameters with optical dependent base emitter capacitance variations at 1Gbps for the $In_{0.49}Ga_{0.51}P/GaAs$ (16×20 μm^2) DHPT

Figure 5.31 shows the simulation results of the capacitance variations as a reduction in eye amplitude and height. The eye height reduces faster than the eye amplitude, and this may be related to the generation of more noise in the device as the C_{be} increase. The effect of this increase also leads to an increase in device charging time as the result of an increase in the device's rise and fall times.

At the same input data rate (1Gbps), the influence of variation of R_{be} to the eye parameters can be seen in figure 5.32. Since R_{be} is inversely proportional to P_{in} (equation(5.6.2)), at higher P_{in} (i.e. higher I_{ph}) one can get better eye parameters. The eye parameters extracted from the eye diagram simulation in ADS are shown in figure 5.32.

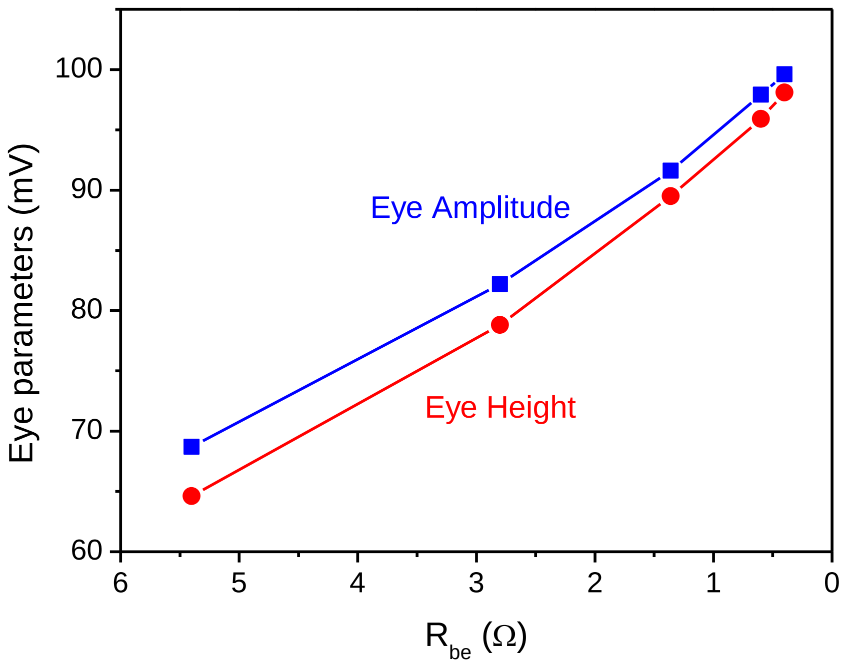

Figure 5.32: Simulated eye amplitude and eye height with optical dependent base emitter resistance variations at 1Gbps for the $In_{0.49}Ga_{0.51}P/GaAs$ (16×20 μm^2) DHPT

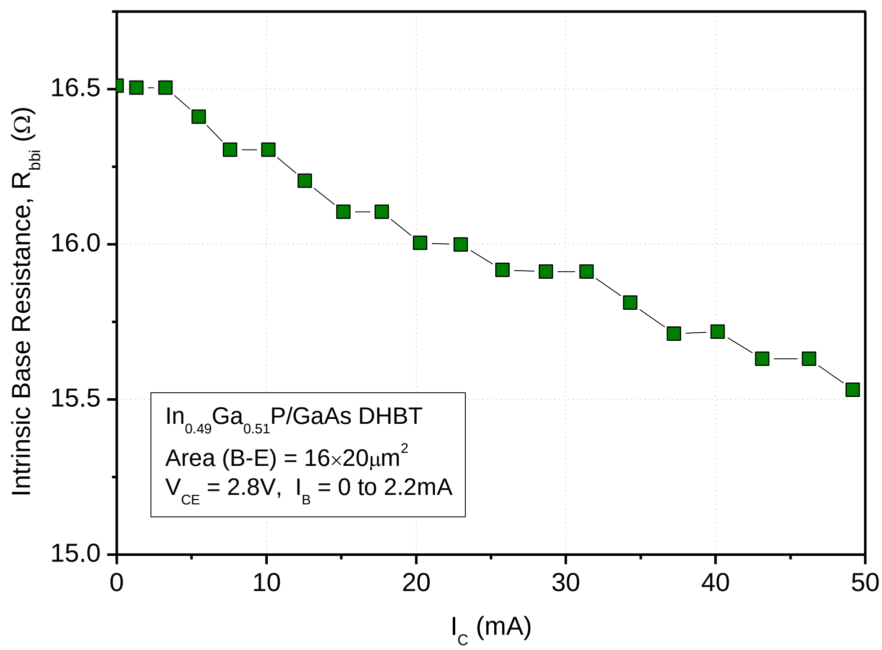

Figure 5.33: Extracted intrinsic base series resistance versus applied bias (optical base current) for the $In_{0.49}Ga_{0.51}P/GaAs$ (16×20 μm^2) DHPT (V_{CE} = 2.8V, I_B = 0 to 2mA) [11]

The optically generated carriers in the base modify its conductivity, and as a result, the intrinsic base resistance R_{bbi} is expected to be modified by emitter crowding. The extracted measurement value of $In_{0.49}Ga_{0.51}P/GaAs$ (16×20 μm^2) DHPT (V_{CE} = 2.8V, I_B = 0 to 2mA) is shown in figure 5.33 [11].

However, circuit simulation in ADS shows that at 1Gbps the variation of photoresponse is minimal with variations of R_{bbi} (figure 5.34).

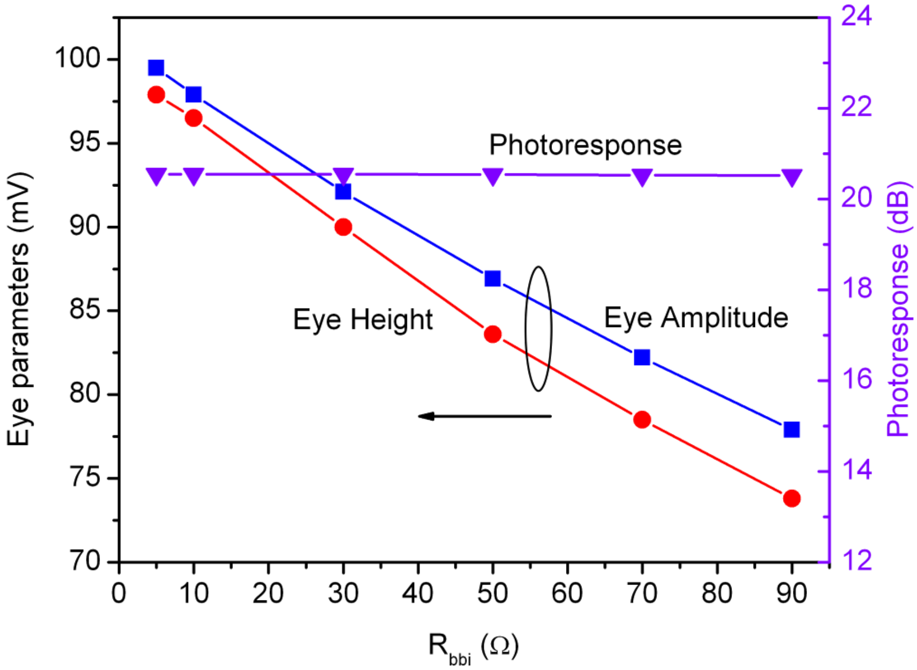

Figure 5.34: Simulated eye parameters with optical dependent intrinsic base series resistance variations at 1Gbps for the $In_{0.49}Ga_{0.51}P/GaAs$ (16×20 μm^2) DHPT

The photoresponse ranges from 20.4 dB to 20.5 dB with a wide range of R_{bbi} and therefore it can be inferred that any variation in R_{bbi} does not have any significant effect on the photoresponse. Thus this parameter is not so important in optical device design. However, using the eye diagram as a tool to analyse the performance of the device, a significant decline both in eye height and eye amplitude can be seen in figure 5.34, even for a data rate as low as 1Gbps. Eye parameters provide evidence of device deterioration with increasing R_{bbi} where other tools would fail, for example, photoresponse analysis. It is proved that through eye parameter analysis, the various physical parameters of the optical device can be redesigned and optimised, which provides valuable and insightful information for device optimisation in future high performance optical components.

5.7 Eye parameter comparisons between InGaP/GaAs SHBT and DHBT

In table 5.3 8×10 μm^2 InGaP/GaAs SHBT and DHBT device layer structures and doping profiles are shown. Both of the devices have similar emitter and base structures with 100nm $p^+ = 4\times10^{19}$ cm^{-3} GaAs, 0.5µm collector layer, and 0.7µm $n^+ = 4\times10^{18}$ cm^{-3} GaAs sub-collector. The only difference is the collector of the SHBT, which is simply $n^- = 1\times10^{16}$ cm^{-3} GaAs, while that of the DHBT is composed of a 20nm undoped GaAs spacer and 0.48µm wide bandgap InGaP to form a B-C heterojunction. As we know, DHBTs show many advantages, like smaller offset voltage, lower leakage current, larger breakdown voltage, which all benefited from the wideband gap heterostructure base-collector junction.

Table 5.3: Layer structure of InGaP/GaAs single and double HBTs (8×10 μm^2) used in simulation [34]

Layer	SHBT	DHBT
Cap Layer	30nm n^+-$In_{0.5}Ga_{0.5}As$ 5×10^{18} cm^{-3}	
	30nm n^+-$In_xGa_{1-x}As$ (x = 0 to 0.5) 5×10^{18} cm^{-3}	
	100nm n^+-GaAs 5×10^{18} cm^{-3}	
	30nm n^+-$In_{0.49}Ga_{0.51}P$ 2×10^{18} cm^{-3}	
Emitter	100nm n-$In_{0.49}Ga_{0.51}P$ 4×10^{17} cm^{-3}	
Base	80nm p^+-GaAs 4×10^{19} cm^{-3}	
n^--GaAs spacer 3×10^{16} cm^{-3}	-	20nm
Collector	0.5µm n^--GaAs 1×10^{16} cm^{-3}	0.48µm n^--$In_{0.49}Ga_{0.51}P$ 3×10^{16} cm^{-3}
Sub-collector	0.7µm - n^+-GaAs 5×10^{18} cm^{-3}	
Semi-insulating GaAs Substrate		

In the previous work [34] in our research group microwave the InGaP/GaAs sHBT and DHBT have been fabricated and characterised. These devices had 8×10 μm^2 B-E area and the small signal parameters for these two devices are given in table 5.4 detailed [34].

Table 5.4: Parameters of the equivalent circuit model for InGaP/GaAs single and double HBTs ($8\times10\ \mu m^2$, V_{CE} = 2.5V) used in simulation [34]

Parameters	SHBT	DHBT	Parameters	SHBT	DHBT
I_C (mA)	19	15	C_{jbe} (fF)	80	67
r_e (Ω)	1.4	1.7	C_{jbc} (fF)	50	55
R_{ee} (Ω)	13	15	C_{pce} (fF)	45	39
R_{cc} (Ω)	10	10	C_{pbe} (fF)	30	33
R_{bb} (Ω)	33	30	C_{pbc} (fF)	13	12
r_{bc} (kΩ)	20	15	τ_b (psec)	1.2	3.3
L_b (nH)	0.44	0.4	τ_c (psec)	1.8	2.8
L_c (nH)	0.44	0.4	α_0	0.952	0.939
L_e (nH)	0.25	0.25	f_t (GHz)	37	21

It is noticeable from table 5.4 that the physical small signal parameter values of the SHBT and DHBT are almost identical. The only significantly different values parameters are τ_b and τ_c, which are larger in the DHBT. The larger τ_b in the DHBT can be attributed to the electrons trapping effect in the quantum-well barrier, which is located between the GaAs spacer and the InGaP collector interface. An additional delay time for electron transfer from emitter to collector may be caused by this barrier. Furthermore, smaller saturation velocity of the electrons in the InGaP, compared to the GaAs, is the reason why larger τ_c appears in the InGaP/GaAs DHBT [3]. Saturation velocity (either measured or calculated using Monte Carlo methods) of $In_{0.49}Ga_{0.51}P$ (in the range of $(4.4\text{-}8.0)\times10^6$ cm/s) is reported, and is about half of the value for GaAs ($(8.0\text{-}10)\times10^6$ cm/s) [35-36]. Therefore, an almost 50% higher τ_c in the DHBT can be expected due to the difference between the saturation velocity of the InGaP and GaAs [34].

It is reported [34] that using a GaAs spacer layer inserted between the GaAs base and InGaP collector layers can lower the potential spike, which is proposed to partly overcome the above limitations in the DHBT. The measured results [34] show that the difference in their respective DC current gains of the two devices is just minimal. The cut-off frequency of the DHBT is almost identical to that of the SHBT at low to moderate current densities, since the emitter-to-collector delay time under such conditions is dominated by the emitter charging time τ_e. However, the current blocking effect due to the potential spike in the B-C heterojunction still exists. At higher current levels, where microwave HBTs are biased for most of the applications, the cut-off frequency of the DHBT, which is shown in table 5.4, is significantly less than that of the SHBT [34].

Using the small signal parameters in table 5.4, eye diagrams simulation of the SHBT and DHBT were carried out. The results and comparisons are shown in the following section.

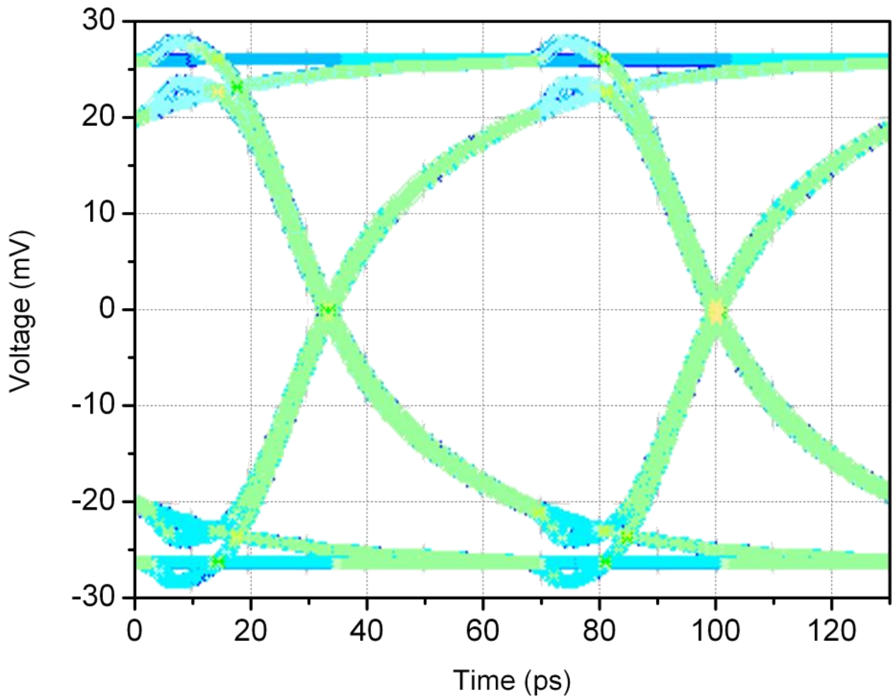

Figure 5.35: Simulation of InGaP/GaAs SHBT eye diagram (8×10 μm^2) with 15Gbps input signal

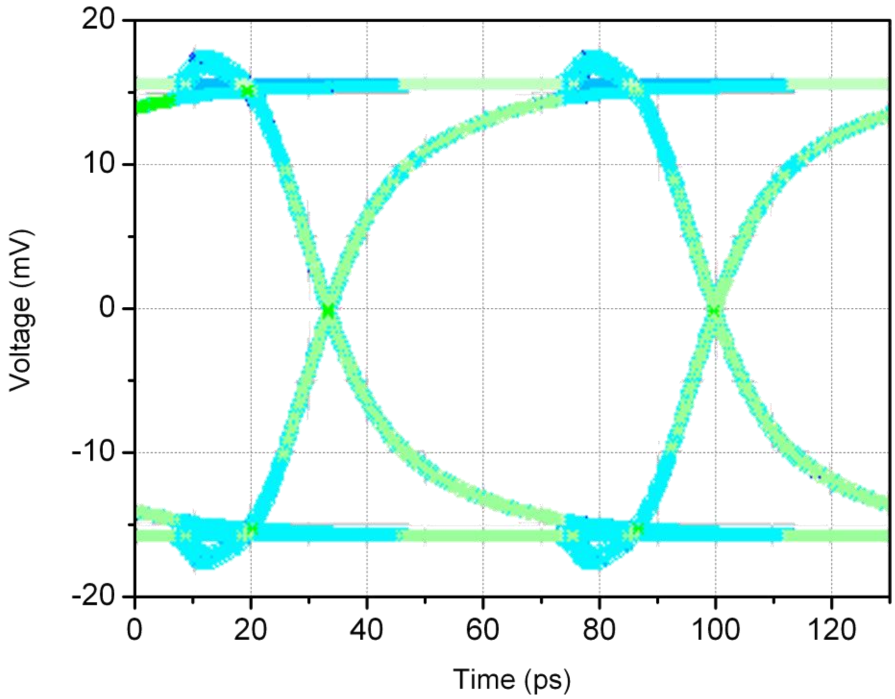

Figure 5.36: Simulation of InGaP/GaAs DHBT eye diagram (8×10 μm^2) with 15Gbps input signal

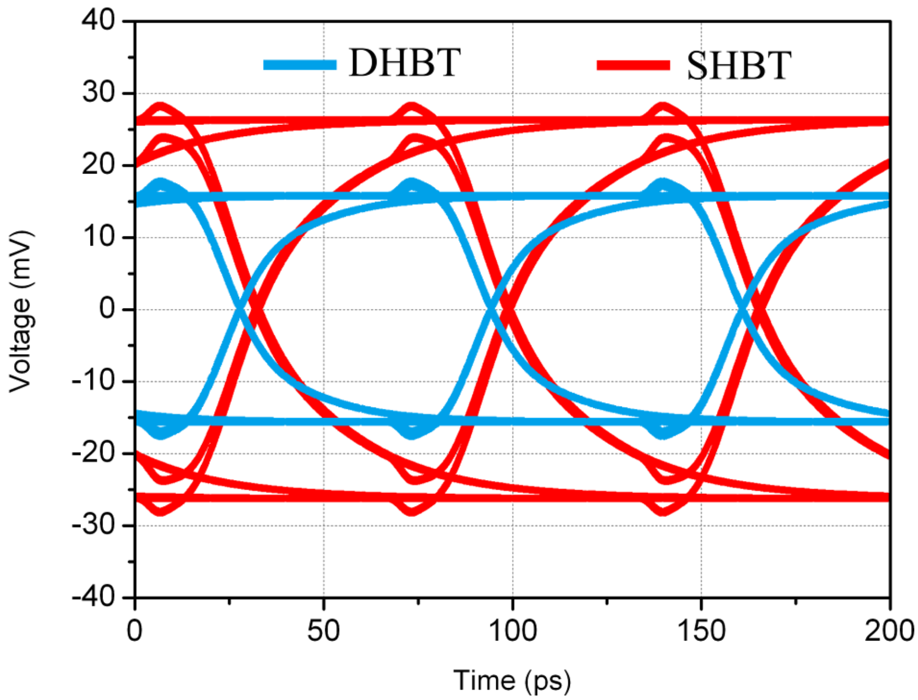

Figure 5.37: Simulated eye diagram response of the InGaP/GaAs SHBT and DHBT (8×10 μm^2) with 15Gbps input signal

Figures 5.35 and 5.36 show eye diagram simulation for the InGaP/GaAs SHBT and DHBT (8×10 μm^2) with 15Gbps input signal. Both devices under test are high speed devices. So even at 15Gbps the eye diagrams are of high quality.

Due to the fact that the two devices (SHBT and DHBT) have different current gain, direct comparison of the eye diagrams for these two devices is not so obvious (figure 5.37). However by normalising the eye parameters with their respective 0.5Gbps performances, more useful information can be extracted.

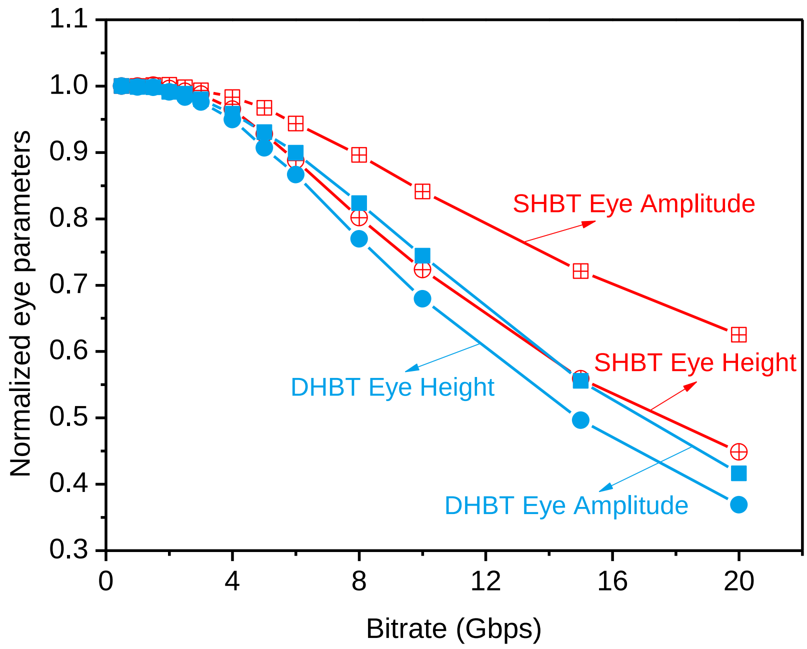

Figure 5.38: Simulated (normalised with respect to 0.5Gbps data) eye amplitude and eye height versus bitrate for SHBT and DHBT InGaP/GaAs (8×10 μm^2) DHPT

Figure 5.38 shows the normalised (with 0.5Gbps) eye amplitude and eye height of the InGaP/GaAs SHBT and DHBT. Firstly, for SHBT, both values of eye amplitude and eye height are higher than DHBT over all data rates. This is attributed to wider SHBT bandwidth (simulated -3dB bandwidth is 4GHz) compared to the DHBT (3.55GHz). Secondly, it is noticeable that at high frequency, that is, over 6Gbps, the decrease rate difference between eye amplitude and eye height for the SHBT is much higher than for the DHBT. The DHBT shows almost the same decease rate for both eye parameters. This means at high bitrate level, although the 8×10 μm^2 InGaP/GaAs SHBT has higher current gain, more noise and distortion is contained in the signal.

This information is extremely important for engineers setting up a sampling threshold and bitrate. Also, this information cannot be obtained by traditional analysis techniques like the S-parameters, but only through eye diagram analysis.

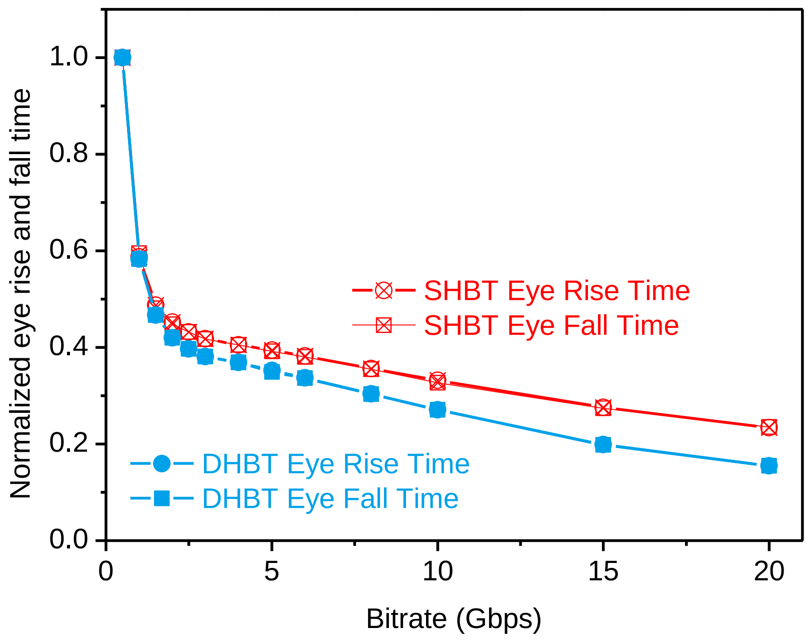

Figure 5.39: Simulated (normalised with respect to 0.5Gbps data) eye rise and fall time versus bitrate for SHBT and DHBT InGaP/GaAs ($8\times10\ \mu m^2$) DHPT

Again, normalised eye rise and fall time comparison confirms the latter observation and discussion. At a high frequency range, the $8\times10\ \mu m^2$ InGaP/GaAs SHBT shows higher rise and fall time than the DHBT. This is since the parameters in figure 5.39 mainly depend on noise and distortion not current gain of the device. One dominating reason for this difference in the high frequency performance is that the DHBT has much lower leakage current due to its wider bandgap B-C heterojuction. Higher leakage current leads to more harmful deterioration, especially at high frequency and lower current gain region.

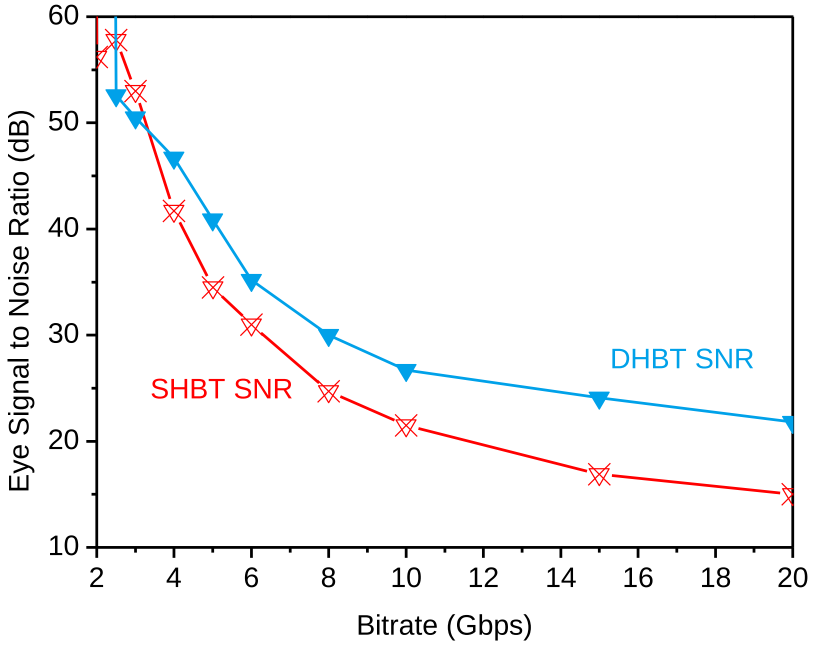

Figure 5.40: Simulated eye signal to noise ratio versus bitrate for SHBT and DHBT InGaP/GaAs ($8\times10\ \mu m^2$) DHPT

Similarly comparison of eye signal to noise ratio in figure 5.40 shows the advantage of DHBT with lower noise level is compared to the SHBT. The difference is clearer at higher bandwidth (8Gbps corresponding to 4GHz).

References

[1] Selli, G., et al. “Validation of equivalent circuits extracted S-parameter data for eye-pattern evaluation” Electromagnetic Compatibility, 2004. EMC 2004, USA, 9-13, vol. 2, pp. 666-671, Aug. 2004.

[2] Foster, G. “Anatomy of Eye Diagram-a Primer”, Synthesis Research, lnc., SR-TN0033/ 140CT04.

[3] Rezazadeh, A. A., Sotoodeh, M. “Design and technology of InGaP/GaAs DHBTs”, Proceedings of ASADM 2000, Slovakia, pp. 119- 125, 16-18 Oct 2000.

[4] Venkatesha, D. “Small signal characterisation of active and passive device using eye diagrams”, Ph.D thesis, Microwave and Communication Systems Research Group, School of Electrical and Electronics Engineering, University of Manchester, 2008.

[5] Ouslimani, A., Gaubert, J., Hafdallah, H., Birafane, A., Pouvil, P., Leier, H. “Direct extraction of linear HBT-model parameters using nine analytical expression blocks”, IEEE Transactions on Microwave Theory and Techniques, vol. 50, pp. 218-221, 2002.

[6] Costa, D. W., Liu, U., Harris, J. S. “Direct extraction of the A1GaAslGaAs heterojunction bipolar transistor small-signal equivalent circuit”, IEEE Transactions on Electronic Devices, vol. 38, pp. 2018-2024, 1991.

[7] Teeter, D. A., Curtice, W. R. “Comparison of hybrid pi and Tee HBT circuit topologies and their relationship to large signal modelling,” IEEE MTT-S, International Microwave Symposium Digest, vol. 2, pp. 375-378, 1997

[8] Suh, Y., Seok, E., Shin, J. H., Kim, B., Heo, D., Raghavan, A., Laskar, J. “Direct extraction method for internal equivalent circuit parameters of HBT small-signal hybrid-pi model,” International Microwave Symposium Digest., IEEE MTT-S, vol. 3, pp. 140 1-1 403, 2000.

[9] Rudolph, M., Lenk, F., Doemer, R., Heymann, P. “Towards a unified method to implement transit-time effects in Pi-topology HBT compact models”, International Microwave Symposium Digest, IEEE MTT-S, pp. 997-1000, 2002.

[10] Teeter, D.A., Curtice, W.R. “Comparison of hybrid pi and Tee HBT circuit topologies and their relationship to large signal modeling”, Microwave Symposium Digest, IEEE MTT-S International, vol. 2, pp. 375-378, 8-13 June 1997.

[11] Chalika, N. D. “Compact semi-physical modelling for HBT circuit simulations”, Ph.D thesis, Microwave and Communication Systems Research

Group, School of Electrical and Electronics Engineering, University of Manchester, 2006.

[12] Schaper, U., Holzapfl, B. "Analytical parameter extraction of the HBT equivalent circuit with T-like topology from measured S-parameters", IEEE Transactions on Microwave Theory and Techniques, vol. 43, pp. 493-498, 1995.

[13] Lundardi, L. M., Rios, J. M. M., Chandrasekhar, S., Miyamoto, Y. "A self-consistent method for complete small-signal parameter extraction of InP-based heterojunction bipolar transistors (HBTs)", IEEE Transactions on Microwave Theory Techniques, vol. 45, pp. 39-45, 1997.

[14] Sotoodeh, M., Sozzi, L., Vinay, A., Khalid, A. H., Hu, Z., Rezazadeh, A. A., Menozzi, R. "Stepping toward standard methods of small-signal parameter extraction for HBT's", IEEE Transactions on Electron Devices, vol. 47, pp. 1139-1151, 2000.

[15] Chitrashekaraiah, S., Vo, V. T., Rezazadeh, A. A. "Linear temperature dependent small signal model for InGaP/GaAs DHBTs using IC-CAP", Microwave Symposium Digest 2006 IEEE MTT-S International, San Francisco, CA, United states, June 11- June 16, 2006.

[16] Wei, C. J., Hwang, J. C. M. "Direct extraction of equivalent circuit parameters for heterojunction bipolar transistors", IEEE Transactions on Microwave Theory and Techniques, vol. 43, pp. 2035-2040, 1995.

[17] Chitrashekaraiah, S., Dharmasiri, C. N., Rezazadeh, A. A. "An automated small signal parameter extraction technique for HBTs using IC-CAP", IEEE High Frequency Postgraduate Student Colloquium, pp. 151-156, 6-7 Sep. 2004.

[18] Venkatesha, D. B., Chitrashekaraiah, S., Rezazadeh, A. A., Thiede, A. "Interpreting InGaP/GaAs DHBT eye diagrams using small signal parameters", 2007 Proceedings of European Microwave Conference Week, pp. 457-462 October 2007, Munich, Germany.

[19] Keiser, G. "Optical Fibre Communications", McGraw-Hill International Editions, 1991, ISBN 0-07-100785-7.

[20] Wasige, E. "Determining the HBT base-collector elements directly from S-parameter data", International Microwave Symposium Digest, JEEE MTT-S, vol. 3, pp. 1019-1021, 2003.

[21] Hattendorf, M., Scott, D., Yang Q., Feng M. "Method to determine intrinsic and extrinsic base-collector capacitance of HBTs directly from bias-dependent S-parameter data", IEEE Electron Device Letters, vol. 22, pp. 116-118, 2001.

[22] Liu, W., Harris, J. S. "Current dependence of base-collector capacitance of bipolar transistors", Solid-State Electronics, vol. 35, pp. 1051-1057, 1992.

[23] Lindholm, F. A., Bowler, D. L. “High Current Regimes in Transistor Collector Regions”, IEEE Transactions on Electron Devices, vol. 20, pp. 257-263, 1973.

[24] Straub, A., Gebs, R., Habenicht, H., Trunk, S., Bardos, R. A., Sproul, A. B., Aberlea, A. G. “Impedance analysis: A powerful method for the determination of the doping concentration and built-in potential of non-ideal semiconductor p-n diodes”, Journal of Applied Physics, vol. 97, issue 8, 2005, pp. 083703-083703-8.

[25] Iwamoto, M., Asbeck, P. M., Low, T. S., Hutchinson, C. P., Scott, J. B., Cognata, A., Qin, X., Camnitz, L. H., D'Avanzo, D. C. “Linearity characteristics of GaAs HBTs and the influence of collector design”, IEEE Transactions on Microwave Theory and Techniques, vol. 48, pp. 2377-2388, 2000.

[26] Stroud, K. A. Engineering Mathematics, 4th ed: Bath Press, 1995

[27] Salles, A. A., Hackbart, A. S., Spalding, L. N. “A simple model for the GaAs HBT high-frequency performance under optical illumination”, Microwave and Optical Technology Letters, vol. 7, pp. 392-5, 1994.

[28] Gartner, W. “Depletion-Layer Photoeffects in Semiconductors”, Physics Review, vol. 116, pp. 84-87, 1959

[29] Matsushima, K., et al. “Small signal equivalent circuit of illuminated HPTs”, Microwave Photonics, International Topical Meeting on, IEEE, 165-168, 5-8 Nov. 2002

[30] Kim, J., et al. “Equivalent circuit Models for InP/InGaAs HPT”,6th Korea-Japan Joint Workshop on Microwave Millimetre-wave Photonics, 27-28 Jan. 2005.

[31] Khan, H. A., Rezazadeh, A. A., Zhang, Y. “Photoresponse Modelling and Analysis of InGaP/GaAs Double-HPTs”, IEEE Journal of Quantum Electronics, vol. 50, issue 12, pp. 1044-1051, 2014.

[32] Sze, S. M. Physics of Semiconductor Devices, 2nd ed. USA: John Wiley & Sons, 2001.

[33] Novak, J., Hasenohrl, S., Alonso, M. I., Garriga, M., “Influence of tensile and compressive strain on the band gap energy of ordered InGaP”, Applied Physics Letters, vol. 79, p. 2758, 2001.

[34] Sotoodeh, M., Khalid, A. H., Sheng, H., Amin, F. A., Gokdemir. T., Rezazadeh, A. A., Knights, A. P., Button, C. C. “Direct extraction and numerical simulation of the base and collector delay times in double heterojunction bipolar transistors”, IEEE Transactions on Electron Devices, vol. 46, no. 6, pp.1081-1086, June 1999.

[35] Khalid, A. H., Sotoodeh, M., Rezazadeh, A. A. “Planar self-aligned microwave

InGaP/GaAs HBTs using He^+ /O^+ implant isolation”, in Proc. 5th Int. Workshop High Performance Electron Devices for Microwave and Optoelectronic Applications (EDMO’97), pp. 279–284.

[36] Pritchard, R. L. Electrical Characteristics of Transistors, New York: McGraw-Hill, 1967.

[37] Liu, W., Henderson, T., Beam III, E., Fan, S. K. “Electron saturation velocity in GaInP measured in a GaInP/GaAs/GaInP double-heterojunction bipolar transistor”, Electron. Letters, vol. 29, pp. 1885–1887, 1993.

Chapter 6 Spectral response modelling and analysis of heterojunction bipolar phototransistors

6.1 Spectral response modelling of HPTs

An accurate spectral response (SR) prediction plays a key role in the design of photodiodes. Numerous published papers describe the modelling of the spectral response for photodiodes [1-5]. However, in most of the papers, HPT modelling merely shows the normalised or relative SR. Many simplistic assumptions about other photodiodes are simply applied to HPTs modelling, which makes the absolute SR prediction lacking in accuracy.

For instance, during p-i-n photodiode modelling, the large intrinsic absorption layer between the p and n terminals is wide enough. Collection efficiency (η_c) which describes the actual amount of flux absorbed by the active layers of a photodiode can be set as unity. However, in surface illuminated HPTs modelling the case is not appropriate. Value of η_c is limited and affected by the depth of the absorbing region, which is not as unity all the time. Also, many other factors like temperature or material properties affect η_c. Because an accurate collection efficiency prediction would further contribute to accuracy of HPTs SR modelling, a careful analysis of η_c is essential. Another parameter, which does not attract extensive attention in the published literature [6-7], is the variation of optical absorption coefficient (α) with doping concentration of devices. In fact, different flux absorption profiles between different layers are required in modelling. The optical absorption and electron-hole generation rate are significantly affected by this factor. Also, even the impalpable variation of the refractive index with incident signal wavelength changes should be considered. All these above factors may simultaneously make the modelling result deviate from the experimental data. Therefore, it is necessary to take all these aspects into account during the modelling process. The fully exposition and understanding of these parameters can help to optimise the HPTs design and enhance the accuracy of the modelling.

An accurate absorption model is a prerequisite of an accurate spectral response prediction. This chapter first focuses on an advanced optical absorption model for our n-p-n $Al_{0.3}Ga_{0.7}As/GaAs$ SHPT working in 2-terminal mode (floating base). The absorption coefficient variation and refractive index variation are also taken into consideration. The model is expected to be a general model which can be used for all material systems.

6.1.1 Methodology

Optical signal propagation and absorption in each layer of the n-p-n $Al_{0.3}Ga_{0.7}As/GaAs$ SHPT working in two-terminal mode (floating base) are described and calculated by equations. Then details of absorption coefficients changing with doping concentration are given. A more accurate extraction method when compared to the published data is provided. After that, the simulation results of optical flux absorption and photogenerated currents in base, collector and subcollector are shown in figures. The spectral response and collection efficiency equation are subsequently summarised and simulated in Matlab. Finally, the accurately modelled and predicted results are provided.

6.1.2 Refractive index

When wave, like light, travels to the interface between two different mediums, part of the wave will be reflected by the surface. In our case, the optical flux shines on the base surface of the device, so part of the incident flux is reflected. Based on Fresnel reflection equation [8], the Fresnel reflection coefficient is given by:

$$R_f = [\frac{(n_b - n_o)}{(n_b + n_o)}]^2 \tag{6.1.1}$$

where n_b and n_0 are the refractive indices of the base layer material and free space, respectively. From the figure below, it is known that the Fresnel reflection coefficient here is a wavelength and material dependent parameter.

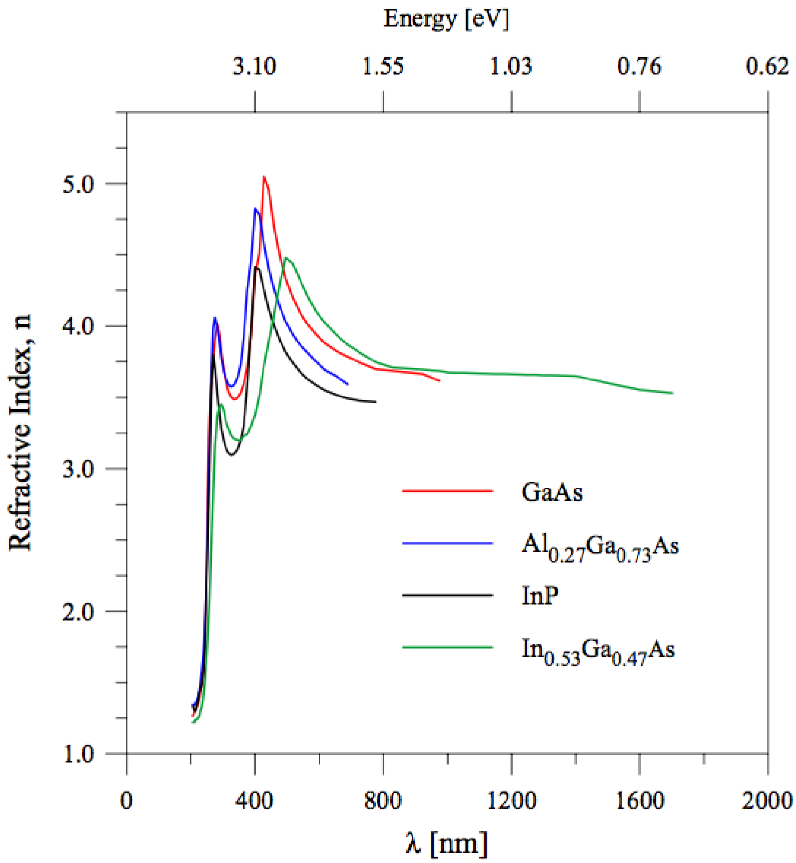

Figure 6.1: A comparison of the refractive indices for AlGaAs/GaAs system semiconductor materials as a function of wavelength [9]

Figure 6.1 shows a plot of the experimentally measured refractive indices [9] vs. wavelength for GaAs and AlGaAs materials. It is noticed that in the AlGaAs/GaAs system, narrower bandgap material exerts a larger refractive index at a specific wavelength. In the figure, it is observed that at beyond 450nm the refractive index value of GaAs is greater than that of AlGaAs. Usually, this property is used for the design of solid state optical waveguides, in order to confine light inside a narrow bandgap material, which is inserted between two layers of large bandgap material. In fact there is a technique called anti-reflective coating, which is used on the surface of the semiconductor layer, and which can minimise the flux reflection. However, the device which is used for our modelling does not utilise this technique. It is essential to account for the reflection effect in our analysis.

6.1.3 Absorption coefficient

Absorption coefficient (α) is a proportionality constant which is used to describe the particular energy photon flux absorption in a given material. It is also a wavelength and material dependent parameter ($1/\alpha$) which can be understood as the average depth of penetration by light into a material.

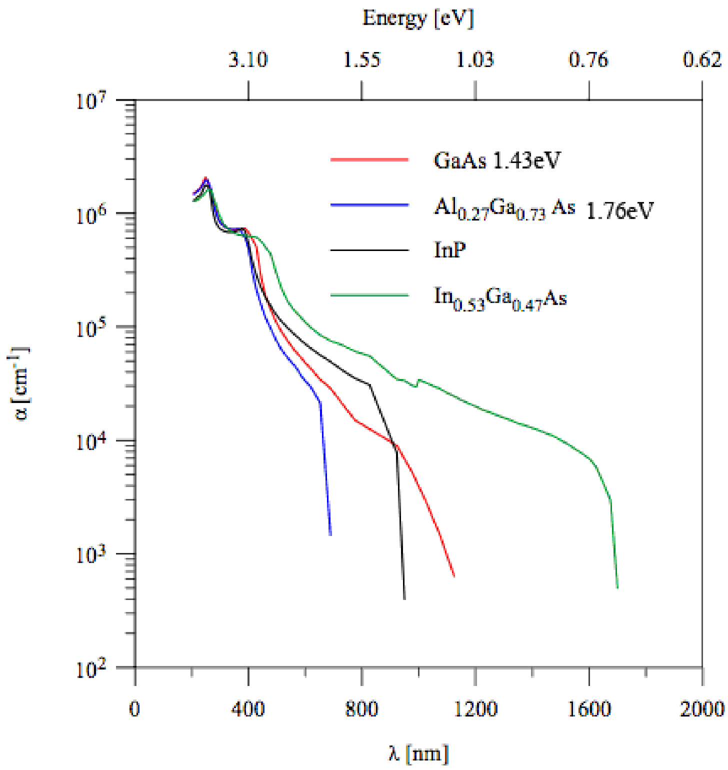

Figure 6.2: A comparison of absorption coefficients, α, versus the wavelength for GaAs and AlGaAs [9]

The figure above shows absorption coefficients of various undoped materials. It is noticed that every curve in the figure decreases rapidly at cutoff wavelength of the material which is the bandgap E_g of the material. From figure 6.2, it is clear that the value of the absorption coefficient is not only related to the wavelength but also to the material's bandgap. As we know, bandgap of material variations occur with a change in doping concentration. Especially at the particularly high impurity concentration levels, majority and minority band edges both appear to experience a noticeable shift which causes shrinkage of the bandgap. This effect is known as the bandgap narrowing effect. In devices such as ours, containing adjacent layers with different doping concentrations, doping-induced shifting of bandgap variation may greatly influence the device's characteristics.

Based on the above analysis, the doping concentration can make a sizable impact on the absorption coefficient. This effect is more obvious for the incident optical signal wavelengths near the bandgap of the material. It is valuable to account for these parameters in our absorption profile analysis.

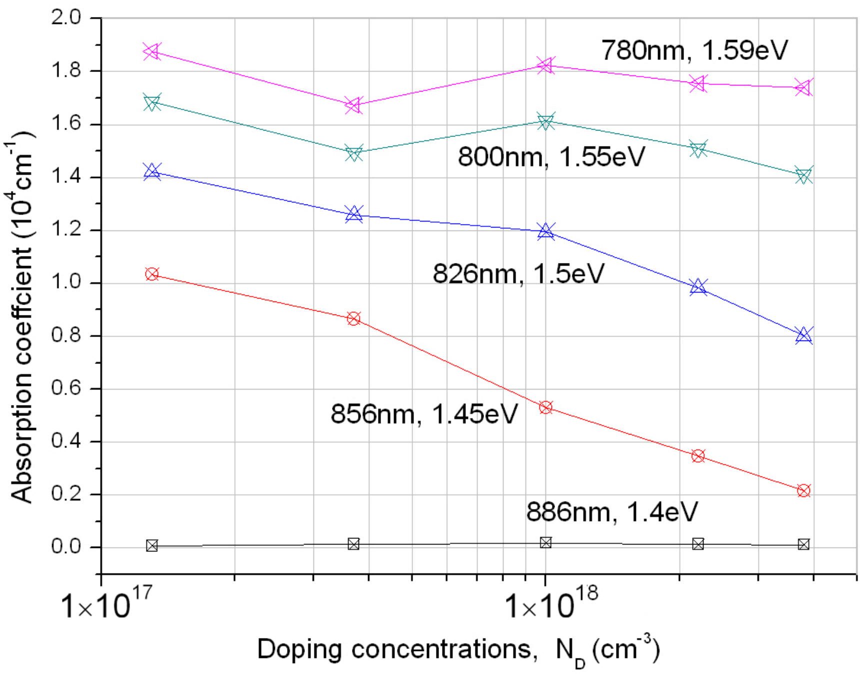

Figure 6.3: Modelling variation of absorption coefficient with doping concentrations for n-type GaAs layers [10]

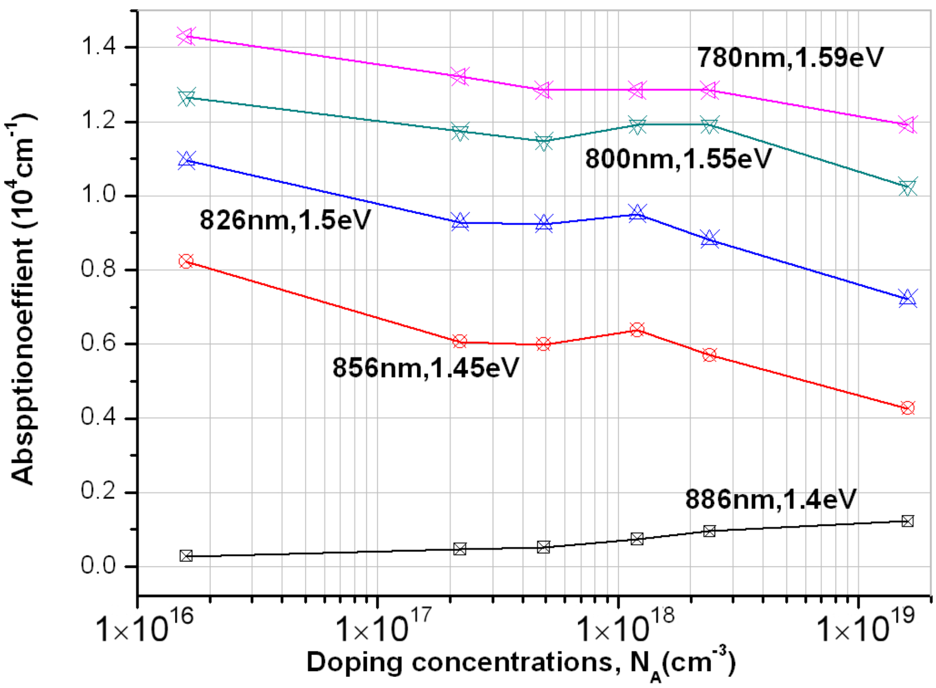

Figure 6.4: Modelling variation of absorption coefficient with doping concentrations for p-type GaAs layers [11]

Here, software called 'Engauge Digitizer' is used for data extraction. It accurately converts an image file into numbers. From published data, concentration dependence of the absorption coefficient for n- [10] and p-type [11] GaAs data is accurately extracted and plotted in figures 6.3 and 6.4. A detailed analysis of the absorption coefficient variation can be achieved from these graphs. In the figures, absorption coefficients with different doping concentrations with optical signal input from 780nm to 886nm are shown. It is noted that for both n- and p-type GaAs, absorption coefficients appear to make a significant change in input signal energy close to the band gap of the material (1.43eV). However, when the wavelength is shorter than 800nm, this effect is negligible. During our modelling, the constant value of the absorption coefficient for the base and the collector layer at a particular wavelength can be used when the input signal energy is not near the GaAs bandgap.

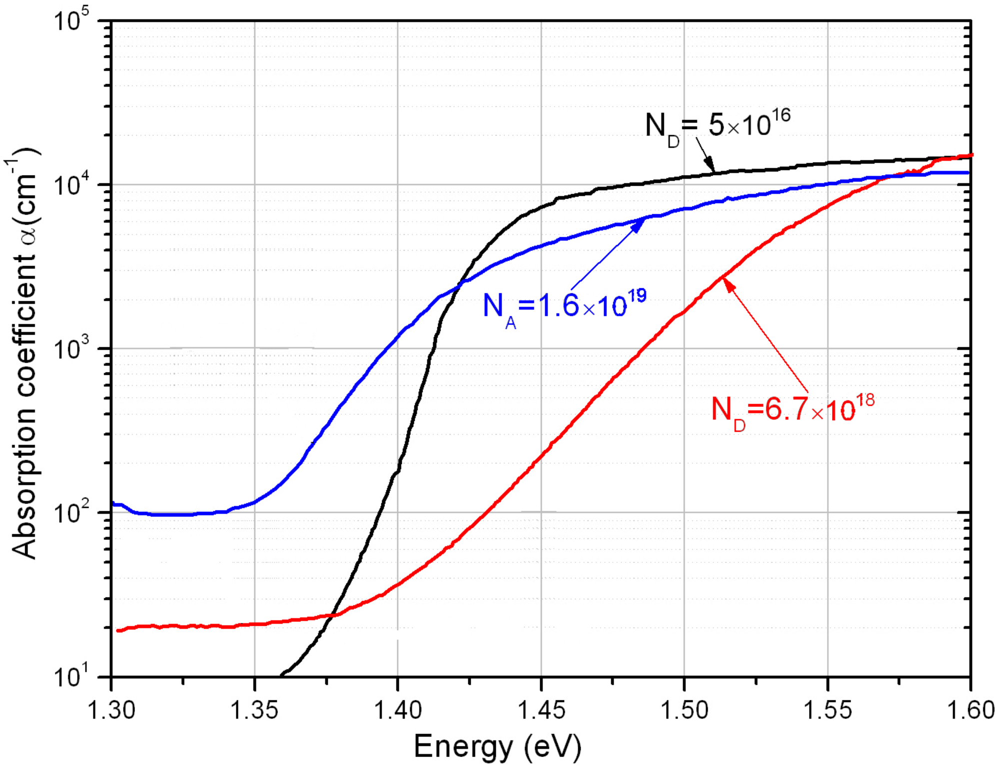

Figure 6.5: Modelling variation of absorption coefficient with input photon energy for different doping concentrations [10-11]

In order to focus on our device, the doping concentration is chosen to represent the actual layers as close as possible from the published data [10-11]. The extracted data is re-plotted in figure 6.5 and used in a later simulation.

6.1.4 Collection efficiency

Collection efficiency describes the conversion efficiency of the device. It is modelled as [12]:

$$\eta_c = 1 - \frac{\phi(d)}{\phi(a)} \tag{6.1.2}$$

where $\phi(a)$ is the flux at the surface of the base layer and $\phi(d)$ is the flux at the end of the subcollector layer.

The equation shows the amount of flux absorbed by active layers over the total amount of optical flux entering the device. In order to achieve high collection efficiency, it is expected that all the flux is absorbed in the base, collector and sub-collector layers without any residual. The value of collection efficiency depends on many parameters, such as the geometric dimension of the device layers, device material, doping concentration of each layer and incident signal wavelength. As we mentioned before, the photo-generated current outside the base, collector and sub-collector layers cannot contribute to the current flow and is not detectable. This can reduce the performance of the whole device. On the other hand, in consideration of the thickness limitation of the device, a tradeoff between collection efficiency and other parameters exists. Therefore, it is important to model this parameter and take it into account in our accurate spectral response prediction.

6.1.5 Absorption model

In order to understand how the optical flux propagates in each layer of the device, an optical flux profile is built and discussed in this section. As we know, the absorption depends on both an incident signal wavelength and material band gap of each layer. The whole process is a wavelength, material and distance dependent phenomenon. So based on the analysis given in the previous section, band gap variation among different layers requires careful modelling for every layer of the device. In fact, due to the recombination, only the absorption occurring in the depletion region and the two diffusion regions on either side, can contribute to the current flow, and is detectable. This part will be discussed in a later chapter, while here we only focus on the flux absorption process.

Assume the device is illuminated under a light source with the energy hv larger than E_g with the photon flux ϕ_0 in units of photons per square centimetre per second. The number of photons absorbed Δx is given by:

$$\begin{aligned} \phi(x+\Delta x)-\phi(x) &\approx \frac{d\phi(x)}{dx}\Delta x = -\alpha\phi(x)\Delta x \\ \Rightarrow \qquad \frac{d\phi(x)}{dx} &= -\alpha\phi(x) \end{aligned} \tag{6.1.3}$$

Using boundary condition $\phi|_{x=0} = \phi_0$, photon flux exists at any point of the semiconductor:

$$\phi(x) = \phi_0 e^{-\alpha x} \tag{6.1.4}$$

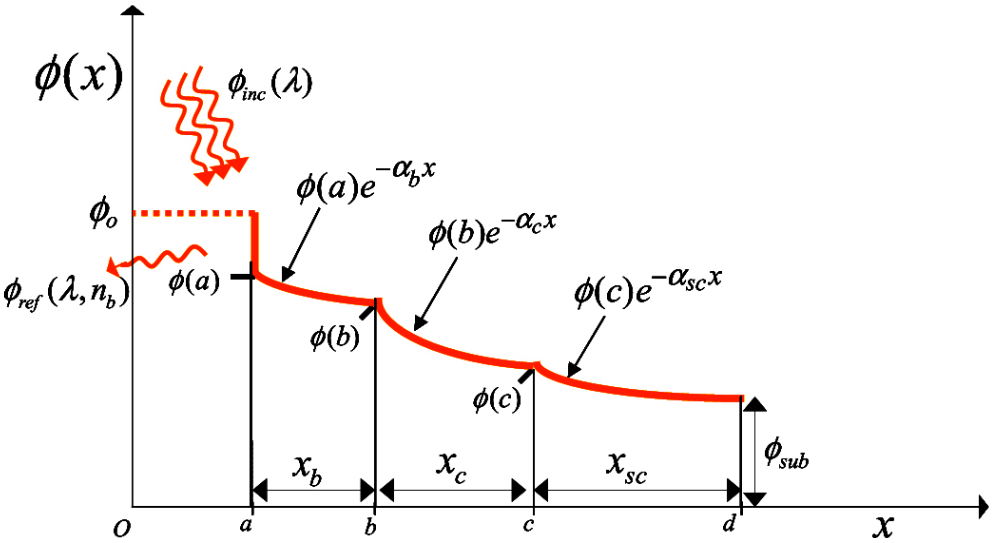

Figure 6.6: Schematic optical flux absorption and propagation in each layer of a SHPT [13]

The device under review contains a single heterostructure between the base and emitter layers. Each of these layers is assumed to have homogenous material properties and constant doping concentration. The base surface of the device is illuminated directly rather than the wide bandgap emitter. Considering figure 6.6, the optical flux absorption process in all active layers of the SHPT is described using the following equations.

$$\phi_{absorption,emitter} = 0 \tag{6.1.5}$$

$$\phi_{absorption,base}(\lambda, N_A) = (\phi_{inc} - \phi_{ref})[1 - e^{-(b-a)\alpha_b}]$$
$$= \phi(a)(1 - e^{-x_b \alpha_b}) \tag{6.1.6}$$

$$\phi_{absorption,collector}(\lambda, N_D) = (\phi_{inc} - \phi_{ref})[1 - e^{-(c-b)\alpha_c}]e^{-(b-a)\alpha_b}$$
$$= \phi(b)(1 - e^{-x_c \alpha_c}) \tag{6.1.7}$$

$$\phi_{absorption,subcollector}(\lambda, N_D^{\ +}) = (\phi_{inc} - \phi_{ref})[1 - e^{-(d-c)\alpha sc}]e^{-(b-a)\alpha_b - (c-b)\alpha_c}$$
$$= \phi(c)(1 - e^{-x_{sc} \alpha_{sc}}) \tag{6.1.8}$$

where $\phi_{absorption,emitter}$, $\phi_{absorption,base}$, $\phi_{absorption,collector}$, $\phi_{absorption,subcollector}$ are the flux absorbed in each layer of the transistor respectively.

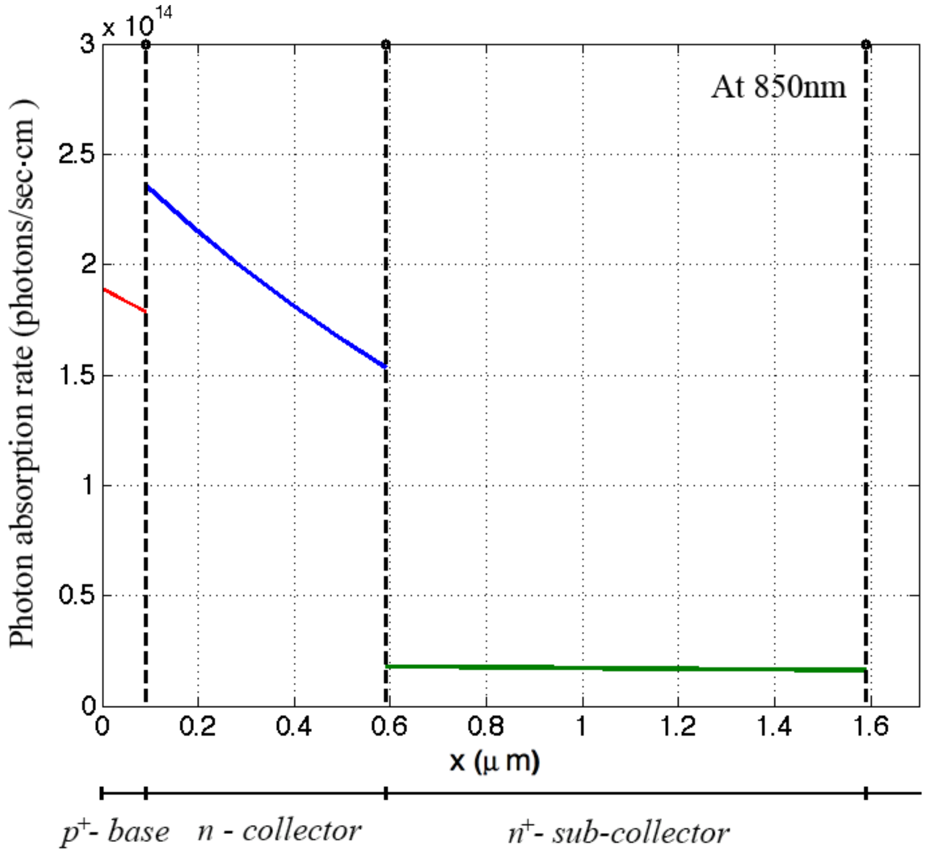

Figure 6.7: Photon absorption rate for each layer of the $Al_{0.3}Ga_{0.7}As/GaAs$ HPT using 850nm radiation

Figure 6.7 shows the photon flux absorbed in our device in unit time and unit distance, with an 850nm input signal. It is noted that the depleted collector absorption rate is greater than the other two layers. This can make sure that, at this particular wavelength, the photon generated electron-hole pair can contribute to the current flow. Also, the figure points out how the absorption coefficient affecting the flux absorption and then confirms the reason why the variation of doping concentration should be accounted for in the modelling.

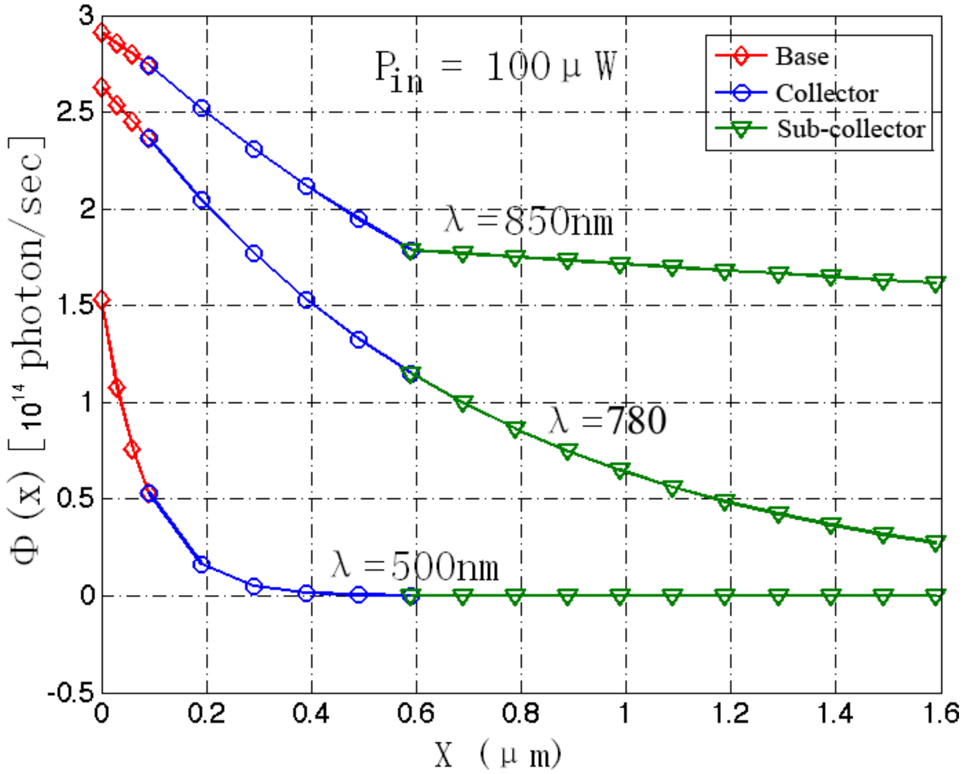

Figure 6.8: Modelling optical flux absorption profile for the $Al_{0.3}Ga_{0.7}As$/GaAs HPT at various incident wavelengths for incident power of 100μW

The optical flux absorption profile of the $Al_{0.3}Ga_{0.7}As$/GaAs SHPT with an incident signal at 500nm, 780nm and 850nm is shown in figure 6.8. Input optical power is fixed at 100μW. Each curve in the figure can be divided into three regions based on our device structure. It is noted that for the 850nm, rapid absorption for the incident signal flux rapid happens in the collector layer, due to the higher absorption coefficient. For 500nm the curve follows a single function. This is because at this wavelength the absorption coefficient is not sensitive to the doping concentration variation. A constant value of the absorption coefficient is used for all layers, resulting in a single exponential curve.

6.1.6 Spectral response

Spectral response is the ratio of photogenerated current to incident optical power. It defines how the performance of a photodetector (the sensitivity of the device) varies with different wavelengths. In order to model the spectral response, the photogenerated current is shown first [12]:

$$I_{ph} = q\beta\int_{0}^{w}(1-R_f)\phi_o\alpha e^{-\alpha x}dx \tag{6.1.9}$$

where q is the electron charge, β is the internal current gain and $(1-R_f)\phi_o\alpha e^{-\alpha x}$ is the optical generation rate.

Due to the incident illumination arrangement of the measurement setup, the optical flux goes through the device directly from the base layer, resulting in no flux absorption in the emitter. Furthermore, the photo-generated current outside the base, collector and sub-collector layers cannot contribute to the current flow, and is not detectable. Therefore, the photogenerated current is extended as:

$$I_{ph} = q\beta\cdot\begin{cases}\phi(a)\alpha_b\int_{a}^{b}e^{-\alpha_b x}dx & \text{for base}\\ \phi(b)\alpha_c\int_{b}^{c}e^{-\alpha_c x}dx & \text{for collector}\\ \phi(c)\alpha_{sc}\int_{c}^{d}e^{-\alpha_{sc} x}dx & \text{for subcollector}\end{cases} \tag{6.1.10}$$

where $\phi(a)$, $\phi(b)$, $\phi(c)$ is input flux at the surface of the base, collector, subcollector layers, respectively, and α_b, α_c, α_{sc} is the absorption coefficient of the base, collector, subcollector layers, respectively.

By definition, the spectral response is:

$$R_{spec}(\lambda) = \frac{I_{ph}}{P_{in}} \tag{6.1.11}$$

where P_{in} equals to input optical power.

Here, between the neutral emitter layer and the base layer, wide-band gap/small-band gap heterostructure suppresses the hole injection [14]. The generation-recombination in the base layer, surface recombination and the leakage current, are considered to be the same as in the forward-active mode of transistor operation. The holes in the base region modify the emitter-base junction so the current can flow in a similar way to the holes injected from the electrical terminal in the forward active mode of operation [13]. The photogenerated electron-hole pairs in a collector which is fully depleted are separated and swept to the base and subcollector regions by the strong electric field. So the recombination effect here for both base and collector can be ignored but the electric field in the sub-collector is not strong enough. The photo-generated carriers move slowly and the process of recombination happens in this layer. But here, in order to make sure the investigation of absorption is unaffected, we entirely focus on the influence of the recombination process in this region, which has been removed. This will be further discussed in a later section.

6.1.7 Modelling results

Using the equation(6.1.10), in Matlab the simulations were carried out. The results are shown in figure 6.9 and 6.10 respectively.

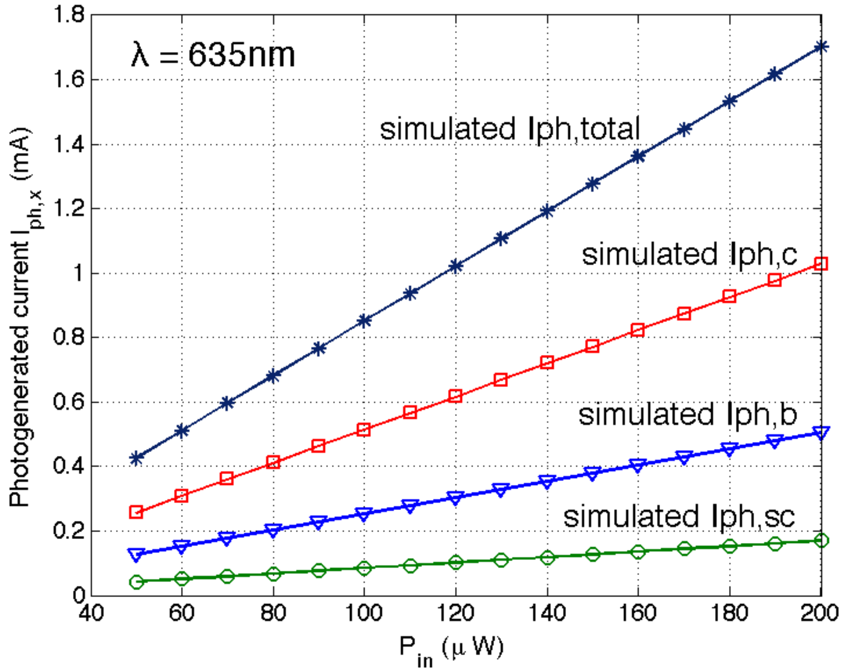

Figure 6.9: Simulated photo-generated currents with input optical power for various $Al_{0.3}Ga_{0.7}As/GaAs$ HPT layers at 635nm

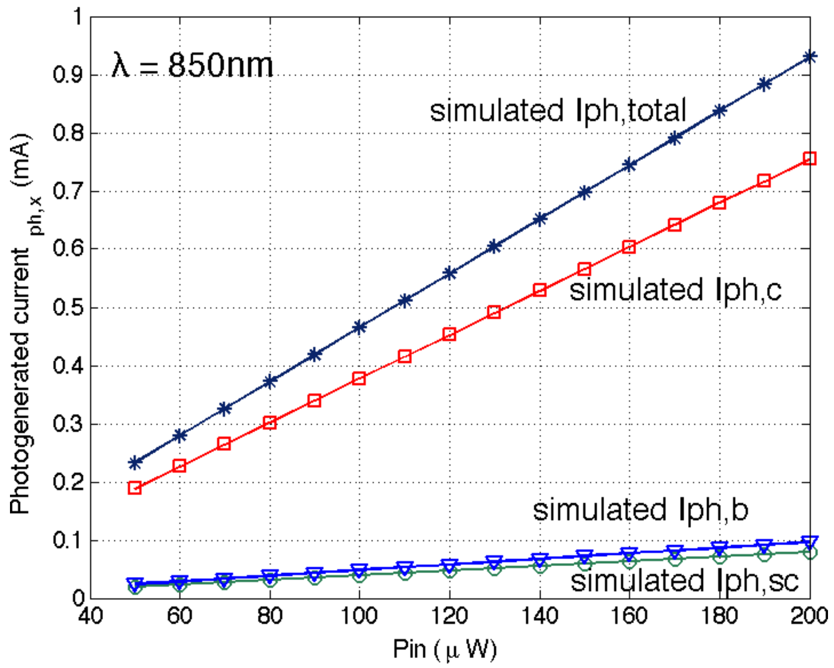

Figure 6.10: Simulated photo-generated currents with input optical power for various $Al_{0.3}Ga_{0.7}As/GaAs$ HPT layers at 850nm

Figures 6.9 and 6.10 show the simulated photo-generated current and incident signal power relationship of each layer of the $Al_{0.3}Ga_{0.7}As/GaAs$ HPT at two different wavelengths. By comparing the two figures, the absorption coefficient variation and the wavelength influence can be observed clearly. Focusing on each figure respectively, it is seen that they correspond to figure 6.8. Due to a greater absorption coefficient in the collector, the photo-generated current in this layer is much higher than in the other layers. Comparing the two figures, and choosing the same incident power, it can be noticed that the total of photo-generated current at 635nm is higher than that at 850nm. By recalling figure 6.8, the total flux absorption at 850nm in all three layers is quite a bit less than at 635nm. In other words, it can be explained as the collection efficiency for 850nm being smaller than that for 635nm. In fact, at 635nm, the collection efficiency is almost equal to unity, which will be shown in figure 6.11. This means that almost all the optical flux is absorbed, with flux rarely arriving at the substrate surface. This can result in high responsivity, although the situation for 850nm is different, with nearly half the flux travelling beyond the sub-collector layer. This leads to lower collection efficiency and lower photo-generated current, which contributes to the responsivity.

By adopting above absorption model (section 6.1.5) and using above equations the $Al_{0.3}Ga_{0.7}As/GaAs$ HPT modelling was carried out in Matlab. Here, the modelling result is shown.

Figure 6.11 shows the spectrum response (SR) and collection efficiency (η_c) simulation. All the parameters discussed before such as absorption coefficient variation by wavelength and doping concentration, refractive index for different wavelengths and so on are taken into account during the Matlab simulation

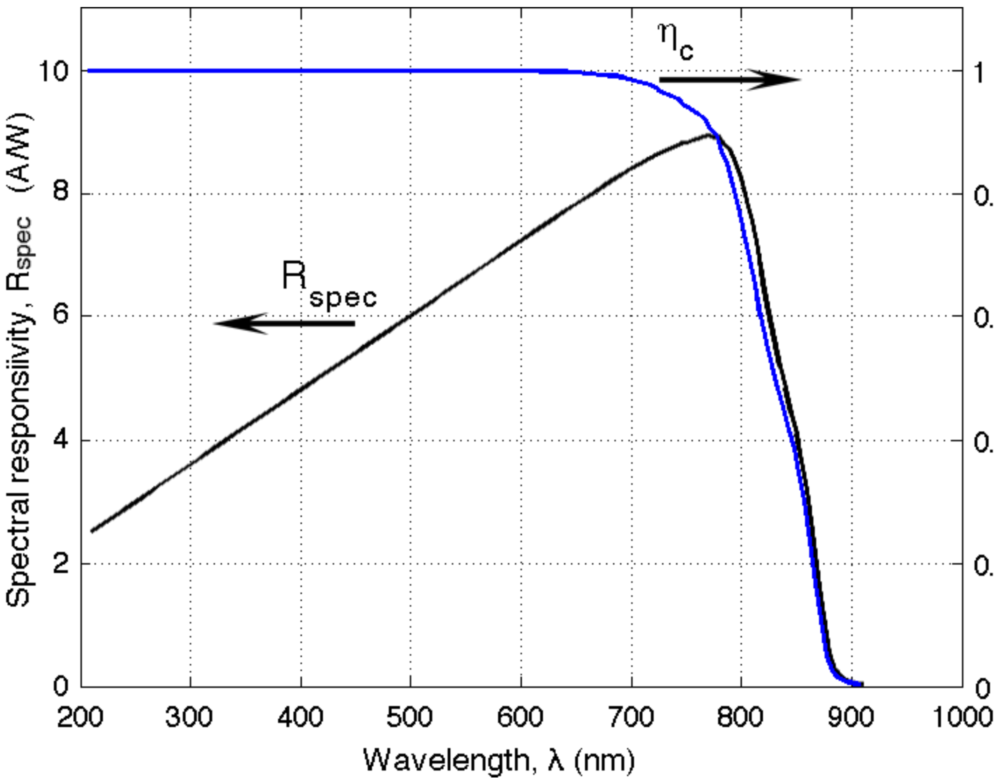

Figure 6.11: Simulated spectral response and collection efficiency for the $Al_{0.3}Ga_{0.7}As/GaAs$ HPT

The whole figure can be divided into two main parts. In the first part, where the wavelength is below 700nm, the spectrum response keeps increasing, while the collection efficiency keeps almost constant unity value. The reason is that in this region for constant incident power the incident flux rate increases, along with the wavelength, which raises the SR. All the flux is absorbed before arriving at the substrate layer. The second region looks more complicated. Prior to 800nm the collection efficiency begins to drop and the spectrum response remains increasing, while the increasing rate becomes quite low. This is due to the value of absorption coefficient, which starts to decrease quickly. However, the increasing flux rate still dominates. After 800nm, the SR and η_c begin to drop fast simultaneously, with a great amount of optical flux going beyond the base collector and sub-collector layers. The absorption in substrate cannot contribute to the detectable current flow. It is necessary to indicate one significant wavelength, 850nm, which is the short wavelength of the transmission. Theoretically, the threshold wavelength of responsivity for the GaAs photodetector should be around 870nm, although in our simulation, the point is around

800nm. This can be explained as follows. According figure 6.5, around this wavelength (800nm, 1.55eV), the absorption coefficient has been changed significantly due to the doping concentration. The wavelength threshold moves to lower value. Further, for our device, the η_c begins to significantly fall at around 780nm, which becomes another major reason for lower threshold [13].

At last, in our lab setup, an optical signal is illuminated directly on the base layer. For more common cases, the optical flux should input through the transparent contact and the wide band gap emitter layer. When the incident signal wavelength is lower than the particular value (dependent on the band gap of the emitter material), the flux can also be absorbed by the emitter. However, this absorption does not contribute to the detectable photo-generated current, which reduces the responsivity in that wavelength.

In order to achieve higher collection efficiency and then higher spectrum response around 850nm, our device structure has to be re-designed. Although many trade-off parameters need to be considered, careful modelling becomes an indispensable step in optical photodetector design. For instance, in order to achieve higher collection efficiency and then higher spectrum response, the device structure need to be wider. But this can increase the carriers passing through time. Further it can reduce high frequency performance of the device.

6.2 Analytical modelling of the spectral response

Heterojunction phototransistors (HPTs) using III-V compound semiconductor materials have been extensively studied over the past two decades. They can offer large optical gain without the excess noise resulting from avalanching. HPTs show high potential as high performance photodetector for lightwave communications and a possible alternative to a p-i-n or APD [15]. Therefore, it is expected to play a key role in the next generation of microwave and optoelectronic integrated circuits. An accurate optical absorption model is used to achieve an accurate spectral response prediction. Many valuable parameters, such as absorption need to be calculated by layers, absorption coefficient variation caused by doping, accurate boundary condition and surface recombination parameters, of HBTs need to be carefully analysed.

Nowadays p-i-n photodiodes are the most commonly used device in the area of photodetection, although the lack of internal gain is one major shortcoming here. Furthermore, the trade-off between the intrinsic absorption layer and capacitance is another limitation if it is employed as a high frequency device. Metal-semiconductor-metal photodiodes can work at high frequency due to the lower capacitance per unit area over the p-i-n photodiode. However, the device still lacks internal gain. Temperature instability is another big drawback. For avalanche photodiodes (APDs), excess high noise limits usage. Other devices, such as MEFETs and HEMTs, require a high frequency operation (millimetre wave and beyond). Compared with the above devices, HPTs do show internal gain, simple biasing conditions, low noise and many other advantages. That makes HPTs an exciting choice for the above devices.

Analytical modelling of the spectral response for HPTs is widely studied. In the published reference [1-5], spectral responsivity (SR) modelling for photodiodes has been studied and investigated. However, some prediction of SR is limited to relative or normalised response [16-17]. In Naresh Chand's paper [18], although the analytical expressions for responsivity are given out, the boundary condition of minority carriers' concentration is not convincing.

In the following section, a detailed analytical responsivity modelling of the AlGaAs/GaAs is given out. Parameters such as the effect of doping on the absorption coefficient, and wavelength dependent refractive index are taken account. The steady state continuity equations are derived from governing the distribution of minority carriers for low-injection state. These incorporate a drift and diffusion mechanism of excess minority carriers along with photo-generation and recombination effects. This analysis provides a valuable optimisation tool for designing HPTs as optical detectors.

6.2.1 Continuity equation

Each type of carrier act gives rise to a change in carrier concentrations with time. There must be a spatial and time continuity in the carrier concentration [19]. The behaviour of carriers in the semiconductor can be described by the continuity equation. This can be written as:

$$\frac{\partial n_p}{\partial t} = \nabla \frac{J_n}{q} + G_n - R_n$$
$$\frac{\partial p_n}{\partial t} = \nabla \frac{J_p}{q} + G_p - R_p \tag{6.2.1}$$

where J_n is electron current density, J_p is hole current density, G_n and G_p are the electron and hole generation rate, respectively, and R_n and R_p are the electron and hole recombination rate in a p and n type semiconductor, respectively

As we know, if an electrical contact is provided, excess carriers combined with a recombination process change the concentration of minority carriers. Also, the photo-generated process is involved, which can also affect the number of carriers.

Here, the system under analysis is assumed to be one-dimensioned, and the analysis is limited to minority carriers. The total diffusion and drift current can be written as current density equation [19]:

$$J_n = qu_n nE + qD_n \frac{dn_p}{dx}$$
$$J_p = qu_p nE - qD_p \frac{dp_n}{dx} \tag{6.2.2}$$

where D is the diffusion coefficient, q is the unit charge, E is applied electric field and u is the mobility of minority carriers.

The diffusion coefficient and mobility can be related by the Einstein relationship [19]:

$$D_n = \frac{kT}{q} u_n$$
$$D_p = \frac{kT}{q} u_p \tag{6.2.3}$$

where k is the Boltzmann constant and T is the absolute temperature.

The continuity equation hence can be re-written as:

$$\frac{\partial n_p}{\partial t} = n_p u_n \frac{\partial E}{\partial x} + u_n E \frac{\partial n_p}{\partial x} + D_n \frac{\partial^2 n_p}{\partial x^2} + G_n - R_n$$
$$\frac{\partial p_n}{\partial t} = p_n u_p \frac{\partial E}{\partial x} + u_p E \frac{\partial p_n}{\partial x} + D_p \frac{\partial^2 p_n}{\partial x^2} + G_p - R_p \tag{6.2.4}$$

The device under consideration is assumed uniform doped and the region outside the fully depleted collector is highly doped. The highly doped region leads to high conductivity. Therefore, it is assumed there is no electrical field outside the depletion region, so, the minority carriers here are only influenced by diffusion. The voltage only drops in the depleted region. Therefore, the equation can be simplified as:

$$\frac{\partial n_p}{\partial t} = D_n \frac{\partial^2 n}{\partial x^2} + G_n - R_n$$
$$\frac{\partial p_n}{\partial t} = D_p \frac{\partial^2 p}{\partial x^2} + G_p - R_p \tag{6.2.5}$$

6.2.2 Photo-generation

When the semiconductor is illuminated and incident photons energy hv is greater than bandgap E_g of the material, absorption and photo-generation occurs. The electron-hole generation rate is given by:

$$G_{photon}(x) = \Phi_0 \alpha e^{-\alpha x} \tag{6.2.6}$$

where Φ_0 is the incident flux density and α is the absorption coefficient of the material.

Here, the thermal generation of carriers is very little when compared with the photo-generation. Therefore, only optical generated carriers are in consideration, with the thermal generation neglected. The minority carrier generation can be written as:

$$G(x) = G_{photon}(x) = \Phi_0 \alpha e^{-\alpha x} \tag{6.2.7}$$

6.2.3 Carrier recombination

The recombination in the base region of the Npn HPT semiconductor material can be described as occurring in three processes. They are given by [13]:

$$\text{Rediative Recombination: } R_{Rad} = \frac{\Delta n}{\tau_{Rad}} \tag{6.2.8}$$

$$\text{SRH Recombination: } R_{SRH} = \frac{\Delta n}{\tau_{SRH}} \tag{6.2.9}$$

$$\text{Auger Recombination: } R_A = \frac{\Delta n}{\tau_A} \tag{6.2.10}$$

The total recombination effect is summarised as:

$$R_n = R_{Rad} + R_{SRH} + R_A = \frac{\Delta n}{\tau_n} \tag{6.2.11}$$

where: $\frac{1}{\tau_n} = \frac{1}{\tau_{Rad}} + \frac{1}{\tau_{SRH}} + \frac{1}{\tau_A}$

τ_n is total effective minority electron recombination lifetime

τ_{rad} is radiative recombination lifetime

τ_{SRH} is SRH lifetime

τ_A is Auger lifetime

6.2.4 Basic assumption

When the device is under steady state, the minority concentration variation rate becomes zero. Here, the steady state condition is considered.

$$\frac{\partial n_p}{\partial t} = 0 \text{ and } \frac{\partial p_n}{\partial t} = 0 \tag{6.2.12}$$

Co-opting all the effects of diffusion, recombination, and photo-generation, using the steady state condition above, the device under illumination can be modelled as:

For base region: $$\mathrm{D}_n \frac{d^2 n_p}{dx^2} - \frac{n_p - n_{p0}}{\tau_n} + \phi(a)\alpha_b \exp(-\alpha_b x) = 0$$

For subcollector region: $$\mathrm{D}_p \frac{d^2 p_n}{dx^2} - \frac{p_n - p_{n0}}{\tau_p} + \phi(c)\alpha_{sc} \exp(-\alpha_{sc} x) = 0 \tag{6.2.13}$$

where:

D_n (D_p) is the diffusion coefficient of minority carrier electrons (holes)

τ_n (τ_p) is the lifetime of minority carrier electron (holes)

n_p (p_n) is the total electron (hole) density contribution

n_{p0} (p_{n0}) is the equilibrium electron (hole) density contribution

α_b (α_{sc}) is the optical absorption coefficients for the base (subcollector) layer

$\phi(a)$ is the value of incident flux density at the emitter-base junction

$\phi(c)$ is the value of incident flux density at the collector-sub-collector junction

Using equation (4.3.24) above, the minority carrier distribution in the highly doped base and subcollector layer can be summarised. The next step is to further analyse and find the most accurate solution.

6.2.5 Solution of steady state continuity equation

The equations for minority carrier (electrons in the base and holes in the subcollector) distribution are described above. The next step is to find the solution of those equations. The equation of the base is solved first. Then a similar method can be used for the sub-collector. The unknown parameter here is n_p. The solution can be adopted from Engineering Mathematic [20] knowledge, which consists of complementary function and particular integral.

Using equation $L_n = \sqrt{D_n \tau_n}$, the equation (4.3.24) can be rearranged.

$$\frac{d^2 n_p}{dx^2} - \frac{(n_p - n_{po})}{L_n^{\ 2}} + \frac{\phi(a)\alpha_b \exp(-\alpha_b x)}{D_n} = 0 \tag{6.2.14}$$

$$\Rightarrow \quad \frac{d^2 n_p}{dx^2} - \frac{n_p}{L_n^{\ 2}} = -\frac{\phi(a)\alpha_b \exp(-\alpha_b x)}{D_n} - \frac{n_{po}}{L_n^{\ 2}} \tag{6.2.15}$$

The complementary function is as the solution of (4.3.26) left part which is in the form of:

$$n_{p,CF} = A\exp(-\frac{x}{L_n}) + B\exp(\frac{x}{L_n}) \tag{6.2.16}$$

where A and B are unknown items.

The particular integral is as the solution of (4.3.26) right part which is in the form of:

$$n_{p,PI} = C\exp(-\alpha x) + D \tag{6.2.17}$$

Where C and D are unknown items

$$\frac{dn_{p,PI}}{dx} = -C\alpha\exp(-\alpha x) \tag{6.2.18}$$

$$\frac{d^2 n_{p,PI}}{dx^2} = C\alpha^2\exp(-\alpha x) \tag{6.2.19}$$

Inserting (4.3.29) and (4.3.30) into equation (4.3.26),

$$C\alpha^2\exp(-\alpha x) - \frac{C\exp(-\alpha x) + D}{L_n{}^2} = -\frac{\phi(a)\alpha_b\exp(-\alpha_b x)}{D_n} - \frac{n_{po}}{L_n{}^2} \tag{6.2.20}$$

Comparing the left and right sides of the equation,

$$\begin{cases} \exp(-\alpha x)[C\alpha^2 - \dfrac{C}{L_n{}^2}] = -\dfrac{\phi(a)\alpha_b}{D_n} \\ -\dfrac{D}{L_n{}^2} = -\dfrac{n_{po}}{L_n{}^2} \end{cases} \tag{6.2.21}$$

$$\Rightarrow \begin{cases} C = -\dfrac{\phi(a)\alpha_b L_n{}^2}{(L_n{}^2\alpha_b{}^2 - 1)D_n} = -\dfrac{\phi(a)\alpha_b\tau_n}{L_n{}^2\alpha_b{}^2 - 1} \\ D = n_{po} \end{cases} \tag{6.2.22}$$

So the solution can be summarised in the form of sum of the complementary function and particular integral:

$$n_p(x) = n_{p,CF} + n_{p,PI} = A\exp(-\frac{x}{L_n}) + B\exp(\frac{x}{L_n}) + C\exp(-\alpha x) + D \tag{6.2.23}$$

Inserting C and D,

$$n_p(x) = A\exp(-\frac{x}{L_n}) + B\exp(\frac{x}{L_n}) - \frac{\phi(a)\alpha_b\tau_n}{L_n{}^2\alpha_b{}^2 - 1}\exp(-\alpha x) + n_{po} \tag{6.2.24}$$

Here from the equation above, there are two unknown items, A and B. Therefore, two more equations are needed to get their values. Boundary conditions of the two sides of the base layer are involved to achieve the equations. For the base region, since the device is working in 2-T configuration, there is no electrical contact at the base terminal. The number of the excess minority carriers (electrons) becomes an input flux dependent parameter. In this modelling unity generation of electron-hole pair with input flux is assumed. At the same time, surface recombination limits the excess minority carrier concentration. Using the absorption model and involving all the parameters, the boundary condition of the base region can be given by:

Interface of E-B junction, where x = 0,

$$n_p(x=0) = n_p(0) = \frac{\phi(a)\exp(-\alpha_b \times 0)}{z(\alpha)S_n} = \frac{\phi(a)}{z(\alpha)S_n} \tag{6.2.25}$$

Interface of B-C junction, where $x = w_b$,

$$\begin{aligned} n_p(x=w_b) = n_p(w_b) = \frac{\phi(a)\exp(-\alpha_b \times w_b)}{z(\alpha)S_n} + n_{po} &= \frac{\phi(a)}{z(\alpha)S_n} \cdot \exp(-\alpha_b w_b) + n_{po} \\ &= n_p(0) \cdot \exp(-\alpha_b w_b) + n_{po} \end{aligned} \tag{6.2.26}$$

S_n is the surface recombination velocity of the electrons. Since the surface recombination reduces the responsivity, it is necessary to carefully model this parameter. As we know, lower incident wavelength photon has higher energy. High energy photons are more easily absorbed near the surface, and correspondingly, the loss of photo-generated carriers is higher. So an additional surface recombination parameter $z(\alpha)$ is added to adjust the value of the surface recombination velocity for electrons. It is a simulation parameter and the value of it is wavelength dependent. By iterating the values of $z(\alpha)$ in equations (4.3.36) and (4.3.37) with reference to the measured value of responsivity at a particular wavelength [13], the value of $z(\alpha)$ can be derived. Furthermore, in the interface of the B-C junction, where $x = w_b$, the equilibrium electron contribution is also considered.

Applying the boundary conditions:

$$\begin{cases} n_p(0) = A + B + C + n_{po} \\ n_p(w_b) = A\exp(-\frac{w_b}{L_n}) + B\exp(\frac{w_b}{L_n}) + C\exp(-\alpha w_b) + n_{po} \end{cases} \tag{6.2.27}$$

$$\Rightarrow \begin{cases} A+B=n_p(0)-C-n_{po} \\ n_p(w_b)=n_p(0)\cdot\exp(-\alpha_b w_b)+n_{po}=A\exp(-\frac{w_b}{L_n})+B\exp(\frac{w_b}{L_n})+C\exp(-\alpha w_b)+n_{po} \end{cases}$$

(6.2.28)

$$\Rightarrow \begin{cases} A+B=n_p(0)-C-n_{po} \\ A\exp(-\frac{w_b}{L_n})+B\exp(\frac{w_b}{L_n})=-C\exp(-\alpha w_b)+n_p(0)\cdot\exp(-\alpha_b w_b) \end{cases}$$

(6.2.29)

Using the equation set above, the solution of unknown items A and B can be solved using the matrix form:

$$\begin{pmatrix} \exp(-\frac{w_b}{L_n}) & \exp(\frac{w_b}{L_n}) \\ 1 & 1 \end{pmatrix}\begin{pmatrix} A \\ B \end{pmatrix}=\begin{pmatrix} -C\exp(-\alpha w_b)+n_p(0)\cdot\exp(-\alpha_b w_b) \\ n_p(0)-C-n_{po} \end{pmatrix}$$

(6.2.30)

$$\begin{pmatrix} A \\ B \end{pmatrix}=\begin{pmatrix} \exp(-\frac{w_b}{L_n}) & \exp(\frac{w_b}{L_n}) \\ 1 & 1 \end{pmatrix}^{-1}\begin{pmatrix} -C\exp(-\alpha w_b)+n_p(0)\cdot\exp(-\alpha_b w_b) \\ n_p(0)-C-n_{po} \end{pmatrix}$$

(6.2.31)

Using matrix property $\begin{pmatrix} a & b \\ c & d \end{pmatrix}^{-1}=\frac{1}{ad-bc}\begin{pmatrix} d & -b \\ -c & a \end{pmatrix}$, and definition of hyperbolic function $\sinh x=\frac{e^x-e^{-x}}{2}$,

$$\begin{pmatrix} A \\ B \end{pmatrix}=\frac{1}{-2\sinh(\frac{w_b}{L_n})}\begin{pmatrix} 1 & -\exp(\frac{w_b}{L_n}) \\ -1 & \exp(-\frac{w_b}{L_n}) \end{pmatrix}\begin{pmatrix} -C\exp(-\alpha w_b)+n_p(0)\cdot\exp(-\alpha_b w_b) \\ n_p(0)-C-n_{po} \end{pmatrix}$$

(6.2.32)

$$\begin{pmatrix} A \\ B \end{pmatrix}=\frac{1}{-2\sinh(\frac{w_b}{L_n})}\begin{pmatrix} -C\exp(-\alpha_b w_b)+n_p(0)\exp(-\alpha_b w_b)... \\ +C\exp(\frac{w_b}{L_n})-n_p(0)\exp(\frac{w_b}{L_n})+n_{po}\exp(\frac{w_b}{L_n}) \\ C\exp(-\alpha_b w_b)-n_p(0)\exp(-\alpha_b w_b)... \\ -C\exp(-\frac{w_b}{L_n})-n_p(0)\exp(-\frac{w_b}{L_n})-n_{po}\exp(-\frac{w_b}{L_n}) \end{pmatrix}$$

(6.2.33)

Multiplying exp($-x/L_n$) with A and exp(x/L_n) with B, the equation above becomes:

$$\begin{pmatrix} A\exp(-\frac{x}{L_n}) \\ B\exp(\frac{x}{L_n}) \end{pmatrix} = \frac{1}{-2\sinh(\frac{w_b}{L_n})} \cdot \begin{pmatrix} -C\exp(-\alpha_b w_b - \frac{x}{L_n}) + n_p(0)\exp(-\alpha_b w_b - \frac{x}{L_n})\ldots \\ +C\exp(\frac{w_b - x}{L_n}) - n_p(0)\exp(\frac{w_b - x}{L_n}) + n_{po}\exp(\frac{w_b - x}{L_n}) \\ C\exp(-\alpha_b w_b + \frac{x}{L_n}) - n_p(0)\exp(-\alpha_b w_b + \frac{x}{L_n})\ldots \\ -C\exp(\frac{x - w_b}{L_n}) - n_p(0)\exp(\frac{x - w_b}{L_n}) - n_{po}\exp(\frac{x - w_b}{L_n}) \end{pmatrix} \tag{6.2.34}$$

$$A\exp(-\frac{x}{L_n}) + B\exp(\frac{x}{L_n}) = \frac{1}{-2\sinh(\frac{w_b}{L_n})} \cdot \begin{pmatrix} -C\exp(-\alpha_b w_b - \frac{x}{L_n}) + n_p(0)\exp(-\alpha_b w_b - \frac{x}{L_n})\ldots \\ +C\exp(\frac{w_b - x}{L_n}) - n_p(0)\exp(\frac{w_b - x}{L_n}) + n_{po}\exp(\frac{w_b - x}{L_n})\ldots \\ +C\exp(-\alpha_b w_b + \frac{x}{L_n}) - n_p(0)\exp(-\alpha_b w_b + \frac{x}{L_n})\ldots \\ -C\exp(\frac{x - w_b}{L_n}) - n_p(0)\exp(\frac{x - w_b}{L_n}) - n_{po}\exp(\frac{x - w_b}{L_n}) \end{pmatrix} \tag{6.2.35}$$

$$A\exp(-\frac{x}{L_n}) + B\exp(\frac{x}{L_n}) = \frac{1}{-\sinh(\frac{w_b}{L_n})} \cdot \begin{pmatrix} C\exp(-\alpha_b w_b)\sinh(\frac{x}{L_n}) + n_p(0)\exp(-\alpha_b w_b)\sinh(-\frac{x}{L_n})\ldots \\ +C\sinh(\frac{x - w_b}{L_n}) + n_{po}\sinh(\frac{w_b - x}{L_n}) \end{pmatrix} \tag{6.2.36}$$

$$A\exp(-\frac{x}{L_n})+B\exp(\frac{x}{L_n})=\frac{1}{\sinh(\frac{w_b}{L_n})}\{\sinh(\frac{x}{L_n})\exp(-\alpha_b w_b)[-C+n_p(0)]$$
$$+\sinh(\frac{x-w_b}{L_n})[C-n_p(0)+n_{po}]\} \quad (6.2.37)$$

By now, the solution of steady state continuity equation is achieved:

$$n_p=\frac{1}{\sinh(\frac{w_b}{L_n})}\{\sinh(\frac{x}{L_n})\exp(-\alpha_b w_b)[\frac{\phi(a)\alpha_b\tau_n}{L_n{}^2\alpha_b{}^2-1}+n_p(0)]$$
$$+\sinh(\frac{x-w_b}{L_n})[-\frac{\phi(a)\alpha_b\tau_n}{L_n{}^2\alpha_b{}^2-1}-n_p(0)+n_{po}]\}-\frac{\phi(a)\alpha_b\tau_n}{L_n{}^2\alpha_b{}^2-1}\exp(-\alpha x)+n_{po}$$
$$(6.2.38)$$

The current at the base-collector junction $I_n(\lambda)$ can be obtained using equation [19]:

$$I_n(\lambda)=qD_nA_{EB}\left.\frac{dn_p}{dx}\right|_{x=w_b} \quad (6.2.39)$$

where:

$$\frac{dn_p}{dx}=\frac{1}{\sinh(\frac{w_b}{L_n})}\{\cosh(\frac{x}{L_n})\exp(-\alpha_b w_b)\frac{1}{L_n}[-C+n_p(0)]+\cosh(\frac{x-w_b}{L_n})\frac{1}{L_n}[C-n_p(0)+n_{po}]\}$$
$$-C\alpha_b\exp(-\alpha_b x)+0$$
$$(6.2.40)$$

$$\left.\frac{dn_p}{dx}\right|_{x=w_b}=\frac{1}{\sinh(\frac{w_b}{L_n})}\{\cosh(\frac{w_b}{L_n})\exp(-\alpha_b w_b)\frac{1}{L_n}[-C+n_p(0)]+\frac{1}{L_n}[C-n_p(0)+n_{po}]\}$$
$$-C\alpha_b\exp(-\alpha_b w_b)$$
$$(6.2.41)$$

and A_{EB} is E-B junction area.

So, the excess minority carriers' (electrons) current in the base region is given by:

$$I_n(\lambda) = \frac{qD_n A_{EB}}{L_n \sinh(\frac{w_b}{L_n})}\{C[-\alpha_b L_n \exp(-\alpha_b w_b)\sinh(\frac{w_b}{L_n}) - \cosh(\frac{w_b}{L_n})\exp(-\alpha_b w_b) + 1]$$

$$+ n_p(0)[\cosh(\frac{w_b}{L_n})\exp(-\alpha_b w_b) - 1] + n_{po}\}$$

(6.2.42)

where: $C = -\frac{\phi(a)\alpha_b \tau_n}{L_n^{\ 2}\alpha_b^{\ 2} - 1}$

Using a similar method, the collector current in the subcollector can be modelled and achieved as:

$$I_p(\lambda) = -\frac{qD_p A_C}{L_p \sinh(\frac{w_{sc}}{L_p})}\{C'[-\alpha_{sc} L_p \exp(-\alpha_{sc} w_{sc})\sinh(\frac{w_{sc}}{L_p}) - \cosh(\frac{w_{sc}}{L_p})\exp(-\alpha_{sc} w_{sc}) + 1]$$

$$+ p_n(w_b + w_{dep})[\cosh(\frac{w_{sc}}{L_p})\exp(-\alpha_{sc} w_{sc}) - 1] + p_{no}\}$$

(6.2.43)

where: $C' = -\frac{\phi(c)\alpha_{sc}\tau_p}{L_p^{\ 2}\alpha_{sc}^{\ 2} - 1}$

6.2.6 Depleted collector absorption

Since the collector here is fully depleted and there is a strong electric field existing inside, it is assumed that there is no generation-recombination but there is a process of photo-generation in this region. So, the optical flux absorption can be modelled by:

$$I_{ph}(\lambda) = qA_C \int_0^{w_c} \phi(b)\alpha_c \exp(-\alpha_c x)dx \qquad (6.2.44)$$

where $\phi(b)$ is the input flux density at the B-C interface, α_c is the absorption coefficient of the depleted collector region and A_C is the area of the collector.

The solution of the equation can be given by:

$$I_{ph}(\lambda) = qA_C\phi(b)[1 - \exp(-\alpha_c x)] \tag{6.2.45}$$

6.2.7 Responsivity

The current flows through the device can be given as the sum of all current components. They are I_n in the base region I_{ph} in the collector region and I_p in the subcollector region. The equation is written as:

$$I_c = I_n + I_{ph} + I_p \tag{6.2.46}$$

Each part of the items in the equation is wavelength dependent. The responsivity is defined as the ratio of photogenerated current to the input optical power. The equation used in the simulation can be given by:

$$R = \frac{I_c}{hv\phi(a)} \tag{6.2.47}$$

6.2.8 Modelling results

Using the parameters in table 6.1, the theoretical responsivity of our HPTs can be simulated.

Table 6.1: Material parameters used for AlGaAs/GaAs HPT simulation

Parameter	Value	Parameter	Value	Reference
$D_n\ (cm^2s^{-1})$	50	$D_p\ (cm^2s^{-1})$	4	[21]
$\tau_n\ (s)$	1×10^{-9}	$\tau_p\ (s)$	1.2×10^{-9}	[19, 22]
$L_n\ (cm)$	2.2×10^{-4}	$L_p\ (cm)$	0.7×10^{-4}	[19]
$S_n\ (cm\cdot s^{-1})$	3×10^{4}	$S_p\ (cm\cdot s^{-1})$	$\sim10^{6}$	[23, 24]
$n_{po}\ (cm^{-3})$	2.2×10^{-7}	$p_{no}\ (cm^{-3})$	8.8×10^{-7}	[24]
$\alpha_b(635nm)$	$3.9\times10^{4}cm^{-1}$	$\alpha_b(850nm)$	$4.7\times10^{4}cm^{-1}$	[11, 21]
$\alpha_c(635nm)$	$3.9\times10^{4}cm^{-1}$	$\alpha_c(850nm)$	$8.3\times10^{4}cm^{-1}$	[11, 21]
$\alpha_{sc}(635nm)$	$3.9\times10^{4}cm^{-1}$	$\alpha_{sc}(850nm)$	$0.3\times10^{4}cm^{-1}$	[11, 21]
$\phi(a)(635nm)$	$2.1\times10^{14}s^{-1}$	$\phi(a)(850nm)$	$2.9\times10^{14}s^{-1}$	
$\phi(b)(635nm)$	$1.5\times10^{14}s^{-1}$	$\phi(b)(850nm)$	$2.8\times10^{14}s^{-1}$	
$\phi(c)(635nm)$	$0.2\times10^{14}s^{-1}$	$\phi(c)(850nm)$	$1.8\times10^{14}s^{-1}$	

Using parameters in table 6.1 and equations from 6.53 to 6.58, the Matlab simulation result is given in figure 6.12. And the measured data is also given for the results' validation.

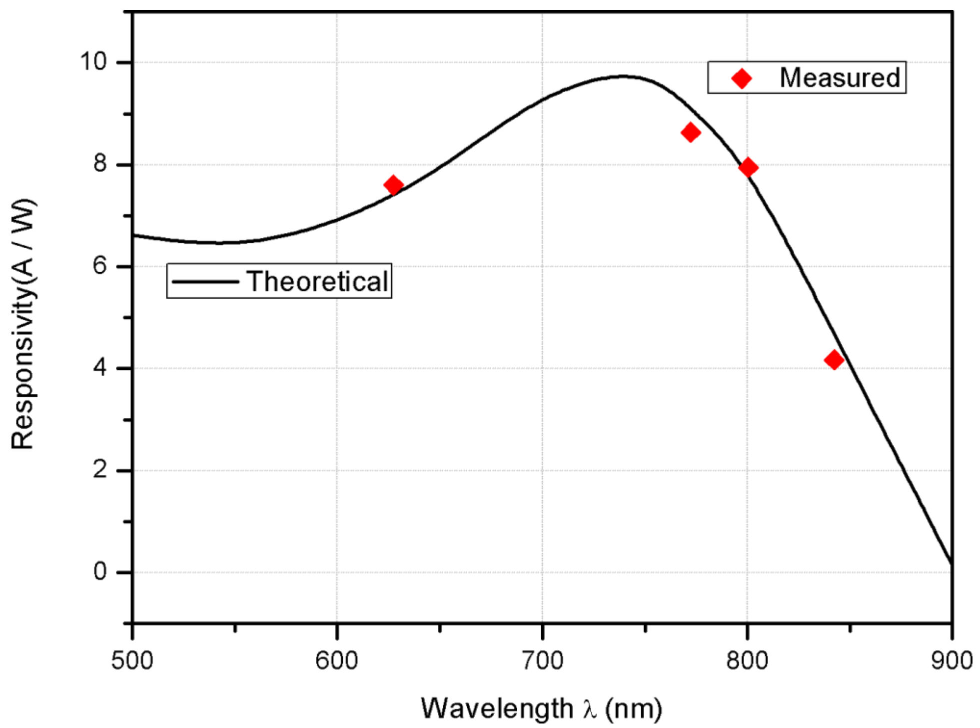

Figure 6.12: Measured and simulated spectral response of the $Al_{0.3}Ga_{0.7}As$/GaAs HPT

Figure 6.12 shows the simulated spectral response with measured data [13]. It is noticeable that the measured results at 635nm, 780nm, 808nm, and 850nm [25] show a good agreement with the predicted response. The difference between the simulation and measurement can be explained as the coupling efficiency is set as 100% here and the signal loss is not included in the calculation. The responsivity achieves the maximum value, of around 760nm. This also shows a good agreement with our absorption model. From 760nm, the value (780nm) of the responsivity begins to decrease, while after the wavelength increases beyond 800nm, the curve drops quickly. This is the reason of the decrease both in η_c and α. The simulated collector currents of the $Al_{0.3}Ga_{0.7}As$/GaAs HPT at 650nm and 850nm in Matlab are shown in figure 6.13.

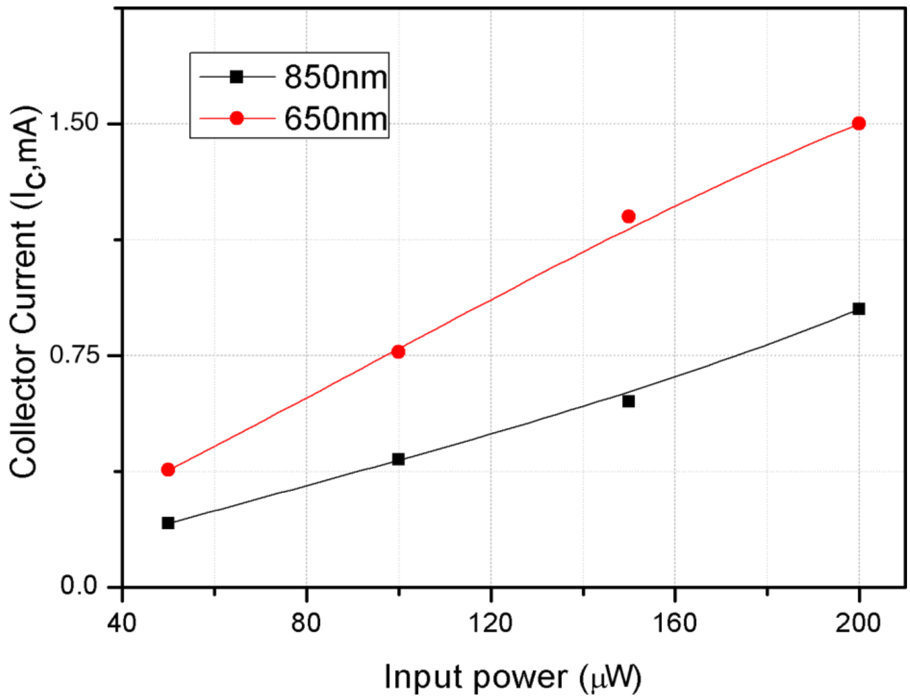

Figure 6.13: Simulated collector current of the $Al_{0.3}Ga_{0.7}As/GaAs$ HPT

It is necessary to point out that the surface recombination is the parameter which reduces the simulation result and needs to be carefully modelled. The grading emitter-base heterojunction interface can minimise the recombination due to misfit dislocations [13]. Despite the widely different surface preparation and measurement techniques, the surface recombination data for GaAs follows the same general trend of proportionality to bulk doping [23].

As we know, lower incident wavelength photons have higher energy. High energy photons are easily absorbed near the surface and correspondingly, the loss of photon-generated carriers is higher. So an additional surface recombination parameter $z(\alpha)$ is added to adjust the value for the surface recombination velocity of the electrons. This is a simulation parameter and the value of it is wavelength dependent. Iterate the values of $z(\alpha)$ in equations (4.3.26) and (4.3.37) with reference to the measured value of responsivity at particular wavelength [23]. The value of $z(\alpha)$ can be achieved and decided.

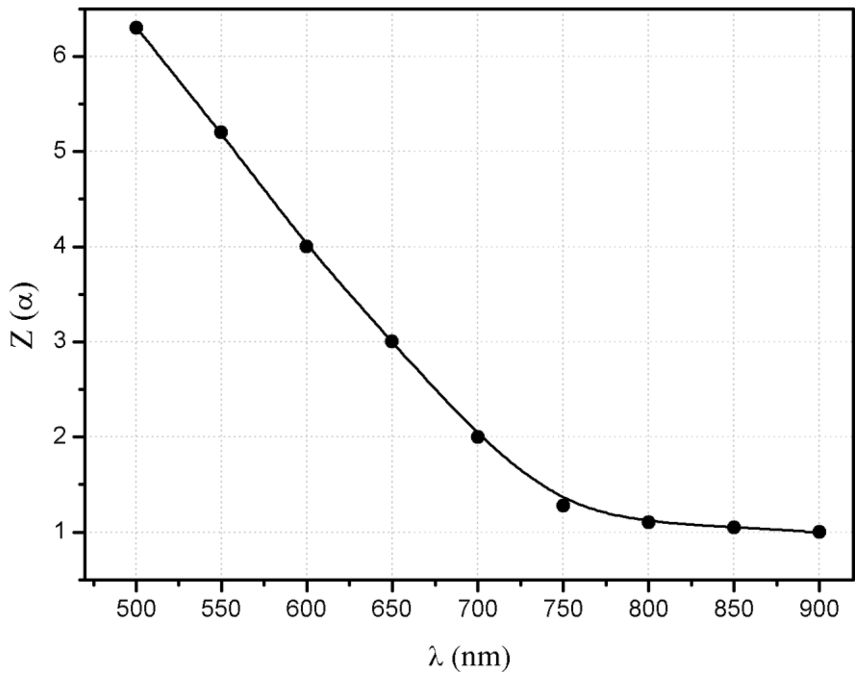

Figure 6.14: Surface recombination parameter z(α) with incident wavelength for the $Al_{0.3}Ga_{0.7}As/GaAs$ HPT

Figure 6.14 shows the modelled *z(α)* with different input wavelength. It is noticed that the shape of the curve in the figure follows a near exponential decay. The value of *z(α)* at the lower wavelength is higher. This indicates that a great number of carriers have been lost due to surface recombination.

References

[1] Bouhdada, A.M., Marrakh, R., Vigue, F., Faurie, J. P. “Modeling of the spectral response of PIN photodetectors impact of exposed zone thickness, surface recombination velocity and trap concentration”, Microelectronics Reliability, vol. 44, pp. 223-8, 2004.

[2] Hanzaz, M.B., Moroy, A., Munoz, E., Cibart, E., Omnes, F. P. “Modelling of the spectral response of $Al_xGa_{1-x}N$ p-n junction photodetectors”, European Physical Journal, Applied Physics, vol.11, pp. 29-34, 2000.

[3] Gonzalez-Cuevas, J.A.R., Abedin, T. F., Elsayed-Ali, M. N., Hani E. “Modeling of the temperature-depndent spectral response of $In_{1-x}Ga_xSb$ infrared photodetectors”, Optical Engineering, vol.45, pp. 044001, 2006.

[4] Zheng, H., Yong, K., Ying-Wen, T., Xue,L., Jia-Xiong, F. “Study on the spectral response of the Schottky photodetector of GaN”, Chinese Physics, vol 15, pp. 1325-9, 2006.

[5] Lai, K.S., Huang, J. C., Hsu, K. Y. J. “Design and properties of phototransistor photodetector in standard 0.35-m SiGe BiCOMOS technology”, IEEE Transactions on Electron Devices, vol. 55, pp. 774-81, 2008.

[6] De Salles, A. A., Hackbart, A. S., Spalding, L. N. “A simple model for the GaAs HBT high-frequency performance under optical illumination”, Microwave and Optical Technology Letters, vol. 7, pp. 392-5, 1994.

[7] Sridhara, R. F., Frimel, S.M., Roenker, K.P., Pan, N., Elliott, J. “Performance enhancement of GaInP/GaAs heterojunction bipolar phototransistors using dc base bias”, Journal of Lightwave Technology, vol. 16, pp. 1101-6, 1998.

[8] Adachi, S. “Optical Functions of InGaAsP Tables”, in Properties of Indium Phosphide: INSPEC, EMIS Data Review Series No. 6, 1991, pp. 416 – 428.

[9] Bashar. S. A. “Study of Indium Tin Oxide (ITO) for Novel Optoelectronic Devices”, Ph.D thesis, King’s College London, 1998.

[10] Lush, G. B., Melloch, M. R., Lundstrom, M. S. “Concentration-dependent optical-absorption coefficient in n-type GaAs”, Journal of Applied Physics, 74, 4694, 1993.

[11] Casey, H. C. J., Sell, D. D., Wecht, K. W. “Concentration dependence of the absorption coefficient for n- and p-type GaAs between 1.3 and 1.6 eV.”, Journal of Applied Physics, vol. 46, pp. 250-257, 1975.

[12] Khan, H. A., Rezazadeh, A. A. “Spectral response modelling of GaAs-based heterojunction phototransistors for short wavelength detection”, Optoelectronics, IET, vol. 4, pp. 57-63, 2010.

[13] Khan, H. "spectral response modelling and analysis of heterojuction bipolar phototransistors", Ph.D thesis, Microwave and Communication Systems Research Group, School of Electrical and Electronics Engineering, University of Manchester, 2010.

[14] Tiwari, S., Wright, S. L., Kleinsasser, A. W. "Transport and related properties of (Ga, Al) As/GaAs double heterostructure bipolar junction transistors", IEEE Transactions on Electron Devices, vol. ED-34, pp. 185-98, 1987.

[15] Tan, S. W., Chen, W. T., Chu, M. Y., Lour, W. S. "A new model for phototransistor", Department of Electrical Engineering, Taiwan Ocean University, Junction Technology, IWJT '04, The fourth International Workshop, 2004.

[16] De Barros Jr, L.E.M., Paolella, A., Frankel, M.Y., Romero, M.A., Herczfeld, P.R., Madjar, A. "Photoresponse of microwave transistors to high-frequency modulated lightwave carrier signal", IEEE Transactions on Microwave Theory and Techniques, vol. 45, pp. 1368-74, 1997.

[17] Bashar, S. A. and Rezazadeh, A. A. "Fabrication and spectral response analysis of AlGaAs/GaAs and InP/InGaAs HPTs with transparent ITO emitter contacts", IEEE Proceedings-Optoelectronics, vol. 143, pp. 89-93, 1996.

[18] Sze, S. M. "Semiconductor Device, Physics and Technology", Bell Telephone Laboratories. Inc, 1985.

[19] Stroud, K. A. Engineering Mathematics, 4th ed: Bath Press, 1995.

[20] Lush, G. B. "Properties of GaAs", in EMIS data review series, 2nd ed: Inspec Publications, pp. 513-528, 1990.

[21] Chand, N., Houston, P. A., Robson, P. N. "Gain of a Heterojunction Bipolar Phototransistor", IEEE Transactions on Electron Devices, vol. ED- 32, pp. 622-627, 1985.

[22] Hwang, C. J. "Doping dependence of hole lifetime in n-type GaAs", Journal of Applied Physics, vol. 42, pp. 4408-13, 1971.

[23] Aspnes, D. E. "Recombination at semiconductor surfaces and interfaces", presented at th Proceedings of the Second Trieste ICTP-IUPAP Semiconductor Symposium on Surfaces and Interfaces, Physics and Electronics, Netherlands, 30 Aug - 3 Sept. 1982.

[24] Acket, G. A., Nijman, W., Lam H. T. "Electron Lifetime and diffusion constant in Germanium-doped Gallium Arsenide", Journal of Applied Physics, vol. 45, pp. 3033-3040, 1974.

[25] Khan, H. A., Rezazadeh, A. A. "Analytical Modeling of the spectral Response of Heterojuction Phototransistors", IEEE Electron Device Letters, vol. 30, no. 11, 2009.

Chapter 7. Conclusions and Future Work

7.1 Conclusions

Here, three distinctive areas of this work can be concluded, mainly the DC and optical characterisation of $In_{0.49}Ga_{0.51}P$/GaAs SHBTs/HPTs and DHBTs/DHPTs; small signal analysis and eye diagram simulations; spectral response modelling and analysis of HPTs. These are concluded as follows:

- **$In_{0.49}Ga_{0.51}P$/GaAs SHBT and DHBT DC and optical characterisations**

In this section both DC and optical characterisations of the $In_{0.49}Ga_{0.51}P$/GaAs SHBT and DHBT have been shown. Firstly, the Gummel plot and IV characterisations of the SHBT were presented. The ideality factor for the collector current is n_C = 1.08, while for the base current it is n_B = 1.29, indicating a high quality E-B interface and low recombination. The off-set voltage was extracted as small as 0.14V, which, along with a low ideality factor, was consistent with a lower conduction band energy difference ΔE_c between $In_{0.49}Ga_{0.51}P$ emitter and GaAs base. Then the optical characterisations of the DUT under a 2-terminal configuration were shown. The ratio of responsivity of the transistor to the responsivity of the B-C photodiode with an optical power of 150μW at 635nm and 850nm showed that these were approximately equal to the current gain β of the transistor. This was in agreement with conventional analysis of a photo transistor operation. The 3-terminal optical characterisations were measured under constant current base bias and constant voltage base bias, respectively. It was shown that current base bias, especially at low input optical power, could greatly improve optical gain of the phototransistor. However, there was no improvement in the optical gain with base constant voltage bias.

Accordingly, similar measurement with $In_{0.49}Ga_{0.51}P$/GaAs DHBT procedures were carried out, and the results were compared with the SHBT. From the DC measurements, the advantages of DHBTs, for example, lower offset voltage (40mV), lower turn on voltage (lower than 0.7V) and lower ideality factors (n_c =1.02 and n_b = 1.06), could be obtained. But since in the DHBT, the collector layer was made by a wide bandgap material InGaP. The responsivity of the DHPT at 850nm was quite a bit lower than the SHPT due to the fact that optical absorption of InGaP at 850nm is minimal. For 3-terminal configuration, the DHPT showed a different performance to the single HPT. No improvement in the DHBT could be obtained with addition of both the base constant current bias and the voltage.

In the optical study of DHPTs a new phenomena has been investigated which is related to the effects of the energy band bending in the base layer. During optical illumination of this device the slow photogenerated hole carriers will be blocked from diffusing towards the base region by the large valence energy band discontinuity of the wide band gap collector (InGaP). In this thesis this phenomena has clearly been demonstrated in the optical characterisations of the DHPT. In effect it is shown that the existence of this effect makes the DHPT a uni-travelling-carrier phototransistor (UTC-PD) with promising higher speed performance than the conventional SHPTs. This observation has been reported in the recent publication by the author (IEEE Quantum Electronics, November 2014).

- **Small signal analysis and eye diagram simulations**

In this work a detailed analysis of the applicability of using eye diagrams for $In_{0.49}Ga_{0.51}P$/GaAs HBTs characterisation, has been presented. As an initial step in the eye diagram simulations, both T- and hybrid-π mode equivalent circuit models were reviewed and compared. The $In_{0.49}Ga_{0.51}P$/GaAs DHBT small signal parameters based on the T equivalent circuit was introduced. The validity of the parameters were confirmed through the good agreement between the experimental results and those obtained by simulation using the commercial circuit simulator ADS. In addition, the estimated results of f_t and f_{max} matched the calculated values. Using these parameters, the eye diagram simulation was established. Firstly, the effects of bitrate increases upon the eye diagram deteriorations were studied. Given the various bitrate simulations, it was found that there was a strong relation between the -3dB bandwidth of the transistor, and the eye diagram qualities. This confirmed that the eye diagram is a power tool in the device performance evaluation. Furthermore, the bias dependent parameters were studied based on experimental data and those related to the eye diagrams. Eye parameters and their dependencies on the device parameters were discussed in detail. It was indicated that by changing device parameters, one could obtain the desired eye pattern to satisfy specific applications. This additional information is a step forward for designers, aiding them in obtaining the desired circuit bias points.

In addition, we have investigated for the first time the $In_{0.49}Ga_{0.51}P/GaAs$ DHPT performance by adopting a modified small signal T-model circuit [1]. It is shown that eye diagrams can provide more insight useful information than the traditional analysis methodology for device working under illumination. For example, at the same data rate, eye parameters can provide evidence of device deterioration with increasing intrinsic base resistance, R_{bbi}, where other tools would fail, such as photoresponse analysis. Through eye parameters analysis, various physical parameters of the optical device can be redesigned and optimised and this provides valuable insight information for device optimisation for future high performance optical components.

Furthermore eye diagram simulation has been used in order to provide a performance comparison between the $In_{0.49}Ga_{0.51}P/GaAs$ SHBT and the DHBT. The effect of layer structures and materials through the base time constant, τ_b and collector time constant, τ_c were clearly shown. By understanding the inter-dependencies of eye parameters and device parameters in the small signal model, the study showed that eye diagrams could help designers to develop a reverse design methodology, and obtain desired output signals. Eye diagrams were shown in this work not only as a mere visual measurement tool but also as a tool to characterise and optimise HBTs devices for demanding digital system applications.

- **Spectral response analysis of HPTs**

In this work, the modelling of the $Al_{0.3}Ga_{0.7}As/GaAs$ heterojunction phototransistors (HPTs) spectral response through a consideration of the structural point of view, as well as several material aspects of this device, including the material absorption coefficient, refractive index and doping concentration, has been analysed and discussed. In order to obtain accurate spectral response modelling results of GaAs-based HPTs for short-wavelength detection, firstly, the advanced absorption model was presented. The photon absorption was discussed for each layer structure in the device. The results show that collection efficiency should not be simply set as a unity during the modelling but as a geometry and incident wavelength dependent parameter.

The optical absorption coefficient shows the variations with doping concentrations which modify the semiconductor's band gap. The carefully extracted parameter profiles were involved in the accurate spectral response modelling. Then the modelling results for the interrelated responsivity and the collection efficiency versus wavelengths were presented.

The analytical spectral response model was developed by solving semiconductor continuity equations. By introducing accurate boundary conditions, the excess minority photo-carrier generation, diffusion and recombination were theoretically described [2]. A wavelength dependent surface recombination parameter $z(\alpha)$ was incorporated to model the surface recombination at lower wavelengths [3]. Since more photo-carriers were generated near the surface for higher energy photons (lower wavelength) [4], a near exponential decay curve was obtained for the $z(\alpha)$ modelling. This implied a considerable amount of photo-generated carriers which would not contribute to the photocurrent, and were lost due to recombination near the surface, particularly at low wavelengths [5]. Then, a good correlation between the modelling and the measured results was shown. Since analytical models do not require a prerequisite of current gain for the device, the above model built in this work can be widely utilised for device performance enhancement and optimisation [5].

7.2 Future work

In this thesis, the electrical and optical characterisations of various materials and geometries in HBTs for optical detection have been investigated. Although a great deal of information have been successfully achieved there are till some further issues which could be studied in the future.

- The optical illumination of RF response for SHPTs and DHPTs under various wavelengths could be performed.

- The effects of device geometry on the performance of the available devices (130µm, 100µm and 70µm) $In_{0.49}Ga_{0.51}P/GaAs$ and $Al_{0.3}Ga_{0.7}As/GaAs$ could be investigated. The experimental set-up may be modified to measure the responsivity of devices at other wavelengths such as 780 nm.

- The optical coupling efficiency of the measurement set-up could be further investigated and further improved.

  For instance, figure 5.2.1 shows optical coupling interface between a 100µm/250µm optical fibre and the device surface. Assuming the output laser from the fibre is a Gaussian beam, the beam profile on the surface of the device is an ellipse and the power intensity distribution the following [6]:

$$P(r) = P_o[1 - \exp(\frac{-2r^2}{{w_0}^2})] \tag{7.2.1}$$

  where r is the radial distance from the centre axis of the beam, P_0 is the total power output from the laser head, w_0 is the Gaussian beam radius and $P(r)$ is the power contained within a radius r.

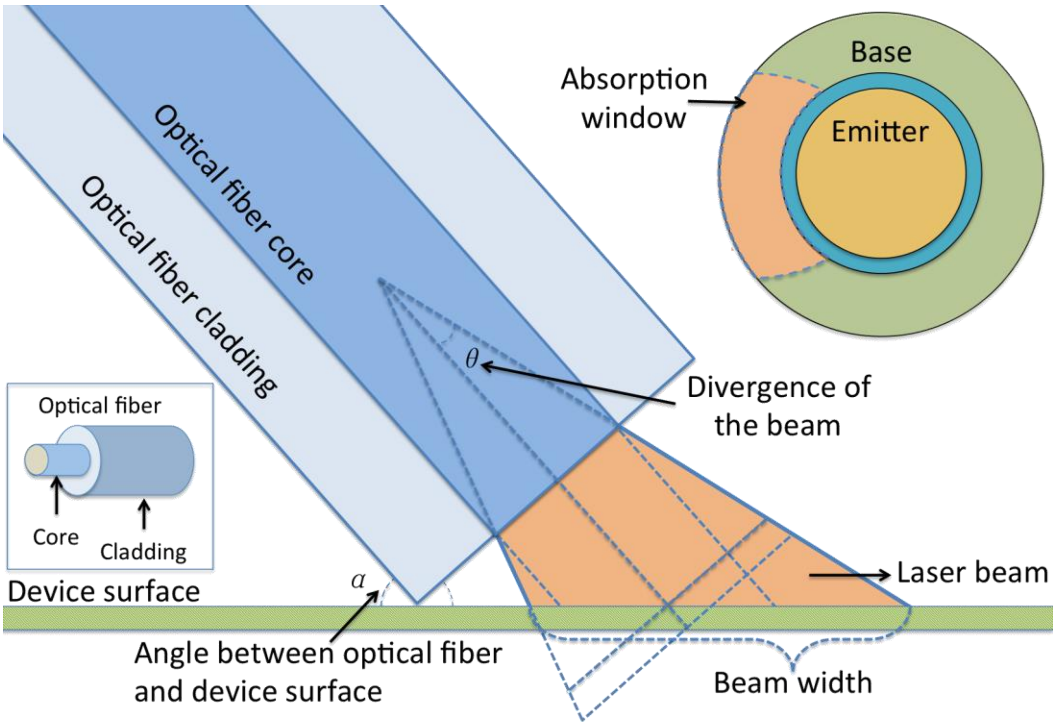

Figure 7.1: Optical coupling interface between 125µm/250µm optical fibre and the device surface

The absorption window of the device is shown at the top right of figure 7.1, which is smaller than the beam profile. The angle between optical fibre and device surface is measured as α = 55°. Calculating the optical coupling efficiency for the 100µm E-B device is 37%. So in future work, the accuracy of the calculation could be reviewed and the effects of the variation of coupling efficacy for different geometry devices included in the modelling.

- Although eye diagrams simulations were carried out in this work for small signal parameters, so it is desirable to carry out the eye diagram simulations using large signal model.

- It is reported in [7-9], that by employing step-graded B-C heterojuction InGaP/GaAs DHBTs, performance can be significantly improved (figure 7.2).

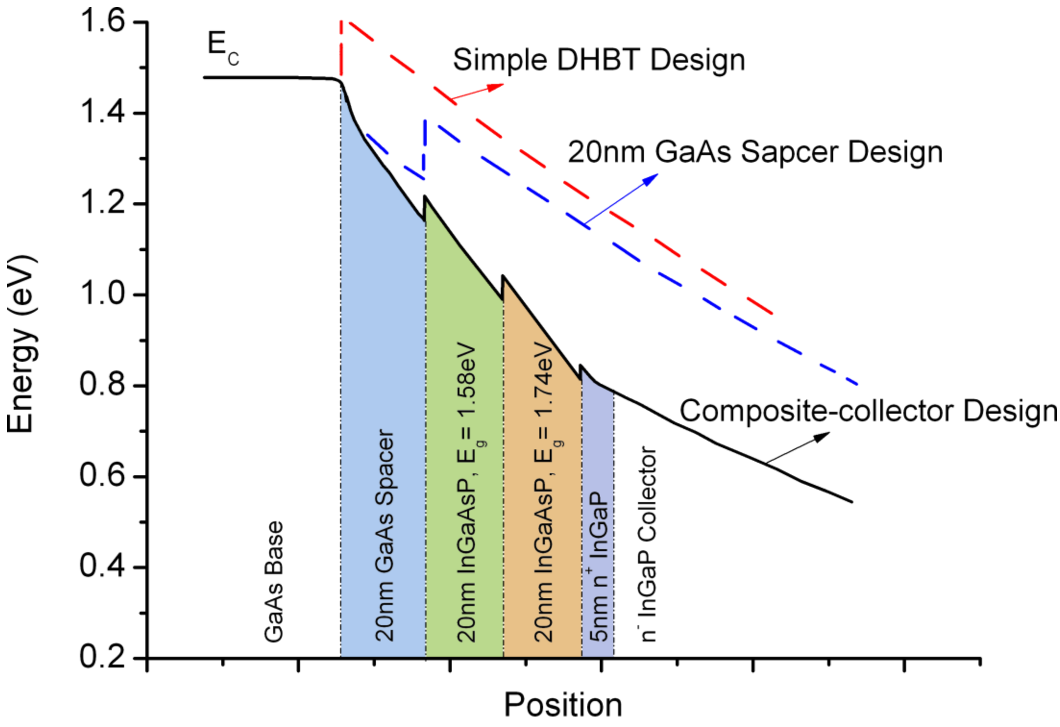

Figure 7.2: Numerically simulated conduction band diagram of the B-C junction of InGaP/GaAs DHBT with various design approaches at thermal equilibrium [7-9]

In the reference [7-9] it is reported that the measurements were made on device where a thin GaAs space layer between base and collector layer (table 3.1.1) inserted. The improvement in the current gain of the $In_{0.49}Ga_{0.51}P$/GaAs DHBT (wafer no. MR1095, emitter contact diameter = 100µm) comparing with the $In_{0.49}Ga_{0.51}P$/GaAs SHBT (wafer no. MR873, emitter contact diameter = 100µm) can be observed in figure 4.33. Evaluation of the effects of the B-C junction step-grading could be further investigated both by eye diagrams and analytical modelling.

References

[1] Zhang, Y., Rezazadeh, A. A., Khan, H. A., Sinulingga, E. P., Kyabaggu, P. B., Alim, M. A. "Simulation and analysis of InGaP/GaAs DHPTs using eye diagrams for short wavelength optical detection", Proceedings of European Microwave Week Conference, Rome, Italy, pp. 524-527, Oct. 2014.

[2] Khan, H. A., Rezazadeh, A. A. "Analytical modelling of the spectral response of heterojunction phototransistors", IEEE Electron Device Letters, vol. 30, pp. 1158-1160, 2009.

[3] Khan, H. A. and Rezazadeh, A. A. "Spectral response modelling of GaAs based heterojunction phototransistors for short wavelength detection", Optoelectronics, IET, vol. 4, pp. 57-63, 2010.

[4] Sze, S. M. "Physics of Semiconductor Devices", 2nd ed. USA: John Wiley & Sons, 2001.

[5] Khan, H. "Spectral response modelling and analysis of heterojuction bipolar phototransistors", Ph.D thesis, Microwave and Communication Systems Research Group, School of Electrical and Electronics Engineering, University of Manchester, 2010.

[6] Quimby, R. S. "Photonics and Lasers: An Introduction", John Wiley & Sons, Inc., 2006.

[7] Sotoodeh, M., Khalid, A. H., Sheng, H., Amin, F. A., Gokdemir, T., Rezazadeh, A. A., Knights, A. P., Button, C. C. "Direct extraction and numerical simulation of the base and collector delay times in double heterojunction bipolar transistors", IEEE Transactions on Electron Devices, vol. 46, no. 6, pp.1081-1086, June 1999.

[8] Sotoodeh, M., Khalid, A.H., Rezazadeh, A.A. "Bias dependence study of the HBT small-signal equivalent circuit elements using a new parameter extraction technique", High Performance Electron Devices for Microwave and Optoelectronic Applications, pp. 9-14, 1999.

[9] Rezazadeh, A.A., Sotoodeh, M., Dharmasiri, N. "Base-collector design optimisation of InGaP/GaAs DHBTs", High Performance Electron Devices for Microwave and Optoelectronic Applications, 8th IEEE International Symposium on, pp. 99-104, 2000.